PLASMA SPRAY DEPOSITION OF

HYDROXYAPATITE BASED COMPOSITES

AS A STEP TOWARDS BONE SCAFFOLDS

Diana García-Alonso García, Ingeniera M.Eng. M.Sc.

PhD   **2009**

PLASMA SPRAY DEPOSITION OF

HYDROXYAPATITE BASED COMPOSITES

AS A STEP TOWARDS BONE SCAFFOLDS

by

Diana García-Alonso García

(Ingeniera M.Eng. M.Sc.)

Supervisors: **Dr. L. Looney**, School of Mechanical and Manufacturing Engineering, Dublin City University, Ireland.

Dr. J. Stokes, School of Mechanical and Manufacturing Engineering, Dublin City University, Ireland.

Industrial Mentor: **Dr. M. Parco**, INASMET-Tecnalia, San Sebastián, Spain.

Declaration

I hereby certify that this material, which I now submit for assessment on the programme of study leading to the award of **Ph.D.** is entirely my own work, that I have exercised reasonable care to ensure that the work is original, and does not to the best of my knowledge breach any law of copyright, and has not been taken from the work of others save and to the extent that such work has been cited and acknowledged within the text of my work.

Signed: Diana García-Alonso García

ID No: 56125895

Date: 17/July/2009

Acknowledgments

First and foremost, I would like to thank Dr. María Parco (INASMET, Spain) for granting access to the Low Energy Plasma Spray facilities, for her suggestions, advices and guidance throughout this work. Also, I would like to acknowledge my supervisors Dr. Lisa Looney and Dr. Joseph Stokes.

I would like to thank, among others, the following people for their help:

- Dr. Tanya Levingstone for her help at the beginning of this work.
- Dr. Barry O'Connell (DCU) and Dr. Jose A. Jiménez (CENIM-CSIC, Madrid) for their advice and guidance on the XRD studies.
- Dr. Jose A. Rodríguez, Mrs. Mercedes Sánchez and Mr. Jesus Pinto for granting access to the attrition milling facilities and for their support while carrying out the powder characterization.
- Dr. Khaled Benyouis for his help on DOE.
- Mr. Carlos Vázquez (INASMET, Spain) for his help operating the low energy plasma spray system.

Thanks to INASMET (San Sebastian, Spain) and LERMPS-UTBM (Belfort, France) for their hospitality during a number of useful placements in their laboratories.

Publications arising from this work

1. '*Dependence of Thick Bio-coating properties on Low energy plasma spray parameters'* (Oral presentation)

   D. García-Alonso, M. Parco, J. Stokes, L. Looney

   International Thermal Spray Conference ITSC 2009. Las Vegas, USA

2. *'Plasma Spray of Free-standing Hydroxyapatite Components'* (Oral presentation)

   D. García-Alonso, M. Parco, J. Stokes, L. Looney

   − In proc. Bioengineering Ireland 15 (2009). Limerick, Ireland

3. '*Plasma Spray of Free-standing Components for Bone Tissue Engineering*' (Oral presentation)

   D. García-Alonso, T. Levingstone, M. Parco, J. Stokes

   − In proc. Bioceramics 21. Búzios, BRAZIL (2008)

   − In Key Engineering Materials 396-398 (2008) pp 695-698

4. '*Plasma Spray of free-standing components for bone tissue engineering*' (Poster)

   D. García-Alonso, L. Looney, J. Stokes

   International Thermal Spray Conference ITSC 2008. Maastricht, The Netherlands

The following presentations have been accepted for upcoming conferences:

1. '*Plasma Spray of Thick Bio-composite Coatings'* (Poster)

   D. García-Alonso, M. Parco, J. Stokes, L. Looney

   22nd European Conference of Biomaterials (ESB 2009). Lausanne, Switzerland

2. '*Low Energy Plasma Spraying of Thick-Biocomposite Coatings as a step towards Bone Scaffolds'* (Oral presentation)

   D. García-Alonso, M. Parco, J. Stokes, L. Looney

   European Materials Research Society fall meeting (E-MRS 2009). Warsaw, Poland

Plasma Spray Deposition of Hydroxyapatite Based Composites as a Step towards Bone Scaffolds
Diana García-Alonso García, Ingeniera M.Eng. M.Sc.

Hydroxyapatite, (HA), is a calcium phosphate bioceramic that has been widely used in orthopaedics and dentistry due to its biocompatibility and osteoconductivity. However, its poor bulk mechanical properties have limited its use to situations where it is applied as a coating on metallic surfaces, generally using plasma spraying. If processing solutions can be identified to improve mechanical characteristics (particularly fracture toughness) and generate the required porous architecture, this material has potential for use as a scaffold in bone substitute applications.

It is hypothesised in this research that the required property profile can successfully be achieved using atmospheric plasma spray (APS) technology and compositions including polymeric and ceramic additions. The aim is to produce thick deposits of such biocomposites as a step towards generating free-standing bone scaffolds. The complex nature of the process, and the different characteristics and thermal properties of these materials make this a challenging study.

Initial tests identified a low energy plasma spray (LEPS) system as the most suitable technique to spray HA without major phase decomposition or crystallinity decrease, but also to accommodate polymer feedstock. A reference HA series of samples was produced and compared with those having Polycaprolactone (PCL) and Titania (TiO_2) additions. Statistically designed experiments were used to determine the effect of three process parameters on HA coating properties. Models relating the effects of the variables on the coating properties were then developed and the optimal parameters were selected to produce the biocomposite coatings.

The addition of TiO_2 was found to improve the fracture toughness of HA up to 60%. PCL only slightly improved the percentage of porosity, but significantly increased interconnectivity. It has been established that LEPS can produce thick HA deposits incorporating either polymeric or ceramic second phases with interconnected porosity typical of cortical bone, and mechanical properties in the range of those of spongy bone. With porosity being a restricting characteristic, results point to limited likelihood that APS can be used to form bone scaffolds. However, they do have significant value for biomedical applications such as implant coating and drug delivery.

Table of Contents

List of figures

List of tables

List of abbreviations

3DP	Three-dimensional Printing
ANOVA	Analysis of variance
APS	Atmospheric Plasma Spraying
ASTM	American Society for Testing and Materials
BS	British Standards
BSE	Back-scattered electrons
CG	Carrier gas
CNT	Carbon nano-tubes
CTE	Coefficient of Thermal Expansion
DDS	Drug Delivery System
DOE	Design of Experiments
DSC	Differential Scanning Calorimetry
DTA	Differential Thermal Analysis
EDX	Energy-dispersive X-Ray Spectroscopy
FTIR	Fourier Transform Infrared Spectroscopy
HA	Hydroxyapatite
HVOF	High velocity oxyfuel
IR	Infrared
ISO	International Organization for Standarization
J.C.P.D.S.	Joint Committee on Powder Diffraction Standards
LEPS	Low Energy Plasma Spraying
LPE	Linear Polyethylene
MDPE	Medium Density Polyethylene
OA	Oxyapatite
PAEK	Polyaryletherketone
PBS	Phosphate Buffered Saline Solution
PCL	Polycaprolactone
PEEK	Polyetheretherketone
PFA	Poly(tetrafluoroethylene-co-perfluoropropylvinylether)
PG	Plasma gas
PGA	Polyglycolic acid
PLA	Polylactic acid
PLGA	Poly (lactid-co-glycolic acid)
PMMA	Polymethyl methacrylate

PP	Polypropylene
PSP	Plasma spray parameters
PSU	Polysulfone
PSZ	Partially Stabilised Zirconia
PTFE	Polytetrafluoroethylene
PVA	Polyvinyl alcohol
PVB	Polyvinyl butyral
PVDF	Polyvinylidene fluoride
s.d.	Stand-off distance
SBF	Simulated Body Fluid
SE	Secondary electrons
SEM	Scanning Electron Microscope
SLS	Selective Laser Sintering
TBC	Thermal Barrier Coating
TCP	Tricalcium phosphate
TGA	Thermo Gravimetric Analysis
TTCP	Tetracalcium phosphate
TZP	Tetragonal Zirconia Polycrystals
UHMWPE	Ultra-high molecular weight Polyethylene
UV	Ultra-violet
XRD	X-Ray Difraction
YSZ	Yttria-Stabilised Zirconia

1. Introduction

The replacement of portions of bone in patients of different needs is nowadays a important surgical intervention, and demand continues to increase. Improvements in global health care and nutrition over the last decades have considerably increased life expectancy. Age and sedentary life styles cause human bones to lose density and thickness, and therefore, be more prone to fracture. Furthermore there is an increasing number of fractures due to transport accidents. Finally, one must also consider the genetic or medical problems that cause bone diseases or loss. To date, most fractures/defects have been treated by orthopaedic implants or bone grafting (autografts, allografts or xenografts), however:

- Orthopaedic implants lack the ability to modify their structure/properties as a response to environmental factors and are unable to interact with the host. They may undergo corrosion and dense fibrous tissue formation can occur at the implant/bone interface [1]. To overcome some of these problems a bioactive ceramic coating can be applied to the surface of implants [2]. However, there may be metal-coating interface adhesion problems [3].
- Autografting (graft from other bone within the same individual) requires an additional surgical procedure in which bone is removed from another part of the patient's skeleton. This has several associated shortcomings and complications, including limited quantities of bone for harvest and donor-site morbidity [4].
- Allografting (graft from other individual of the same species) and xenografting (graft shared between different species) have disadvantages such as provoking an immune response and transmitting diseases [5, 6].

As a result, there is a need for the development of artificial bone substitute materials that could be supplied in suitable amounts and on demand.

Bone tissue engineering is the interdisciplinary field that focuses on trying to overcome the problems and risks of using bone grafting or orthopaedic implants. It has potential clinical applications in bone replacement on maxillofacial, craniofacial, orthopaedic,

reconstructive and trauma surgeries, as well as in the treatment of bone tumours [7]. The basic idea is to regenerate or replace bone function either temporally or in the long term by using three basic components: carrier three-dimensional artificial structures (scaffolds), cells and signalling molecules.

Despite the efforts of the research community to make bone tissue engineering the preferred option for reconstructing large bone defects, corticocancellous bone grafts have been the mainstream solution to date. Inhomogeneous cellular proliferation and differentiation from the periphery towards the centre of the scaffolds caused by a scarce supply of oxygen and nutrients are seen as a major drawback of currently produced scaffolds [8]. Further investigation into scaffold design and manufacturing technologies, stem cell differentiation, growth factor addition and body-seeded scaffold interaction have been identified as essential to be able to construct living tissue implants and, therefore, further develop bone tissue engineering applicability [8-11].

The aim of this research is to manufacture components which meet many of the necessary requirements to be used as bone substitutes. Specifically, the goal of this research is to produce thick composite deposits as a step further towards the production of free-standing composite components (scaffolds) for cortical bone substitution, using a technique that has never been used for this purpose.

The technique selected to produce the bio-components is an experimental low energy version of conventional atmospheric plasma spraying (APS) equipment. This technique has been widely used to produce biocoatings onto metallic substrates with excellent results. This research proposes to broaden its application scope within the biomedical industry.

The main material selected is Hydroxyapatite (HA) due to its bioactivity and chemical resemblance to mineral natural bone. Furthermore, it has been shown to perform exceptionally well when applied using the APS technique. Plasma Sprayed Hydroxyapatite has been widely used on femoral stem or dental implants. The coating

allows bone in-growth and regeneration to occur in order to fix the implant to the human bone while the implant withstands mechanical loading.

However, plasma sprayed HA deposits have mechanical and structural shortcomings. The Young's Modulus is nearly half of that of cortical bone, the fracture toughness is one order of magnitude lower and the compressive strength is even lower. In addition, the manufacturing process of thick free-standing components generates important residual stresses which further reduce the mechanical properties of the components. Plasma sprayed HA components are also quite dense (porosity < 20%), so a mechanism should be found to increase the porosity of the components to the level required for cellular ingrowth.

Figure 1.1 shows the experimental plan to achieve the fabrication of scaffolds that meet porosity and mechanical properties requirements for bone tissue engineering. First of all, a series of selection tests were conducted in order to choose the plasma spray system and the HA powder size to be used. Feasibility tests on spraying different second phase materials for the selected system were also conducted. Spraying polymers without degradation is in itself a challenge, which requires process optimization. Once those preliminary tests were finished, a HA reference series was produced as a control sample group.

In order to improve the mechanical properties of the resultant components, the HA was reinforced with second phase materials. An increase of the components porosity was attempted by using pore former materials via separate injection. Finally, both modifications would be brought together in an attempt to obtain free-standing biocomposites with improved mechanical properties and pore structure.

The results and conclusions of this research will show whether the desired free-standing component, with its mechanical and bio-properties, can be achieved through plasma spraying a combination of Hydroxyapatite with polymer and ceramic reinforcements. In conclusion, the work will be used to demonstrate whether the technique and materials selected can be exploited to produce bone substitute components.
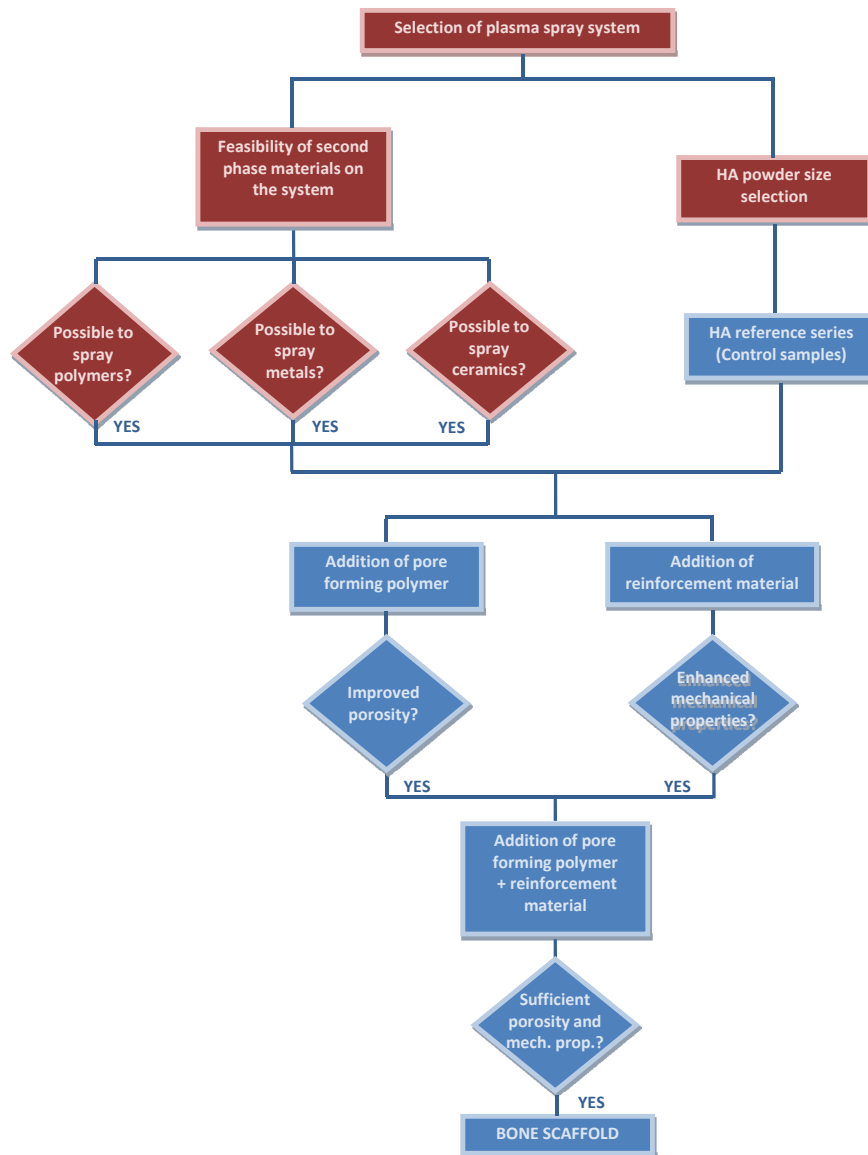
Figure 1.1. Schematic of the hypothesis being targeted

Chapter 2 contains a comprehensive literature review. This encompasses an overview of the targeted field of application of this research, bone tissue engineering. The requirements for bone scaffolds are discussed. This is followed by a review of a number of candidate biomaterials for this research. Finally, the plasma spray process is described along with the theory of coating formation. Some relevant selected applications of the technique are also presented. This is followed by Chapter 3, where the materials and equipment used in this work are presented.

Chapter 4 detail the experimental methods used in this work. Firstly, the statistical DOE experiments used for the investigation is discussed. The powder processing, target preparation and spray procedure are detailed. Finally, the various material and thick coating characterisation methods used are outlined.

The results from this work are presented and discussed in Chapter 5. Firstly, the results from characterisation of the feedstock material used are given. Following this, the findings of the selection and feasibility tests are reported. The results from the HA reference series, which set the basis for comparison for the composite deposits is then presented. The set of plasma parameters arising in the best crystallinity, layer thickness and roughness within HA reference series were used to produce the composite coatings series (HA/PCL and HA/TiO$_2$), results of which are then presented. The conclusions drawn from this research and some recommendations for future work are outlined in Chapter 6.

2. Literature review

In this Chapter several bone tissue engineering concepts are reviewed. Also, the structure of bone and the candidate biomaterials for bone substitution are described. An overview of the various thermal spray techniques used for bio-applications is then provided, paying particular attention to the type used for the purpose of this research, atmospheric plasma spraying (APS). The chapter concludes with a summary of some of the selected process applications relevant to this research.

2.1. Bone Tissue Engineering

Tissue engineering is an interdisciplinary field that brings together engineering and biological principles to design and manufacture functional components which would be used to regenerate of malfunctioning or lost tissue. Bone tissue engineering strategies aim to mimic the *in-vivo* process of bone repair in a laboratory setting. The three key elements for generating bone tissue are osteogenic cells, osteoinductive molecules and osteoconductive three-dimension artificial structures (scaffolds).

The idea behind bone tissue engineering is to isolate specific cells from an individual, and to seed and grow those cells within a scaffold under controlled conditions. The seeded scaffold is then placed into the individual's body to cause new tissue ingrowth while withstanding the loading conditions at the implantation site. The process of bone regeneration starts at this point. In optimum conditions, the artificial structure ideally degrades at the same pace while the new tissue forms and, thus, assumes its original functionality [12]. The process is summarised in Figure 2.1.
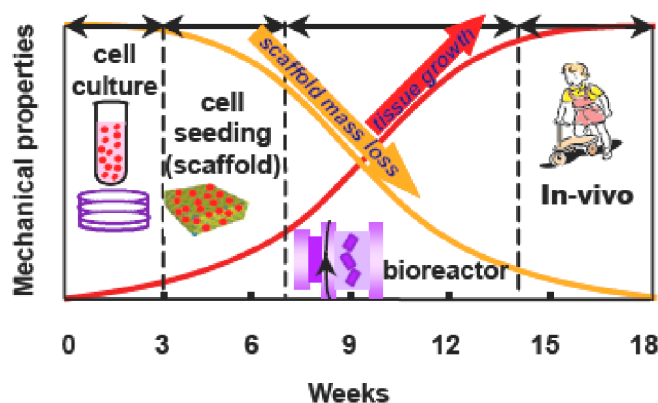
Figure 2.1. Optimum mechanical performance of scaffolds [13]

One of the challenges is the identification and isolation of suitable cells for seeding the scaffolds. The cells must differentiate, maintain the correct phenotype, and at the same time, perform specific biological functions [14]. For example, mesenchymal stem cells, present in adult bone marrow, have been shown to differentiate into osteogenic, chondrogenic and other cell lines [15]. There is currently a lot of research ongoing in this area.

The *in-vitro* and *in-vivo* performance requirements for the scaffold must be taken into account during the design and manufacturing stage. In most of the *in-vivo* cases, the scaffolds need to withstand mechanical loads. Ideally, they should fulfil a series of requirements [16-18], such as:

1. Being biocompatible, osteoconductive, osteoinductive and bio-reabsorbable.
2. Being non-toxic, non-carcinogenic and non-allergenic.
3. Having an appropriate surface topography and chemistry to promote cell attachment and differentiation.
4. Possessing 3D structure, highly porous with an interconnected pore network, to allow cell in-growth and flow transport of oxygen, nutrients and metabolic waste. Microporosity (<10 µm) is needed for capillary ingrowth and cell-scaffold interactions; macroporosity (150–900 µm) allows nutrient supply and waste removal for cells growing on the scaffold [11]. The minimum pore diameter for angiogenesis and bone ingrowth has been reported as 100 µm [19].
5. Matching the mechanical properties of the tissue they will be replacing during the biologic tissue regeneration. Unfortunately, good mechanical properties and high porosity are contradictory requirements for the majority of the materials that meet the biological requirements.

Finally, the addition of adequate signals (growth factors) to achieve the tissue regeneration is also required.

2.2. Bone structure

Bone is a composite made of cells (osteoblasts, osteoclasts and osteocytes), organic elements such as collagen and polysaccharides, and inorganic apatite crystals. The collagen provides bone with high tensile and flexural strength and the apatite with stiffness and high compressive strength [14].

Bone in mammals is generally classified into two types, which are very different in their density and unit microstructure: cortical (compact) and spongy (trabecular, cancellous) bone. Figure 2.2 shows a sketch of the long bone structure.
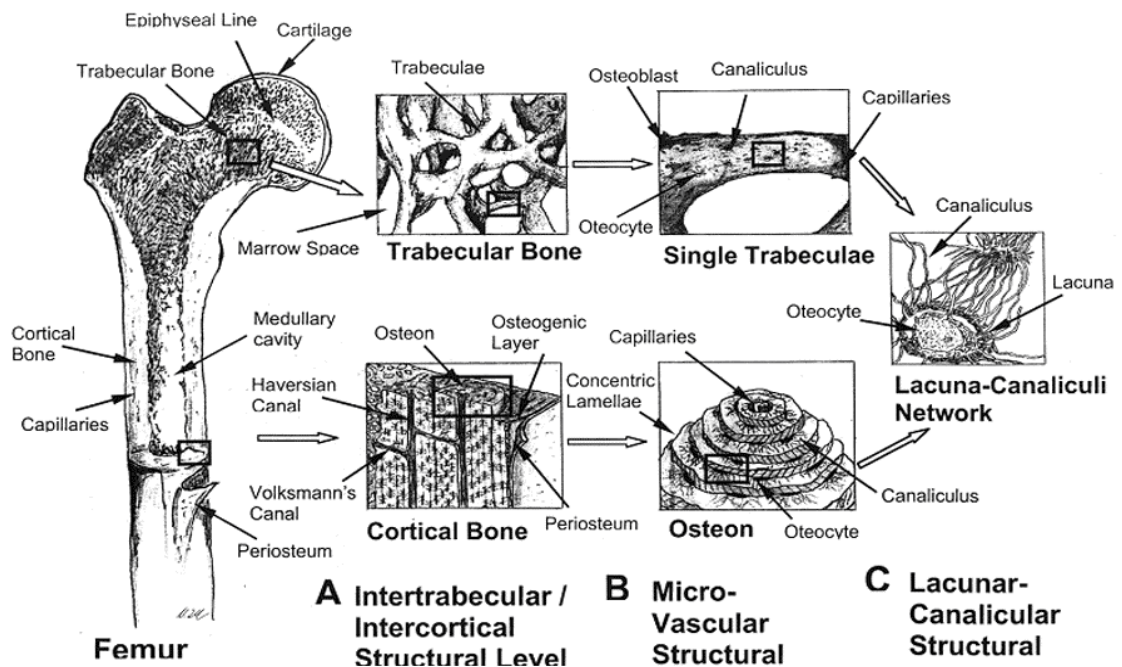
Figure 2.2. Bone Hierarchy [12]

Spongy bone is found at the end of long bones where the bone marrow is produced. It is anisotropic in configuration and its porosity lies between 30 and 90%. It has low mechanical properties (Table 2.1). The elastic modulus and strength values show substantial variation with respect to age and health condition of the individual, anatomic site, loading mode and direction respect to the principal trabeculae orientation [20].

Cortical bone contains three major anatomic cavities: Harvesian canals or osteons (~50 μm), which contain nerves, arteries, veins and lymph vessels; osteocytic lacunae, where the bone cells are (few micrometers); and canaliculi (< 1 μm) which contain the capillaries connecting arteries/veins in Harvesian canals to bone cells in lacunae [21]. The Harvesian canals are longitudinally interconnected through transverse canals (Volkmann Canals). Cortical bone mean thickness in femoral cortex is 4.82-5.5 mm in males and 3.63-4.5 mm in females, with an average porosity of 8.26% and 9.72% respectively [22]. The maximum porosity can be as high as 26% [23]. The mechanical properties are much higher than those of spongy bone (Table 2.1), having a compressive strength of 100-230 MPa and a Young's modulus of 7-30 GPa compared with the 2-12 MPa and 0.01-3 GPa respectively [20, 24]. Young's modulus of trabecular bone can vary 100-fold within a single epiphysis and 3-fold depending on loading direction [20].

Table 2.1. Bone mechanical properties

Property	Spongy bone	Cortical bone
Porosity, %	70-95[5]	5[3]-30[5]
Pore size, μm	500-1500[5]	5-100[5]
Crystallinity, %	-	-
Density, g/cm^3	0.1[5]	1.85-2[5]
Compressive Strength, MPa	2-12[1]	100-230[1]
Tensile Strength, MPa	1.5[2]-20[1]	50[2]-150[1]
Flexural Strength, MPa	10[1]	50[1]
Young's Modulus, GPa	0.01-3[5]	7-30[1]
Poisson ratio	0.03-0.6[5]	0.4-0.6[5]
Elongation at break, %	5-7[1]	1[4]-3[1]
Fracture Toughness, MPa·m$^{1/2}$	2[1]	12[1]

References: [1] Hench et al. [24] [3] Wachter et al. [23] [5] Kutz [20]
[2] Sun et al [25] [4] Bronzino [18]

2.2.1. Artificial bone structures: Scaffolds

Major advantages of using scaffolds over autologous bone grafts are their availability, controlled variation in size and the elimination of a second surgery on the patient. It is for this reason that intensive research has been conducted to date to find the optimal manufacturing technique for these scaffolds.

There are some traditional techniques used for manufacturing artificial bone structures with adequate porosity (Table 2.2), however, most of them use solvents which are poisonous to cells or contaminate the scaffolds. Additionally, there are economic-related drawbacks, such as long fabrication periods; and manufacturing-related disadvantages, such as poor repeatability, irregularly shaped pores, insufficient interconnectivity of pores and thin structures.

Table 2.2. Traditional techniques of scaffolds manufacturing [26]

Method	Porosity/Pore size	Advantages
Fibre bonding-unwoven mesh	81%/500 μm	Highly porous Interconnected porosity
Solvent casting / Particulate leaching	87%/100 μm	Strength Electrical conductivity
Gas foaming	93%/100 μm	Biocompatible
Phase separation / Emulsification	95%/13-35 μm	Variable pore size Variable % of porosity

There are also emerging techniques for scaffold fabrication such as rapid prototyping. In this technique the external and internal geometries can be designed in advance, using computer aided design, and mechanical properties can be analysed and optimised by Finite Element Analysis. However, the processing times are long (several hours). In general, the dimensional accuracy, mechanical properties, and applicable materials are restricted by the particular rapid prototyping technology. For instance, three dimensional printing (3DP) and selective laser sintering (SLS) can produce porous scaffolds for tissue engineering [26, 27]. However, these techniques were not developed to manufacture scaffolds, which requires micro-scale features, and therefore, resolution is limited. Scaffolds produced by each of those techniques can be seen in Figure 2.3.
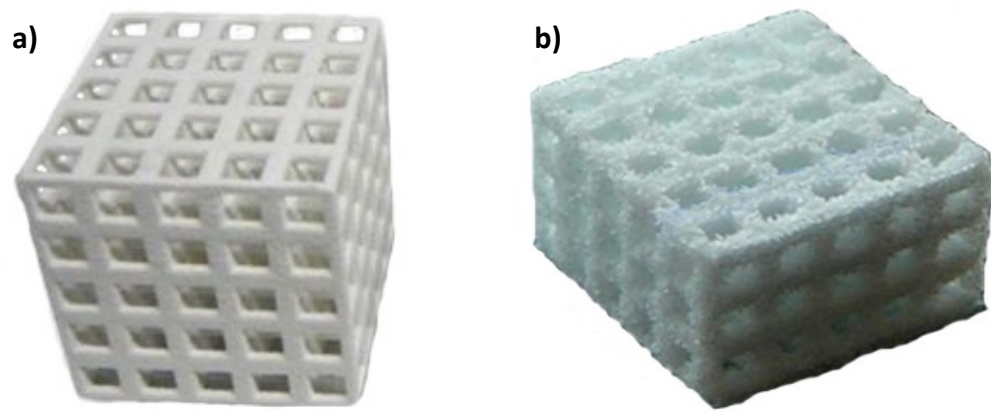
Figure 2.3. Scaffolds produced by: a) 3D printing [26] and b) SLS [27]

2.3. Biomaterials

Biomaterials in general and bioceramics in particular can be classified into three groups according to the response they elicit on a living tissue or cells: bioinert, bioactive and bioresorbable (Table 2.3).

Table 2.3. Classification of Biomaterials [28]

Biomaterial	Tissue response	Interaction	Examples
Bioinert	Minimal/no-response	Mechanical fixation	Al_2O_3, ZrO_2, TiO_2, Ti, PEEK, etc.
Bioactive	Positive response	Chemical bonding	HA, bioactive glasses, etc.
Bioresorbable	Gradually dissolve	Replacement by tissue	TCP, PCL, etc.

Bioinert materials do not release toxic substances. The response of the body to these bioinert materials is usually to form a non-adherent capsule of connective tissue around it. On the other hand, bioactive materials undergo an interfacial interaction with surrounding tissues which results in the formation of a biologically active apatite layer on the surface of the synthetic material [29]. This apatite is equivalent to the mineral phase in bone.

Most of the metallic alloys (steels, titanium alloys, etc.) and structural ceramics (alumina, zirconia or titania) used for biomedical applications belongs to the group of bioinert materials. However metals, such pure titanium and pure tantalum, have been

classified under both categories, bioinert and bioactive [30]. Magnesium and its alloys are currently under research due to its excellent osteoconductive bioactivity [31]. Polymers, such as poly-ethylenes, polyetheretherketone (PEEK), polysulfone (PSU) or poly-metyl-metacrylate (PMMA) are bioinert [32].

Bioreabsorbable materials dissolve and are replaced or incorporated into biological tissue. There is an important number of polymers belonging to this group of materials; among them are polyanhydrates, polyorthoesters, polyurethanes and aliphatic polyesters (polylactic acid (PLA), poly-lactid-co-glycolic acid (PLGA), polycaprolactone (PCL)) [26]. Some bioceramics, such as tricalcium phosphates (TCP) and tetracalcium phosphates (TTCP) are also biodegradable.

Ideally, scaffolds should be made of a singular element or a mixture of the elements which belong to this last group of biomaterials. However, a disadvantage of using re-absorbable structures is the decrease in strength that occurs during the resorption process, which can lead to the fracture of the scaffold during healing. For this reason, the rate of resorption of biomaterials should match the rate of bone formation, and the reduction of load that the scaffold is able to withstand should match as closely as possible the increase in strength of the new bone formed [33]. The biomaterials used should also encourage bone growth through a porous network and facilitate integration of bone-scaffold. The mechanical performance of different materials should be taken into account as well (Figure 2.4).

Among synthetic biomaterials, calcium phosphate bioceramics, and in particular hydroxyapatite (HA) and Tricalcium phosphate (TCP), have been used as a base material to make scaffolds due to their resemblance, chemically and in mechanical properties, to the mineral phase of bone and their biocompatibility, bioactivity and osteoconductivity [11].
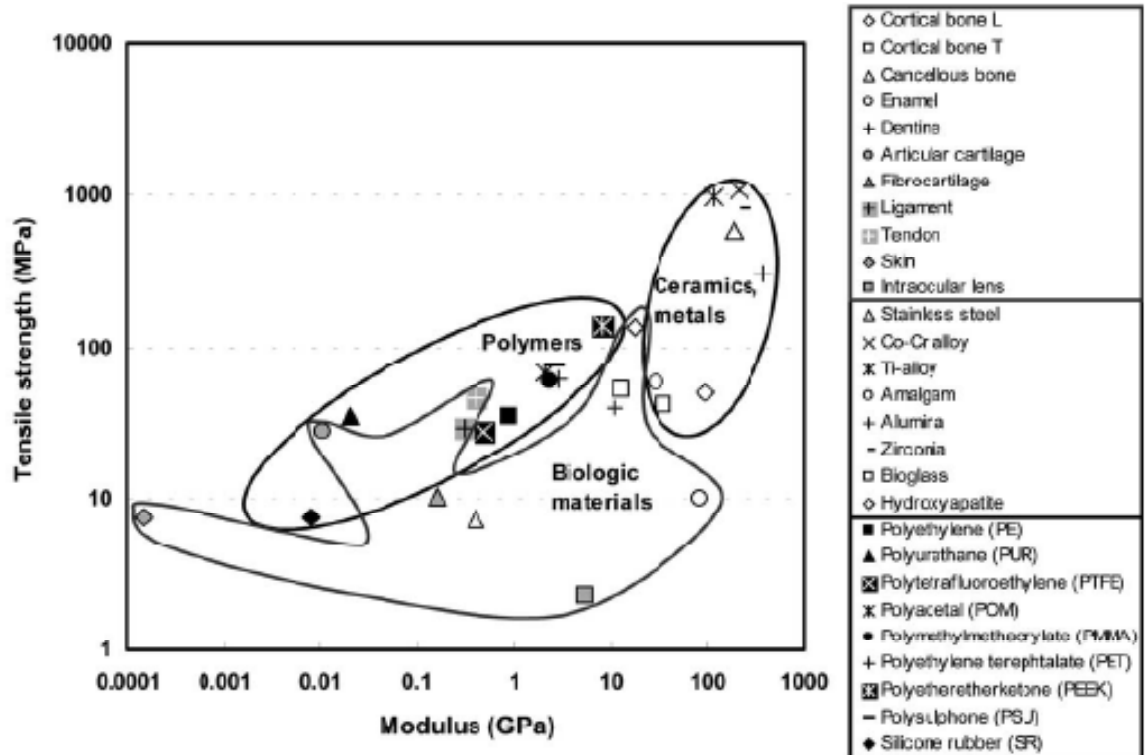
Figure 2.4. Tensile strength vs. modulus of several biomaterials [32]

Unfortunately, the use of bioceramics to manufacture scaffolds adds a difficulty to the design process i.e. the extremely low fracture toughness compared with other materials, which means that ceramics have very little resistance to crack-like defects. These internal defects reduce ceramics strength. Fracture stress of a ceramic containing an internal crack of length *2a* is given by Griffith relationship (Eq. 2.1):

$$\sigma_f = \sqrt{\left(\frac{2E\gamma}{a}\right)}$$
Eq. 2.1

where *E* is the Young's modulus, γ is the surface energy of the crack surface . Assuming this is a linear elastic fracture problem, the stresses at any point with cylindrical coordinates (*r*, θ) surrounding the crack (Figure 2.5) can be defined as:

$$\sigma_{ij} = \frac{K}{\sqrt{2\pi r}} f_{ij}(\theta)$$
Eq. 2.2

13

where the condition at the tip of the crack can be defined by the stress intensity factor (K), $f_{ij}(\theta)$ is a function of the angle θ. The fracture occurs when K reaches a critical value K_{IC} (MPa·m$^{1/2}$) which is the unit to measure the fracture toughness [33].
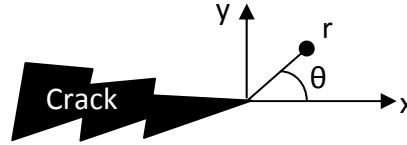
Figure 2.5. Crack tip and a surrounding point (r, θ)

The low fracture toughness of ceramics has its origin in their inherent sensitivity to the presence of defects in them (inclusions, pores, thermal stresses, etc.). The most common way of increasing the fracture toughness is to add a second phase as reinforcement to the ceramic [33]. The role of the reinforcement is to block the growth of cracks, and thus increase the mechanical properties of the matrix material. For example, protein-hydroxyapatite composites with considerable strength have been manufactured [34], but their mechanical properties lie far from those of natural bone. Glass (2.5 wt%) reinforced Hydroxyapatite has been reported to improve the mechanical properties of HA and further more improvement has been proven with the addition of titanium particles (20 vol%) [35]. Zirconia particles have effectively been used to reinforce HA [36].

2.3.1. Hydroxyapatite (HA)

HA is a calcium phosphate bioceramic that belongs to the family of apatites. The apatite family is formed of a number of elements characterised by having similar crystallographic structures but not necessarily identical compositions (Table 2.4). HA has a specific composition, $Ca_{10}(PO_4)_6(OH)_2$, a Ca/P ratio of 1.67 and its crystal structure is hexagonal (Figure 2.6) with a space group P6$_3$/m (a=b=9.432 Å, c=6.881 Å) [24, 37].
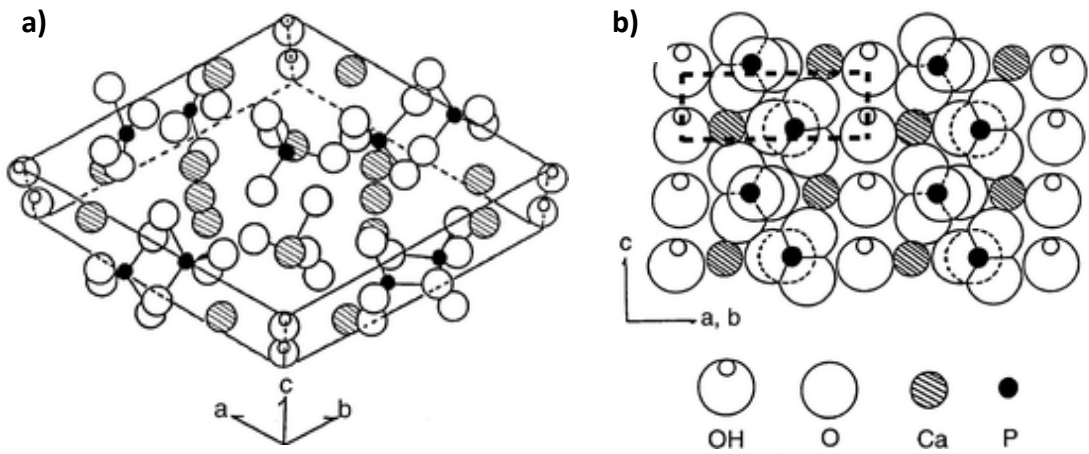
NOTE: The area enclosed by dotted lines represent the side-view of the unitary cell

Figure 2.6. Hydroxyapatite: a) crystal structure and b) ac or bc side-view [38]

Phosphate groups provide the apatite with chemical stability. OH^- groups can be substituted by either fluoride forming fluoroapatite or chloride forming chloroapatite. The suitability of apatite for substitution with other ions can be used to modify the hexagonal symmetry and obtain changes in the degree of crystallinity or in the crystal size which are associated with the increase of stability of the structure and therefore a reduction in solubility [24], which are essential parameters for coatings in biomedical applications.

Crystalline HA shows the slowest degradation rate, compared with other calcium phosphate phases (Table 2.4). The dissolution rate decreases as follows [24]:

$$ACP \gg \alpha\text{-TCP} \gg \beta\text{-TCP} \gg TTCP \gg OA \gg HA \qquad \text{Eq. 2.3}$$
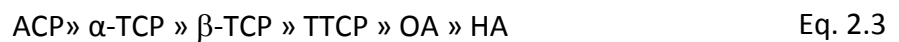
Table 2.4. Some Calcium Phosphate phases [25]

Phase	Chemical Formula	Symbol	Solubility Constant	Ca/P ratio
Hydroxyapatite	$Ca_{10}(PO_4)_6(OH)_2$	HA	6.62×10^{-126}	1.67
Amorphous calcium phosphate	-	ACP	-	-
α-Tricalcium phosphate	$\alpha\text{-}Ca_3(PO_4)_2$	α-TCP	8.46×10^{-32}	1.50
β-Tricalcium phosphate	$\beta\text{-}Ca_3(PO_4)_2$	β-TCP	2.07×10^{-33}	1.50
Tetracalcium Phosphate	$Ca_4P_2O_9$	TTCP	N/A	2.00
Oxyapatite	$Ca_{10}(PO_4)_6O$	OA	$\sim 10^{-69}$	1.67

However, the dissolution rates of the calcium phosphates presented above are relative as they depend on several factors such as Ca/P ratio, porosity and pH. For instance, Figure 2.7 shows the solubility of various phases in the system $CaO-P_2O_5-H_2O$ as function of pH, where k is the solubility constant indicating the maximum product of ion concentrations which can exist in solution at equilibrium.
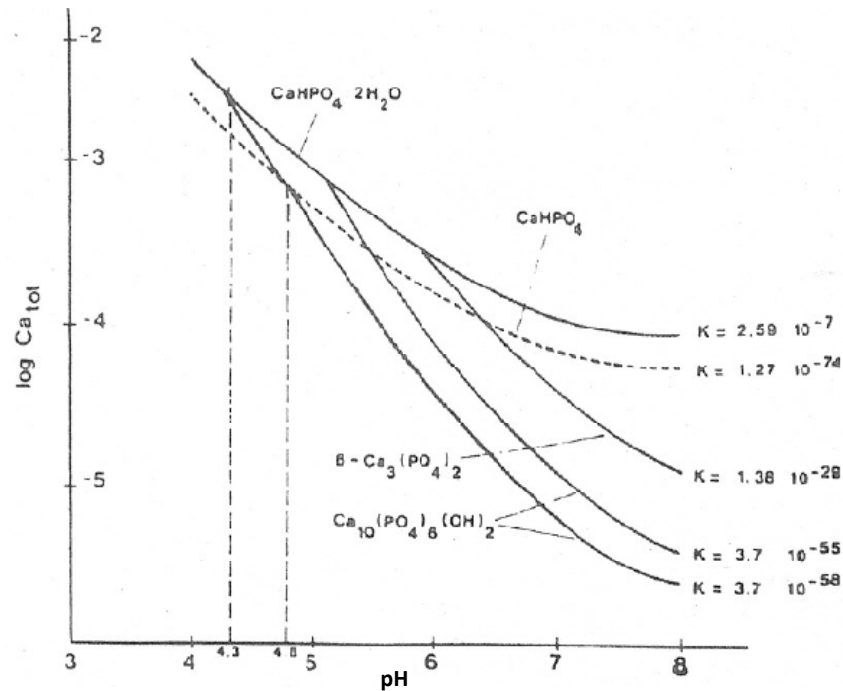
Figure 2.7. Solubility of various phases in the system $CaO-P_2O_5-H_2O$ as function of pH [24]

HA is not osteogenic nor osteoinductive, but it is osteoconductive and shows excellent biocompatibility with hard tissues [5, 39]. However, the in-vivo behaviour of HA ceramics depends on several factors like Ca/P ratio, crystallinity or degree of porosity in the component, which determine the dissolution behaviour [24, 40]. Some of these properties (size, shape, Ca/P ratio and crystallinity) would be affected by the different HA powder production methods. The manufacturing methods to produce the HA components will further affect these properties and the structural ones: mechanical properties, roughness and pore structure.

Suchaneck et al. [41] reviewed various production methods for HA powders and forming techniques for HA products (Table 2.5). The vast majority of techniques to produce porous HA bulk materials use volatile or water-soluble particles that are removed after processing by sintering and dissolving them respectively. Volatile pore

forming materials such as paraffin, naphthalene, chitosan, starch, flour, almond crusts, wax, hydrogen peroxide or synthetic polymers (PMMA, PVB, PVA, nylon etc.) were mixed to HA powders before processing [42, 43]. Among the soluble pore formers were salt and some water soluble polymers [44].

Plasma Spraying has been the most common commercial method for producing HA coatings for orthopaedic applications. From an economic point of view, Plasma Spraying need a short production time compared with other coating techniques, which leads to production efficiency. In addition, this technique enables control of the resulting coating characteristics such as those mentioned above. The control is carried out by modifying the spraying parameters (further details in Section 2.4 and 2.5).

Table 2.5. Some HA production methods (adapted from [41])

HA powder	Bulk HA ceramics	HA Coatings
1. Precipitation	*Dense HA:*	1. Plasma Spraying
2. Hydrolysis of another Calcium Phosphates	1. Pressing	2. Hot isostatic pressing
3. Sol-gel	2. Slip-casting	3. Oxy-fuel combustion spraying
4. Flux Method	3. Tape-casting	4. Magnetron sputtering
5. Electrocrystallization	4. Injection moulding	5. Flame spraying
6. Spray-Pyrolysis	*Porous HA:*	6. Ion-beam deposition
7. Freeze-drying	1. Sintering (pore-former)	7. Electrochemical deposition
8. Microwave irradiation	2. HA Casting in $CaCO_3$ skeleton	8. Metal-organic CVD
9. Mechano-chemical Method	3. Hydrothermal hot pressing	9. Sol-gel
10. Emulsion Processing		10. Pulsed-laser deposition
		11. Electrophoresis

Most of the processing techniques used to produce HA coatings or bulk materials, involve elevated temperatures which lead to HA decomposition. Thermal decomposition of HA occurs in several steps: evaporation of water, dehydroxylation, decomposition and melting (Table 2.6). Figure 2.8 shows the phase diagram of the system $CaO-P_2O_5$ at high temperature.

Table 2.6. Thermal decomposition of HA [28]

Temperature	Reaction
25-200°C	Evaporation of absorbed water
200-600°C	Evaporation of lattice water
600-800°C	HA decarbonation
800-900°C	HA dehydroxylates to form oxyapatite (OA)
1120-1470°C	β-TCP, stable up to 1120°C, transform to α-TCP
1550°C	Incongruent melting of HA
1630°C	TTCP melting temperature. Formation of CaO
1730°C	TCP melting temperature
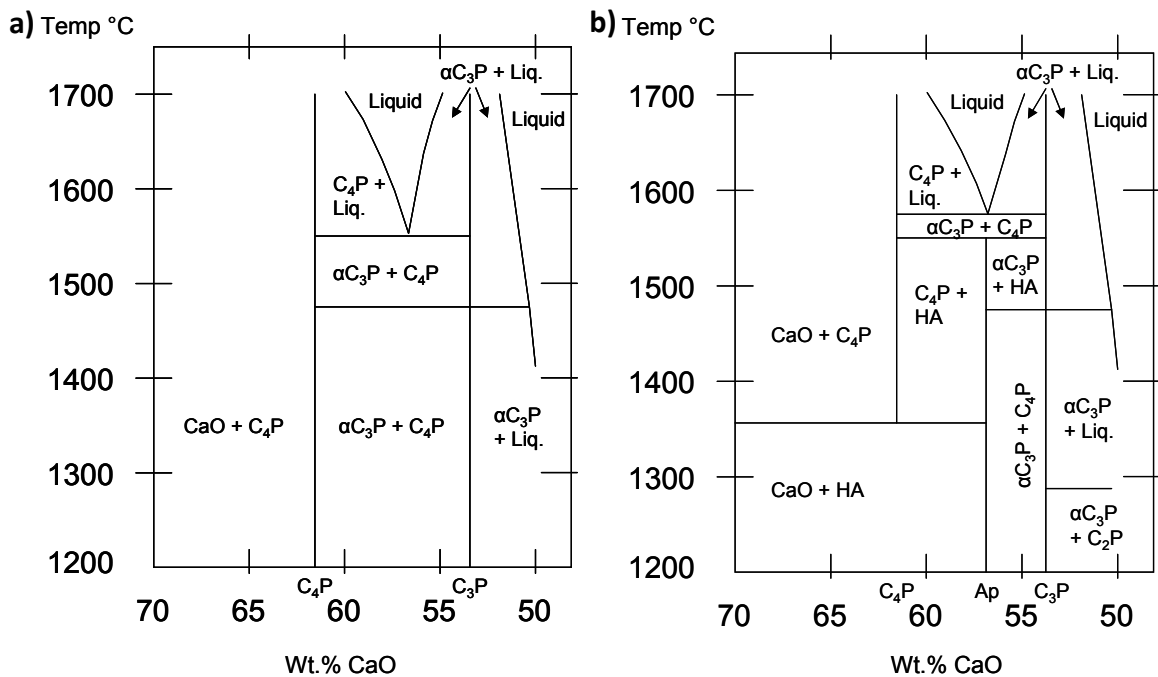
Figure 2.8. Diagram of the system CaO-P$_2$O$_5$ at high temperature: a) no water present and b) water vapour P H$_2$O=500mmHg [24]

Table 2.7 shows that bulk dense HA exhibits mechanical properties which are almost suitable for bone substitution. However, porosity is required to fulfil the biological requirements and an increase in porosity entails an unavoidable decrease in mechanical properties. The fracture toughness of pure dense HA (1 MPa·m$^{1/2}$) has been reported to decrease almost linearly with the increase in porosity [41]. In terms

of resistance to fatigue failure, the Weibull modulus[1] of HA has been reported to be 50 in dry conditions and only 12 in wet physiological environment, which means HA behaves as a brittle ceramic [24]. Table 2.7 also shows that HA as a coating exhibits weaker mechanical properties than those of bone, even though the porosity level is still in the cortical bone lower range.

Table 2.7. Bone and HA mechanical properties

Property	Spongy bone	Cortical bone	Bulk dense HA	PS HA
Porosity, %	70-95[6]	5-30[4]	~0	1[2]-18[8]
Pore size, μm	500-1500[6]	5-100[6]		7[9]
Crystallinity, %	-	-	-	40-80[1]
Density, g/cm^3	0.1[6]	1.85-2[6]	3.16[5]	1.2[7]-2.8[2]
Compressive Strength, MPa	2-12[1]	100-230[1]	500-1000[11]	0.5-3.4[2]
Tensile Strength, MPa	1.5[3]-20[1]	50[3]-150[1]	78-196[12]	7-80[1]
Flexural Strength, MPa	10[1]	50[1]	115-200[11]	-
Young's modulus, GPa	0.01-3[6]	7-30[1]	11[1]-117[5]	0.28[2] – 5.3[3]
Poisson ratio	0.03[6]	0.4-0.6[6]	0.27[5]-0.3[2]	0.28[13]
Elongation at break, %	5-7[1]	1[5]-3[1]	3-4[10]	-
Fracture toughness, MPa·m$^{1/2}$	2[1]	12[1]	1[11]	0.28-1.41[3]

References: [1] Hench et al. [24]   [5] Bronzino [18]   [8] Khor et al. [47]   [11] Black et al. [50]
[2] Tsui et al. [45]   [6] Kutz [20]   [9] Li et al. [48]   [12] Legeros [51]
[3] Sun et al [25]   [7] Rokkum et al.[46]   [10] Gibbons [49]   [13] Yang et al.[52]
[4] Wachter et al. [23]

2.3.2. Yttria-stabilised Zirconia (YSZ)

Zirconia-based ceramics are biomaterials with high mechanical strength, similar to metals [53], and high fracture toughness, due to the transformation toughening mechanisms that occur within their microstructure. They are used in total hip replacements, but still research is ongoing to further extend their applicability to other medical devices.

---

[1] Weibull modulus: Dimensionless number that reflects the distribution of flaws in a brittle material by reflecting the statistical variability in measured strength from sample to sample under the same testing conditions. High Weibull modulus indicates little variation and thus, the average strength of the material is a good representation of the performance of the material.

Pure Zirconia (ZrO_2) has three polymorphs [53]: monoclinic (up to 1170°C), tetragonal (1170°C - 2370°C) and cubic (2370°C). The transition associated with the tetragonal-to-monoclinic phase transformation involves an important volume expansion (~5%) and shear stresses which can cause fracture upon cooling, preventing the use of pure zirconia as a structural ceramic [54, 55]. To overcome this limitation, additives such as calcia (CaO), magnesia (MgO) or yttria (Y_2O_3) can be added to stabilise ZrO_2 at room temperature into either a cubic or tetragonal phase, creating multi-phase materials known as Partially Stabilised Zirconia (PSZ) [28]. At room temperature, Mg-PSZ and Ca-PSZ usually consist of cubic phase (50 - 100 μm) with precipitates of tetragonal phases (0.1 - 0.25 μm). In the ZrO_2-Y_2O_3 system, it is also possible to obtain ceramics formed at room temperature with a tetragonal phase only (TZP) for Y_2O_3 contents of 2-3 mol% [56].

Stabilised zirconia ceramics with tetragonal symmetry retained as the primary structure have improved mechanical properties due to transformation-toughening mechanisms preventing crack propagation [56]. This stress-induced mechanism involves the transformation of metastable tetragonal phase to monoclinic at the crack tip, which produces compressive stresses due to the volumetric expansion, thus, reducing crack propagation.

The toughening mechanisms mentioned above make these ceramics suitable for use in structural applications as they have superior mechanical properties. For instance, Mg-PSZ exhibits a tensile strength of 600-700 MPa, a fracture toughness of 11 to 14 MPa·m$^{1/2}$ and an elastic modulus of 210 GPa [57]. Manicone et al. [53] reported the following mechanical properties for Y-TZP ceramics: a tensile strength which can be as high as 900-1200 MPa, a compressive strength around 2000 MPa and a fatigue resistance under cyclic tensile loading of 28 kN, which is 50 billion cycles. Some other properties of zirconia ceramics can be seen in Table 2.8.

Zirconia ceramics soon became popular as materials for biomedical applications. Since late the 60's, Zirconia ceramics have been mainly used for artificial joint replacement [53]. In the early research of zirconia as a biomaterial, several stabilisers were tested (MgO,CaO and Y_2O_3) but in the following years the efforts focused on ZrO_2-Y_2O_3 (YSZ),

due to their finer grained microstructures [56]. Thus, ZrO_2-Y_2O_3 (YSZ) has been the most studied combination for medical applications to date [53].

Despite YSZ being bioinert [58], wet environments have a negative effect on these ceramics, provoking what is known as zirconia aging (slow transformation from tetragonal-to-monoclinic phase which provokes micro-cracking). However, this effect has the most effect at temperatures around $250^{\circ}C$ and is therefore less important at body temperature [55]. The British Medical Device Agency (MDA) and subsequently the US Food and Drug Administration (FDA) reported that steam sterilisation of YSZ at $121^{\circ}C$ can also cause hydrothermal aging of these ceramics.

Although these ceramics have been used during nearly half a century in the biomedical sector, there is no agreement on the response they provoke on cells and tissues. The biocompatibility of YSZ has been tested for cytotoxicity giving good results [59]. Yamashita et al. [60] studied the proliferation of osteoblast-like cells on these ceramics *in-vitro* and found an increased density of cells with numerous cell-to-cell contacts after 6 days incubation. *In-vivo* testing conducted in these ceramics proved that they had very good short-term *in vivo* biocompatibility, good cyto-compatibility and a non-mutagenic or inflammatory response [50]. On the other hand, these ceramics have been proven not to be very conductive for cell growth and during degradation produce some by-products that may be toxic to cells and inhibit their growth [56].

In order to compensate its lack of bioactivity but to exploit its excellent mechanical properties, YSZ could be used as a reinforcing phase in a biocomposite whose main component is a bioactive ceramic (Section 2.3.7.).

2.3.3. Titanium (Ti)

Titanium is the fourth most abundant metallic element in the earth after aluminium, iron, and magnesium. Even though, it was recognized as an element 200 years ago, it was not extensively produced until Kroll discovered a relatively safe and economical method to produce it in the late 1930's [61]. It was after World War II when titanium started to gain the commercial importance that it has nowadays. Titanium exists in two different crystallographic forms: Ti-α has a hexagonal close-packed (hcp) crystal structure (a=2.95 Å, b=4.683 Å) and Ti-β a body-centred cubic (bcc) structure

(a=3.29 Å) [57]. The α-phase exists at room temperature and transforms very slowly to β-phase at around 880°C, which is stable up to Ti melting point temperature (1677°C) [62].

Some of the mechanical properties of Titanium can be seen in Table 2.8. The importance of this metal is mainly due to its high specific strength and corrosion resistance to dilute sulphuric and hydrochloric acid, most organic acids, moist chlorine gas and chloride solutions [63]. Its main users are the aerospace industry and the biomedical sector. Examples of the importance of this material in the biomedical industry can be seen in Figure 2.9. Unfortunately, the high cost of titanium and its alloys made them a second choice when other lower-cost alloys can be used instead. The high pyrophoricity of titanium powder makes transportation very expensive and slow, adding an important cost to the production budget.

Titanium metal is physiologically inert, due to its nanometric surface amorphous oxide layer (2-6 nm), and this is why the use of it in implants is widespread and successful; however, Titanium powder itself can be carcinogenic [63].

Titanium has an extremely slow corrosion rate in biological media, meaning it is biostable, and it does not release ions under normal operating circumstances. Steinemann [64] pointed this out as a reason for commercially pure titanium integrating better in bone than titanium alloys. However, the corrosion kinetics of Ti can accelerate under stress and wear circumstances. Ratner [65] reviewed many publications addressing the issue of proteins adsorption by titanium (albumin, collagenase, fibronectin, etc.) and affirms that titanium surfaces can support cell growth and differentiation.

Thomsen et al. [66] performed in-vivo tests and found that the bone was in close apposition to titanium, but there was an amorphous biological layer (5-10 nm) separating both. They also reported no sign of chronic inflammation but a risk of development of foreign-body giant cells[2].

---

[2] A foreign-body giant cell is a cluster of fused macrophages, in which nuclei are arranged in a disorganised manner. These cells are generated as a response to the presence of a large foreign body.

Titanium has already been used to control regenerative processes, either to enhance or repress tissue growth or proliferation. Two examples of this are intravascular stents and spinal cage systems. However, the bioactivity of titanium is a matter of controversy; *in vitro* studies demonstrated the absence of cytotoxic effects, but other studies found a marked negative biological response [30]. Titanium soaked in NaOH and heat treated to form sodium compounds on its surface has proven to directly bond to living bone forming an apatite layer [67].

Ti plates, mesh and acrylic are used in cranioplasty/neurosurgery.

Ti anchoring devices for bone conduction hearing aids.

Ti pegs used for attach false eyes and ears. Ti implants for interorbital fractures fixation.

Ti dental implants act as artificial roots. Ti orthodontic braces.

Maxiofacial prosthetics can be made of Ti.

Shoulder and elbow joint implants are commonly made of Ti.

Expandable rib cages made of Ti allows a child's rib cage to 'grow' with the patient.

Heart valves, pacemaker cases and vascular access ports are made of Ti. Ni-Ti superelastic tubing is used in coronary angloplasty catheters.

Spinal fusion cages, implants, correction parts and fixation are made of Ti.

Ti-Ni shape memory alloys are used in medication mini-pumps that flex due to an electric current that creates a heating/cooling cycle that changes shape of a chamber.

The most common biomedical use of Ti is hip replacements.

Ti is used for urethral stents.

Nearly half of all knee replacements are made of Ti.

Tibial nails made from Ti are used for reinforcement in lower leg fractures.

Toe and finger implants are made of Ti.

Instrumentation made from Ti includes surgical devices, dental drills, laser electrodes, stents, marker bands, vena cava clips, needles, staples, blades, etc.

Reconstructive Ti bone plates and mesh that supports broken bones are commonly used today. Other Ti fixation devices include bone screws, plates, rods, hooks and nails, cable and staples.

Figure 2.9. Use of Titanium in biomedical applications (adapted from [68])

2.3.4. Titanium oxide (TiO$_2$)

Titanium oxide can exist in three different crystal structures: brookite, rutile and anatase. Anatase is a metastable phase with tetragonal structure that transforms to rutile at temperatures above 907°C. The rutile phase has tetragonal structure and it is stable at high temperatures [69]. Brookite has an orthorhombic structure. Some of the mechanical properties of titanium oxide can be seen in Table 2.8 at the end of this section.

Brohede et al. [70] verified anatase bioactivity *in vitro* by the spontaneous formation of hydroxylapatite upon storage in phosphate buffered saline solution (PBS) at 37°C for one week. The rutile surfaces were found to be highly bioactive, being covered by a several-micrometers-thick layer of bone-like apatite after seven days of immersion in PBS [71]. Svetina et al. [72] pointed that rutile bioactivity is due to its lower isoelectric point 5.9 compared with the pH of body fluids (~7.4). This difference leads to the formation of negative Ti–O$^-$ groups on the surface, which attract Ca^{2+} ions from the body fluid. As a result, a layer of amorphous calcium titanate is formed and the surface, thus, becomes slightly positive attracting negatively charged phosphate ions. These phosphate ions bind to the surface growing a metastable phase of calcium phosphate. In terms of particles, rutile debris have been shown to be less bioreactive than pure titanium ones; improved biocompatibility has been reported for the oxide [73].

Enhanced bioactivity and cell response of UV-irradiated titanium oxide coatings have been reported [74]. Light irradiation provides TiO$_2$ with another interesting and special property: its photocatalytic activity, which degrades inorganic materials and organic compounds, and destructs bacteria such as Escherichia coli (E. coli) and Pseudomonas aeruginosa (P. Aeruginosa) [75]. Photocatalysis refers to the chemical reaction occurring when light (UV or white) strikes a chemical compound that is light sensitive, such as titanium oxide. Electron-hole pairs are thus created on the surface of TiO$_2$, which react with the surface's absorbed moisture to form free hydroxyl radicals (OH$^-$). These radicals participate in secondary reactions with organic compounds, resulting in decomposition of the organic compounds or bacteria [76]. Although, both rutile and anatase are used in photocatalysis, anatase shows higher photocatalytic activity [77].

Fostad et al. [78] manufactured TiO_2 scaffolds with porosity above 85% using the polymer sponge method. They found that the scaffolds were not cytotoxic; and that mouse osteoblasts adhered well to the surface and spread throughout the entire structure.

2.3.5. Polyetheretherketone (PEEK)

Polyetheretherketone (PEEK) was first synthesised in a laboratory in 1977 [50]. It is a rigid semi-crystalline thermoplastic polymer whose chain disposition can be seen in Figure 2.10. The chain stiffness and aromatic ring positions cause PEEK to remain mostly amorphous, with the maximum crystallinity reported at 48% [79].
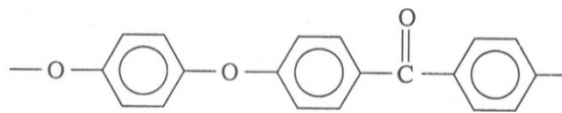
Figure 2.10. PEEK structure [79]

PEEK has excellent mechanical and electrical properties, thermal stability and good chemical properties [80] compared to other polymers. It is highly resistant to thermal degradation, as well as to both organic and aqueous environments. It has low flammability and very slow gas and smoke emission, which is an advantage for applying it using plasma spraying [50]. Some of its thermal/mechanical properties are shown in Table 2.8. PEEK has often also been used as matrix for composite materials [81].

Since the 80's, the polymer family of PEEK, polyaryletherketones (PAEKs), have been increasingly employed as biomaterials for orthopaedic implants, particularly spinal implants [81]. They are biocompatible but bioinert; their poor interaction with bone is due to their hydrophobicity and chemical inertness [82]. Kurtz et al. [81] reviewed the biological performance of PEEK. They reported that it is resistant to simulated *in-vivo* degradation, including damage caused by lipid exposure; equally they did not find adverse side effects relating to the systemic and intracutaneous toxicity and intramuscular implantation. Finally, they found no sensitisation reported after tests in accordance with ISO 10993-10-1995 and no chromosome aberration testimonies

under gene toxicity tests. Sagomonyants et al. [83] studied the response of human osteoblasts to PEEK and found that implantable grade PEEK, in general, has a similar *in-vitro* response as that of rough titanium.

2.3.6. Polycaprolactone (PCL)

PCL belongs to the aliphatic polyester family (PLA, PGA, PLGA, etc.) and it can be prepared by ring opening polymerisation of ε-caprolactone [20], as can be seen in Figure 2.11. Its molecular weight lies between 10,000 and 42,500 [84]. PCL has low glass transition (-60^oC) and melting (60^oC) temperatures. Its decomposition occurs at above 350^oC, while other members of its polymer family decompose at temperatures below 100^oC [26]. Some of the PCL mechanical/thermal properties can be seen in Table 2.8.
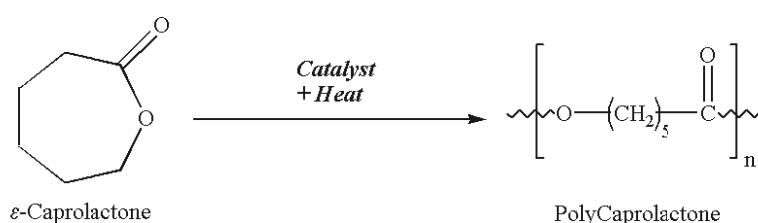
Figure 2.11. PCL synthesis [85]

PCL is semi-crystalline, hydrophobic and biodegradable. It chemically degrades very slowly by bulk hydrolysis of the ester bonds [84], using two steps – firstly, a hydrolytic chain scission occurs, which provokes a molecular weight loss; secondly, the low molecular fragment and polymer particles are solubilised in the body fluid or/and phagocyted, which results in further molecular weight loss [86]. Its degradation kinetics can be controlled by different factors, among them crystallinity and porosity [87]. Complete degradation and elimination of PCL can take 2-4 years depending on the molecular weight (the greater the molecular weight, the longer the degradation time) [85]. As PCL is a synthetic biodegradable polymer, then not only tissue-PCL interaction has to be taken into account, but also the potential toxicity of the degradation by-products. This polymer has shown a non-inflammatory and non-mutagenic response when implanted in animals [85]. However, Rezwan et al. [87], in their review, indicated that acidic degradation products of PCL and its copolymers have

provoked adverse tissue reactions in the past. Ciapetti et al. [88] studied osteoblasts growth in PCL scaffolds. They found that cells were spread maintaining intercellular connections through cytoplasmic elongations after cell-culturing for 3 weeks.

The most important biomedical applications of PCL are as drug delivery systems (DDS) and tissue engineering, particularly in the bone tissue engineering field [87]. PCL has been successfully used in the release of anti-inflammatory agents and protein moieties in *in vitro* and *in vivo* experimental studies [89]. It was shown to remain active as long as a year for drug delivery due to its slow degradation rate so it is considered ideal for implantable long-term DDS; one of its applications, already commercialised, is a 1-year contraceptive (Capronor®) [90]. In the area of bone tissue engineering, Rai et al. [91] studied a drug delivery system (DDS) consisting of polycaprolactone (PCL) and recombinant bone morphogenetic protein-2 (rhBMP-2) for bone regeneration. Recently a new protein which is used for tumour therapy was encapsulated using PCL microspheres [92].

2.3.7. Biocomposites

Composites are materials consisting of two or more different components. There are two constituent materials: the matrix and one or several dispersed phases (also called additives or second phases). The additives are responsible for enhancing the properties of the matrix. Most of the composites target an improvement in matrix mechanical properties such as stiffness, toughness or/and strength. The prefix "bio" implies that the materials used are biocompatible.

Many rigid biological structures such as the human skeletal system, sea shells or insect cuticles are made of composite materials [93]. Bone particularly is a natural composite made of collagen and calcium phosphate mineral, whose mineral phase accounts for 60–70% of the total dry bone weight [94]. Therefore, as a biomimetic approach, it seems reasonable to consider biocomposites as adequate artificial substitutes in bone tissue engineering.

The most commonly used bioactive ceramic in the manufacture of scaffolds is HA due to its chemical resemblance to mineral bone. However, as it was shown in Table 2.7,

HA mechanical properties after manufacturing processes are lower than those of bone. Extensive research has been carried out and an enormous number of papers have been published about improving HA mechanical properties and pore structure by using it as a matrix of a composite material. However, the ideal reinforcement for HA has not yet been found. Among the properties that should be taken into account to choose the second phase materials are: melting point, volatility, density, Elastic modulus, coefficient of thermal expansion, creep characteristics, strength, fracture toughness and interaction between matrix and reinforcement [33].

Dorozhkin [95] comprehensively reviewed the state of the art of calcium orthophosphate-based biocomposites in 2009. Some of the reinforcement materials for HA matrices referred to in this review are: zirconia or PSZ, alumina, titania, other oxides, silica and/or glasses, wollastonite, metals and alloys, calcium sulfate, silicon carbide, barium titanate and zeolite.

Table 2.8 shows a number of properties of the bulk dense HA and some of the second phase materials used as additives in literature [69, 96-99]: Yttria-stabilised Zirconia, Titania, Titanium, Polyetheretherketone (PEEK) and Polycaprolactone (PCL). These were also the candidate materials chosen for this research, and each is framed in more detail below. As it was detailed before, polymers are added to HA as pore formers. Therefore, polymeric materials will be explored as candidates to improve pore structures of the biocomposites.

Table 2.8. Mechanical/thermal properties of HA bioceramic matrix and used additives

Property	HA	ZrO$_2$	TiO$_2$	Ti	PEEK	PCL
Density, g/cm³	3.16[9]	6.08[11]	4.23[8]	4.506[8]	1.26-1.41[2]	1.09-1.2[7]
Compressive Strength, MPa	500-1000[11]	7500[11]	n/a	n/a	80-120[11]	n/a
Tensile Strength, MPa	78-196[12]	420[11]	n/a	138[6]-500[8]	70-208[11]	20.7-34.4[10]
Flexural Strength, MPa	115-200[11]	1000[9]	n/a	n/a	3700[2]	n/a
Young's Modulus, GPa	11^1-117[9]	150-200[1]	230[15]	105-110[11]	3.9[3]-13[11]	0.34[10]
Poisson ratio	0.27[9]	0.30[11]	0.27[15]	0.34[8]	0.38-0.43[11]	n/a
Elongation at break, %	3-4[5]	n/a	n/a	16[11]-54[6]	1.3-50[11]	700[7]
Fracture Toughness, MPa·m$^{1/2}$	1[11]	7[1]-15[11]	3.2[15]	n/a	2.3-2.5[11]	n/a
Vickers Hardness, HV	300-700[14]	1000-3000[14]	880[15]	120-200[11]	21.7[3]	n/a
Knoop Microhardness	430[8]	1200[8]	n/a	n/a	n/a	n/a
CTE, 10^{-6}·K^{-1}	n/a	10[11]- 12[4]	9[15]	8.6[8]-9[11]	161-669[2]	n/a
Thermal conductivity, W/mK	n/a	2[4]-2.5[8]	6.5[8]-12[15]	17[11]-22[8]	0.25[2]-0.92[11]	n/a
T$_{melting}$, °C	1550[13]	2400[4]	1640[8]	1668[6]	335-343[2]	58-63[10]
T$_{glass}$, °C	-	-	-	-	137-152[2]	-60[10]

References: [1] Hench et al. [24]   [5] Gibbons [49]   [9] Bronzino [18]   [13] Levingstone [103]
[2] Fried [79]   [6] Brady et al. [62]   [10] Kutz [20]   [14] Kehoe [29]
[3] Kuo et al. [100]   [7] Iroh [102]   [11] Black et al. [50]   [15] Ceram Research Ltd. [104]
[4] Warren et al. [101]   [8] Lide [63]   [12] Legeros [51]

Notes:
n/a: Not available
ZrO$_2$ refers to Zirconia stabilised with Yttria
TiO$_2$ refers to rutile phase

- *HA/YSZ biocomposites:*

A well studied candidate to reinforce HA is YSZ [36], which retains high mechanical strength and toughness when incorporated as a second phase [97]. It is well known that during the sintering of HA/Zirconia composites above 1000° C, a diffusion of CaO in ZrO$_2$ occurs which facilitates the change from metastable tetragonal phase to a stable cubic one [105]. This change makes toughening by zirconia transformation unlikely to happen. Furthermore, other resorbable phases occur: CaZrO$_3$, α-TCP and β-TCP [56, 106]. This thermal decomposition, which leads to changes in the physical-chemical properties (lowered dissolution rate, etc.) of the composite, which can affect its performance when implanted in-vivo [106]. The following reaction occurs during sintering [97]:

$$Ca_{10}(PO_4)_6(OH)_2 \rightarrow 3Ca_3(PO_4)_2 + CaO + H_2O \qquad \text{Eq. 2.4}$$

$$ZrO_2 + CaO \rightarrow CaZrO_3 \hspace{4cm} \text{Eq. 2.5}$$
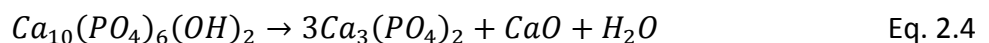
It has been reported that HA decomposition is controlled by the amount of Ca incorporated into the zirconia lattice [107]. If this reaction does not take place, the flexural strength and toughness of HA are improved significantly: 50%HA/50%ZrO$_2$ composites can reach 439 MPa and 2.5 MPa·m$^{1/2}$ respectively [108]. In fact, YSZ is an effective reinforcing phase for the HA ceramic-matrix, satisfying the following conditions [24, 58]:

- Mechanical properties of YSZ are higher than those of HA (Table 2.8)
- The interfacial strength HA-YSZ is neither too weak nor too strong
- YSZ and HA have similar coefficients of thermal expansion (Tables 2.7 & 2.8)
- YSZ is biocompatible

There are two different YSZ reinforcements used within the on-going plasma spraying HA/YSZ biocomposite research: zirconia stabilised with 3 mol% or 8 mol% of Y$_2$O$_3$ (from now on 3YSZ and 8YSZ respectively). Chang et al. [109] studied plasma sprayed HA/8YSZ composite coatings and found an increase in porosity due to the presence of Zirconia in the HA matrix. It was also observed that the formation of CaZrO$_3$ was insignificant due to the short residence time of the powder in the plasma flame. Finally it was pointed out that 8YSZ reinforcement provokes a greater improvement in the mechanical properties of the composite than the 3YSZ reinforcement.

Fu et al. [110] found that, by varying the addition of 8YSZ from 10 to 50 wt% to HA, the porosity, fracture toughness and Young's modulus of the composite coating increased as the amount of phases produced by thermal decomposition decreased. However, Lee et al. [111, 112] showed that 10 wt% of 8YSZ inhibits the formation of an apatite layer *in-vitro* and the osteointegration *in vivo*, suggesting a decrease in this percentage as a solution. Thus, an optimum balance should be established between mechanical and biological properties through 8YSZ addition. On the other hand, Evis et al. [113] studied the addition of 3YSZ in the range 10-40 wt% and found an increased osteoblast adhesion for the smallest addition of zirconia to HA.

- *HA/Ti biocomposites:*

Most metals react with HA to form oxides, TCP and TTCP [58]. Titanium accelerates dehydroxylation so the decomposition of HA occurs at a temperature as low as 800° C; the products of HA decomposition at this temperature are TTCP and calcium oxide [96]. At higher temperatures (~1200° C) the decomposition product are CaO and amorphous phases, as is observed in the following equation [114]:

$$Ti + Ca_{10}(PO_4)_6(OH)_2 \rightarrow CaTiO_3 + CaO + Ti_xP_y + (Ti_2O) + (Ca_4P_2O_9) + H_2O \quad \text{Eq. 2.6}$$
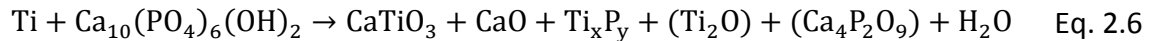
Chu et al. [115] reported that HA-40 vol% Ti obtained by hot pressing has excellent Young's modulus (79.3 GPa), Vickers hardness (294 HV) and fracture toughness (2.7 MPa·m$^{1/2}$), which could satisfy the requirements of some load-bearing applications. Ning et al. [116] found that a thick layer of apatite formed on the surface of the Ti/HA composite, obtained via hot pressing, after 1-week soaking in simulated body fluid (SBF). *In vivo* tests carried out on New Zealand white rabbits demonstrated the excellent biocompatibility of HA-40 vol% Ti and the ability of this composite to actively grow new bone on its surface after 4 weeks of implantation; full osteointegration was achieved after 3 months of implantation [115].

- *HA/TiO₂ biocomposites:*

Li et al. [117] found that the addition of less than 20 vol% of TiO$_2$ to HA improved the Young's modulus, fracture toughness and shear strength of HVOF coatings. The thermal degradation of HA is accelerated in the presence of oxide additives such as TiO$_2$, however it is possible to slow it down by adding CaO-containing compounds [118].

HA/TiO$_2$ coatings produced by electrodeposition were demonstrated to precipitate and grow an apatite layer with preferred orientation in SBF solution [119]. Human osteosarcoma cells were found to spread and grow actively on HA/TiO$_2$ coatings manufactured via sol-gel technique [120]. The presence of OH$^-$ groups on the surface of these components seems to be responsible for good interaction with osteoblastic cells [121].

- *HA/PEEK biocomposites:*

PEEK is a bioinert material, but when blended with HA the formed biocomposite presents bioactivity, which is directly proportional to the HA content [122]. HA/PEEK biocomposite can show ductile and brittle behaviour depending on the content of HA. The melting temperature of the biocomposite also depends on the HA content, varying from $341^{\circ}C$ to $339.8^{\circ}C$ for HA-content range varying from 10 to 40 vol% [123]. HA/PEEK composites, after 16 weeks implanted in vivo, showed areas of mature bone within the pores of the implant and fibro-vascular tissue in the other areas [98].

- *HA/PCL biocomposites:*

PCL, as an additive to HA, has been shown to improve the fracture performance of the composite, changing the crack propagation behaviour from catastrophic to a controlled one: crack bridging [124]. After in vitro culture, HA/PCL composite materials were found to have a suitable surface to promote osteoblast attachment and growth [125]. Marra et al. [126] also found cell viability and collagen formation into a (PCL-PLGA blend)/HA composite scaffold. Their experiment involved using fresh bone marrow and bone marrow stromal cells.

2.4. Thermal Spray Technology

The history of thermal spraying dates back to the late 1800's. Early experiments consisted of breaking up liquids into fine particles by a stream of high-pressure gas in an attempt to produce powders rather than coatings [127]. It was in the early 1900's when Schoop first proved that a stream of molten lead and zinc particles impinging on a substrate could build-up a protective coating. Schoop developed the first patent on the use of a combustion process to melt wire and to drive it towards the substrate. The addition of an electric arc as a heat source was the subject of his second patent in 1908 [128]. These findings resulted in the establishment of the thermal spray technology, which industry and researchers use today.

Nowadays the thermal spray process still relies on the same principles but has broadened in versatility: the heating of a feed-stock material (wire but also powder, rod or suspension at present) up to a semi-molten or molten state. The heat required

can be produced by electrical or chemical means depending on the process. The softened particles are propelled towards the substrate where they are deposited, cool down and built up into a coating. Thus, a thermally sprayed coating is composed of a large amount of individual particles chemically and mechanically interlocked which adheres to the substrate through a mechanism of mechanical anchoring. The air gaps left between particles cause a variable percentage of porosity in the coating depending on the process used [129]. Among the advantages of using thermal spraying as a coating technique are [128, 130]:

- High deposition rate (up to 45 kg/h), which results in low processing costs.
- Porosity or oxides trapping can be controlled to some extent by selecting adequate process and material.
- Coating thickness from 50 μm to 6.5 mm can be achieved depending on the process and feedstock.
- Wide choice of materials (ceramics, metals, cermets[3] and polymers) depending on the particular process.
- Wide choice of substrates as the surface does not heat up significantly.
- Environmentally friendly when compared with other processes such as plating.

The main disadvantage of the thermal spraying process is its line-of-sight limitation which typically prevents plasma spraying been used to coat holes or other topographical features on a work-piece. The anisotropic properties of the coatings can be an important disadvantage for some applications.

The thermal spraying technology itself includes a number of different processes (Figure 2.12):

---

[3] Cermets: Materials consisting of processed ceramic particles bonded with metal. High-strength and high-temperature applications are their main use.

THERMAL SPRAY

```
                              THERMAL SPRAY
        ┌──────────────┬──────────────────┬──────────────────┐
    Combustion        Plasma        Electric/wire arc    Kinetic
  ┌─────┼─────┐      ┌────┴────┐     ┌────┼─────┐           │
Powder Wire  Rod  Air (APS) Chamber  Air Inert Chamber  Cold Spray
```

Combustion:
- Oxy-fuel
- D-Gun
- High Velocity
  - HVOF
  - HVIF
  - HVAF

Plasma — Air (APS):
- Low velocity
- High velocity

Plasma — Chamber:
- Vacuum (VPS)
- Inert (CAPS)
- Underwater (UPS)
- Shrouded (SPS)

Kinetic — Cold Spray:
- Helium
- Nitrogen
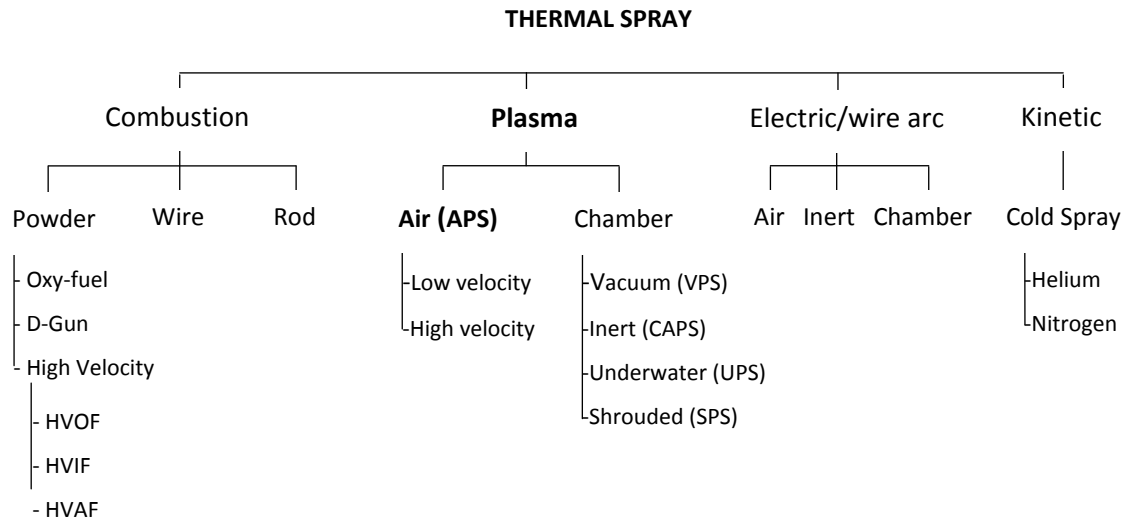
Figure 2.12. Thermal Spray processes (adapted from [128])

Figure 2.13 [127] shows a list of various industrial segments using different thermal spraying processes. As can be seen, the most extensively used techniques are flame spray (oxy-fuel or D-gun), high velocity oxyfuel (HVOF) or atmospheric plasma spray (APS). Vacuum techniques are more expensive so they are limited to special applications such as aeronautical, medical and electronics. The thermal spray processes most used within the medical industry are mainly plasma processes but also HVOF.

The manufacturing technique selected to carry out this research was an experimental low energy version of a conventional APS process designed by INASMET (Spain). Therefore, the basics of the APS process will be reviewed in detail in this section. In addition, the combustion processes will be briefly described below as they have been used in the past to spray biomaterials and polymers.

INDUSTRY	Oxy-fuel	Spray/fuse	HVOF	D-gun	Air plasma	Vac-plasma	Shroud plasma
Aero gas turbine	X		X	X	X	X	X
Stationary gas turbine	X		X	X	X	X	
Hydro-steam turbine	X		X	X	X	X	X
Automotive engines	X		X		X		
Diesel engines	X		X		X		
Transportation non-engine	X			X	X		
Agriculture implementations	X	X			X		
Railroad	X		X		X		
Iron and steel manufacture	X	X			X		
Steel rolling mills	X	X	X		X		
Iron and steel casting			X		X		
Forging	X		X				
Copper and brass mills	X						
Ship and boat manufacture and repair	X						
Oil and gas exploration	X	X	X	X	X		
Mining, construction and dredging	X	X	X		X		
Rock products Screening	X	X	X		X		
Cement and structural clay	X	X	X				
Chemical processing	X	X	X	X	X		
Rubber and plastic manufacture	X	X	X		X		
Textile	X		X	X	X		
Food processing	X	X	X	X	X		
Electrical utilities			X		X		
Pulp and paper	X		X		X		
Printing equipment			X	X	X		
Defense and aerospace	X		X	X	X	X	
Nuclear			X	X	X		
Medical			X	X	X	X	X
Business equipment			X	X	X		
Electrical and electronic			X	X	X	X	
Architectural	X	X			X		
Glass manufacture		X		X	X		

Figure 2.13. Thermal spray processes by industries [127]

2.4.1. Combustion processes

The oxy-fuel process, most commonly known as Flame spray, uses the chemical energy produced in the combustion of combustible gases to heat the material feedstock (powder, wire or rod). Oxyacetylene torches are the most commonly used processes. Jet gas speeds are below 100 m/s and jet flame temperatures are above 2600°C [131]. Conventional flame spray has not changed significantly since the 50's [128]. The detonation gun (D-gun) system was simultaneously developed by Paton Welding Institute (Ukraine) and Union Carbide (USA) (nowadays Praxair Surface Technologies) in order to improve coatings' density, cohesion and adhesion. This process produces higher thermal and kinetic energy jets ($T^{e} > 3000^{o}$C and $v > 1000$ m/s [128]) due to confined combustion within a chamber. Powders are fed followed by a jet expansion.

The high-velocity oxyfuel (HVOF) process was developed in the late 50's by Praxair as well, but it was not commercialised extensively until the late 70's [128]. Compared

with the classic flame spray process, HVOF produces higher thermal and kinetic energy jets using a continuous high pressure internal combustion within the volume where the powder is injected. The fuel gases used in this process, together with the oxygen, can be: hydrogen, methane, propylene, propane, acetylene, heptane and kerosene. Jet gas speeds above 1200 m/s and jet temperatures greater than 3000°C can be achieved [131].

2.4.2. Atmospheric Plasma Spraying (APS)

The first plasma sprayed coating was made by Reinecke in 1939 [131]. The Atmospheric Plasma Spraying (APS) process employs an ionised gas to melt and accelerate the feedstock powders propelling them towards the surface of a substrate to form a coating or a forming die to produce free-standing components. The layout of the process can be seen in Figure 2.14.
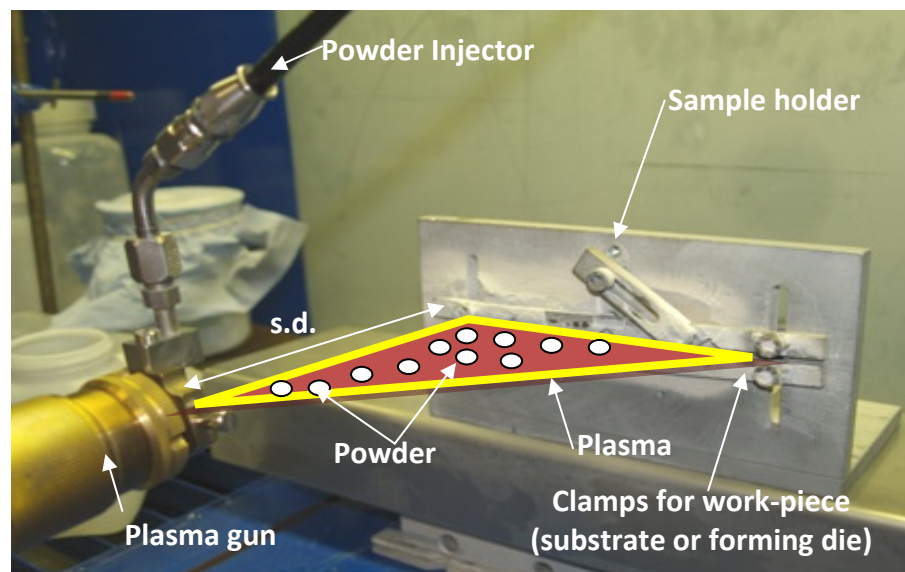
Figure 2.14. APS process schematics

The process gases (plasma forming gases) are injected with a spinning momentum to stabilise the electric arc formed inside the gun, between a central thoriated tungsten cathode and a water-cooled concentric copper anode (nozzle) [130]. The nozzle design also helps to stabilise the arc and accelerate the exiting gases through an expansion (velocities in the range 200-1000 m/s), resulting in a plasma plume. The plume temperature can be as high as 20000°C [128], depending on the process gas properties and electrical characteristics. The plasma-forming gases normally used are: Argon (Ar),

Helium (He), Hydrogen (H_2) and Nitrogen (N_2). Mono-atomic gases, such as Argon and Helium, have lower enthalpies than diatomic gases (nitrogen, hydrogen) which have to dissociate before ionising to form the plasma. As an example, argon plasmas require a large arc current (800-1000 A) to allow materials to melt, but this results in extremely high gas velocities and, therefore reduced particle residence times in the plume. This prevents adequate melting of materials such as ceramics (high melting points). Thus, a secondary gas is supplied to increase the gas energy to an adequate level. The most popular gases and combinations of gases used are (from higher to lower enthalpy): N_2/H_2, N_2, Ar/H_2, Ar/He, Ar.

The feedstock material is carried by a gas stream and delivered to the nozzle through a powder injector. The particle heat input depends not only on the process-gas energy, but also on the particle in-flight trajectory during the dwell time[4]. The particles' trajectory is influenced by the injection arrangement, which can be accommodated depending on the physical/thermal properties of the powders been deposited. The injectors can be changed in geometry (diameter) and can be placed inside the nozzle (internal configuration) or outside (external configuration) regulating the position respect to the plasma plume (angle and radial/axial distance).

The ionised gas melts and accelerates the feedstock powders towards the work-piece. One single impacted particle is called a 'splat'. The spray pattern, formed by many overlapping splats, produces a Gaussian-shaped bed with width (d_{bed}) and height (h). A layer is produced when several spray paths are performed with an overlapping distance Δy (Figure 2.15). The coating/component is produced when a series of layers are sprayed one on top of the other.

---

[4] Dwell time: The length of time in which the sprayed particles remain in an optimized heat zone.
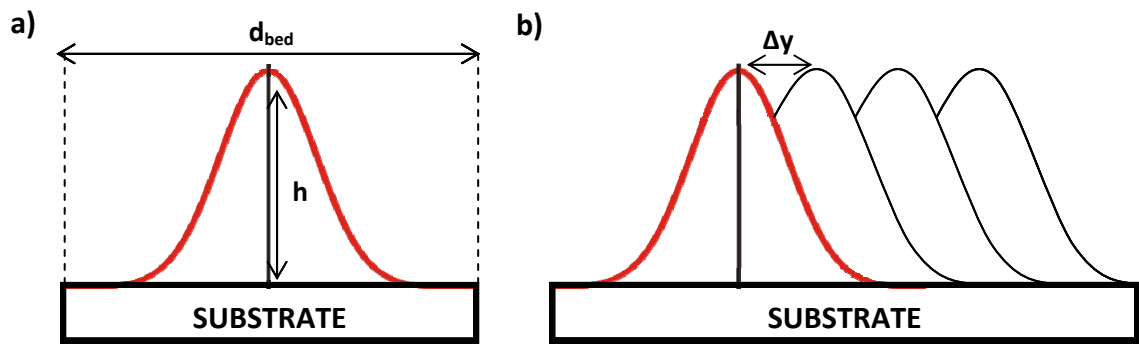
Figure 2.15. Schematics of: a) spray pattern and b) layer overlapping pattern

The resultant coating characteristics are strongly influenced by the material feedstock intrinsic properties and the APS parameters used. The main parameters affecting the resultant coatings are listed below, some of which can be directly controlled by the users [128, 131, 132]:

- **Powder**
  - Particle size distribution, density and shape
  - Thermal, physical and chemical properties

- **Powder injector**
  - Carrier gas composition and flow rate
  - Powder feed rate
  - Injector geometry, location and angle

- **Plasma gun**
  - Nozzle diameter

- **Plasma**
  - Gas composition and flow rate
  - Energy (current, voltage)
  - Plasma plume properties (temperature, velocity, air dilution)
  - Powder dwell time and trajectory in plasma stream

- **Sample holder**
  - Relative movement to the gun (direction, velocity)
  - Stand-off distance (s.d.)
  - Cooling system

- **Work-piece**
  - Temperature
  - Surface roughness
  - Residual stress control (cooling down rate)
  - Particle quenching rate and impact energy

There are some coating properties that are mainly influenced by the thermal input given to the particles during the process, such as: porosity, crystallinity, purity, thermal/residual stresses and colour [128]. Furthermore, the thermal input is intimately interrelated to the kinetics of the process. Original feedstock characteristics such as crystalline and impurities content are also influential in the properties of coatings [130].

The thermal input can be controlled modifying spray parameters (such as current/voltage; and plasma gas composition and flow rate) and powder characteristics (such as particle size distribution). The thermal content at the substrate surface can be controlled by attaching a cooling jet (air, liquid CO_2 or liquid nitrogen) parallel to the gun [133], which will also minimise the amount of debris on the coating [128]; or/and by allowing the sample holder to act as a thermal sink (water-cooled copper block)[134].

Porosity: The standard range of porosity in APS coatings/free-standing components varies between 3-20% [47] depending on the particle characteristics and spraying parameters selected. The main sources of porosity are: shadowing effect (high spraying angle), narrow holes and/or gas trapped between particles, unmolten particles, inter-intra splat cracking and poor cohesion, material shrinkage on cooling from the molten state and satellite particles formed when particles impact the substrate [110, 135]. The porosity can be minimised by increasing the particles thermal input and velocity. The smaller the particles the more dense the coating obtained [136]. If the porosity is greater than 10%, it can be interconnected, which is only a benefit for applications such as thermal barrier coatings (TBCs), oil/grease retention and biomedical coatings [128]. Post-thermal processing can be used to decrease the level of porosity [137].

Crystallinity/phase purity: Particles in-flight temperature gradients and cooling rates within the coating vary the crystallinity and phase purity of the material feedstock. Dyshlovenko et al. [138] studied the crystallinity of Hydroxyapatite coatings finding that it was mainly affected by electric power, primary gas composition and injection type (internal/external). Coating thickness has been reported to influence the

crystallinity [139]; and thickness is essentially dependant on sprayed lines overlapping (Δy), relative velocity gun/sample holder, stand-off distance and powder feed rate. The phase content and crystallinity has also been reported to vary through the thickness of the coating [140]. There are several other works studying the effects of plasma spray parameter variations on the crystallinity and purity [3, 103, 141].

Colour: The colour of the coating may change due to thermal degradation [142, 143] or chemical variation of feedstock material during processing [144, 145]. Typically non degraded HA is deposited as a white coating but it can also form grey/blue colour variations [103].

Residual stresses: This is one of the major problems in plasma spraying, especially in the production of thick coatings [146] (like that of scaffolds). The plasma temperature can be as high as 20000^oC, but it decreases abruptly from the nozzle tip to the sample holder position where the temperature could be only a few hundred degrees [128]. This extreme temperature gradient provokes micro-scale quenching stresses in the individual particles. In addition, as the splats solidify on the coating they contract, but are constrained by each other and the substrate/die, thus tensile stresses are generated. Once spraying finishes, macro-scale cooling stresses appear due to the mismatch in the thermal expansion coefficients of the substrate and the coating (cooling stress can be tensile or compressive depending upon the relative values of these coefficients) [147-149]. There is a third type of residual stress generated by phase transformation within the material, which can induce volume changes [150, 151]. The overall residual stress is equal to the sum of the phase transformation, quenching and cooling stresses.

Three parameters have been reported to affect the coating final stress magnitude and sign (tensile or compressive): deposition temperature, particle energy and coating thickness per pass [152]. The importance of the thickness per pass has been reflected in an analytical model for residual stresses in plasma spraying coatings [148].

To conclude this section on the APS process, it must be stated that the major advantage of this process is the possibility of spraying a wide range of materials (from polymers to ceramics). The large number of independent variables involved, as shown above, makes control of the process difficult; however this can be seen as an advantage because it increases the flexibility of the process. The high deposition rate which allows coatings to be quickly produced is another benefit of the APS. However, the high temperature during spraying causes the development of residual stresses within the deposit, which essentially limits the thickness of the final deposits that can be obtained. On the other hand, the low electrical efficiency and the difficulty to achieve reliable coating reproducibility are the main drawbacks of this technique.

2.5. Specific Thermal Spraying applications

Some selected applications, which are relevant to this research, will be reviewed in this section. The aim of producing scaffolds requires free standing-composites components to be produced rather than coatings. Therefore, the techniques available to remove a coating from a substrate are detailed. Following this is a review on the different methods to produce composite coatings: feedstock and injection-based methods. The final two sections review the research carried out to date with polymers and biomaterials.

2.5.1. Plasma Spray of free-standing components

Fang et al. [153] reviewed two different approaches used to produce free-standing components based on traditional moulding techniques (Figure 2.16).
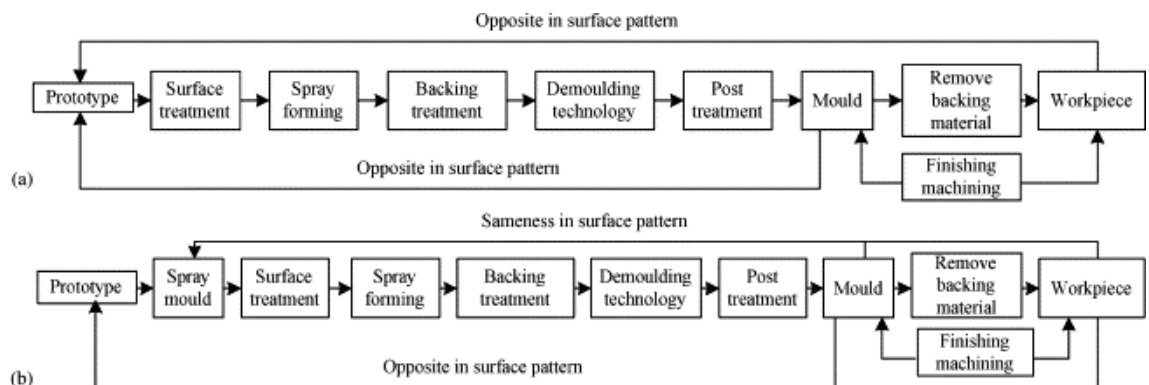
Figure 2.16. Techniques to form free-standing components [153]

One of the key problems of forming free-standing components is the removal of the coating from the substrate. Therefore, it is important to control the mechanical bonding coating-substrate during deposition in order to maintain a minimal bonding to allow the coating to form. On the other hand, a strong bonding would make difficult to remove the two parts afterwards.

A great deal has been written about the adhesion mechanism theory [154] and a lot of research has been carried out to find the process parameters which improve the bonding of the coating to the substrate [155, 156]. All the parameters shown as essential to improve the adhesion play an important role on this opposite application: to ease the removal of the coatings. For instance, if oxide-free surfaces are desired to improve the coating adhesion to the substrate [154], the opposite may ease coating removal. However, a minimum adhesion is still required in order to build up the coating.

The technological solutions adopted by the research community to release the coatings have been diverse, some of them are:

1. Pre-spraying a salt interlayer before coating deposition, which was followed by immersion in water [45].
2. Pre-spraying an aluminium-based interlayer via HVOF, which is melted away in a furnace after spraying [157].
3. Placing an aluminium foil lined along the internal surfaces of a die, which is melted away on a furnace afterwards [158].
4. Using mandrels made of materials with very different thermal expansion coefficients (larger) to that of the deposited material [159].
5. Not preparing the surface to be sprayed, just cleaning it, and cooling it with liquid nitrogen after spraying (thermal shock) [160].
6. Using a thin layer of commercially available Crown #9105 anti-seize agent [161]

Not all of the solutions listed are suitable for all materials: the salt interlayer method is not suitable for feedstock materials sensitive to water; equally the aluminum interlayer

methods are not suitable for biomedical applications because any residual compromises the biocompatibility of the sprayed material due to its cytotoxic effects.

2.5.2. Thermal Spraying of composite components

There are a number of possibilities when two different powders are sprayed to build composites or functionally graded materials:

1. Through the same feeding system: The powders can be blended [162] or a composite powder can be fabricated by spray drying [163], mechanical alloying [25, 164-166] or ceramic slurry mixing (cladding: core material coated) [47, 165, 167].

2. Through separate feeding systems, namely co-injection [165, 168, 169].

Blending the powders leads to inhomogeneous composite coatings due to the different in-flight trajectories and residence times of the different powder particles depending on their densities and sizes [170]. Agglomeration by spray drying allows the combination of different materials in order to produce a composite powder which behaves homogeneously [171] and mechanical alloying can be used to tailor the chemical composition and size of the powders with homogeneous behaviour also. Cladding is the preferred option if the core material needs to be protected from the thermal input of the plume, the adhesion of the coating needs to be improved or the wetability/flowability of the core powder needs to be improved [154], but it is not always an easy process to perform. Co-injection of the powders eases the spraying of materials of different types but requires a good optimisation to balance the two carrier gas flows which introduce the powders into the plume. For instance, co-injection of ceramic/polymer has been conducted using this method; the polymer was fed into a cooler part of the plume whereas the ceramic was injected in a hotter part [172].

2.5.3. Thermal Spraying of polymers

Polymers have been thermally sprayed since the 80's for different applications, exploiting one or more of their exceptional characteristics (electrical insulation, high chemical resistance, low coefficient of friction, ductility and high toughness) [128]. Petricova et al. [173] extensively reviewed the thermal spraying of polymers, forecasting the role that this technique will play in finding new applications for this

type of coatings. However, a full understanding of the relationship of the process parameters and coating structure/properties is noted as being essential. The thermal sensitivity of most of the polymers makes it necessary to tightly control the heat input during the spraying. Therefore, the process window is quite narrow and different for each polymer, where poor particle melting defines the bottom line and burning the upper one [174]. Even in this narrow window the polymer can undergo changes such as cross linking, chain scission and/or oxidation.

Polymer properties influence final characteristics of the coating; for instance, melt viscosity and decomposition products affect the porosity of the coating, and a large particle size or molecular weight distribution assist the formation of microstructure inhomogeneity [128]. Particle size was shown to have an enormous influence on the polymer degradation; small particle sizes increase the degree of degradation [174].

Powder Flame spray and HVOF have been the most widely used thermal spraying techniques to apply polymeric coatings. However, plasma spray is the preferred choice if a ceramic-polymer or metal-polymer composite material has to be produced [165]. Polymers that have been plasma sprayed to date to form polymer or composite coatings include PTFE [165]; PFA [172]; nylon-11 [175]; PEEK [176]; PP, LPE, UHMWPE, PVDF, polyester and nylon 6/12 [177]; MDPE [168]; PMMA [178]; and polyamide [174].

2.5.4. Thermal Spraying of biomaterials

Plasma Sprayed coatings used for biomedical applications are usually bioactive ceramics, such as Hydroxyapatite or other calcium phosphate containing materials. There has been extensive work conducted on the production and performance of HA coatings produced by thermal spray techniques [25, 45, 103, 146, 179-182]. Thermal degradation and a decrease in the crystallinity of HA during plasma spraying have been reported in nearly all of the publications and reviews on the topic of thermal sprayed HA and special care has been taken to reduce this effect. HA has also been proven to have poor adhesion to substrates, a problem that has been solved using bond coatings [183].

Bioinert oxide ceramics (alumina, zirconia or titania) and pure titanium and its alloys (Ti6Al4V, etc.) have been extensively plasma sprayed for biomedical applications. They have been used alone or as particulate reinforcements for bioactive ceramic or bioglass coatings [59, 110, 184]. Thermally sprayed composite coatings (ceramic + polymer) have been shown to have a great potential for bone implants applications due to the decreasing of bone-ceramic Young's modulus mismatch [166]. Recently, carbon nano-tubes (CNT) have been used to reinforce HA achieving promising results [185]. However, whether CNT are cytotoxic or/and carcinogenic is still under discussion within the research community. Complex biomaterials, such as $CaO-P_2O_5-TiO_2-ZrO_2$, have also been plasma sprayed and have been proven to enhance mechanical properties and chemical stability compared with pure calcium phosphates [186].

2.6. Summary

The first part of this chapter has presented the field of application for this research. The main requirements for the scaffolds have been established and the different types of biomaterials have been classified. Hydroxyapatite (HA) is seen as a good matrix candidate for composites; it is biocompatible, bioactive and osteoconductive, and has similar composition and Young's modulus to mineral bone. However, HA has low fracture toughness, which may be improved by adding second phase materials. Titania (TiO_2) and Yttria-stabilised Zirconia (YSZ) are thought to be good candidates to reinforce HA, as they have higher toughness. An introduction to the mechanical and biological properties of candidate second phase materials was presented.

The second part of this literature review introduced the fundamentals of Thermal Spraying techniques, specifically those used within the biomedical industry. Within this field, Plasma Spraying has mainly been used to produce biocoatings onto metallic substrates. However, it has been shown that this technique is able to produce thick free-standing components, namely scaffolds. The main drawback of this technique for the targeted application is the final pore structure (porosity < 20%). However, the idea of adding pore formers (polymers) as a solution to improve the pore network has been introduced. Polyetheretherketone (PEEK) and Polycaprolactone (PCL) have been selected as possible candidates to act as pore former.

3. Materials and Equipment

This chapter details specific technical information regarding the materials and equipments used in the experimental work.

3.1. Raw Materials

As mentioned in the introduction chapter, the main material used in this project is Hydroxyapatite (HA). Different types of second phase materials were added to the "matrix" material in order to improve the mechanical properties and pore structure of the final composites.

In this section the commercially available powders used and their properties provided by the suppliers are reported. For two of the powders, Titanium and Poly-ether-ether-Ketone (PEEK), the suppliers are unknown. These powders, donated by INASMET, were used to check the performance of the different types of powders on the system. Polyvinyl alcohol (PVA) powder was only used as a binder during the attrition milling process of some of the powders. The raw powders characterisation procedures are presented in Section 4.5.

3.1.1. Hydroxyapatite (HA)

The Hydroxyapatite powder used in this project was supplied by Plasma Biotal Ltd. The company completed XRD analyses on the powders after sintering to check thermal stability and whether minor quantities of other phosphates had not formed during their production process. Two different sizes were used under commercial names HA CAPTAL 90 (HA90) and HA CAPTAL 60-1 (HA60):

1. HA90 (Batch # P250): This powder was produced as a wet paste, which was tray dried and sintered at 1300°C. Finally, the product was passed through a set of calibrated sieves, removing the particles outside the size limits. The final particles were minigranules. The HA powder specification indicated traces of Tetra-calcium Phosphate (TTCP) and an average particle size of 82.48 μm. The powder was reported to be totally crystalline. Table 3.1 shows the chemical analysis of this powder.

2. HA60 (Batch # P280S): The production method followed was spray drying/sintering at 1150°C/sieving. The final particles were spherical. The powder specification shows traces β-TCP (< 1%) and batch particle size of d(0.5)= 46.32 μm and d(0.9)= 77.40 μm. The powder was reported to be totally crystalline. The impurity content can be seen in Table 3.1.

Table 3.1. HA90 and HA60 impurity contents

Component	HA90	HA60
Heavy metals	<10 ppm	<10 ppm
Arsenic	<0.5ppm	<1ppm
Cadmium	<0.1 ppm	<1 ppm
Mercury	<0.5 ppm	<1 ppm
Lead	<0.1 ppm	<1 ppm

3.1.2. Polycaprolactone (PCL)

The PCL (product # 440744) was supplied by Sigma Aldrich Co. Some of the PCL properties provided by the supplier are shown in Table 3.2.

Table 3.2. PCL properties supplied by Sigma Aldrich

Property	Value
Linear formula	$(C_6H_{10}O_2)_n$
Appearance	White to off-white beads
Form	Crystalline
Density, g/cm^3	1.145 (@25°C)
Molecular weight (M_n)	74,441
Polydispersity	1.26
Melting point, ^{o}C	60

The powder was cryogenically milled under 300 μm by Solid Composites, spin-off from Fraunhofer Institute (Germany) and finally sieved to under 125 μm at DCU.

3.1.3. Yttria-stabilised zirconia (YSZ)

The Yttrium Partially Stabilised Zirconium Oxide Y3 grade (3 mol % or 5.2 wt %) was donated by HiCharms (product number HiC-2047), as a white high purity milled powder. The Y3 powder was processed via two different chemical precipitation stages which generated very low traces of impurities. The impurity content of the powder is shown in Table 3.3. The powder was reported to have an average particle size of 1 μm, a density of 5.97 g/cm^3 and a specific surface area of 8-15 m^2/g.

Table 3.3. YSZ impurity content

Component	Quantity
SiO_2	<0.01 wt%
TiO_2	<10 ppm
Fe_2O_3	<10 ppm
Na_2O	<10 ppm

3.1.4. Titania (TiO$_2$)

The Titanium oxide, under the commercial name of AMPERIT 782.1 was supplied by Flame Spray Technologies Ltd. The particle size analysis carried out by the supplier shows that the powder's particle size was below 88 μm, 99% of the particles were below 62 μm and just 5% were below 15 μm. The average particle size was reported to be in the range of 30-35 μm. The apparent density was reported to be 1.98 g/cm^3. The impurity content is shown in Table 3.4.

Table 3.4. TiO$_2$ impurity content

Component	Quantity
SiO_2	0.05 wt%
Fe_2O_3	0.02 wt%

The powder phase composition was given by means of X-Ray Diffraction analysis, and it mainly consists of Rutile phase with a mixture of 3 other titanium oxides: Ti_8O_{15}, TiO and Ti_4O_7.

3.1.5. Polyvinyl Alcohol (PVA)

The PVA (product # 341584) was supplied by Sigma Aldrich Co. Some of the PVA properties provided by the supplier are shown in Table 3.5.

Table 3.5. PVA properties supplied by Sigma Aldrich

Property	Value
Linear formula	$(-CH_2CHOH-)_n$
Appearance	White powder
Form	Crystalline
Density, g/cm^3	1.269 (@25^oC)
Molecular weight (M_w)	average 89000-98000
Viscosity, Ns/m^2	13.6×10^{-3} (4%, H_2O @ 20^oC)
pH	5.37
Polydispersity	1.26
Melting point, ^oC	200
Flash point, ^oC	> 113
Residue on ignition, %	0.38 wt%

3.2. Target formers

Two types of targets were used during this research:

1. Thick coatings were produced in order to evaluate the microstructure, roughness and some mechanical properties. The substrates used were steel plates ($19 \times 49 \times 2$ mm^3).

2. Free standing circular components (diameter: 10 mm) were produced using a stainless steel die Figure 3.1.

Figure 3.1. Three-hole die used to produce free-standing components

3.3. Plasma spray equipment used

Selection tests were conducted using different plasma spray systems (LEPS, F4 and 9Mb). The selected system was an experimental low energy plasma system designed by INASMET-TECNALIA (San Sebastian, Spain). The descriptions of the systems with the different guns are described below.

In general, the components of any plasma spray system can be classified into the following groups:

- Core Components: This group includes the atmospheric plasma spray gun, the feedstock powders; the powder feed delivery system; a plasma gas supply system; a control system that controls the gas, electrical and cooling water requirements; and a power source.
- Handling Components: Gun and workpiece manipulators.
- Auxiliary Components: Spray booth, water chiller, extraction system and air filter.

3.3.1. Low Energy plasma system (LEPS)

The LEPS system is a low energy plasma deposition device designed specifically for the deposition of Calcium Phosphate coatings on small sized bone implants without major phase degradation and decreasing crystallinity levels. It is characterised by highly reliable and reproducible behaviour, low cost and portability. The special system core components are:

- A standard DC power source up to 15 kW from a TIG-welding system. It has an electronic auto ignition control (Praxair, Triton 400).
- The low energy plasma gun. The gun design (Figure 3.2) was optimised by INASMET for the deposition of commercial plasma spray HA powders with different particle size distributions. It works with a turbulent gas jet.
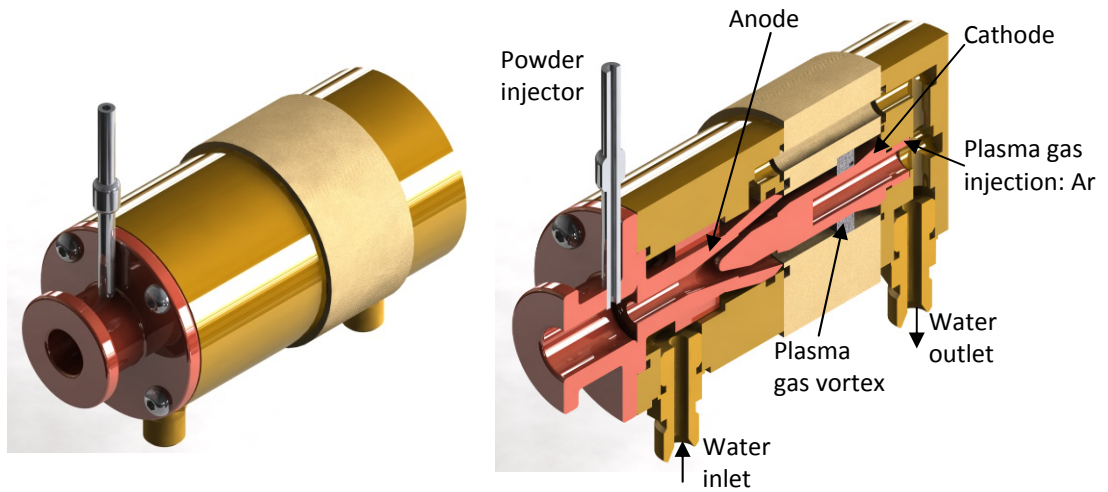
Figure 3.2. LEPS gun main components [187]

The rest of the core components are conventional. Two volumetric powder feeder units of the drilled wheel type, one twin unit and one standard unit, provide the system with flexibility to spray different powders at different positions. The powder feeding rate obtained at the minimum wheel rotational velocity was proven to be too high in certain cases (i.e. PCL). A further reduction in the feeding rate was achieved reducing the channel of the feeding plate to 1/3 of its original volume (Figure 3.3).
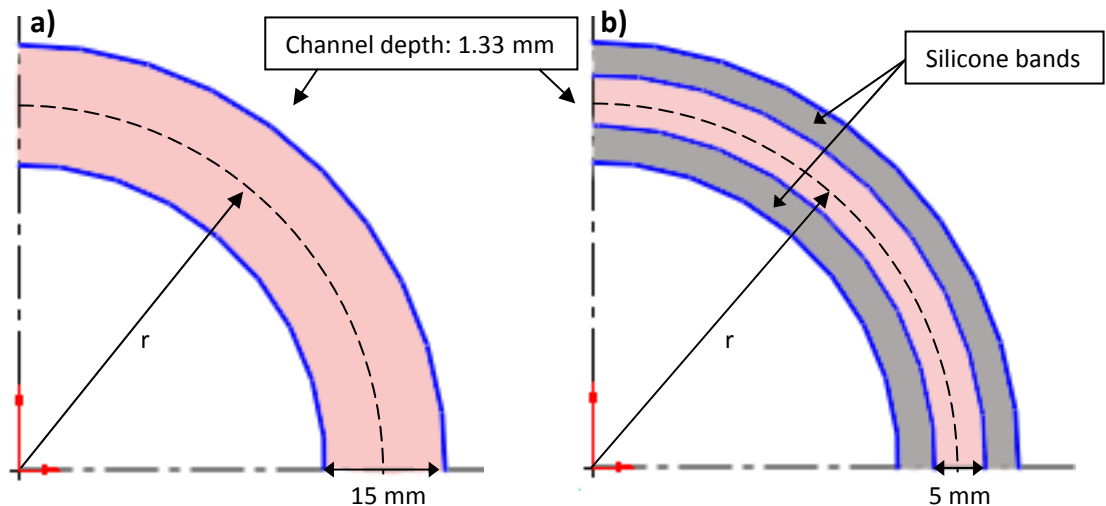
Figure 3.3. Schematics of: a) Original and b) reduced channel in the feeding plate

The handling and auxiliary component are standard too: a robot that controls the gun 2D movement and its velocity; a sample holder which is adjustable in height and distance from the gun exit; a spray booth with an extraction system and access to a compress air cooling system; and a water chiller. The system overview can be seen in Figure 3.4.
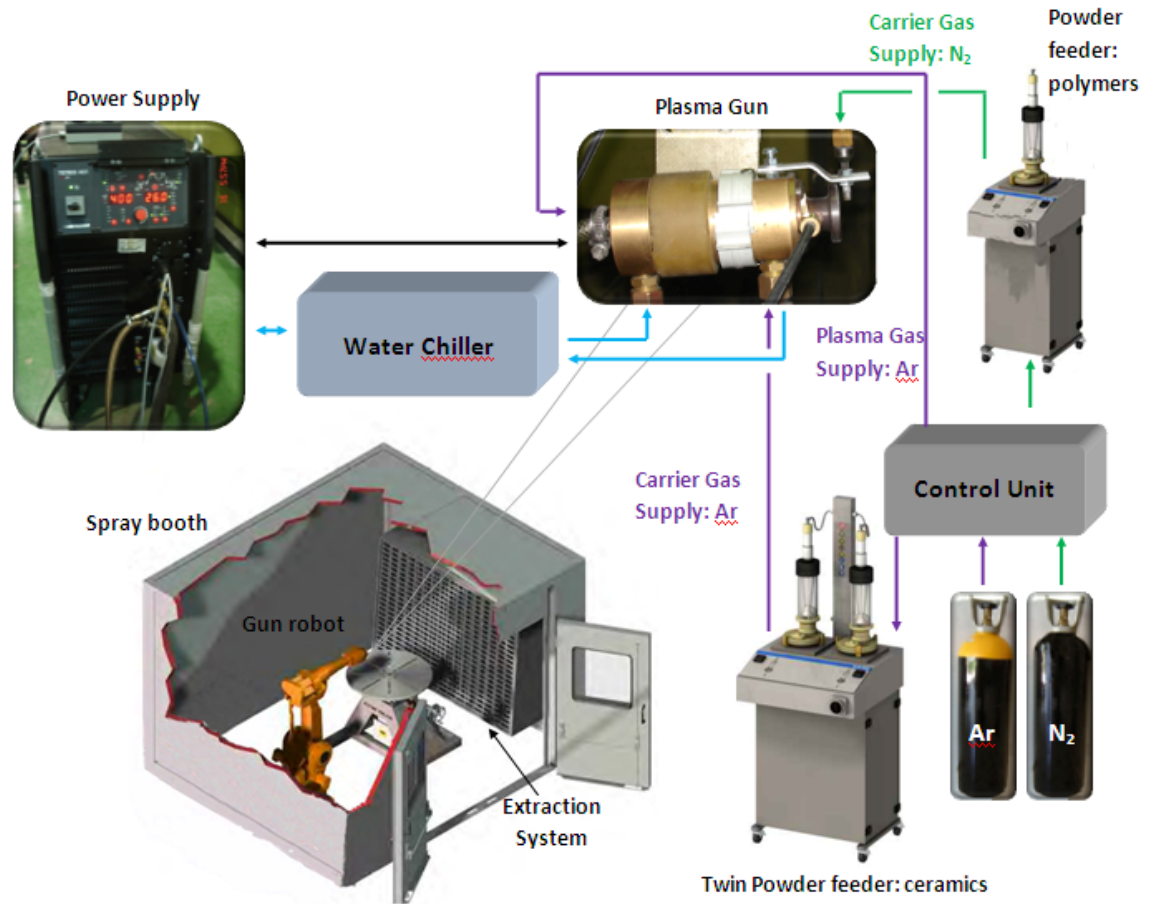
Figure 3.4. Low Energy Plasma System (adapted from [187, 188])

The features that make this system unique and its use advantageous over other standard plasma spraying process are:

- The low energy DC power source used to generate the plasma.
- The sole plasma gas is Argon. The reduced size of the power source together with the absence a secondary plasma gas (Hydrogen, etc.) makes the system portable.

- The gun design allows the system to work in a turbulent plasma gas jet flow using a low energy input without becoming unstable. It can also be easily modified to make it adaptable to the specific spraying requirements. During this research several gun modifications were performed in order to feed the different powders, resulting in three different gun configurations (Appendix A).

- The y-increment (Δy) is in the range of 2-3 mm, which means that a small overspray will take place. Thus, the sprayed target can be smaller (dental implants, spine implants, etc.) than in a regular APS process. In this way, the powder deposition efficiency is increased.

- Substrate cooling is not always required because there is low thermal transfer into the spraying target due the low energy input on the system.

The main drawback of the system is the limitation on the type of materials that can be processed, which are calcium phosphates, since the plasma flow rate and the energy transferred to the spray particles is limited by the power source. Therefore, to spray different types of materials was an important challenge during this research.

3.3.2. F4 gun system

The F4 gun system, placed in INASMET facilities is practically the same as the one used for the LEPS system, which is shown in Figure 3.4. The main differences are the gun, the power supply (up to 55 kW) and the use of just the twin powder feeder. In addition, two plasma gases are used in this system: Argon (primary gas) and Hydrogen (secondary gas). The control unit for this arrangement regulates several spraying parameters: arc current, plasma gas ratios and flow rates. A commercial standard powder injector ring was attached to the tip of the F4 plasma gun to allow the feeding of two different powders in counter-flow (one at 90°, the other at 75° towards the gun). A schematic of the F4 plasma gun configuration can be seen in Figure 3.5 and its features, taken from Sulzer Metco product catalogue [188], can be seen in Table 3.6.
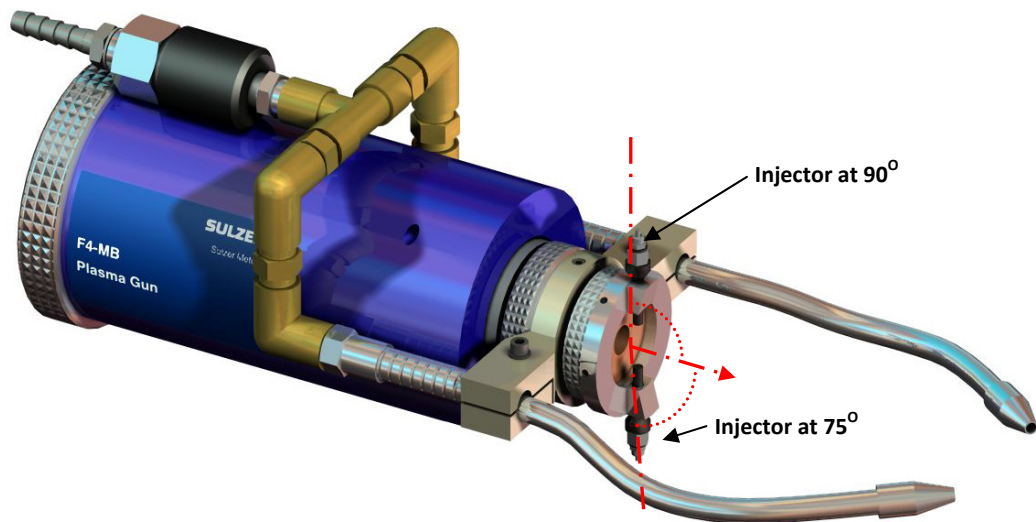
Figure 3.5. F4 plasma gun [188]

3.3.3. 9MB gun system

The 9MB gun facility located at Dublin City University was provided by Sultzer Metco. It consists of three main units: the 9MCE plasma control unit, the 9MB-dual plasma spray gun and the 9MPE closed-loop powder feeder system (Figure 3.6).
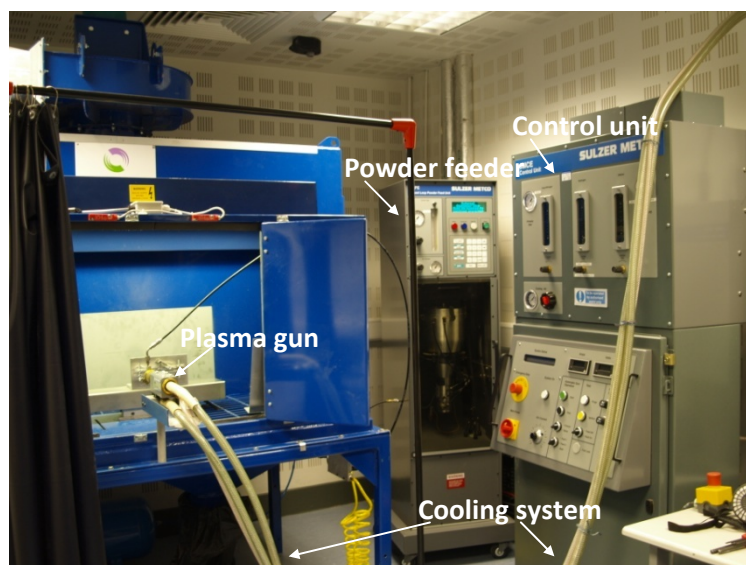
Figure 3.6. 9Mb gun rig configuration

The control unit regulates several spraying parameters: arc current, plasma gas ratios and flow rates. The parameters related to the powder feeding are controlled by the powder feeder unit: powder feed rate and carrier gas flow rate. The powder feed rate is continuously adjusted by a weight loss metering system. The powder injection is external to the gun nozzle and perpendicular to the gun horizontal axis.

The 9MB gun is comprised of a 9MB63 electrode, a 3M7-GH nozzle and a close-loop cooling system to avoid overheating of the gun parts. The cooling system circulates water at a rate of 12 l/min. The main features of the 9Mb gun, based on Sultzer Metco catalogue data [188], are listed in Table 3.6. The plasma gun and sample mover are enclosed in a booth, which is fitted with an extraction system.

Table 3.6. Features of F4 and 9Mb plasma guns [188]

Feature	F4 gun	9Mb gun
Power capability, kW	$\leq$55	$\leq$80
High heat output capability, ^{o}C	$\leq$16000	$\leq$16000
High plasma gas velocity, m/s	>3050	>3050
High Particle velocities, m/s	<610	<610
Deposit efficiency, %	50-80	75
Typical spray rate, g/min	40-80	75
Cooling water flow rate, l/min	10-14	12-17

4. Experimental methods

A description of the statistical design methodology chosen to design the experiments is firstly provided. An overview of the different processing and characterisation techniques used during this research is also presented in this chapter. In addition, the different equipment used is described and the experimental procedures followed are outlined.

4.1. Experimental Design approach

The experimental approach followed in this work was done over several stages: selection tests, optimisation of HA deposition and improvement of HA coatings' characteristics through the optimisation of the second phase addition.

The selection tests consisted of selection and feasibility tests. The plasma spray system and the matrix material to use in this work were selected. The identification of the important LEPS parameters affecting the coating properties was carried out during the selection tests. After this series of tests the goal was set to obtaining thick coatings rather than free-standing coatings due to economic reasons. Feasibility tests were then conducted for different kinds of materials and their mixtures. A reasonable indication of the range of parameters to use for optimisation purposes was found during selection and feasibility tests.

The optimisation experiments were statistically designed to obtain mathematical models, which correlate the variation of the main process parameters (factors) with the resulting coating properties (responses). The optimisation of the process parameters for HA deposition (Series HA) was the first step to be accomplished, since the HA was employed as the matrix material of the composites coatings and played an important role on the final coating thickness. Following initial screening tests, the most critical process parameters were established and used as factors. The factors were selected from those enumerated in Section 2.4.2. However, this list of parameters was reduced by taking into account the following issues:

- the substrate related parameters were not taken into account as the final application was to produce free-standing components,

- the powder related parameters were those provided by suppliers,

- the plasma gas and carrier gas compositions were those available at INASMET facilities and,

- the current/voltage parameter variations do not affect significantly the coatings' properties due to the narrow energy window of the selected process.

The most sensitive coating properties (thickness, crystallinity and roughness) were selected as responses. In addition, the porosity and different mechanical properties (Young's modulus, fracture toughness and microhardness) were studied to quantitatively compare the manufactured composite structures.

The addition of the selected second phase materials (PCL (Series HP), TiO_2 (Series HT)) was optimised using the reference process parameters established for the deposition of pure HA. The factors investigated for each series are shown in Table 4.1.

Table 4.1. Factors investigated for the optimisation of the different series (HA, HP, HT) following a DOE concept

Series HA (Box-Behnken)	Factor code	Low level (-1)	Centre point (0)	High level (+1)
Plasma gas flow rate (slpm)	A	30	36	42
Stand-off distance (cm)	B	3.5	4	4.5
HA feed rate (g/min)	C	5	7	9
Series HP (HA/PCL) (2-level factorial)	Factor code	Low level (-1)	Centre point (0)	High level (+1)
PCL feed rate (mg/min)	A	40	80	120
Injector distance d (mm)[*]	B	17	22	27
PCL carrier gas (slpm)	C	5	7	9
Series HT (HA/TiO$_2$) (Box-Behnken)	Factor code	Low level (-1)	Centre point (0)	High level (+1)
Plasma gas flow rate (slpm)	A	30	36	42
TiO$_2$ carrier gas flow (slpm)	B	4.5	5	5.5
TiO$_2$ added to HA, wt%	C	5	15	25

* This distance (d) is measured from the exit of the gun. Therefore, the injector distance from the substrate is: d' = *stand-off distance – d*.

4.1.1. Design of Experiments (DOE)

The Handbook of Statistical Methods [189] defines Design of Experiments (DOE) as follows: "DOE is a systematic, rigorous approach to engineering problem-solving that applies principles and techniques at the data collection stage to ensure the generation of valid, defensible, and supportable engineering conclusions. In addition, all of this is carried out under the constraint of a minimal expenditure of runs, time, and money".

Statistically designed experiments were used to carry out the optimisation stage, using the software *Design Expert 7.0* by Stat-Ease Inc. The optimisation of HA deposition and TiO_2 addition were studied by response surface methodology, using a Box-Behnken design. On the other hand, the addition of polymers was studied using a 2-level full factorial design because fewer experimental runs to build the mathematical models were required. The factorial design is therefore preferred for expensive materials such as PCL and when less material consumptions are desired. A brief description of both design methods is presented below.

- 2-level full factorial design

This design allows the study of the effect of each factor and the interaction between factors on each response. Given a number of factors (k), each with 2 discrete possible values (levels), a 2-level full factorial design consists of 2^k experiments (runs). This means that all possible combinations of these levels across all such factors are considered in this design (Figure 4.1 a). *Design Expert 7.0* software also recommends testing at least 4 centre points in order to get an adequate test for curvature (non-linearity between factorial points) and lack of fit (variation of the data around fitted model).
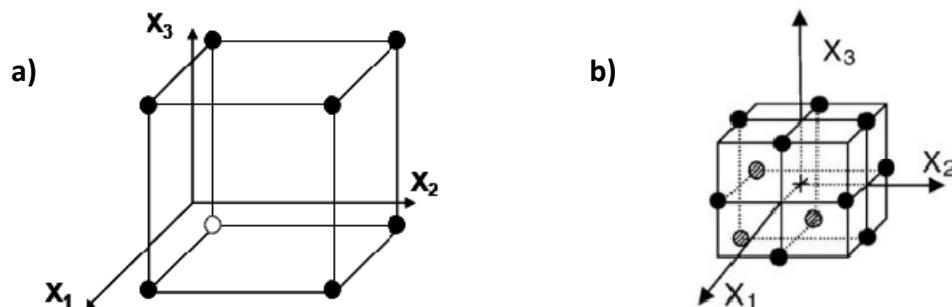
Figure 4.1. Graphical representation of: a) 2-level full factorial design and b) Box-Behnken design for 3 factors [190]

The model produced consists of a series of coefficients multiplied by the factors (or combination of factors). The best values of the coefficients are those for which the resulting predicted values are close to the measured ones, and the statistical uncertainty connected with each coefficient is small. A response (Y) can be obtained as follows:

$$Y = b_0 + \sum_{i=1}^{k} b_i X_i + \sum_{i,j=1}^{k} b_{ij} X_i X_j + \sum_{i,j,w=1}^{k} b_{ijw} X_i X_j X_w \ (i \neq j \neq w) \qquad \text{Eq. 4.1}$$

where k is the number of factors; b_0 is the mean of responses of all the experiment; b_i represents the effect of factor X_i; and b_{ij}, b_{ijw} represents the effect of the interactions between the factors $X_i X_j$ and $X_i X_j X_w$ respectively. The coefficients of main effects (b_i) and the first order interaction (b_{ij}) are the most interesting terms [190].

- Box-Behnken design

The Box-Behnken design is sufficient to fit a quadratic model, which contains squared terms and products of two factors. This design consists of a fraction of the experiments required for a 3-level factorial design (3^k runs). It combines 2-level factorial designs with incomplete block designs [191].

For instance, the Box-Behnken design for 3 factors involves three blocks, in each of which 2 factors are varied through the 4 possible combinations of high and low. The resulting subset of experiments, graphically shown in Figure 4.1, includes the middle points of the edges of the cube that represent the experimental space. Testing of 4-5 replicates of the centre point is required to estimate the global standard deviation.

4.1.2. Analysis of Variance (ANOVA)

Analysis of variance was used to study the statistical models. There are number of statistical terms that helped to evaluate the statistical significance of the models, which are defined in Appendix B. Basically, a model is adequate if the series of hypothesis shown in Table 4.2 are true. It is also advisable to achieve a Predicted R^2 and Adjusted R^2 values from the model as high towards R^2 as possible ensuring good model fitting. The best scenario happens when all the three values are close to 1.

Table 4.2. Hypothesis for a valid model in DOE

Term	Hypothesis
Model Prob>F	< 0.05
Lack of fit (LOF) Prob>F	>0.1
R^2	$0.6<R^2\leq1$
Predicted R^2 – Adjusted R^2	≤ 0.2
Adequate Precision	> 4

4.2. Powder processing

This section describes the powder processing stage. The sampling method which assures that the sample extracted is representative of the full range of the particle size distribution is presented. The small particle size of some of the powders prevents adequate flowability in the system. The production of composites containing small-sized powder requires a pre-spray powder processing stage (agglomeration). The agglomeration procedure, consisting of attrition milling and sintering stages, is described in this section.

4.2.1. Powder sampling

Transportation and storage of powders provoke stratification in particle sizes within the containers; larger powders tend to lie on the bottom region. Therefore a sampling method was required to assure that the sample extracted was representative of the full range of the particle size distribution. A glass tube was introduced perpendicularly into the powder container, so the powder sample contains particles of all the different size regions (elementary extraction). Several extractions were conducted using this method and the powder was then placed in a smaller container, which was mixed for at least 15 minutes. This homogeneous powder was finally allowed to flow through a Hall flowmeter onto a watch glass. In this way a circular path of powder is produced along the outer circumference of the glass. This causes the bigger particles to flow towards the centre of the glass, leaving the smaller particles behind at the path.

The amount of powder needed to measure each selected property was taken from a section of this circular path, which contained all the different sizes within the powder [192].
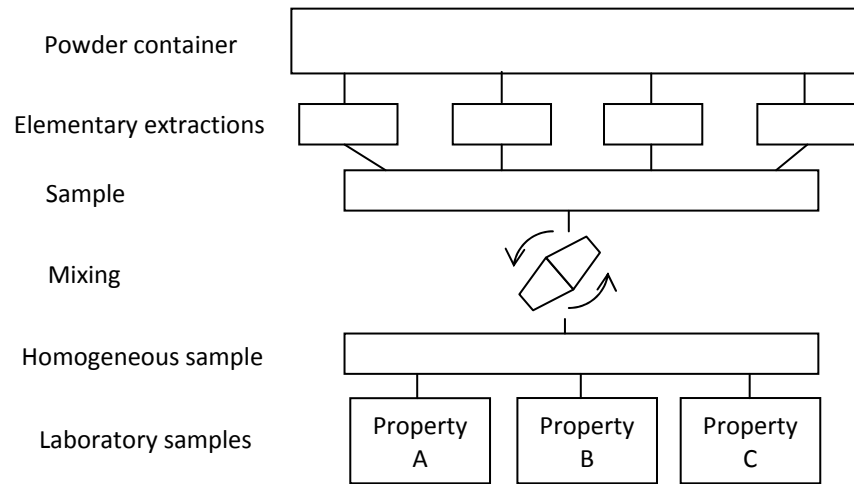
Figure 4.2. Method to extract representative samples (adapted from [193])

4.2.2. Attrition Milling

The attrition milling process was developed by J.S. Benjamin in the 60's when trying to produce oxide dispersion in iron and nickel based super alloys [194]. This technique has been applied since then to process metals, ceramics, polymers and composite materials.

Attrition milling processing was carried out by the author at University of Seville (Spain) and all the process parameters were set following the advice of laboratory technicians. The atmospheric attrition milling system used was a *Research model 01-HD Attritor* from Union Process, with a 1/4HP motor and velocity range 0-650 rpm. The attritor mill consists of a water cooled vessel (750 cm^3), which contains 1800 g ball bearings (diameter: 4.6 mm) moved by a rotating impeller. The rate of balls/powder was set to 30:1, which means that only 60 g of powder can be processed for each run of the mill.
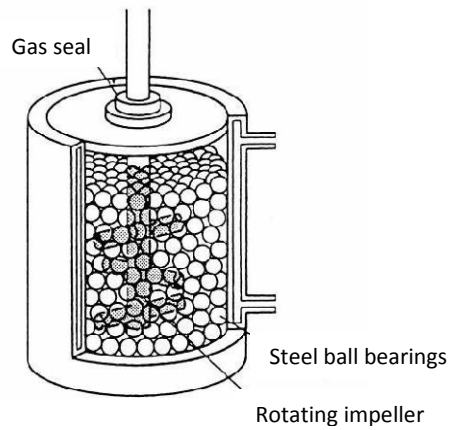
Figure 4.3. Schematic diagram of an attrition mill [195]

Attrition milling was used to obtain an agglomerate of Hydroxyapatite with the fine Yttria-stabilised Zirconia (YSZ), using 1% of poly-vinyl-alcohol (PVA) as a binder. Polyvinyl alcohol was selected because it has been used as a binder in milling processes in previous research [196, 197]. As the materials to be milled were ceramics, which are brittle in nature, the milling time was set to 30 min and the velocity to 300 rpm, to avoid excessive breakdown of the particles. Table 4.3 shows the composition of the fabricated powders.

Table 4.3. Powders fabricated by attrition milling

Batch name	Powders content
HA5YSZ	HA60 + 5%wt YSZ + 1%wt PVA
HA15YSZ	HA60 + 15%wt YSZ + 1%wt PVA

The powder compositions shown in Table 4.3 were obtained from the laboratory samples of each powder. The mixture was introduced in a small container and then agitated for 30 minutes in a *Turbula Type T2 C* mixer. The homogeneous powder mixture was then introduced into the vessel, once the mill was running at 150 rpm. The velocity was increased to the value selected (300 rpm) and the powder particles then began to collide with each other being repeatedly trapped between the ball bearings. The process of powder trapping between two balls can be seen in Figure 4.4.
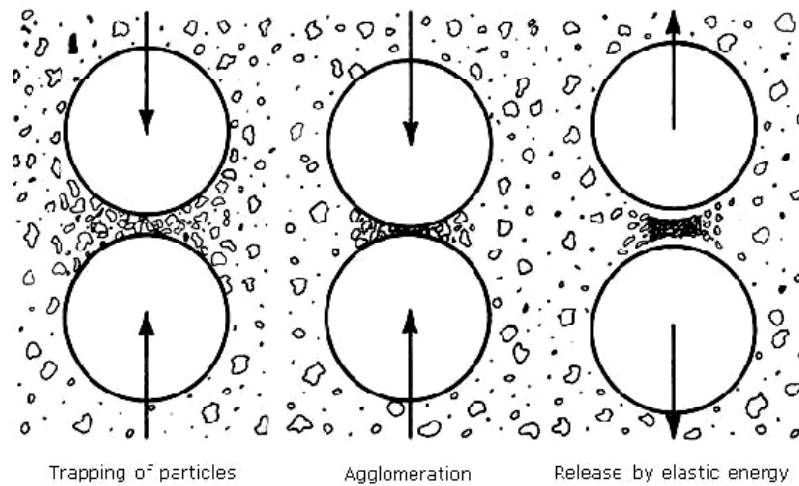
Figure 4.4. Schematic of balls-powder collision in attrition milling process [198]

An initial mill was run for each composition. This ensured that vessel, balls and impeller are covered with a thin layer of the material being milled. The powder obtained after this first mill was not used to avoid contamination.

Finally, the powder was separated from the balls by putting the mill contents into a sieve (mesh 0.2 mm) and vibrating it for 15 min. The system was carefully cleaned and the process described above repeated after processing each composition.

4.2.3. Sintering

The attrition milled powders were placed in alumina crucibles and sintered in a *Carbolite RHF Eurotherm* oven. The sintering was carried out, in air, at 1000°C for 1.5 hours, following the processing methodology of Plasma Biotal Ltd. The specific sintering program followed is shown in Figure 4.5. A heating rate of 10°C/min was set up to reach 970°C. From 970 to 1000°C the heating rate was set to a slower value (5°C/min) to avoid overheating due to furnace thermal inertia. The powders were left in the furnace to freely cool down.
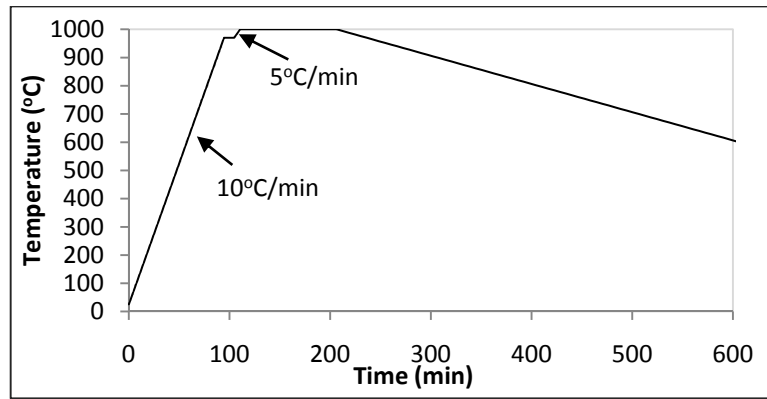
Figure 4.5. Sintering program for attrition milled powders

4.3. Target preparation

- <u>For free-standing components production:</u> The procedure to prepare the target focused on facilitating the coating removal process post deposition. A two step preparation procedure was used to prepare the three-hole die: cleaning and polishing to reduce the roughness as much as possible.

- <u>For thick coating production:</u> Each steel substrate was prepared just before spraying. As a first step the substrates were cleaned with alcohol to remove grease and dust present on the surface. Then the steel substrates were grit blasted with alumina (Al_2O_3 F24, 600 - 850 µm) size and a blasting pressure of 6 bar. The samples were grit blasted to ensure that the full surface was roughened and free of oxides. Following grit blasting the samples were blown using a compressed air jet, and cleaned with alcohol to remove any traces of the grit material. The cross-sections of the samples were observed to ensure that no alumina particles were present in the coating-substrate interface.

4.4. Plasma spraying procedure

The target preparation normally causes the surface of the samples to be more reactive and responsive to oxidise. Therefore, each target was placed in position just after preparation and processed immediately. The process started once the process parameters were set to the desired values and the movement and velocity of the robot, which holds the gun, were adjusted. The plasma spray processes, even the low energy one, are hazardous processes which involves high-level noises, gas emissions,

UV light, etc. For this reason personal safety protection was worn at all times when the systems were running. A full description of existing hazards and required safety equipment is shown in Appendix C.

Temperature of the coating/component was measured just after finishing the process using a Würth Pyrometer (*#0853600*). Finally, the target was removed from the holder and placed over an aluminium plate to cool down.

4.5. Powder characterisation

The best conditions when plasma spraying a powder is to uniformly melt all of the particles into the plume to produce good quality coatings. Different particle sizes within the distribution travel through the plume at different velocities and follow different trajectories; and receive different heat input as a result. In addition, to efficiently introduce the powder into the plume the carrier gas flow rate should be optimised for the particular distribution average size; hence much smaller particles may not have the sufficient momentum to enter the plume and much larger particles might cross the plume, thus, decreasing the efficiency of the process. For these reasons, the ideal powder for plasma spray is preferred to have a narrow particle size distribution. However, it has been also reported that wider particle size distributions leads to greater porosities within the coatings [133], which is a benefit for scaffolds.

The particle sizes should be also within a certain range. Finer particles, as they are lighter, need a greater carrier gas flow rate to enter the plume, therefore the bottom limit (5-10 μm) is defined by the maximum carrier gas flow that can be used without perturbing the plasma plume. Particles below 20 μm have been reported to drastically increase collisions against the injector walls resulting in divergent trajectories at the injector exit [133]. The upper limit of the range depends on the thermal properties of the material to be sprayed and therefore size limit should be located at the size where particles start bouncing-off when striking the substrate due to a lack of melting. Particle size within the range 20-45 μm has been reported to produced optimal HA coatings [199]. Polymeric powders, due to their low density need to be larger than other powders (ceramics or metals) in order to feed them inside the plume; for

instance, a PCL particle needs to have an almost 1.5 fold-diameter in order to have the same mass as an HA particle ($\rho_{HA}/\rho_{PCL} \approx 3 \rightarrow r_{PCL} = \sqrt[3]{3} \ r_{HA}$).

The powder composition is an important characteristic to take into account when selecting the feedstock material, as it would unavoidably affect the final composition of the coatings. However, modifications on the initial composition may occur if the powder undergoes thermal degradation/decomposition due to the high temperatures involved during the processing.

For all this, powder characterisation is important because the final characteristics and properties of the coated samples are influenced by the feedstock powder characteristics. The powders can be characterised by either considering the individual particles (morphology, etc.) or the powder as a whole (flowability, etc.) [200]. In this section, the basics of a number of characterisation techniques are reviewed. The procedures followed and the equipment used are also described.

4.5.1. Flowability

An important powder characteristic is its flowability on the feeding system, which becomes critical if this is gravitational based. Generally, powders flow worsen as the amount of irregular particles increases [103] and as particle size becomes smaller [201]. However, there is no absolute value for this property as it depends on the process in which the powder is flowing [202]. This parameter was not as critical in this research as the powder is pushed by a carrier gas, but it will be studied to gain a fair idea of the relative flowability of the powders.

The Standard ISO 3252 [203] defines flowability as a qualitative term describing the behaviour of a powder flowing through a hole. In practice, flowability is defined as the property of a powder to flow through a hole on the base of a calibrated conic vessel (Hall flowmeter) which contains a specific amount of this powder.

The Standard ISO 4490 [204] states the procedure to follow to measure the powder flowability and was used in the current work. A fixed amount of powder (50 ±0.1 g) was introduced into a Hall flowmeter funnel while the hole (diameter: 2.5 mm) on its base

was closed with a finger. The flowability (g/s) is defined as the time required for 50 g of powder to flow through the Hall funnel with time to be counted from the hole is opened, with a precision of 0.1 s.

4.5.2. Density

Three different densities values are described in this section: apparent, tap and absolute density. The apparent density together with the tap density measures the densification capacity of the powder without pressing it, and gives an idea of its flowability. The absolute density describes the density of the powders produced by attrition milling based on the theoretical densities of the raw powders used.

- Apparent density

The standard followed to measure this density was the ISO 3923. Two parts of the standard were used: "Part 1 - Hall funnel method" [205] and "Part 2 - Scott volumeter method" [206]. The standard defines apparent density as the powder weight per volume unit obtained using the first method in the case that powder flows through a hole smaller than 5 mm of diameter; or the second one if the first approach does not work. It is important to mention that the volume in this case includes the gaps between particles.

This standard indicates that the Hall funnel/Scott volumeter should be placed at a preset height over a cylindrical tin vessel with a volume of 25±0.05 cm^3. The funnel/volumeter was then filled with 50±0.1 g of powder which was allowed to flow up to overflow the vessel. The powder was levelled out without pressing on it. Finally, the powder contained in the vessel was weighted with a precision of 0.05 g. The apparent density ρ_a (g/cm^3) is calculated with a precision of 0.01 g/ cm^3 using the following formula:

$$\rho_a = \frac{m}{V} = \frac{m}{25}(g/cm^3)$$ Eq. 4.2

where V is the volume of the vessel in cm^3 and m is the measured mass of the powder in grams.

- Tap density

The standard followed to measure the tap density was the ASTM B527-2000 [207]. The test started by placing 5 grams of powder in a calibrated tube with a precision of 0.1 cm^3. The tube was then vibrated for a minute. After this time, the tap density (ρ_t) was calculated measuring the volume filled by the powder:

$$\rho_t = \frac{m}{V} = \frac{5}{V} (g/cm^3)$$ Eq. 4.3

where *V* is the measured volume of powder in cm^3, *m* is the mass of powder used in the test in grams.

- Absolute density

This density was calculated for the attrition milled composite powders. The mass fractions and the theoretical densities of each component in the mixtures were considered to calculate the absolute density following the equation below:

$$\rho_{abs} = \frac{m_{total}}{V_{total}} = \frac{\sum_{i=1}^{n} m_i}{\sum_{i=1}^{n} V_i} = \frac{\sum_{i=1}^{n} m_i}{\sum_{i=1}^{n} \dfrac{m_i}{\rho_i}} (g/cm^3)$$ Eq. 4.4

where m_{total} and V_{total} are the mass and volume of the milled powder; and m_i, V_i and ρ_i are the mass, volume and density of the powder *i* in the mixture.

4.5.3. Particle size distribution

The method used to measure the particle size distribution and, therefore, the average particle size was laser diffraction. This method is based on the fact that intensity of light dispersion depends on the particle size; specifically the dispersion angle is inversely proportional to the particle size.

The particle size analysis results are important as the particle size and distribution will affect the final properties of the components. The particle size analyses were performed by the author using a *Mastersizer 2000* analyzer from Malvern Instrument placed at University of Seville facilities. This equipment has a He-Ne laser to measure 'big' particles and a blue light source laser (λ=466 nm) with enhanced resolution to

measure the smallest particles. This setting enables the measuring of particles sizes in the range of 0.2-2000 μm with high precision.

4.5.4. Powder morphology

Powder morphology was studied using a Scanning Electron Microscope SEM (*EVO LS15* SEM from Zeiss). It has detectors to detect the 3 signals: secondary electrons back-scattered electrons and characteristic x-rays, which will be described below.

The SEM works by scanning a high-energy beam of electrons, which interacts with the atoms of the sample. These interactions produce signals which provide information about the surface of the sample: topography, composition, etc. The most important signals interpreted by special detectors included in SEM, which lend their name to the different SEM working modes, are:

1. Secondary electrons (SE). These low energy electrons are ejected from the k-orbital of the atoms of the sample by inelastic scattering interactions with the beam electrons.
2. Back scattered electrons (BSE). These high-energy electrons originating in the electron beam are reflected out of the sample by elastic scattering. They are detected by a semiconductor ring-shape detector concentric to the electron beam.
3. Characteristic X-rays. They are emitted when the electron beam removes an inner shell electron from the atoms of the sample, causing a higher energy electron to fill the vacancy by releasing energy. They are measured using an Energy-dispersive X-Ray Spectroscopy (EDX) system.

The SE mode produces high resolution images (1-5 nm) with a large depth of field yielding images with 3D appearance. Therefore, this mode is preferred to study the surface topography. BSE and Characteristic X-rays are used to obtain information about the distribution of different elements in the sample since the intensity of both signals is intimately related to the atomic number (Z) of the chemical elements present in the sample. Heavy elements (high Z) will produce a stronger BSE signal and, thus, will appear lighter on the image.

The materials used in this research are non-conductive, so they need special preparation to prevent electrical charging during SEM examination. The powders were first fixed to an aluminium stub especially designed to fit into the SEM stage holes, using conductive double-sided tape. Excess powder was then removed using low pressure compressed air. The samples were then placed into the chamber of an *Edwards Scancoat* sputtering coater in which a gold nanometric layer is deposited onto the powders over 80 seconds. This layer ensures the electrical conductivity of the samples, thus, improving the imaging of the 3D powder morphology. Using the Secondary Electron (SE) signal it is also possible to examine the roughness and open porosity of the particle surfaces. The powder morphological features have a great influence on the final deposits obtained through Plasma Spray processing and on the mechanical properties.

Some of the powders to be studied were fabricated by attrition milling. As this is a high energy process the powders produced by this technique were also studied by means of the SEM back-scattered electron signal (BSE) and the EDX in order to study any possible chemical reaction between the powders.

4.5.5. Powder crystallinity

Powder crystallinity was measured just for HA since this property affects the re-absorption behaviour of the material. In order to study this property XRD scans were performed following the standard ASTM F 2024-00 [208].

The XRD is a non-destructive technique broadly used to characterise crystalline materials. Some of the most common applications are: phase identification, quantitative analysis and structural imperfections determination. Diffraction is based on the optical interference produced when a monochromatic radiation crosses a slit, which has a comparable width to the radiation wavelength. Therefore, when the X-ray beam strikes the electrons of a crystalline material, the beam is scattered into many different directions, in the form of spherical waves. Most of the spherical waves cancel out in most directions through destructive interferences. However, the waves are added constructively in few directions which are specified by Bragg's law:

$$n\lambda = 2d_{hkl}\sin\theta \qquad\qquad \text{Eq. 4.5}$$

where λ is the X-Ray wavelength, d_{hkl} is the distance between crystallographic planes, which produces the constructive interference (diffraction), θ is the angle between the X-Ray beam and the crystallographic planes producing the diffraction and n is a natural number.

In crystalline materials different crystallographic planes exist with different Miller indices (h k l) and so a number of angles would follow the Bragg's law. As the crystalline structure is unique for each material, the set of d_{hkl} spaces is also exclusive. Therefore, no two crystals have the same diffraction pattern, and this technique fully enables the distinction of the different phases which are present in any crystalline material. Bragg's law shows that in ideal conditions the diffraction is produced for discrete θ values. However, in practice and due to equipment limitations and sample imperfections the diffraction occurs in an angular interval around θ, which will broaden the peaks in the diffraction patterns.

The X-Ray Diffractometer used was a *Bruker AXS D8 Advance* in Bragg-Brentano geometry, with a CuK$_\alpha$ monochromatic beam (λ = 0.15406 Å) produced at 40kV and 40mA. The selected scan type was a Locked Couple scan, with the scan velocity set to 5 sec/step and step size to 0.02^o. The scanning range was 2θ= 20-60°. EVA software was used for the analysis of the XRD patterns obtained.

The best method to calculate the crystallinity of HA is by using calibration curves. This method involves scanning different mixtures of pure crystalline HA and pure amorphous HA. The preparation of pure amorphous HA powder makes this method difficult and tedious. Instead, the alternative method selected to measure the crystallinity in this work gives a quick estimate of the amorphous content and has been used by other researchers [45, 103]. The HA crystallinity values were calculated from the XRD patterns using the following equation [103]:

$$Crystallinity(\%) = \frac{\sum A_c}{\sum A_c + \sum A_a} x100 \qquad\qquad \text{Eq. 4.6}$$

where $\sum A_c$ is the sum of the areas of all HA crystalline peaks and $\sum A_a$ is the sum of the area under the amorphous peak. These values were obtained using the EVA software.

4.5.6. Powder composition

Powder phase content was measured using X-ray diffraction (XRD) technique detailed above. The X-Ray Diffractometer used was a *Bruker AXS D8 Advance* in Bragg-Brentano geometry with a CuK_α monochromatic beam (λ = 0.15406 Å) produced at 40kV and 40mA. The selected scan type was a Locked Couple scan. The scan velocity was set to 5 sec/step and step size to 0.02^o. The scanning range for each powder can be seen in Table 4.4.

Table 4.4. XRD scanning range for powders

Powder	2θ
HA60, HA90 [208]	20-60
PEEK	20-40
PCL	20-40
Ti	30-80
TiO₂	20-95
YSZ	20-80
Agglomerated powders	20-80

EVA software was used for the analysis of the XRD patterns obtained. Phase identification was performed using powder diffraction files of the Joint Committee on Powder Diffraction Standards (Appendix D) included in EVA software.

The phase content was evaluated for all the raw and attrition milled powders. In the case of HA, if other calcium phosphates were present in the powder, the HA purity can be qualitatively assessed from the XRD patterns using the following equation [103]:

$$Purity(\%) = \frac{\sum A_c - \sum A_i}{\sum A_c} x100$$

Eq. 4.7

where $\sum A_c$ is the sum of the areas of all HA crystalline peaks and $\sum A_i$ is the sum of the area under the non-HA peaks. These area values can be obtained using the EVA software.

The Fourier transform infrared (FTIR) spectroscopy technique was used to further study the composition of the powders. This technique enables the identification of the molecular groups present in the powders.

Infrared spectroscopy is based on the property of molecules to vibrate/rotate under specific frequencies at discrete energy levels (vibration modes). The FTIR is a fast way of measuring the Infrared (IR) spectrum of a sample, as the information at all frequencies is collected simultaneously. A beam of IR light is guided through an interferometer and then through the sample to obtain an interferogram. The IR spectrum is then obtained by doing a Fourier transform on this signal.

The FTIR equipment used in this research was a *FTIR Spectrum GX* from Perkin-Elmer. A mixture of the powder to be tested (2 mg) and potassium bromide salt (200 mg) was ground in a marble mortar for 10 minutes, to avoid scattering from large crystals [209]. The ground powder was then added into a die and pressed at 12 kPa for 15 minutes to form a translucent pellet, which allows the IR beam to pass through it.

4.5.7. Powder thermal behaviour

It is important to determine the thermal characteristics of the feedstock powders, specially the polymeric ones, in order to predict how they will perform in the plasma spraying plume. The thermal techniques used are reviewed in this section. Differential scanning calorimetry, differential thermal analysis and thermogravimetric analysis were used to thermally characterise the polymers used in this research.

- Differential Scanning Calorimetry (DSC)

DSC is a destructive technique that measures the difference in heat input required to follow a temperature programme ($T_p(t)$) for a sample (S) and a reference sample (R), each one contained in a pan. The holders, where both pans are placed, have independent heaters and temperature sensors. The $T_p(t)$ is set by the user and controlled by the instrument. The control system takes instantaneous temperatures of both pans (T_S, T_R) and compares them with the programmed value, $T_p(t)$. Subsequently, the system assumes that the energy instantaneous supplied to each sample is proportional to these increments of temperature, following these equations [210]:

$$E_S = W_S(T_S - T_p) \quad \& \quad E_R = W_R(T_R - T_p)$$ <div style="float:right">Eq. 4.8</div>

where E_S and E_R are the heating energy supplied to each pan; W_S and W_R are the material constants.

The DSC result graph shows the energy difference $\Delta E = E_S - E_R$ required to keep both pans at the programmed instantaneous temperature versus temperature or time. This curve can be used to study phase transitions and its enthalpies: melting, glass transition, crystallisation, exothermic decompositions, chemical reactions, etc. The enthalpies are calculated by integrating the peak corresponding to a particular transition.

The DSC tests were performed at the University of Seville. The DSC used was a *DSC Q100* from TA Instrument. The pans used were made of Aluminium. The temperature program used for the DSC analysis of the polymers is described in Table 4.5. A double cycle heating-cooling was carried out to eliminate the thermal history of the polymers. Therefore the second heat step is the one shown in the results chapter.

Table 4.5. DSC procedure used

❖ Hold 1 min at 0°C
❖ Heat at 5°C/min from 0°C to 130°C
❖ Hold 5 min at 130°C
❖ Cool down at 5°C/min from 130°C to 0°C
❖ Hold 1 min at 0°C
❖ Heat at 5°C/min from 0°C to 130°C
❖ Free cool down

- Differential Thermal Analysis (DTA)

DTA is a similar technique to DSC. The main difference is that this time the measurement made is the difference between sample and reference temperatures. Nowadays, DTA technology is incorporated into the TGA equipment, which provides both mass loss and thermal information.

- Thermo Gravimetric Analysis (TGA)

The TGA used was a *STA 781 thermal analyser* from Stanton Redcroft. This test is based on the weight change of materials with temperature. Ten milligrams of a sample are placed inside a ceramic pan in a high-precision balance. The whole is placed in an electrically heated oven. Three measurements are conducted during the test: weight, temperature (using a built-in thermocouple) and temperature variation. The analysis was carried out by linearly increasing the temperature by 5°C/min from 30°C to 530°C, resulting in a weight loss curve that gives information about degradation temperature, absorbed moisture content of samples, solvent residues, etc.

4.6. Thick coatings characterisation

The coated samples were characterised along the surface and in cross sectional areas. In order to analyse the cross-sections the samples were prepared using metallographic techniques.

4.6.1. Cross-section metallographic preparation

The samples were sectioned in order to prepare the cross-section for examination. The samples were mounted using Struers Epofix Resin (15 parts by volume) and Epofix Hardener (2 parts by volume). The Epofix mixture was dye in phosphorescent yellow (Epodye, Struers) to distinguish the polymers used from the epoxy resin. The samples were placed in moulds which were then filled with the resin. They were then placed in a vacuum chamber for 5 minutes to ensure the epoxy penetrated into the open porosity of the cross section and, therefore, avoid modifications during the metallographic preparation. The next step consisted of curing the samples for 24 hours prior to removal from the moulds.

Grinding and polishing was carried out on the Buehler *Motopol 2000* semi-automatic specimen preparation unit. Three samples were prepared at a time following a procedure adapted from previous work in the department [103], which is shown in Table 4.6. The sample holder was set at 60 rpm counter clockwise for all the steps followed except for the final polishing step which was set at 30 rpm counter clockwise. After every step in the procedure the samples were rinsed in water, cleaned with

acetone, dried and observed in the optical microscope to ensure the previous grinding/polishing marks disappeared.

Table 4.6. Metallographic procedure for cross-sectional areas

Process	Surface	Abrasive	Lubricant	Time	Plate speed (rpm)	Force (N)
Grinding	SiC-paper	P60	water	until planar	300	100
		P200	water	6 min	300	100
		P600	water	4 min	300	100
		P1200	water	4 min	300	100
Polishing	TEXMET Perfoiert cloth	6μm DS	-	4 min	150	100
		3μm DS	-	4 min	150	80
		1μm DS	-	4 min	150	80
Final Polishing	Chemomet cloth	0.05μm MPS	-	45 s	100	100
			-	45 s	100	80
Note: DS - Diamond suspension (Buehler); MPS – Masterprep Polishing suspension (Buehler)						

As a first step, grinding on a coarser SiC paper was conducted until the sample was planar. Polishing cloths and MetaDi monocrystalline diamond suspensions (1, 3 and 6μm) from Buehler were used to polish the samples. A 0.05μm Masterprep Polishing Suspension from Buehler was used for the final polishing stage.

4.6.2. Thickness and Layer thickness

The number of layers and consequently the thickness of the final component are important parameters to take into account when producing free-standing samples. The number of layers should be enough to allow component removal from the die (lower limit). A higher number of layers provoke a decrease in cohesion between layers due to the residual stresses build-up, making it difficult to handle the components.

The thickness of the samples was measured with a *Deltascope mp0r-fp* portable device from Fischer instruments. It was determined as the average of ten measurements. The layer thickness, which is equivalent to the deposition rate, was calculated as the overall thickness divided by the number of sprayed layers.

4.6.3. Surface morphology

The surface of the specimens was characterised using a scanning electron microscope *SEM EVO LS15* from Zeiss. A *Surftest-402* profiler from Mitutoyo was used to determine the average surface roughness (R_a). The average Ra value for each deposit was calculated as the average of 10 measurements, each one over a line of 5 mm.

4.6.4. Crystallinity

The HA crystallinity content was evaluated using XRD (Bruker AXS D8) as was explained in Section 4.5.5. This method to measure crystallinity was preferred to the one which compares peaks heights with those from the feedstock HA powder, since it has been reported that features such as crystal size may affect the height of a crystalline peak [45].

4.6.5. Composition

The phase content of the HA coatings was also studied by XRD means, as was explained in Section 4.5.6. Detailed scans were performed to check the presence of other calcium phosphates. The scanning parameters used are detailed in Table 4.7.

Table 4.7. Detailed XRD scan parameters around β-TCP and OA peaks

Phase	2θ	Velocity	Step size
β-TCP	30.9^{o}-32.5^{o}	7 sec/step	0.005
OA	52°-53.5^{o}	7 sec/step	0.005

The FTIR technique was used to further study the HA coatings. The powders spectra were used to check by comparison possible phase transformation or new compound formation within the formed coatings using Plasma Spraying.

4.6.6. Porosity

There are numerous methods to measure porosity of plasma sprayed coatings, such as digital image analysis, Archimedean displacement, mercury intrusion porosimetry (MIP), Brunauer-Emmet-Teller (BET) gas absorption, and small-angle neutron scattering (SANS). Among these methods, digital image analysis is widely used to evaluate porosity of thermally sprayed coatings.   Du et al [211] described this method as the most adequate due to its reproducibility, economy, simplicity, and versatility for

analysis and characterisation of porosity. The digital image analysis method quantifies porosity and, therefore average volume fraction of porosity, by image analysis of the cross-sections views of pore average surface fraction. However, the accuracy of this method depends significantly in the metallographic preparation of the samples.

The porosity of the components was measured by means of digital image analysis as an average of ten SEM micrographs on the cross-sections of the samples. The images were taken at a magnification of 1000x using the backscattered electron imaging mode [211]. The porosity within each micrography was calculated using a MATLAB routine implemented for this purpose (Appendix E).

4.6.7. Mechanical Properties by indentation technique

The characterisation of microhardness, elastic modulus and fracture toughness was carried out on a microhardness tester *Miniload 2* from Leitz. The micro-hardness was measured at various positions using a Vickers indenter. The indentations were made at 50 grams load [212] with a loading time of 15 seconds in the middle part of the coatings' cross sectional area. The resultant micro-hardness ($\overline{H_v}$), shown in Eq. 4.9, was given as an average of 10 indentations to obtain a statistically reliable value.

$$\overline{H_v} = \frac{\sum_{i=1}^{10} 1854.4 \frac{F}{d^2}}{10}$$

Eq. 4.9

where *F* is the indentation load in grams and *d* the imprint half-diagonal in mm.

The Vickers imprints were also used to measure the indentation fracture toughness. This method, based on Eq. 4.10, produces large standard deviations but is an effective method to estimate toughness [213]:

$$K_{IC}(MPa/m^2) = 0.079 \frac{P}{a^{3/2}} \log\left(\frac{4.5a}{c}\right)$$

Eq. 4.10

where: K_{IC} is the indentation fracture toughness, *P* is the indentation load (mN), *a* average Vickers indentation half-diagonal length (µm) and *c* average crack length (measured from indentation centre) (µm). The formula is valid in the range

0.6 < c/a < 4.5. The crack and half-diagonal lengths were measured by means of a Reichert *Me F2 Universal Camera* optical microscope at a magnification of 500x for at least 10 Vickers indentation per sample.

Knoop indentation tests can be used to measure the elastic modulus of the deposits with an error lower than 10% [214, 215]. The method is based on the measurement of elastic recovery of the surface imprint made by the Knoop indenter once the load is released. The elastic recovery is independent of the indentation load and is proportional to the hardness (H_v)/elastic modulus (E) ratio [214]:

$$\frac{b'}{a'} = \frac{b}{a} - \alpha \frac{H_v}{E}$$

Eq. 4.11

where: *b* and *a* are the short and large diagonals of the Knoop imprint before and b_i' and a_i' after the elastic recovery; α is a constant equal to 0.45 for a wide range of materials. The value of *b/a* depends on the geometry of the Knoop indenter and it is equal to 0.14.

The coating elastic modulus ($\bar{E}$) was calculated, using Eq. 4.12, as an average of ten singular values (E_i), measured using ten Knoop indenter imprints and the averaged Vickers hardness value ($\overline{H_v}$) obtained using Eq. 4.9. The Knoop indentations were made between the Vickers indentations and the substrate, leaving a space of at least 3 diagonals. The indentations were performed using a 50 grams load with a loading time of 15 s. Values a' and b' for each imprint were measured by means of a Reichert *Me F2 Universal Camera* optical microscope at a magnification of 400x.

$$\bar{E} = \sum_{i=1}^{10} E_i = \sum_{i=1}^{10} \frac{0.45 \overline{H_v}}{\left(0.14 - \frac{b'_i}{a'_i}\right)}$$

Eq. 4.12

5. RESULTS AND DISCUSSION

The results of the experimental work carried out as part of this research are presented and discussed in this chapter. Firstly, the results from characterisation of the feedstock materials used are presented. Following this, the results from the selection and feasibility tests are described. The results from HA reference series, which are the basis for comparison with the subsequent composites series, are then presented. The two last sections present the results obtained for composites series, HA/PCL and HA/TiO$_2$. The addition of PCL is performed with a view to improving the porosity of the coatings where the addition of TiO$_2$ aims to improve the mechanical properties.

5.1. Powder Characterisation

In this section, the characterisation of raw and attrition milled powders is presented. Flowability tests were conducted and densities of the different powders were obtained following the procedures described in Section 4.5.1. The average size, size distribution and morphology of the particles were studied by means of particle size analysis and SEM. The powders were also studied by X-Ray diffraction. The polymeric powders were further characterised by means of thermal analysis (TGA, DSC) due to their thermal sensitivity. No thermal characterisation was conducted in the remainder of the powders (HA60, HA90, YSZ, Ti and TiO$_2$) because they have been widely processed by plasma spraying and have been proven to perform adequately at the plasma plume temperatures. Hydroxyapatite FTIR spectra was also studied for comparison with the coatings, as it can identify HA dehydroxylation during the process. Polymeric powders were also characterised by means of FTIR to identify any degradation during the deposition process.

5.1.1. Hydroxyapatite (HA)

Two different available Hydroxyapatite powders were used and characterised: HA Captal 60 (namely HA60) and HA Captal 90 (namely HA90). The particle size distribution of the Hydroxyapatite powders is shown in Figure 5.1. The average particle size of HA60 and HA90 powders were found to be 52.1 μm and 89.7 μm, respectively. These values were slightly bigger than those reported by the supplier. The size range of the HA60 powder seems to be ideal in order to obtain an appropriate degree of

melting of the particles within the LEPS system and the wider particle size distribution may help to produce greater porosity within the coatings.

The different morphology of the two different powders can be seen in Figure 5.2. This is due the different methods by which the powders were fabricated. The spherical HA60 powder was produced by spray drying whereas the polyhedral HA90 powder was produced by tray drying.
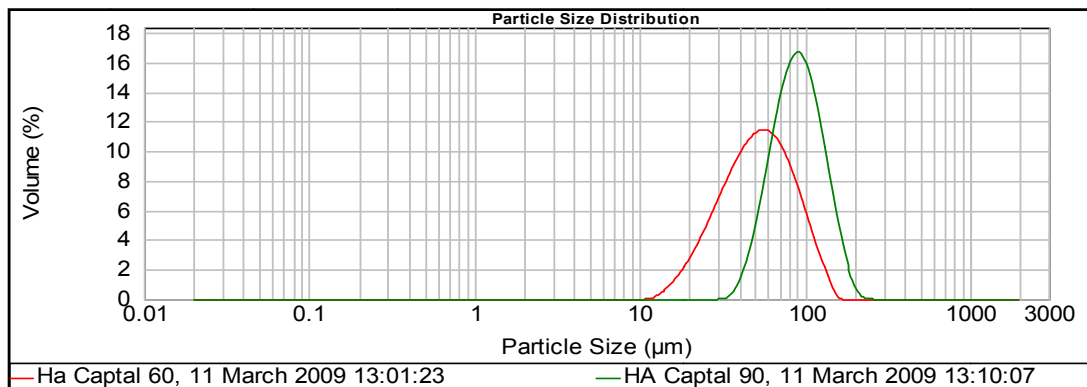
Figure 5.1. HA60 and HA90 particle size distributions
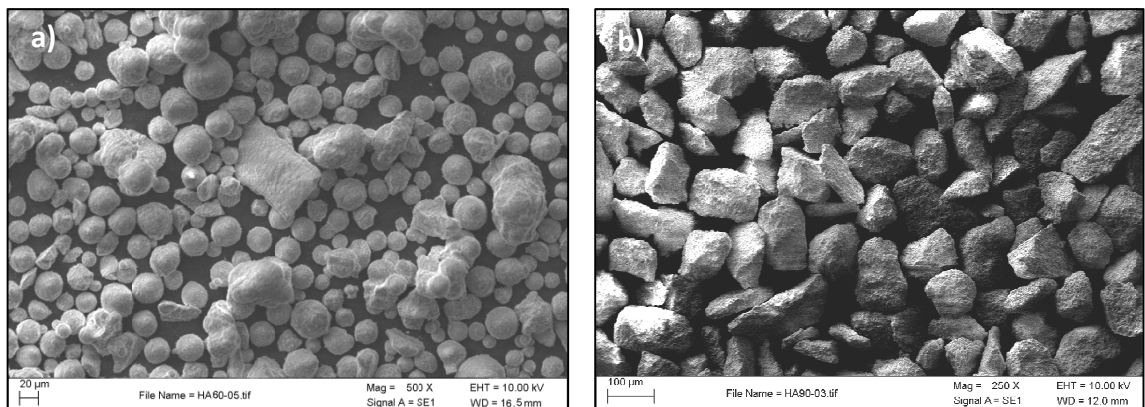
Figure 5.2. Morphology of: a) HA60 and b) HA90 particles

The flowability and density values for both powders are shown in Table 5.1. The HA60 was helped to flow as the standard indicates, whereas the HA90 flowed naturally. This difference in behaviour seems to be caused more by the particle size and size distribution than by the morphology of the powder. Smaller particle size implies

greater specific surface area of the powder and consequently a decrease in flowability [201].

Table 5.1. Flowability, apparent and tap density of HA60 and HA90 powders

Powder	Flowability (g/s)	Apparent Density (g/cm^3)	Tap Density (g/cm^3)
HA60	0.10	0.934	1.136
HA90	0.56	1.013	1.250

The tap density of HA90 was greater than that of HA60. Greater specific surface area powders show smaller tap density values due to the greater surface-to-volume ratio [216]. Apparent density measures the level of inter-particle friction in the powder. A greater friction, which also means reduced flowability, leads to smaller values on apparent densities [217]. The flowability and densities found for both powders were not vastly different to choose one of the powders as more suitable than the other for this research and, therefore, a selection test was performed in order to choose the better performing one. The results from this test are presented in Section 5.2.2.

The XRD patterns of both powders are shown in Figure 5.3. The HA60 powder was 100% pure Hydroxyapatite whereas the HA90 had a minor amount (2.8%) of Tetra calcium phosphate (TTCP), calculated following Equation 4.7. Both powders were found to have crystallinity of over 99%. The initial composition of the powders is important as it would influence the final coating composition. Therefore, the presence of traces of TTCP in the HA90 powder means that the final coating would also have traces of TTCP, as its melting temperature is higher than that of HA (Table 2.6).

The HA60 powder FTIR spectrum is shown in Figure 5.4. The stretching mode band (3571 cm^{-1}) and flexural mode band (635 cm^{-1}) of the OH$^-$ groups can be seen on the spectra. The characteristic bands due to PO$_4^{3-}$ ions (v_1 band at 963 cm^{-1}, v_3 bands at 1090 and 1052 cm^{-1}; and v_4 bands at 573 and 602 cm^{-1}) are also present [218]. The band of carbonate ion might indicate some carbonate substitution in the HA structure. In addition there is a band, which corresponds to the aliphatic C-H bond indicating the

presence of an organic compound [45]. The comparison of this spectrum with the one of the coatings would indicate the degree of dehydroxylation of HA during the process.
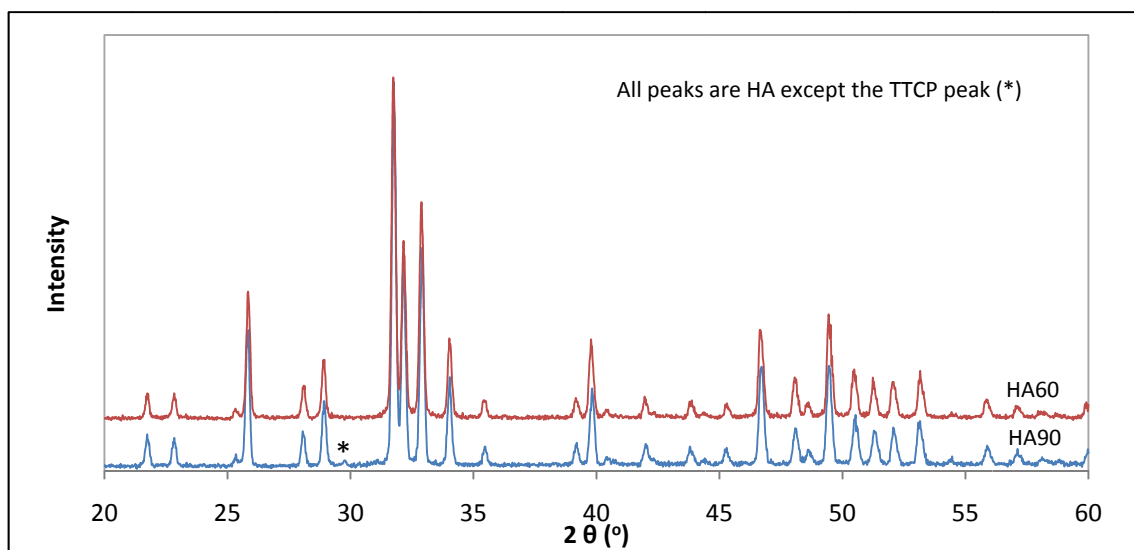
Figure 5.3. XRD patterns of HA60 and HA90 powders
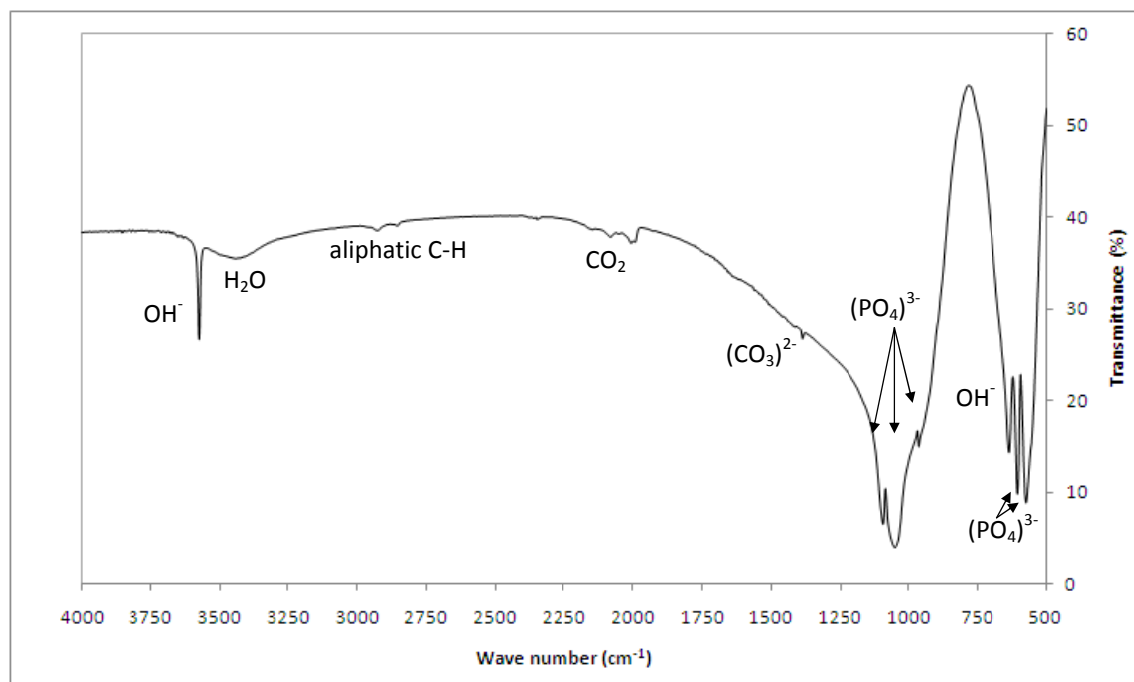
Figure 5.4. FTIR spectra of HA60 powder

5.1.2. Polyetheretherketone (PEEK)

A small quantity of PEEK was donated by INASMET. The powder particle size distribution followed a Gaussian distribution (Figure 5.5). It showed a small bump on the left-hand side, which may be provoked by the agglomeration of finer particles during testing. However, this cluster could have also been caused as a result of the PEEK processing and size reduction methods employed by the supplier. The PEEK average particle size was 75.4 μm and the morphology of the particles was irregular (Figure 5.6). The feasibility of this powder in the LEPS system is studied and discussed in Section 5.2.3.
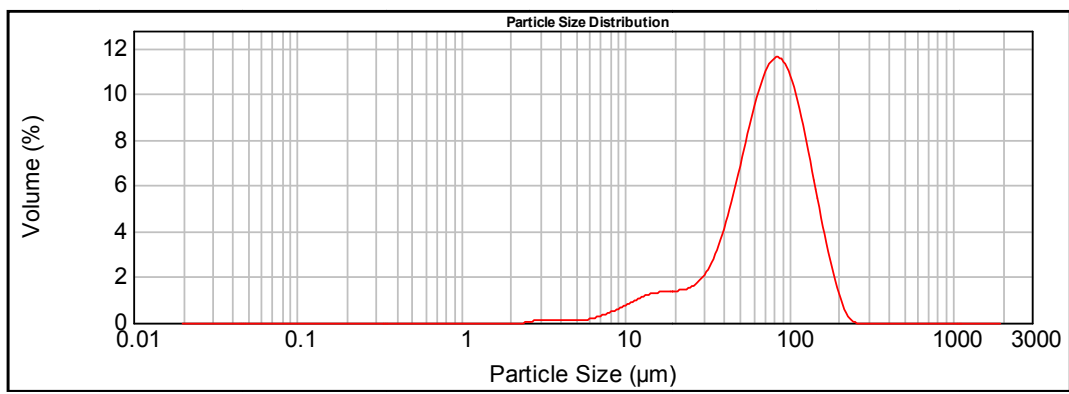
Figure 5.5. PEEK particle size distribution
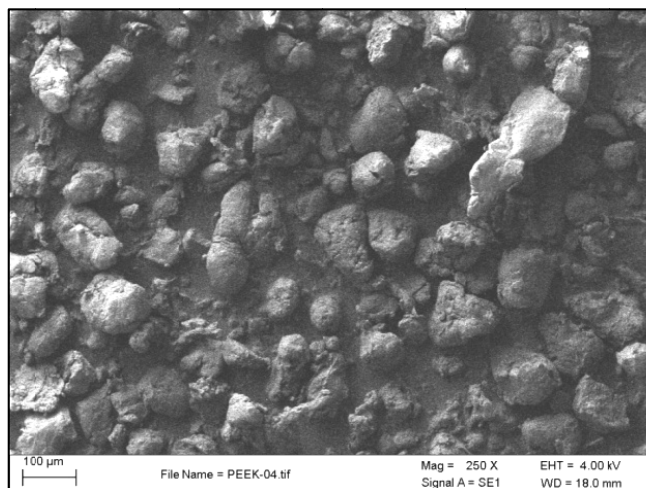
Figure 5.6. Morphology of PEEK particles

PEEK powder was also studied by means of thermal analysis (DSC) (Figure 5.7). The polymer partially crystallises at 170°C (exotherm peak) and melts at 350°C (endotherm peak) [219]. The degradation of the polymer started at 525°C, when the DSC signal started to increase.
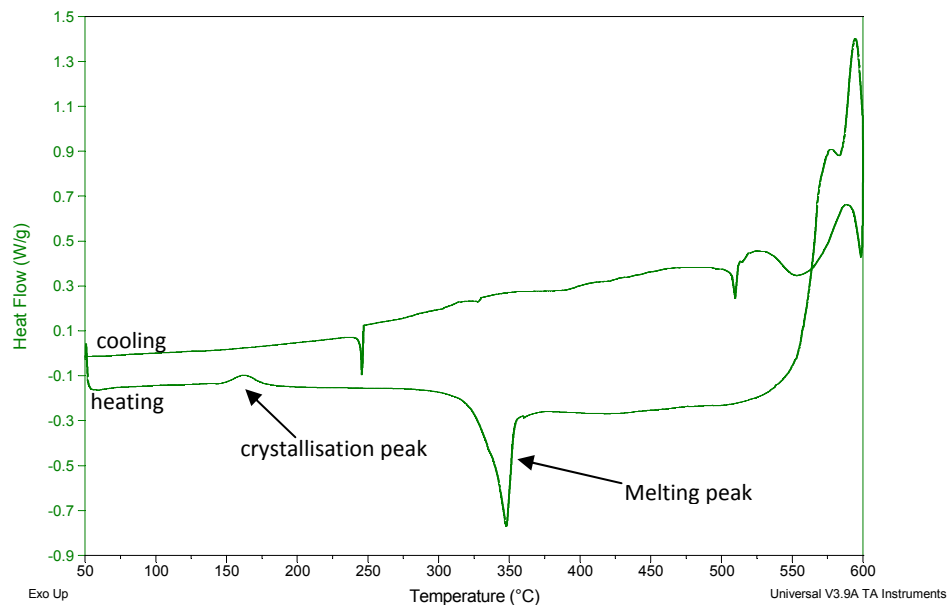
Figure 5.7. DSC of PEEK powder

5.1.3. Polycaprolactone (PCL)

The flowability and densities were determined. PCL did not flow and the values of apparent and tap densities were: 0.39 g/cm^3 and 0.435 g/cm^3, respectively. The PCL particle size distribution almost followed a Gaussian distribution (Figure 5.8) with an average particle size of 85.3 μm. The small bump on the left-hand-side is likely to have resulted from the agglomeration of finer particles during testing. However, as stated before for PEEK powder, it could also have been caused as a result of the PCL processing and size reduction methods employed. The feasibility of PCL in the LEPS system is tested later on this chapter. The morphology of PCL powder (Figure 5.9) was irregular and angular due to the method used to reduce its size (cryogenic milling process).
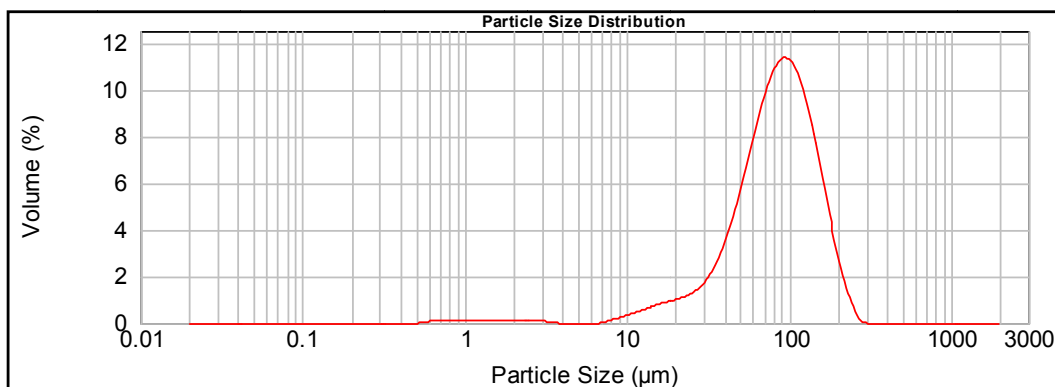
Figure 5.8. PCL particle size distribution
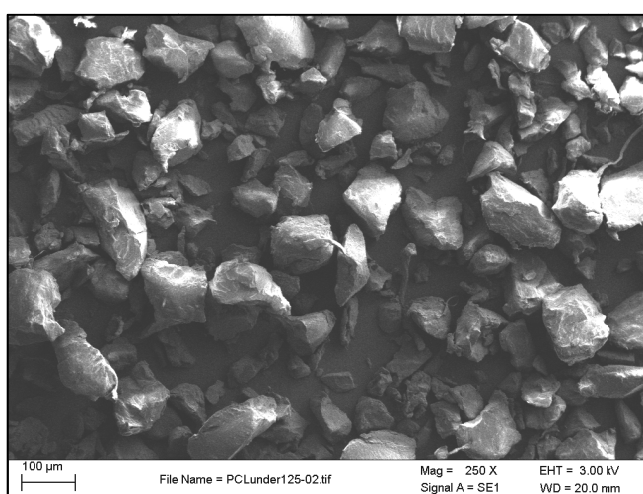
Figure 5.9. Morphology of PCL particles

PCL was studied using thermal analysis (TGA, DTA and DSC). The DSC plot is shown in Figure 5.10 and the TGA and DTA results in Figure 5.11. The melting temperature of PCL, shown as a peak in DTA curve and DSC curve, was 60°C. The degradation of the polymer begins at 260°C, when the TGA signal starts to drop away from 50 μV.
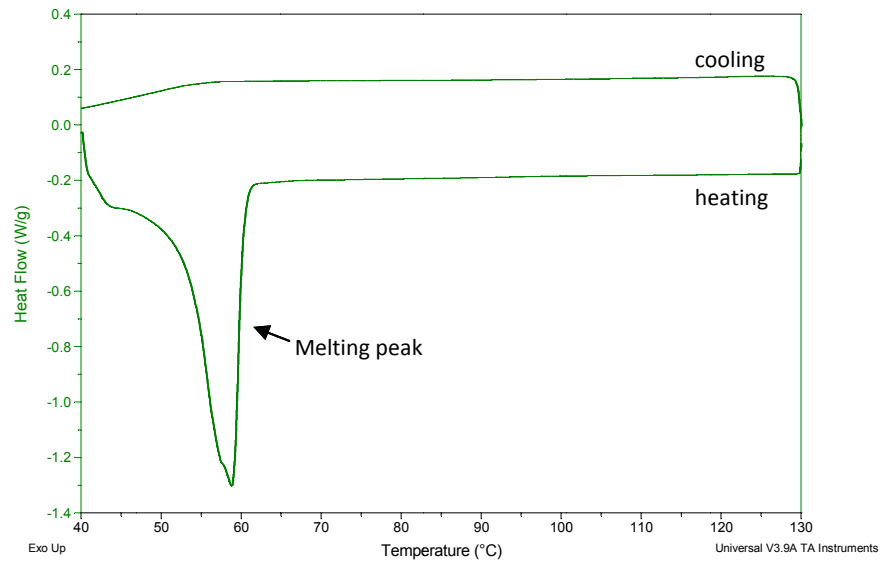
Figure 5.10. DSC of PCL powder
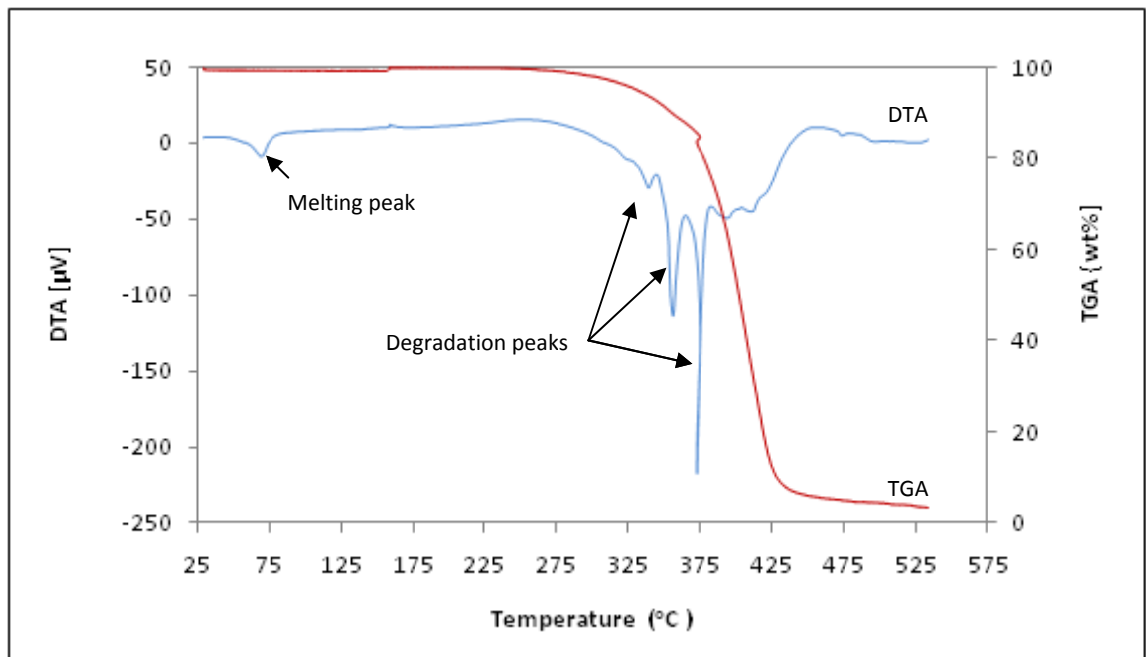
Figure 5.11. TGA and DTA of PCL powder

5.1.4. Yttria-stabilised Zirconia (YSZ)

The particle size analysis results (Figure 5.12) indicate that particles fall within three separate size clusters, one in the range 0.1-1 µm (approximate Gaussian distribution) and the others in the ranges 1-10 µm and 10-100 µm. The particles sizes towards the right hand-side of the Gaussian distribution are most likely present as a result of

agglomeration of the finer YSZ particles during the characterisation. The average powder particle size, 0.6 µm, was found to be slightly smaller than that reported by the supplier. The average size and size distribution would make YSZ difficult to feed into the plasma spraying system on its own, hence an agglomeration stage should be considered before plasma spraying. The powder morphology can be seen in Figure 5.13. YSZ did not flow during the flowability test due to its small particle size. The values of apparent and tap densities were 1.068 g/cm^3 and 1.351 g/cm^3 respectively. The XRD pattern of YSZ powders is shown in Figure 5.14. The powder composition was found to be 62.4% of tetragonal phase and 37.6% of monoclinic phase (Baddeleyite).
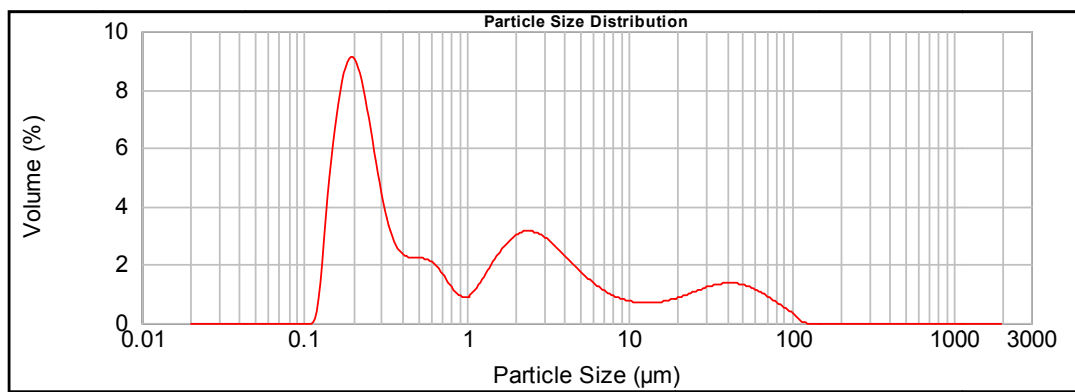
Figure 5.12. YSZ particle size distribution
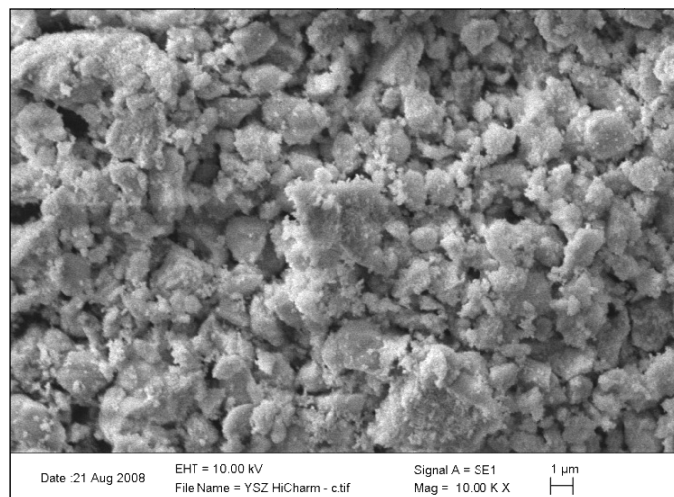
Figure 5.13. Morphology of YSZ particles
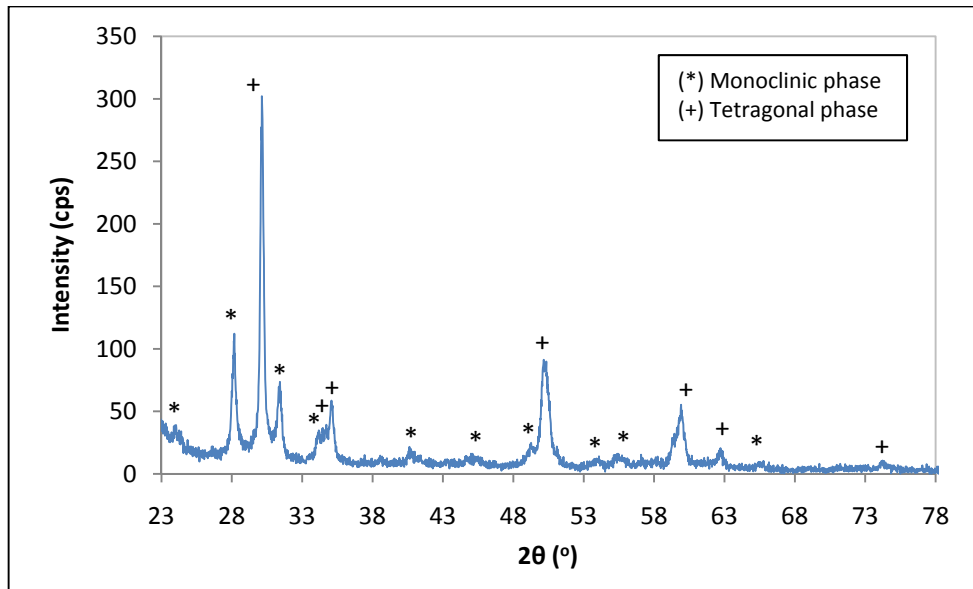
Figure 5.14. XRD pattern of YSZ powder

5.1.5. Titanium (Ti)

A small quantity of pure titanium powder was donated by INASMET to tests the feasibility of a metallic powder in the system. The particle size followed a Gaussian distribution (Figure 5.15), which has an average size of 137.4 µm. This average size seems too large to achieve an optimum melting degree of all particles however its feasibility in the system was tested and the results are reported in Section 5.2.3.
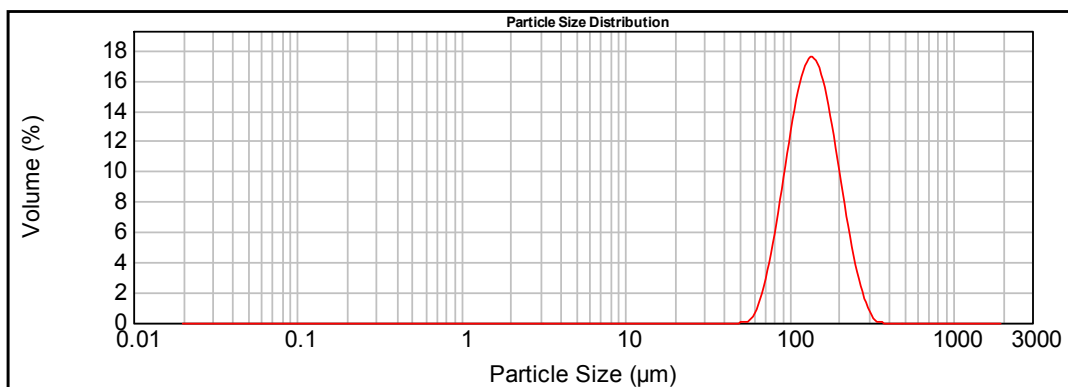
Figure 5.15. Titanium particle size distribution

The morphology of the particles was irregular as can be seen in Figure 5.16. The titanium XRD pattern (Figure 5.17) shows that the powder was form by 100% pure hexagonal Titanium (space group P6₃/mmc).
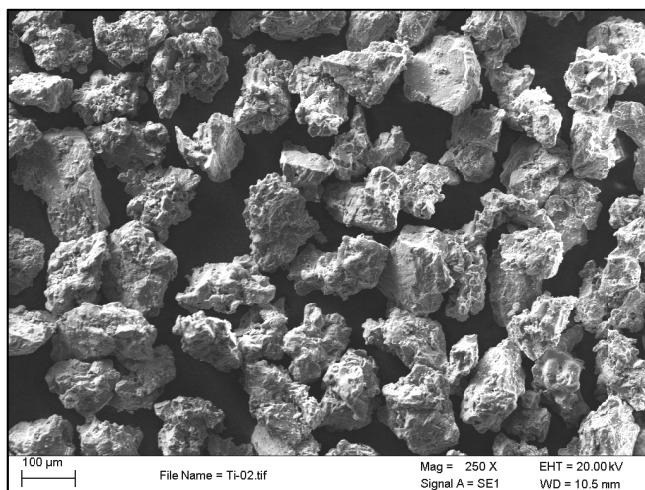
Figure 5.16. Morphology of Titanium particles
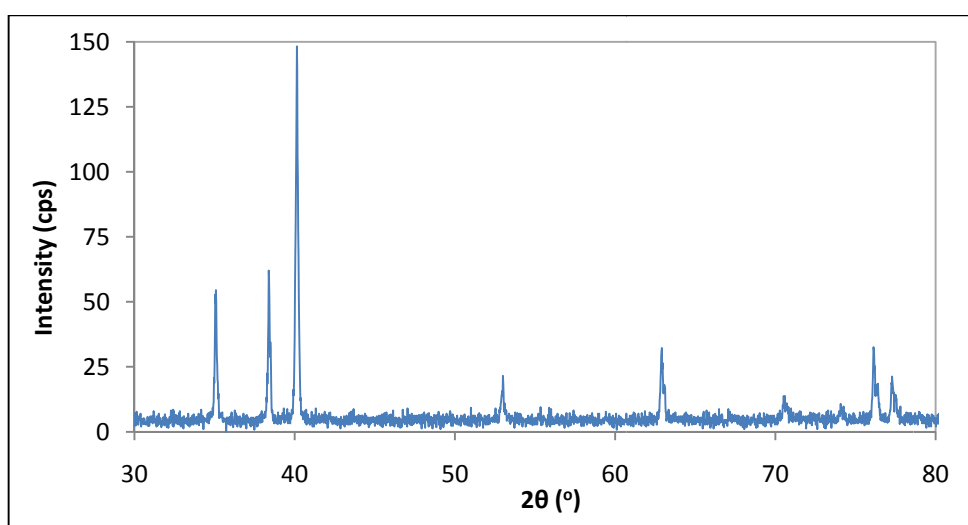
Figure 5.17. XRD pattern of Titanium powder

5.1.6. Titanium oxide (TiO₂)

The TiO_2 flowability was 0.49 g/min and the values of apparent and tap densities were 1.956 g/cm^3 and 2.381 g/cm^3 respectively. The particle size distribution is a Gaussian distribution (Figure 5.18) with average particle size of 31.3 µm. These average particle size and size distribution make TiO_2 an optimal feedstock for the system. The angular

powder morphology can be seen in Figure 5.19. The XRD pattern (Figure 5.20) shows that the titanium oxide powder is formed by rutile phase and a mixture of body-centred triclinic titanium oxides which belongs to the family of Ti_nO_{2n-1} ($4 \leq n \leq 9$), also known as Magnéli phases [220]. This family have phase structures derived from rutile by regular crystallographic shear on the (1 2 1) planes. A comprehensive review of the crystallography of this series was conducted by Le Page et al [221].
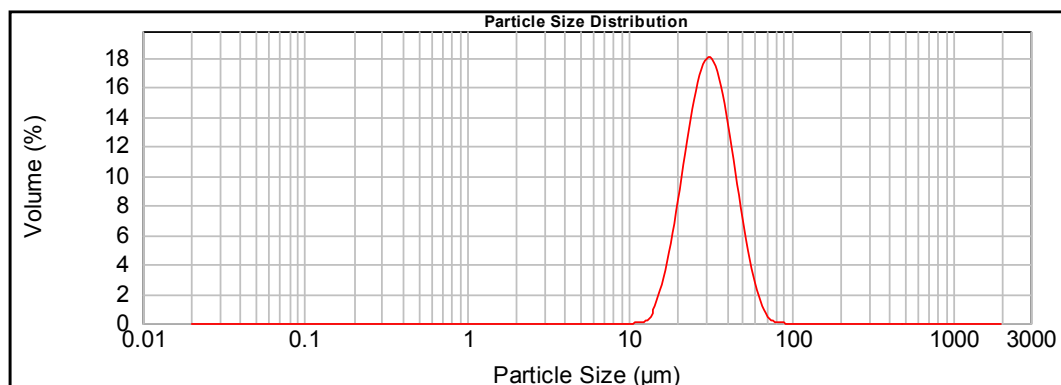
Figure 5.18. TiO$_2$ particle size distribution
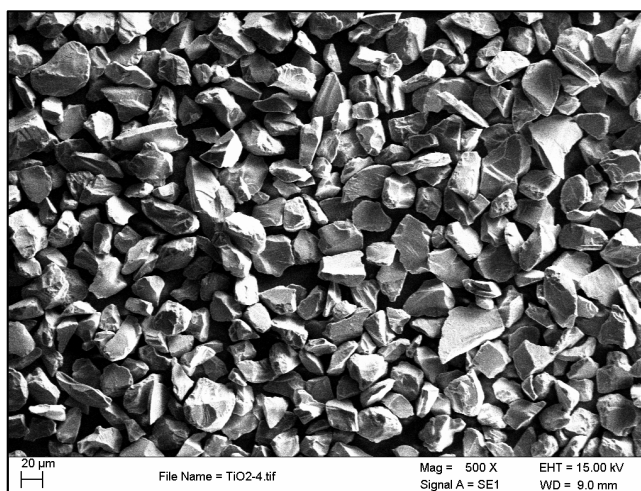
Figure 5.19. Morphology of TiO$_2$ particles
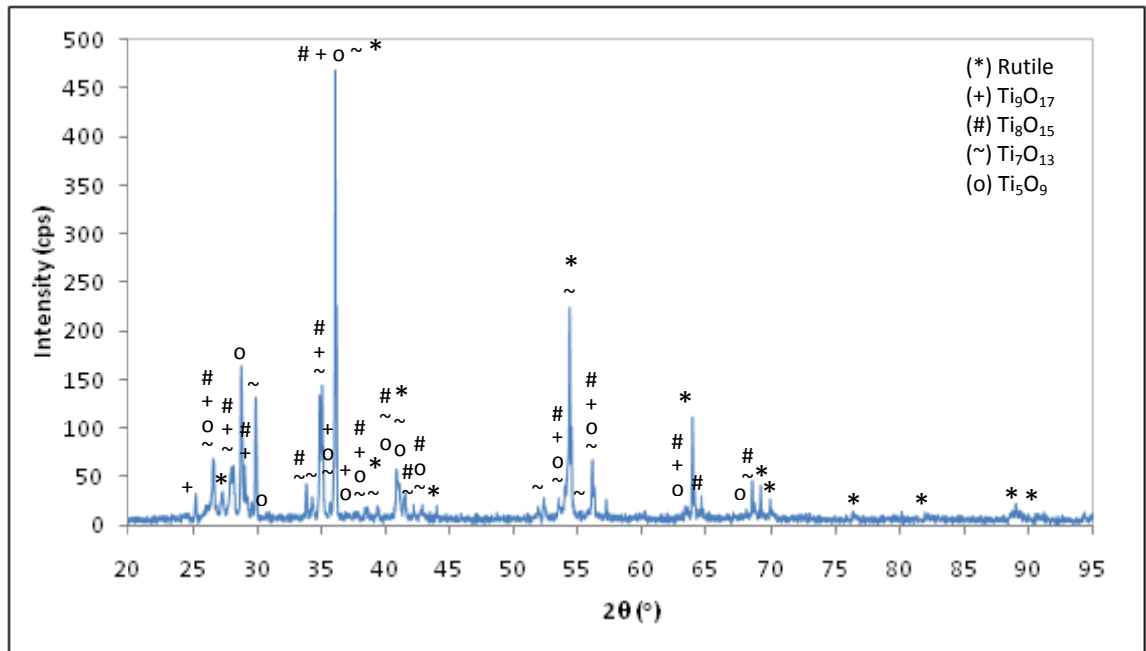
Figure 5.20. XRD pattern of TiO$_2$ powder

5.1.7. Agglomerated powders

Polyvynil alcohol (PVA) was used as a binder during the attrition milling process to obtain different agglomerated powders. The average powder particle size was 225.6 μm. The morphology of the powder can be seen in Figure 5.21a. The DSC scan for this polymer shows that its melting temperature occurs at 220°C.
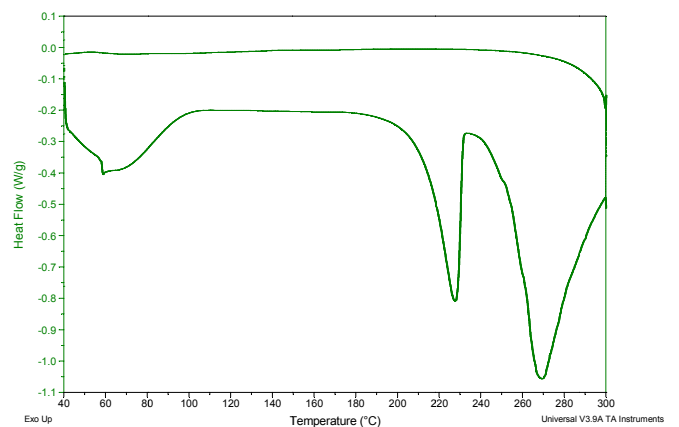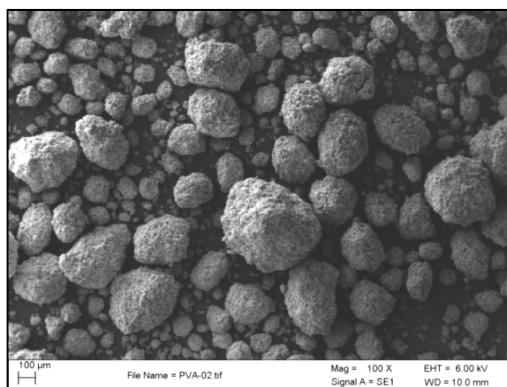
Figure 5.21. PVA powder: a) Morphology and b) DSC plot

The flowability and densities of the produced powders were determined following the procedure described in Section 4.5.1. None of the powders flowed, even after sintering. This may be caused for the presence of the great amount of small particles within the particle size distribution clusters 0.3-1 µm and 1-10 µm (Figure 5.22), which did not significantly changed after sintering. The densities are shown in Table 5.2.

Table 5.2. Absolute, apparent and tap densities of agglomerated powders

Powder	Absolute density (g/cm^3)	Apparent Density (g/cm^3)	Tap Density (g/cm^3)
HA(60)5YSZ	3.189	0.789	1.282
HA(60)15YSZ	3.347	0.846	1.250

The particle size distributions were trimodal in all cases (Figure 5.22). The average particle sizes after milling were 21.1 µm (HA5YSZ) and 27.8 µm (HA15YSZ). The average particle sizes increased after sintering to 43.8 µm (HA5YSZ) and 48.2 µm (HA15YSZ). The morphology of the powders after milling (Figure 5.23) shows a certain amount of particles smaller than 3 microns, validating the data obtained using the particle size analyser. The morphology, particle size and size distributions of the agglomerated powders before and after sintering are consistent with the lack of flowability observed during the flowability test and might make this powders unsuitable for plasma spraying using a standard feeding system. Nevertheless, feasibility tests were conducted for these powders and the results are shown in Section 5.2.3.
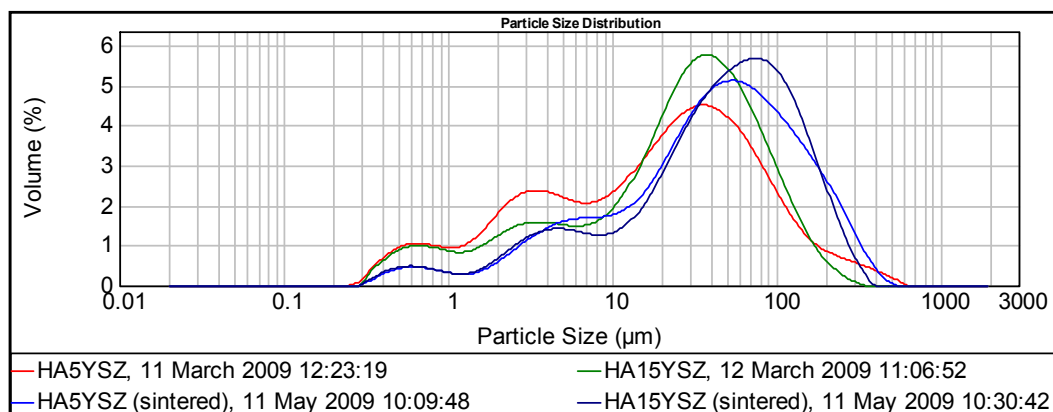
Figure 5.22. Agglomerated powder particle size distributions
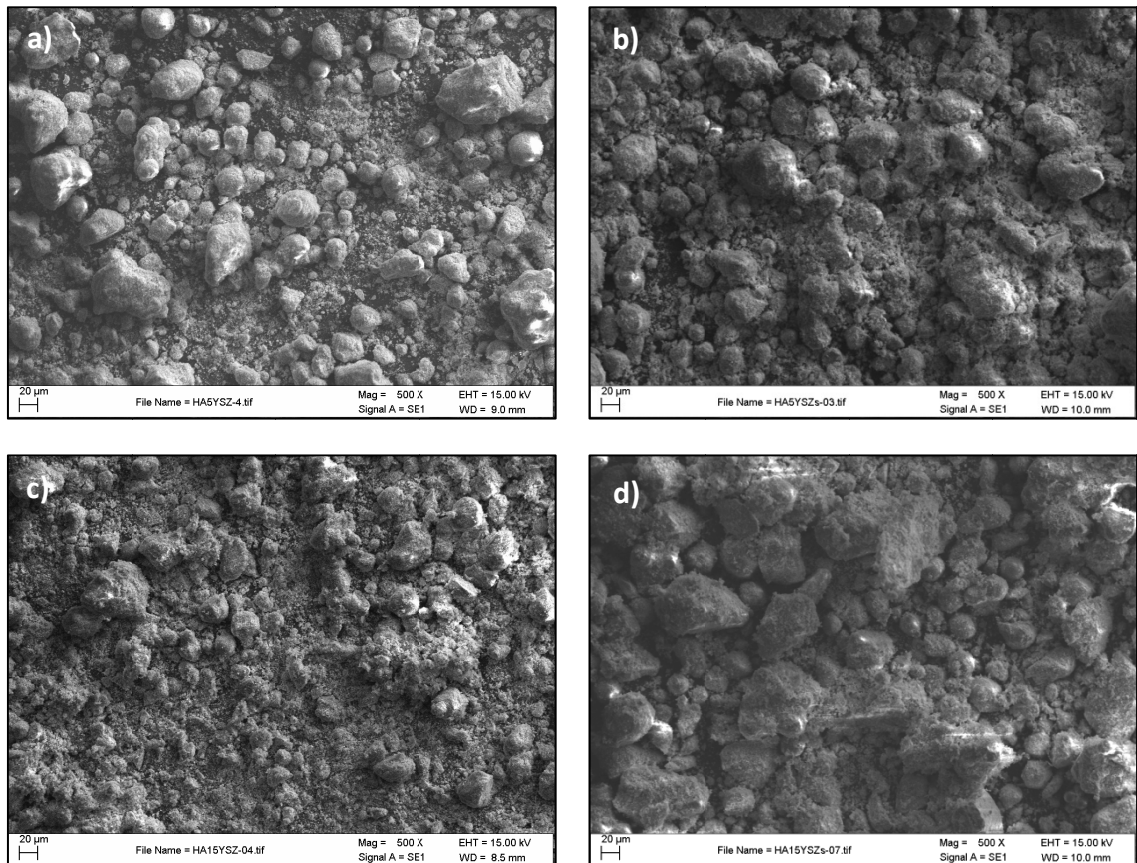
Figure 5.23. Morphology of HA5YSZ particles: a) before and b) after sintering; and HA15YSZ particles: c) before and d) after sintering

5.1.8. Summary

The size range of HA60 seems to be more adequate than that of HA90 for the purpose of this research. The lower average particle size would improve the particles melting degree and, thus, the powder deposition efficiency. The wider particle size distribution may also help to increase the porosity of the coatings. Finally, the purity of HA60 is seen as another advantage compared with the HA90 powder which contains TTCP.

The polymeric powders, PEEK and PCL, need to be tested in order to assess their feasibility in the system as their melting/degradation temperatures are lower than the temperatures involved in the process. Adjustable external injection and cooling systems are expected to be needed in order to avoid degradation of these powders.

The small particle size of Yttria-stabilised Zirconia powder makes it necessary to agglomerate the particles in order to feed them in the system. Attrition milling of YSZ and HA was attempted using PVA as a binder. Unfortunately, the morphology, particle size distribution and lack of flowability of these powders, seems to indicate that a good performance in the system is unlikely.

The Titanium large average particle size and irregular morphology are expected to cause poor particle deposition efficiency during the process. On the contrary, the TiO_2 powder presents suitable average particle size, size distribution and morphology for plasma spraying processing.

5.2. Selection tests

Screening tests were carried out at the beginning of this work to select the plasma spray system and the optimal particle size of the matrix material, hydroxyapatite. Feasibility tests were performed for different materials and their mixtures. A better understanding of the plasma spraying process and the influence of process parameters (PSPs) on the final characteristics of the coatings was gained while carrying out these tests. The outline of these tests is shown in Figure 5.24.
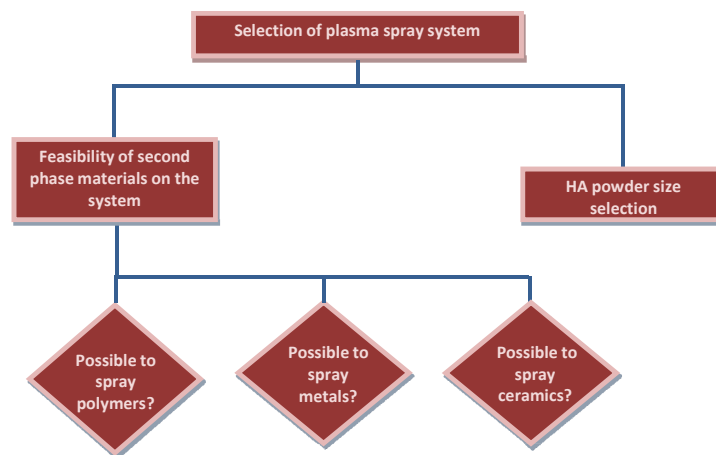
Figure 5.24. PERT diagram of the screening and feasibility tests undertaken

In short, the following was established:

- The ability of a conventional plasma spraying process to manufacture free-standing ceramic components was firstly examined and it was found that severe cracking occurred in the deposits. An experimental low energy plasma spray (LEPS) system was selected to proceed with the work as the lower energy input might reduce the residual stresses, which contribute to induce cracking and it seems more suitable to spray polymers without causing major degradation. This lower energy made it possible to study the LEPS process parameters by observing their effects on the plume shape and colour, how powder entered the plume, and so on while the system was running.

- The ability of the LEPS system to spray different powder sizes was tested with the two hydroxyapatite powders (HA60, HA90). Due to its limited power, the LEPS system was not able to sufficiently melt the larger particles of the HA90 powder, which resulted in a relatively low deposition efficiency and poor coating quality. The HA60 powder proved to have a particle size distribution more suitable for this process and was therefore used as the matrix material of reference in the following results.

- Composites were produced as thick coatings rather than free-standing components to minimise the amount of powder used and the processing time. The composites were produced by separately feeding the two feedstock materials (matrix and second phase). The feasibility of the second phase materials in the system was tested in first place to establish the most suitable parameters: stand-off distance, dimension and positioning of the injector, plasma gas and carrier gas flow rates and powder feeding rate.

By the end of this series of tests knowledge on the use of the process and a better understanding of the process parameters' effect on coatings was acquired. A reasonable indication of the range of parameters to use for optimisation purposes was also found. The ability of the system to spray different materials was also tested. The following sections discuss the findings.

5.2.1. Selection of plasma spray process

Process screening tests were performed paying special attention to the process parameters windows and studying the resulting samples. Three plasma spray systems - two conventional systems (9MB gun and F4 gun) and an experimental (LEPS) one - were studied using the powder HA60.

Process parameters windows

It is important to compare the different parameter windows of the processes in order to understand the actual limitations and advantages of each of them. The working ranges for five parameters (current, primary gas flow rate, carrier gas flow rate, powder feeding rate and stand-off distance) were studied. The process parameters windows were plotted using data collected by the author from experimental tests at INASMET (LEPS), from previous work at DCU (9MB gun) [103] and from literature (F4 gun) [45, 134, 222-224]. This data refers to plasma spraying of Hydroxyapatite. Information from technical data sheets was also used [187, 188].

The power limit of the guns, as defined in Sulzer Metco product catalogue [188], are 15 kW (LEPS), 55 kW (F4 gun) and 80 kW (9MB gun). Figure 5.25 shows the process windows for the applied current. For both conventional plasma spraying guns (9MB and F4) the lower limit is set by their incapacity to melt the HA powder at low energies, thus, producing weak coatings. The upper limit causes instability problems of the systems due to the high energy, causing a power supply fault. These high currents can cause damage to the electrode in the gun [103]. The LEPS system was designed to work as a portable device for small scale applications, and it is therefore limited to a relatively narrow power range. Within each of their working ranges an increase in current results in an increase in the energetic input. Therefore, the melting degree of the powder and heat content of the target increase, which can affect some coating characteristics such as porosity and surface roughness [225, 226].
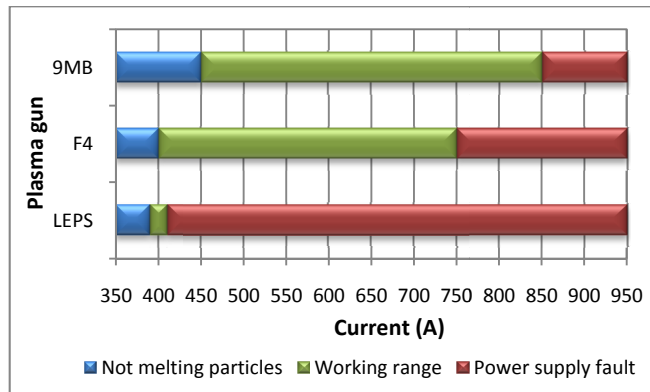
Figure 5.25. Ranges for current for the different plasma spray systems

Plasma gas flow rates outside the working range (Figure 5.26a) result in low quality thin coatings, but for different reasons. Below the working limit, the flow rate is not sufficient to accelerate the powder particles towards the substrate, thus decreasing the deposition efficiency. On the other hand, if the upper limit is exceeded the particles travel faster towards the substrate, decreasing their residence time in the plume and their degree of melting as a result. Therefore, particles bounce off the substrate instead of contributing to the coating build-up. Within the working range, an increase in the flow rate increases the kinetic energy of the particles and decreases their heat content. However for other materials than HA, these limits may vary.

It is pertinent to note, that the process conditions specified for 9MB and the LEPS systems are based on a sole plasma gas (Argon). The PG flow rate window for the conventional plasma guns is usually similar. However, the collected data for F4 gun showed a smaller working range compared to that of 9Mb gun. This is due to the fact that F4 gun operates with H_2 as a secondary plasma gas and, therefore, a smaller primary gas flow rate is required.
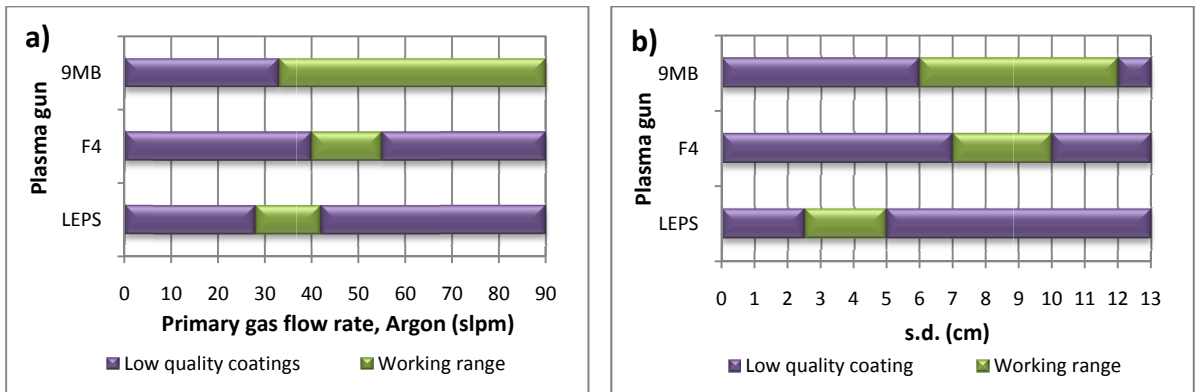
Figure 5.26. Ranges for the different plasma spray systems of: a) Plasma gas flow rate and b) stand-off distance (s.d.)

The working range for the stand-off distance (s.d.) is shown in Figure 5.26b. Values below the lower limit result in low quality coatings which peel off and crack due to the high heat input received from the proximity of the plasma plume. If the upper limit of the s.d. is exceeded, no coating builds up because the particles start to cool down before arriving to the substrate and bounce off, reducing the deposition efficiency. There is a suitable distance for optimum deposition efficiency within the working range, which depends on the material used and the rest of the selected process parameters.

The parameters related to the powder injection are compared in Figure 5.27. The powder feed rate can provoke flow stabilisation problems inside the powder feeder unit when it is set outside of its working range. The feeding rate can be expected to directly influence the deposition efficiency of the process, but it is not the only parameter affecting it. For instance, greater powder feed rates tend to cool down the plasma. As a result, the particle thermal input decreases and, therefore the deposition efficiency drops which lead to thinner coatings. This can be overcome by selecting the appropriate settings of the other PSPs.

The smaller upper limit observed for LEPS compared to conventional systems is attributed to its limited power and thus to its incapability to sufficiently melt a great quantity of powder. The greater upper limit shown for F4 gun compared to that of 9Mb gun is again caused by the presence of a secondary plasma gas (H_2), which

increases the enthalpy of the plasma and, therefore, enables the system to process a greater amount of powder.

The working range for the carrier gas flow rate was established to assure that powder particles enter the plasma plume and have a proper trajectory. An excessively low flow rate fails to drive the powder into the plasma plume due to the low carrier kinetic energy, whereas an excessively high flow rate makes the powder cross through the plasma plume and disturbs the plasma jet [133].
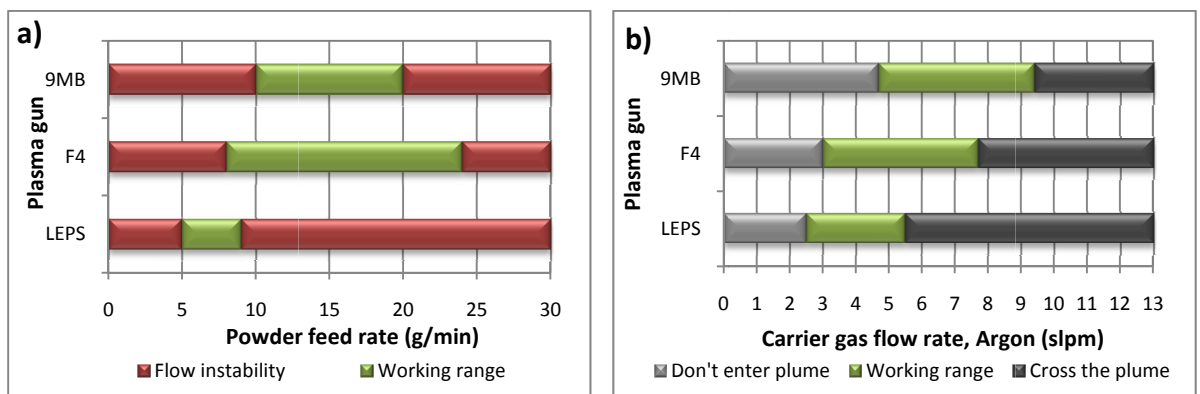
Figure 5.27. Powder feeding related parameters for the different plasma spray systems: a) powder feeding rate and b) carrier gas flow rate

Samples study

Each gun system was studied to ascertain its functionality for producing thick biodeposits. Different HA60 series of samples were produced using the 3 different systems in order to compare the grade of cracking and the properties of the coatings produced. The series produced using the 9MB gun also studied the thickness evolution by varying the spraying time parameter. The free-standing coupons for these series were produced using the in-house stainless steel cavity die which is described in Section 3.2.

- 9Mb

A series of samples (HA60-9MB) were produced at Dublin City University's facilities using a conventional plasma spray system (9MB gun). These tests also aimed to demonstrate the ability of plasma spraying to produce HA free standing components.

The process parameters used were optimised in a previous research work [103]. Therefore, the sole process parameter varied for this test was the spraying time (70, 90, 120, 150 and 240 s) whilst the remaining plasma spray parameters were set as shown in Table 5.3. The gun remained fixed and the substrate holder was moved at a constant horizontal velocity of 3.8 cm/s.

Table 5.3. Plasma spray parameters used for Series HA60-9MB

Parameter	Value
Current (Power)	750 A (30 kW)
Primary gas (PG), flow rate	Argon, 50 slpm
Secondary gas, flow rate	None
Carrier gas (CG), flow rate	Argon, 4.7 slpm
Powder feeding rate	20 g/min
Stand-off distance (s.d.)	7 cm
Relative gun velocity	3.8 cm/s
Increment y-direction (Δy)	None
Injector position	External
Injector size (diameter)	1.5 mm
Injector-centre of plasma distance	8.5 mm

The resulting sprayed components were easily removed from the die and formed a near-conical shape (Figure 5.28). This shape is attributed to the linear x-movement of the gun, and reflects the typical spray pattern profile. The densest part of the deposit is built up at the centre where the plasma jet is focused and where the most melted particles arrived. The periphery of the samples is formed from the finest particles in the powder size distribution [128], and usually they do not adhere to the sample. The area between the centre and the periphery of the samples is composed of particles partially melted and, therefore, it tends to be more porous.

These three areas (centre, periphery and in between) were distinguished in all of the fabricated samples. The production of flat even components requires overlapping of a number of singular spray lines. Therefore, a two-dimensional movement (X-Y) of the

gun is required. However, some conclusions can be drawn from this test and they are presented later in this section.
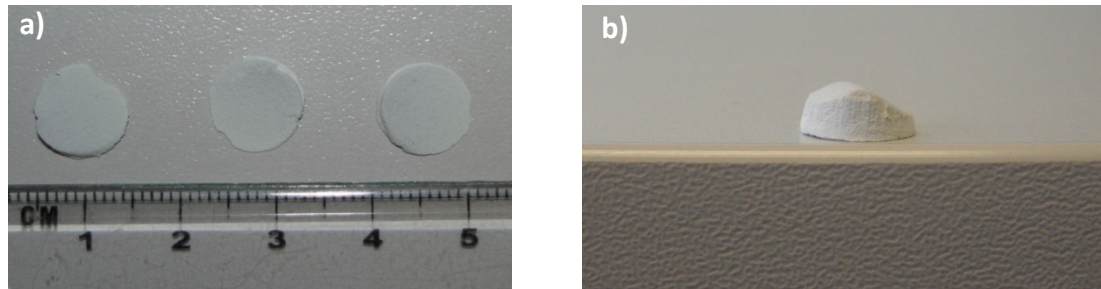
Figure 5.28. Shape of HA free-standing samples as sprayed: a) 70 s (HA60-9MB-1) plain view and b) 240 s (HA60-9MB-5) elevation view

The resultant average thickness and layer increment (thickness per pass) are listed in Table 5.4. The standard deviations of thickness measurements were important due to the shape of the samples. Therefore, the minimum, maximum and average of 15 layer thicknesses over the 3 produced samples for every spray time have been plotted in Figure 5.29. It can be seen that the layer thicknesses stabilised after 90 seconds of spraying. The reason for this may be the heat content of the coating, which increases with increased spraying time, thus, improving the adhesion of incoming particles as they strike flattening more per pass.

Table 5.4. HA free-standing average thickness for Series HA60-9MB

Sample	Time (s)	Number of layers	Total thickness (µm)	Layer thickness (µm)
HA60-9MB-1	70	24.2	640	26.3
HA60-9MB-2	90	31.1	1250	40.2
HA60-9MB-3	120	41.5	1800	43.4
HA60-9MB-4	150	51.8	2450	47.1
HA60-9MB-5	240	82.9	3650	44.0
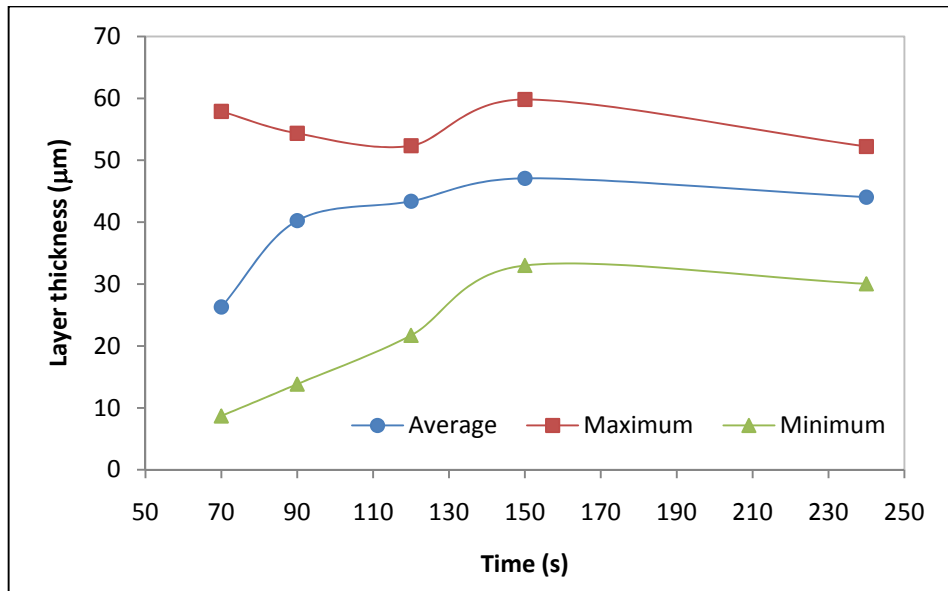
Figure 5.29. Minimum, maximum and average layer thicknesses for Series HA60-9MB

According to the surface characterisation of the free-standing components under SEM (Figure 5.30) it seems that the surface of the samples becomes smoother with increased spraying time. This can be attributed to the better flattening behaviour of the powder particles by higher coating temperatures. However, the measured surface roughness were not significantly different, all lying around an average R_a value of 6 µm. The surface of the sample HA60-9MB-4 (Figure 5.30b) presented some cracking caused by the residual stresses relaxation as a result of the high temperatures reached by the substrate.
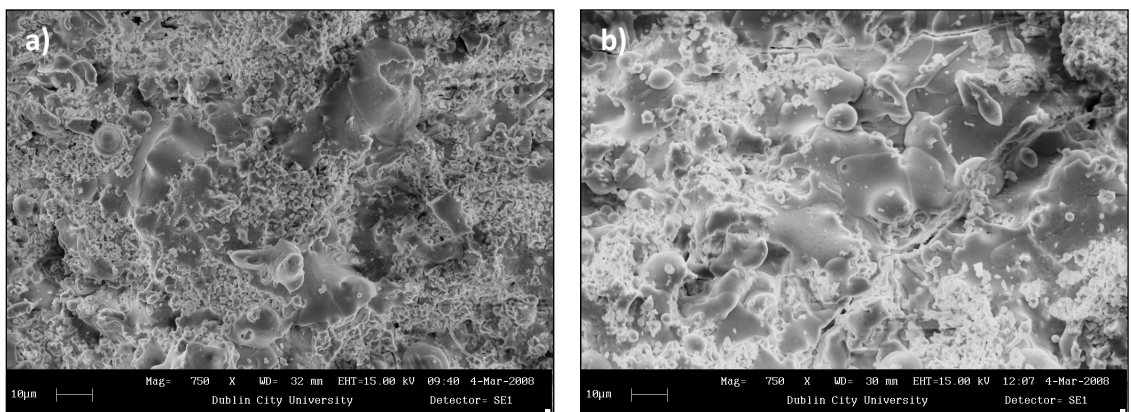
Figure 5.30. SEM images of the surfaces of: a) HA60-9MB-1, b) HA60-9MB-4 samples

Cracks were found in all the samples, not only on the surface but also across the sections (Figure 5.31). Cracks increased in size and number as the components became thicker, particularly after sample HA60-9MB-2, possibly because of the high layer increments (average>40 μm/layer, maximum≈60μm/layer) which induced greater thermal stresses. The optimum layer increment value depends on the process and material used; for conventional plasma spaying (APS) of brittle materials like HA it is not advisable to go above 30 μm/layer, a value, which is thought to prevent the build up of residual/thermal stresses [128].
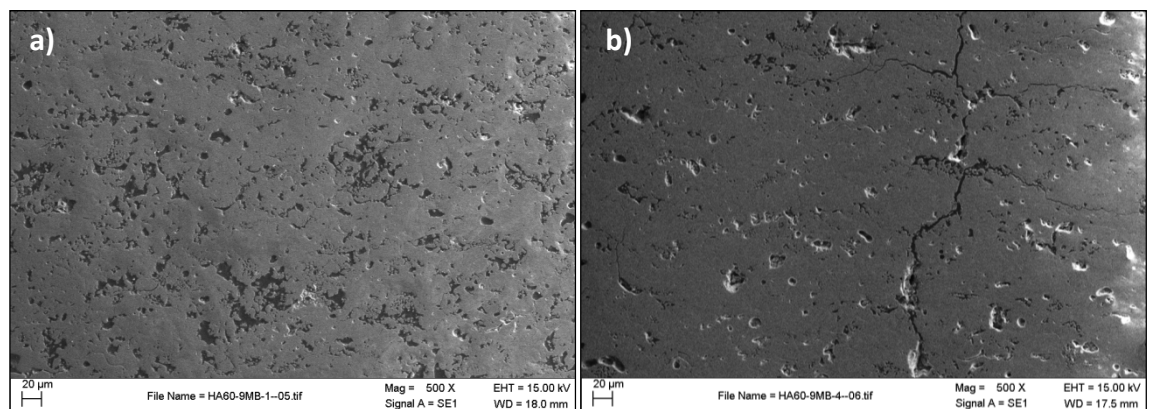
Figure 5.31. SEM images of the cross sections: a) HA60-9MB-1, b) HA60-9MB-4

Traces of β-TCP were found in all of the samples. However, purity greater than 95% was found in all cases, which complies with BS ISO 13779-2:2000 [227]. The influence of spraying time on the crystallinity and average thickness of the specimens was studied and the results are shown in Figure 5.32. The crystallinity increased as the spraying time increased following a second-order polynomial trend (R^2=0.99). The lesser crystalline sample was HA60-9MB-1 (86%) and the most crystalline HA60-9MB-5 (90%). The average thickness also followed a second-order polynomial trend (R^2=0.98), ranging between 640 and 3650 μm for HA60-9MB-1 and HA60-9MB-5 respectively.
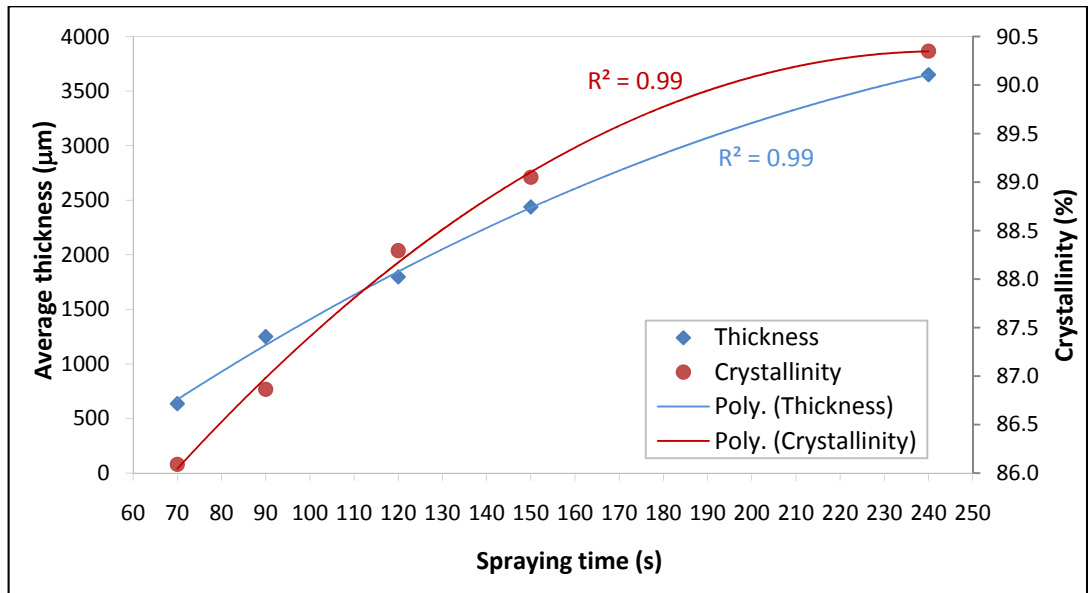
Figure 5.32. Effect of spraying time on average thickness and crystallinity in Series HA60-9MB

A linear relationship (R^2=0.97) was found between the average thickness of the deposit and its resulting crystallinity (Figure 5.33). This can be attributed to the heat stored in the sample with each spray pass as result of the low thermal conductivity of the coating material, which may decrease the cooling rate of the lamellae, therefore, allowing their re-crystallisation to hydroxyapatite. This effect has also been observed by other researchers [103, 228].
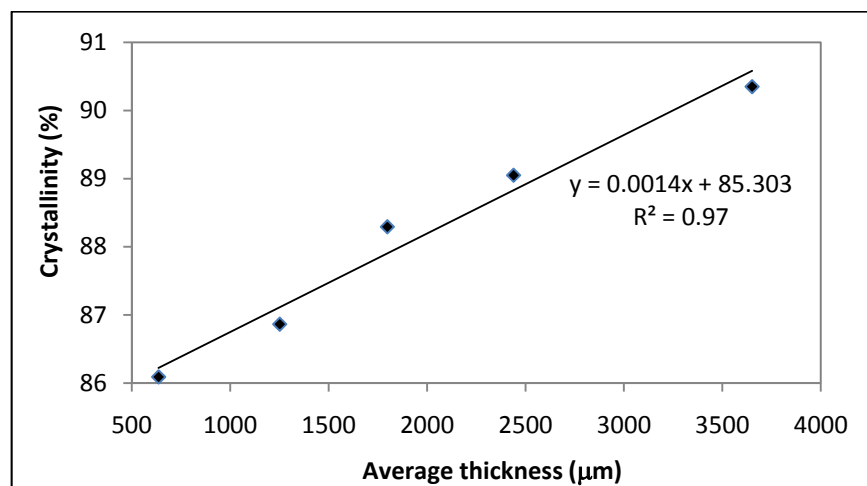
Figure 5.33. Average thickness - crystallinity relationship in Series HA60-9MB

- F4 gun

A series of samples (HA60-F4) were produced at INASMET's facilities by the author using a conventional plasma spray system (F4 gun). The process parameters were set at the values presented in Table 5.5, which are standard parameters used at INASMET to spray hydroxyapatite powders with similar sizes to that within this research.

Table 5.5. Standard plasma spray parameters for Series HA60-F4

Parameter	Value
Current (Power)	550 A (32 kW)
Primary gas (PG), flow rate	Argon, 50 slpm
Secondary gas, flow rate	Hydrogen, 3 slpm
Carrier gas (CG), flow rate	Argon, 4 slpm
Powder feeding rate	9 g/min
Stand-off distance (s.d.)	7 cm
Relative gun velocity	5 cm/s[*]
Increment y-direction (Δy)	-4 mm
Injector position	external
Injector size (diameter)	1.8 mm
Injector-centre of plasma distance	6 mm

[*] Relative gun velocity usually range between 20 and 50 cm/s, but for this specific case a relatively slow velocity was set to achieve a high deposition rate and thus achieve the desired coating thickness at a reasonable processing time.

A layer increment of 137 μm/layer was achieved for the initial set of parameters. The sample was observed under SEM showing a large number of cracks (Figure 5.34 and Figure 5.35). The cracking was not surprising as the layer increment was significantly higher than the one recommended (30 μm/layer). The relatively slow gun velocity would have also contributed to the coating overheating and thus generate cracks due to residual stress relaxation. On the other hand, the number of spray passes required to achieve a thick coating (> 2mm) increases significantly when lower deposition rates or higher gun velocities are used, thus leading again to a high heat transfer to the substrate. The substrate overheating is an important issue to control when producing thick ceramic layers and may therefore represent one of the limiting factors to achieve reproducible process conditions at industrial scale using this F4 system.

A colour change of the samples from white to bluish also occurred within this series, suggesting that the deposit had overheated and HA underwent some phase changes. The crystallinity and purity of the samples produced with the F4 gun were expected to be similar to those of the samples produced with the 9Mb gun as the power of the system was similar.
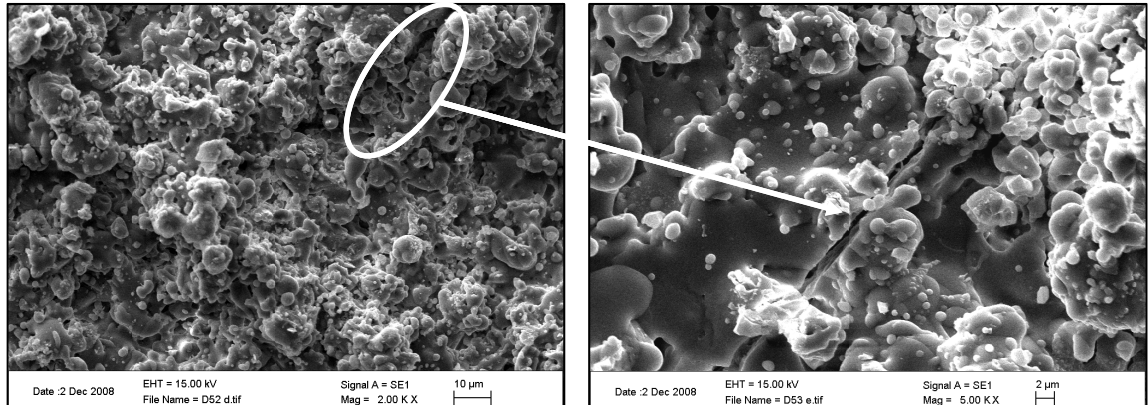
Figure 5.34. SEM images of HA60-F4 free standing surface
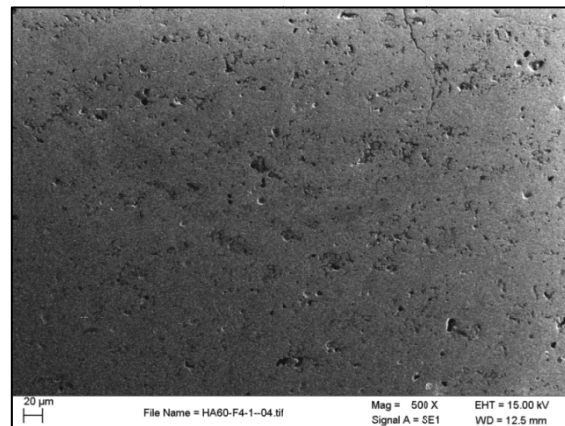
Figure 5.35. SEM image of HA60-F4 free standing cross section

Several tests were performed in order to understand which process parameter had the most influence on crack formation and colour change. The change in colour was avoided by increasing the horizontal speed of the gun from 5 cm/s to 10 cm/s. This change also decreased the layer increment to 64 μm/layer. However, cracking in the components was still observed.

- LEPS

A series of samples (HA60-LEPS) were produced at INASMET's facilities by the author using a low energy plasma spray system. The process parameters were set at the values presented in Table 5.6, which are standard parameters used at INASMET to spray hydroxyapatite powders with similar sizes to those used in this research. As described in Chapter 3, the LEPS operates with a reduced power input and only one process gas with a reduced flow rate. Therefore, the spray distance and the increment in y-axis displacement (Δy), which dictates the overlapping between spraying lines, must be set to lower values than those of conventional APS processes in order to produce homogeneous coatings.

Table 5.6. Initial plasma spray parameters for Series HA60-LEPS

Parameter	Value
Current (Power)	400 A (12kW)
Primary gas (PG), flow rate	Argon, 24 slpm
Carrier gas (CG), flow rate	Argon, 4 slpm
Powder feeding rate	5 g/min
Stand-off distance (s.d.)	3.5 cm
Relative gun velocity	5 cm/s
Increment y-direction (Δy)	-3 mm
Gun configuration[*]	1
Injector position	Internal

[*]See Appendix A

HA60 particles were found to accumulate inside the nozzle of the gun using the initial parameters listed above (Table 5.6) and, therefore, the primary gas flow rate was increased from 24 to 28 slpm to prevent such an effect. However, this change caused the plasma plume to become larger, compromising the quality of the deposit due to its proximity to the substrate. For this reason, the stand-off distance was increased from 3.5 to 4 cm.

The layer increment obtained, with these new settings (PG=28 slpm; s.d.=4 cm), was 72 μm/layer. A 2900 μm white cylindrical free-standing component was obtained; the white colour gave an indication of minimal HA degradation due to the reduced thermal input during the process. The lower heat input was also demonstrated by the lower temperature of the samples directly after spraying (160°C), which was significantly lower than the temperature after conventional plasma spraying (F4 ~ 300°C).

Figure 5.36 shows the surface and cross-sectional area of this sample. Cracking across the thickness and the surface of the sample can be observed, but this was much less than the cracking produced by the 9MB gun.
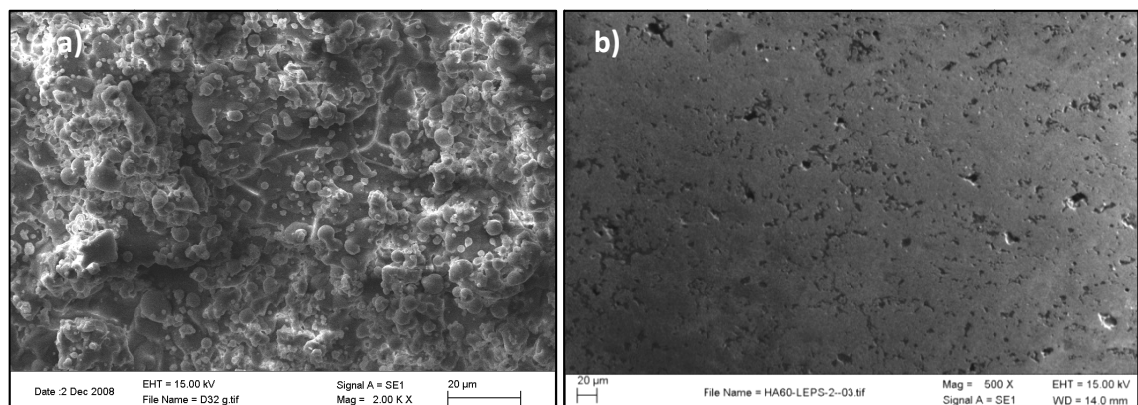
Figure 5.36.SEM images of HA60-LEPS free-standing sample: a) surface and b) cross section

The HA60-LEPS sample shown in Figure 5.36 was deposited at a greater layer increment (72 μm/layer) than the HA60-9MB samples and HA60-F4 samples shown in Figure 5.30/Figure 5.31 and Figure 5.34/Figure 5.35 respectively. Despite this greater layer increment the cracking was much less for the HA60LEPS sample due to the lower thermal energy applied to the particles.

Summary

From an economic point of view, using the low energy plasma gun is advantageous because it works with a lower energy input, it requires a lesser volume of gases and it has the lowest powder consumption. Comparing the F4 and 9MB plasma conventional

guns, the F4 is less demanding in energy input and the consumption of gases and powder used is significantly lower.

Although it is the most cost-effective system, the LEPS has technical limitations. It was initially designed just to spray calcium phosphate ceramics without causing phase degradation in the produced coating. As shown before, the LEPS has a narrow range of variation for some of the important parameters as in the case of primary gas flow and stand-off distance. As a result, it represents a technical challenge to spray other materials such as metals, polymers, other ceramics or composites using the same process parameters and gun configuration. However, being an in-house designed gun, it is possible to modify the equipment to meet the needs of the research. On the other hand, the conventional plasma guns have a wider range of parameter choice, allowing the adjustment of conditions to feed two different powders with different properties.

In terms of coating quality, the energy involved in the conventional plasma spray processes (9MB and F4) seems to be too high to prevent cracking within the components and produces some degree of degradation in the HA. The one-dimensional relative movement between the gun and the sample holder on the 9MB system is seen as an additional cause of intensifying the HA degradation. The low energy system decreases the thermal input of the in-flight particles and the component, so the thermal/residual stresses generated are lower. As a result, the cracking through the final component is significantly smaller using the LEPS system. The phase change of hydroxyapatite during processing was also minimised.

Consequently, the use of a low energy plasma spray (LEPS) system with a 2D movement (X-Y) control available at INASMET facilities was proposed as a good option to progress further with this research.

5.2.2. Selection of HA powder size

Apart from the influence of the PSPs, HA average particle size and distribution plays an important role in the heat content of in-flight particle, which influences the final properties of the coating (crystallinity, phase content, roughness, porosity and mechanical properties) [199, 229]. For instance, HA between 20-45 μm have been reported to produce coatings with enhanced mechanical properties [137]. However, it

has also been shown that the use of larger powders (~100 μm) produced greater porosity and surface roughness [230].

HA60 samples produced during the process selection tests were compared with samples produced with the larger powder (HA90, 89.7 μm), using the selected LEPS system. Table 5.7 shows the initial parameters used to produce the HA90-LEPS samples, which were based on the parameters shown in Table 5.6 for HA60-LEPS samples. The only different parameter chosen was the powder feed rate, which was increased to 10 g/min. Using the same feed rate would have led to a smaller quantity of HA90 particles flowing in the system as HA90 is larger and, therefore, the powder feed rate was adjusted to compensate for this fact.

Table 5.7. Initial plasma spray parameters for Series HA60-LEPS

Parameter	Values
Current (Power)	400 A (12kW)
Primary gas (PG), flow rate	Argon, 24 slpm
Carrier gas (CG), flow rate	Argon, 4 slpm
Powder feeding rate	10 g/min
Stand-off distance (s.d.)	3.5 cm
Relative gun velocity	5 cm/s
Increment y-direction (Δy)	-3 mm
Gun configuration[*]	1
Injector position	Internal

[*]See Appendix A

The initial parameters did not cause HA90 particles to accumulate in the nozzle. However, the layer increment for sample HA90-LEPS, 25 μm/layer, was one third of that achieved for HA60-LEPS even though the powder feed rate was twice that of HA60 powder. This is attributed to the insufficient melting degree of the powder particles as result of the limited power of the system, resulting in a large number of particles bouncing-off the substrate. An additional cause could be the erosion of the coating due to the arriving unmelted particles. Unfortunately, a decrease in plasma gas flow

rate was proven to be insufficient to accelerate the particles towards the substrate, causing them to accumulate inside the nozzle. The sample produced with the initial PSPs was observed under SEM (Figure 5.37). Even though the cross section seems to be more porous than that of HA60-LEPS samples, the microstructure exhibited cracking and poor melting of the HA particles which might led to lower mechanical properties.
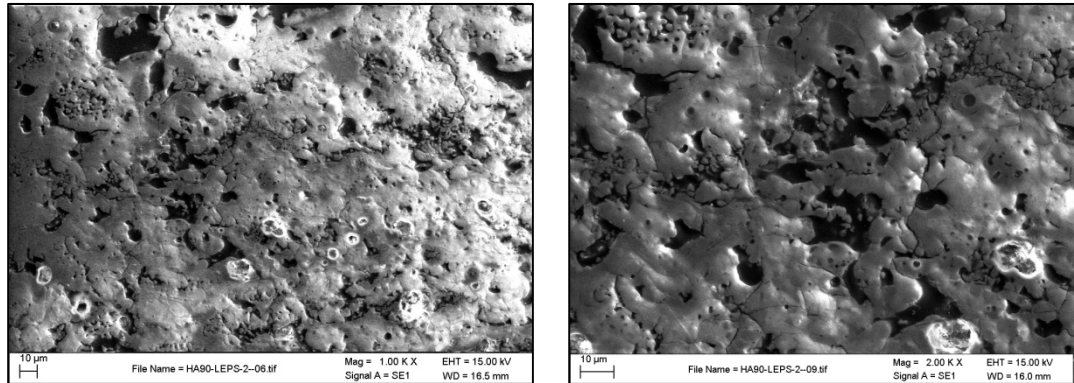
Figure 5.37. SEM images of HA90-LEPS sample cross section

In summary, it can be said that the finer powder (HA 60) performed better in the LEPS system, demonstrating a greater layer increment (3 times greater than using HA90) and better coating cohesion. Therefore, HA60 was selected as the matrix material for the remaining composites study and used when carrying out the optimisation tests.

5.2.3. Materials feasibility tests

The LEPS system, as previously stated, was designed specifically to spray calcium phosphates. The ability of the system to spray other materials, which are added to the HA later in this research as reinforcements or pore formers, is essential. Therefore, several materials (PEEK, PCL, YSZ and Titanium) were tested on their own using the LEPS system.

A study of the spraying parameters was carried out later for the composites, using a separate injection to spray HA/PEEK, HA/PCL and HA/Ti combinations. The challenge of this series of tests was to simultaneously spray two powders with different thermal and physical properties, thus, requiring in principle different processing conditions. The principal spraying parameters for HA were used as a reference. Then, the process was

tested, modifying the feeding system of both powders (gas flow rate, injector size, injector position and powder feed rate). Finally, the performance of the agglomerated powders, containing HA and YSZ, was tested.

PEEK

Polymers are difficult to process using conventional plasma spraying because of the high enthalpy involved in the process. LEPS is a low energy version of it that could prove suitable to spray polymers without major degradation. Polyetheretherketone (PEEK) is a structural polymer with the highest melting temperature (350°C) among the polymers used within the biomedical field. Therefore, it makes sense to study the performance of this bioinert polymer on the system prior to moving towards more sensitive bioresorbable polymers such as PCL.

The parameters (Table 5.8) were initially set using the reference parameters obtained for HA before, since the ultimate goal will be to spray the two powders together. The gun was set to configuration 2 (Appendix A) to allow the feeding of PEEK through an external injector placed at a cooler zone of the plasma plume. For this series, there was no second powder fed through the internal injector, but a minimal flow of carrier gas was employed in the internal injector to avoid overheating of the same.

Table 5.8. Initial plasma spray parameters for PEEK feasibility test

Parameter	PEEK-LEPS
Current (Power)	400 A (12 kW)
Plasma gas (PG), flow rate	Argon, 28 slpm
Carrier gas 1 (CG1), flow rate	Argon, 4 slpm
Carrier gas 2 (CG2), flow rate	Nitrogen, 5 slpm
Powder feeding rate 1 – HA60	0 g/min
Powder feeding rate 2 – Additive	PEEK: 0.65 g/min
Stand-off distance (s.d.)	4 cm
Relative gun velocity	5 cm/s
Increment y-direction (Δy)	-3 mm
Gun configuration[*]	2
Injector 1 position	Internal
Injector 2 position (d/e/α)[*]	External (5mm/10.5mm/90°)
Cooling system	None

[*]See Appendix A

The PEEK was found to be completely degraded (Figure 5.38a) using these initial parameters, therefore a decrease in heat input was required. The coating was surprisingly easy to remove from the substrate and a thickness of up to 500 μm was achieved after 5 spray passes (layers).
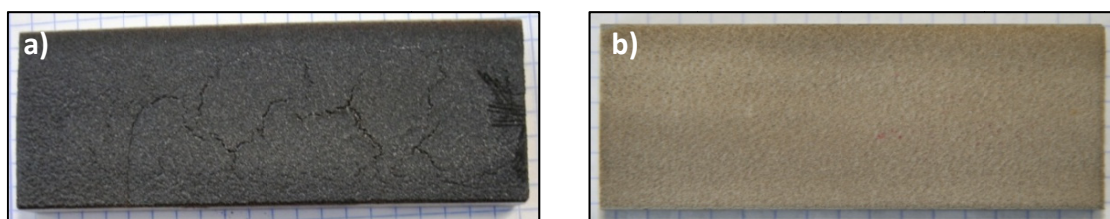
Figure 5.38. PEEK coatings: a) completely degraded (black) and b) slightly degraded (light brown)

In order to reduce PEEK degradation, the injector position was modified (angle shifted to 80°, d increased to 18 mm), the primary gas flow increased to 35 slpm and a compressed air cooling system (6 bar) was attached to the gun. The cooling system consisted of two nozzles parallel to the axis of the plasma plume in which compressed air flowed at a controllable pressure of up to 6 bar. After these modifications to the parameters, degradation of the polymer was still noticeable (dark brown), even when using the maximum compressed air pressure.

Further parameter modifications consisted of increasing the relative traverse velocity of the gun to 15 cm/s. The thickness decreased to 358 μm (5 layers), but the coating colour was light brown (Figure 5.38b), which indicates just a slight degradation of PEEK. As a last step, the carrier gas was increased to 6 slpm and the stand-off distance to 6 cm. The deposition efficiency dropped more, but the deposit produced using this set of parameters did not undergo degradation, presenting a beige colour.

The FTIR characteristic bands for PEEK powder are: $v_{C=O}(1600cm^{-1})$, $v_{ph-CO-ph}(1217cm^{-1})$, $v_{C-O}(1025cm^{-1})$ and $v_{ph-C=O-ph}(929cm^{-1})$ [231]. As observed in the FTIR spectra (Figure 5.39), there are no new or missing peaks on the FTIR spectra of the sprayed PEEK compared to that of the PEEK powder. This is promising result as PEEK degradation has been reported to occur even when using flame spraying system [232].

In order to prevent PEEK undergoing any degradation at different parameter settings, liquid CO_2 or liquid nitrogen cooling system could be used. Unfortunately, no such system was available at INASMET facilities.
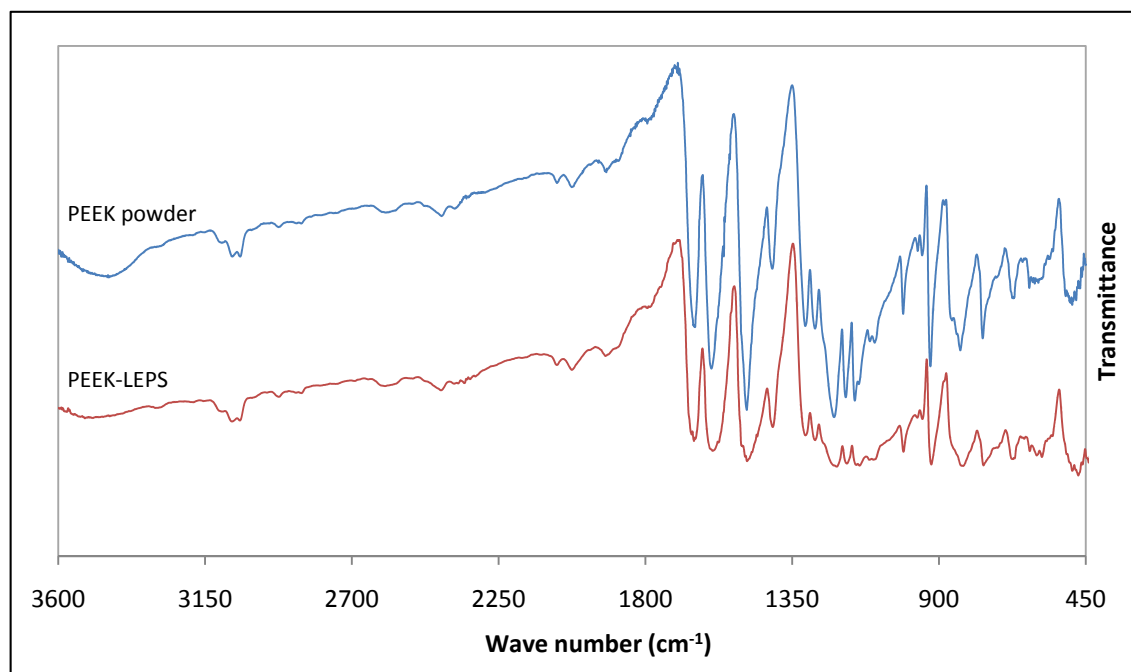
Figure 5.39. FTIR spectra of PEEK-LEPS compared to PEEK powder

PCL

As it was possible to spray PEEK without degradation, the feasibility of a lower melting temperature polymer in the LEPS system was tested. The selected polymer was Polycaprolactone (PCL), which has a melting temperature of 60°C. The process parameters were based on the ones found to produce less degraded PEEK coatings and they are detailed in Table 5.9.

The coatings obtained with these process parameters were sticky, showing a degree of melting, and their colour was transparent. The initial gun velocity was increased from 15 to 50 cm/s and as a result the coating turned solid. The FTIR of the latter coating demonstrated that the PCL can be sprayed with very little degradation (Figure 5.40).

Table 5.9. Initial plasma spray parameters for PCL feasibility test

Parameter	PCL-LEPS
Current (Power)	400 A (12 kW)
Plasma gas (PG), flow rate	Argon, 35 slpm
Carrier gas 1 (CG1), flow rate	Argon, 4 slpm
Carrier gas 2 (CG2), flow rate	Nitrogen, 6 slpm
Powder feeding rate 1 – HA60	0 g/min
Powder feeding rate 2 – Additive	PCL: 0.65 g/min
Stand-off distance (s.d.)	6 cm
Relative gun velocity	15 cm/s
Increment y-direction (Δy)	-3 mm
Gun configuration[*]	2
Injector 1 position	Internal
Injector 2 position (d/e/α)[*]	External (18mm/10.5mm/80°)
Cooling system	Compressed air @ 6 bar

[*]See Appendix A

Figure 5.40. FTIR spectra of PCL-LEPS compared to PCL powder

YSZ

The YSZ powder did not flow through the feeding system of the LEPS due to its small size. Fine powder can be fed through special feeding systems which were not available at INASMET. In this study the solution proposed was to feed the YSZ powder as an agglomerate combined with the HA powder using PVA as a binder. The results are discussed later in this section.

Titanium

LEPS system feasibility tests to spray pure titanium were performed. The initial parameters set-up can be seen in Table 5.10. The powder injectors were set at configuration 2 (Appendix A) to allow titanium feeding through the external injector. There was no powder fed through the internal injector for this series but the carrier gas was allowed to flow in order to avoid overheating of the injector tip.

Table 5.10. Initial plasma spray parameters for Ti feasibility test

Parameter	Ti-LEPS
Current (Power)	400 A (12 kW)
Plasma gas (PG), flow rate	Argon, 28 slpm
Carrier gas 1 (CG1), flow rate	Argon, 4 slpm
Carrier gas 2 (CG2), flow rate	Nitrogen, 5 slpm
Powder feeding rate 1 – HA60	0 g/min
Powder feeding rate 2 – Additive	Ti: 8 g/min
Stand-off distance (s.d.)	4 cm
Relative gun velocity	5 cm/s
Increment y-direction (Δy)	-3 mm
Gun configuration[*]	2
Injector 1 position	Internal
Injector 2 position (d/e/α)[*]	External (5mm/10.5mm/90°)
Cooling system	None

[*]See Appendix A

A layer increment of 20 μm/layer was obtained using the initial PSPs. This low layer increment indicates that the plasma spray parameters presented in Table 5.10 are inadequate to achieve good deposition efficiency. Several tests, modifying the stand-off distance, gun velocity, feed rate and carrier gas flow rate, were carried out to increase the layer increment. In summary, it can be said that:

- The layer increment increased from 20 to 35 μm/layer when the stand-off distance was increased from 4 to 10 cm, with the remainder of the parameters as listed in Table 5.8.

- The layer increment decreased from 35 to 15μm/layer when the velocity was increased from 5 to 15 cm/s, with the remainder of the parameters set the same as in Table 5.8.

- Several samples were produced to establish the plasma gas flow rate, which led to the greatest layer increment (Figure 5.41). The layer increment was found to drop to 6 μm/layer when the gas flow rate was increased to 49 slpm. The maximum layer increment was achieved using a 35 slpm plasma gas flow rate, with the parameters fixed to the same as those listed in Table 5.10. The plasma gas flow rate could be further decreased by adapting the powder feed rate and the carrier gas flow rate. As an example, producing a good coating with 25 slpm and a feeding rate of 4 g/min requires a carrier gas of 3.8 slpm, as found in this research.
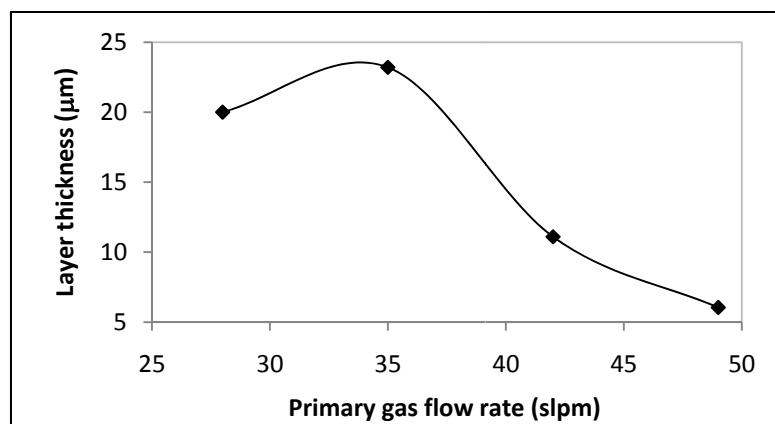
Figure 5.41. Plasma gas flow rate effect on layer thickness for Ti-LEPS series

The visual aspect of all samples (Figure 5.42) indicated that the LEPS system lacks the required power to melt the titanium powder with a particle size of 137.36 μm. This leads to low process efficiency due to a high quantity of rebounding unmelted powder. Even though Ti is seen as unsuitable for this system, HA/Ti feasibility tests were conducted to fully assess the performance of this powder in the system.

Figure 5.42. Visual aspect of Ti samples sprayed with the LEPS system

HA/PEEK

The spraying of HA and PEEK to form a composite coating was the objective of these feasibility tests. As both materials were able to flow easily in the feeding system, they were fed separately using two hoppers. The separate injection allowed control of the thermal input of the polymer. The HA60/PEEK-LEPS series were sprayed using the parameters shown in Table 5.11.

Table 5.11. Initial plasma spray parameters for HA/PEEK feasibility tests

Parameter	Value
Current (Power)	400 A (12 kW)
Plasma gas (PG), flow rate	Argon, 35 slpm
Carrier gas 1 (CG1), flow rate	Argon, 4.5 slpm
Carrier gas 2 (CG2), flow rate	Nitrogen, 6 slpm
Powder feeding rate 1 – HA60	9 g/min
Powder feeding rate 2 – PEEK	1.3 g/min
Stand-off distance (s.d.)	6 cm
Relative gun velocity	15 cm/s
Increment y-direction (Δy)	-3 mm
Gun configuration[*]	2
Injector 1 position	Internal
Injector 2 position (d/e/α)[*]	External (18mm/10.5mm/80°)
Cooling system	Compressed air, 6 bar

[*]See Appendix A

A deposit of 1760 μm was obtained after 15 layers (117.3 μm/layer), which was easily removed from the substrate. Part of this coating was characterised by DSC (Figure 5.43) and FTIR (Figure 5.44). The HA did not undergo any phase change within the DSC temperature range tested, but it underwent water loss (dehydration), adding a slope to the DSC graph. The PEEK peaks on the DSC graph remained the same as those in the original powder.
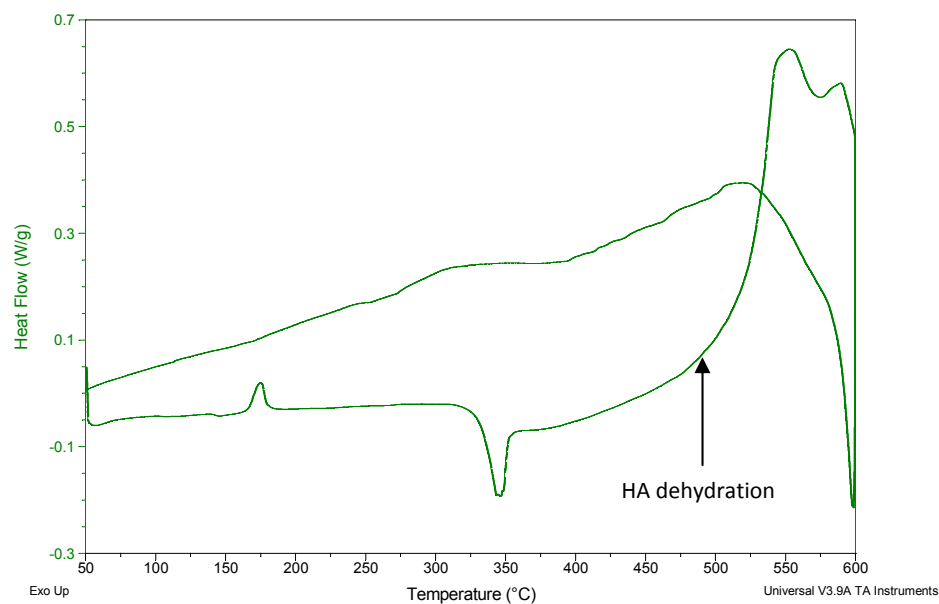
Figure 5.43. DSC of HA/PEEK-LEPS

The FTIR spectra (Figure 5.44) shows that HA underwent dehydroxylation during the process, which can be noticed as the OH$^-$ peak at 635 cm^{-1} disappeared and the one at 3571 cm-^{1} decreased. The degradation of PEEK is difficult to assess as the bigger PO$_4^{-3}$ peaks overlapped part of the PEEK spectra. The rest of the PEEK powder peaks are present in the coating spectra. Therefore, from the analysis of DSC and FTIR results it can be said that PEEK underwent slight degradation, if any, due to the thermal content of HA particles.
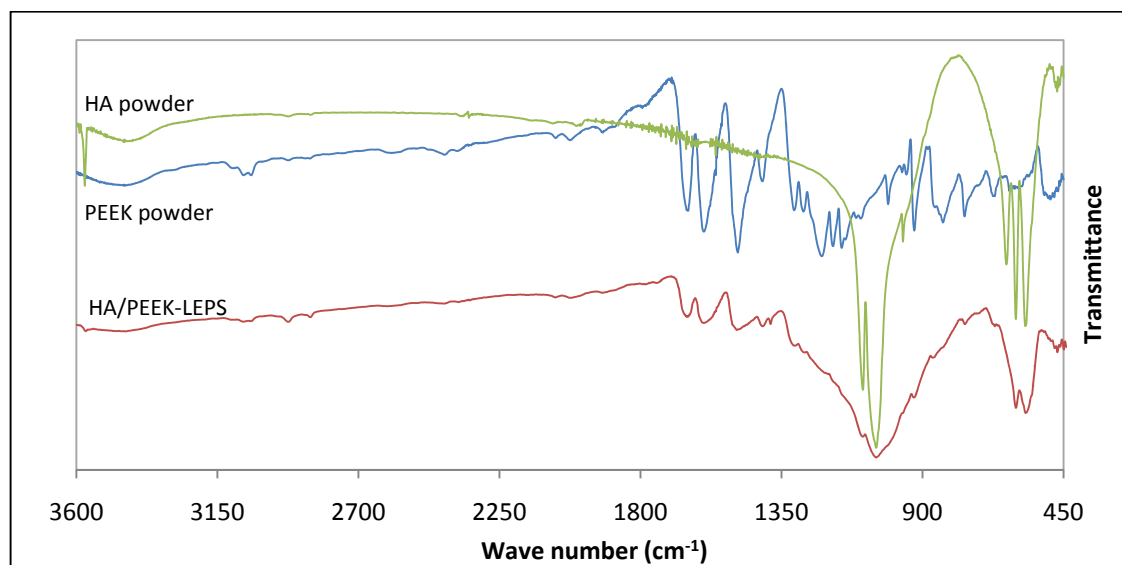
Figure 5.44. FTIR spectra of HA/PEEK-LEPS

The microstructure of this composite coating was difficult to distinguish using SEM images. As can be seen in Figure 5.45a HA particles appear to be evenly distributed in a PEEK matrix. However, this distribution may be occurring due to HA particles being pulled off during metallographic grinding of the sample and, consequently, the gaps being covered by the epoxy resin during the metallographic preparation. In Figure 5.45b, it can be seen that the surface of the sample is formed by round particles covered, or surrounded, by a melted phase, and so particle de-bonding may be occurring. HA particles de-bonding in HA/PEEK was also reported elsewhere [81, 98].

EDX was performed and HA particles were found to be the white particles marked in Figure 5.45a. Unfortunately, differences between the epoxy and PEEK could not be distinguished by this technique due to their similar elemental composition.
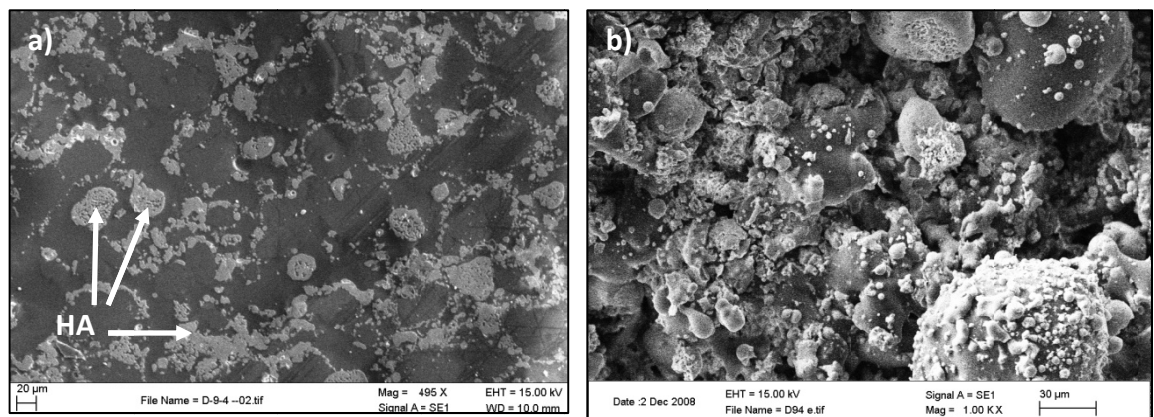
Figure 5.45. SEM images of HA/PEEK-LEPS: a) cross section and b) surface

HA/PCL

The spraying of HA and PCL was the object of this new series of tests. As both materials were able to flow easily in the feeding system, they were fed separately using two hoppers, thus, allowing control of the PCL thermal input. The HA60/PCL-LEPS series were sprayed using the parameters shown in Table 5.12.

Table 5.12. Initial plasma spray parameters for HA/PCL feasibility tests

Parameter	PEEK-LEPS
Current (Power)	400 A (12 kW)
Plasma gas (PG), flow rate	Argon, 35 slpm
Carrier gas 1 (CG1), flow rate	Argon, 4 slpm
Carrier gas 2 (CG2), flow rate	Nitrogen, 6 slpm
Powder feeding rate 1 – HA60	5 g/min
Powder feeding rate 2 – Additive	PCL: 0.65 g/min
Stand-off distance (s.d.)	6 cm
Relative gun velocity	50 cm/s
Increment y-direction (Δy)	-3 mm
Gun configuration[*]	2
Injector 1 position	Internal
Injector 2 position (d/e/α) [*]	External (18mm/10.5mm/80°)
Cooling system	Compressed air @ 6 bar

[*]See Appendix A

The parameters studied to achieve a high layer increment without degrading the polymer were: plasma gas flow rate, injector position, polymer carrier gas flow rate, HA and polymer feed rate. As a summary of these changes it can be said that:

- The polymer seemed to evaporate during coating formation. As the polymer feeding rate was large, this evaporation caused the layers of the coating to partially peel off. The polymer feeding rate was, therefore, decreased to 0.15 g/min by setting the rotational speed of the feeding plate to a minimum. A slight improvement on the coating formation was observed. However, this change made it difficult to feed the polymer at a constant rate due to PCL's low density. Unfortunately, this fact introduced noise in the statistical models examined in the Section 5.4. The only way of avoiding this feeding problem is to use a special feeding system, which was not available at INASMET.
- The plasma gas flow rate was increased to 36 slpm to prevent the coating from turning brownish and the polymer from clogging the injector. The thermal content of the HA particles also caused the polymer to undergo a slight degradation.

- The carrier gas flow rate of the polymer required an adjustment after decreasing the PCL feed rate and increasing the plasma gas flow rate. The clogging was avoided and the feeding stability improved by increasing the carrier gas flow rate from 6 slpm to 8 slpm. As a result, the building up of the coating was improved.
- At the 8 slpm setting it was possible to increase the layer thickness via two routes:
  - By keeping the injector position at 14 mm from the gun and increasing the HA feed rate from 5 g/ min to 11 g/min. It was found that for 8 slpm flow rate the layer thickness depended quadratically on the HA feed rate (Figure 5.46). The layer thickness increased from 15 to 32 μm.
  - By keeping the HA feed rate at 7 g/min, and changing the injector position from 14 mm to 27 mm from the gun. This increased the layer thickness from 15 to 24 μm.
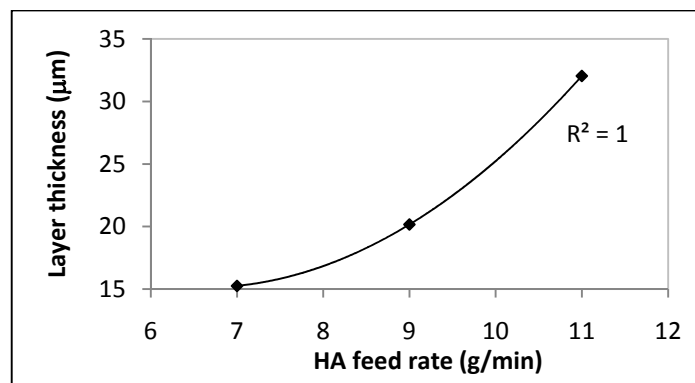
Figure 5.46. Influence of HA feed rate on layer thickness of HA/PCL-LEPS series

HA/Titanium

For this series both powders, HA and pure Titanium, were fed separately using two hoppers. The initial set of parameters chosen (Table 5.13) was based on the parameters for Series HA60-LEPS.

Table 5.13. Initial plasma spray parameters for HA/Ti feasibility tests

Parameter	Value
Current (Power)	400 A (12 kW)
Plasma gas (PG), flow rate	Argon, 28 slpm
Carrier gas 1 (CG1), flow rate	Argon, 4 slpm
Carrier gas 2 (CG2), flow rate	Nitrogen, 5 slpm
Powder feeding rate 1 – HA60	5 g/min
Powder feeding rate 2 – Ti	8 g/min
Stand-off distance (s.d.)	3.2 cm
Relative gun velocity	5 cm/s
Increment y-direction (Δy)	-3 mm
Gun configuration[*]	2
Injector 1 position	Internal
Injector 2 position (d/e/α)[*]	External ($5mm/10.5mm/80^o$)
Cooling system	None

[*]See Appendix A

A layer increment of 63 μm/layer was obtained using the initial set of parameters. However, it was observed that titanium particles were not properly melted and most of them bounced off the substrate. In order to increase Titanium melting degree and, therefore, its deposition efficiency, several parameters were adjusted. These parameters were: the stand-off distance and powder injection parameters (carrier gas flow rate, Ti feed rate and injector position). In summary, it can be said that:

- The layer thickness decreased by 16% when the stand-off distance was changed from 3.2 to 5 cm. A maximum layer thickness occurred for a stand-off distance close to 4 cm. This trend can be seen in Figure 5.47.
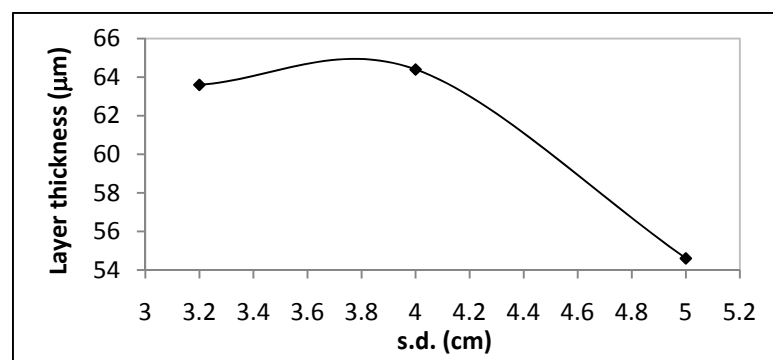
Figure 5.47. Influence of stand-off distance on layer increment for HA/Ti-LEPS series

- The titanium feed rate was varied from 4 to 12 g/min to test its influence on the layer thickness, using the PSPs listed in Table 5.13 with a s.d. of 4 cm. This parameter did not affect the layer thickness (range of variation: 54-56 μm/layer). This could be explained by the fact that the majority of the titanium particles did not melt enough and bounced off the substrate, not contributing to the thickness built-up. Unmolten Ti particles can be seen in the cross sections of all the samples with two examples shown in Figure 5.48.
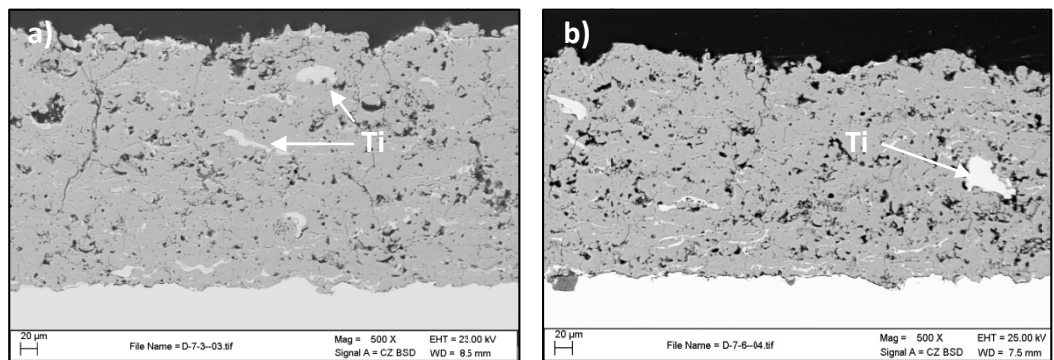
Figure 5.48. Cross sections of HA/Ti-LEPS samples: a) 8 g/min and b) 12 g/min titanium feed rate

- However, the layer increment was increased from 63 to 100 μm/layer when the HA powder feed rate increased from 5 to 9 g/min, with the remainder of the parameters being set as listed in Table 5.13 with a stand-off distance of 4 cm.

- The titanium injector was placed in a hotter part of the plume to increase Ti particles heat input without affecting the thermal input to HA particles. The gun configuration 3 (Appendix A) was therefore adopted, feeding titanium through injector 2. Unfortunately, the carrier gas required to introduce the titanium into the plume disturbed the plasma jet making it unstable.

- In order to avoid this, the injection position was switched, feeding Ti particles through injector 1 and HA through injector 2. A number of tests were performed using this new configuration, taking into account that changing the HA injector position required some extra tests. A summary of these tests is shown as follows:

  - The HA carrier gas had to be set to at least 4 slpm to avoid accumulation of HA inside the gun. A smaller carrier gas normally lacks the kinetic energy to

introduce HA inside the plasma plume. However, it was possible to decrease the HA carrier gas to 3.5 slpm by introducing the tip of the injector 1 mm inside the orifice of the nozzle. Therefore, it was possible to obtain deposition rates around 20 μm/layer, but some HA still got stuck inside the nozzle.

- No matter how much the titanium carrier gas was decreased, the plasma still became unstable also at this gun configuration.

The conclusion that can be drawn from the Ti and HA/Ti feasibility tests is that the LEPS system lacks the required energy to melt titanium powder with average particle size of 137.36 μm. Therefore, titanium of 45 μm average particle size was ordered to perform the optimisation tests, but due to the long supplier delivery time the powder was discarded. TiO_2 of 45 μm average size was used instead. There was no need to conduct feasibility tests on this TiO_2 powder as it has a slightly lower melting temperature than titanium (Table 2.8) and therefore is expected to properly perform in the LEPS system.

Agglomerated powders

None of the two agglomerated powders (5%wt and 15%wt YSZ), which were obtained using attrition milling and sintering, flowed in the system. This could be due to the amount of binder used during the attrition milling process or the size trimodal distribution of the final powders after sintering. Optimisation of the agglomerating process, which is outside the scope of this work, should be performed to improve powder flowability in the system.

Summary

The LEPS system can spray polymers, such as PEEK and PCL, without major degradation. For this, the injection system should be adjusted, the velocity of the gun set to a value higher than 15 cm/s and a cooling system should be attached to the gun. On the other hand, the system was found to be unable to feed a powder with a small average particle size, such as YSZ (<5 μm); and unable to sufficiently melt a powder with coarse particles, such as the tested Titanium powder (>100 μm).

The HA/PEEK composites coatings were difficult to characterise and a reduction of the polymer quantity is seen as a solution to understanding the formation of these coatings. It was also found that a great amount of PCL powder (>0.15 g/min) added to the HA caused the coating to peel off due to its evaporation during the process. The rotation of the feeding plate, which controls the powder feeding rate, was already set to its minimum, but a further reduction in the polymer feeding rate would be desired. However, as mentioned previously, the low density of the polymer, together with an even more reduced feeding rate resulted in inconstant feeding of the polymer, which led to inhomogeneity in the coating.

After all the attempts were carried out in HA/Ti series, it was concluded that the main limitation is the process itself. The feeding of 2 materials with such different thermal properties in the LEPS system narrowed the range of variation of process parameters, and it was not possible to find adequate PSPs to obtain good quality coatings. The remaining option of feeding 2 powders inside the hottest part of the plasma, without perturbing the plume, is to feed them through the same injector, either by mixing the two powders or agglomerating them.

Agglomerated HA/YSZ powder did not flow in the system and further research should be carried out on optimising the agglomerating process. Unfortunately, powder processing optimisation lies outside the scope of this project and this will be proposed as part of future work.

Selection for optimisation tests

As observed, LEPS system was able to produce HA/PEEK and HA/PCL composites. However, the availability of PEEK powder for this research was limited. Therefore, PCL was the polymer chosen to proceed with the HA/polymer optimisation stage, which attempts to improve the porosity of the coatings. The enhanced biological properties of PCL (resorbable) are seen as an additional reason to proceed with this selection.

TiO_2 was the powder selected to optimise the "mixing powders" option, which is expected to improve the mechanical properties of the composite coatings. HA and TiO_2

powders were mixed in different %wt and then fed through the injector using gun configuration 1 (Appendix A).

5.3. HA reference samples study

As mentioned previously, HA60 (from now on HA) was selected as the matrix of the composite coatings to be produced during this research work. Three properties (responses) were statistically modelled for this series: layer thickness, roughness and crystallinity. The layer thickness of the produced composites based on this series would depend in some extent on the deposition rate of the most abundant material, Hydroxyapatite. In addition, the roughness, crystallinity and purity of the HA matrix, will influence the biological behaviour of the composites later and, therefore, need to be optimised prior to adding the second phase material. Finally, the porosity and mechanical properties are not expected to vary significantly among the samples of the series, but they were studied to set the basis for comparison of the composite series.

HA optimisation tests were the reference series for this work. Therefore, the addition of second phases was made based on the best combination of parameters obtained in this section. The LEPS parameters used to produce this series are shown in Table 5.14. These parameters were set taking into account the observations made during the selection tests. It is pertinent to highlight that as velocity increases the HA deposition efficiency decreases and, as velocity decreases the polymer added as a second phase would undergo further degradation. Therefore, the relative gun velocity was set to 20 m/s as a compromised value.

Table 5.14. Plasma spray parameters for optimisation of HA deposition (LEPS)

Parameter	Parameter	DOE factor code
Current (Power)	390 A (12kW)	-
Primary gas (PG), flow rate	30-42 slpm	A
Carrier gas (CG), flow rate	Argon, 4.6 slpm	-
Powder feeding rate	5 - 9 g/min	C
Stand-off distance (s.d.)	3.5 – 4.5 cm	B
Relative gun velocity	20 cm/s	-
Increment y-direction (Δy)	-3 mm	-
Gun configuration[*]	1	-
Injector position	Internal	-

[*]See Appendix A

The optimisation of HA deposition was carried out using the response surface methodology. The experiments were statistically designed using a 3 factor Box-Behnken design (Table 5.15) consisting of 17 experimental runs from which 12 were design points ($3*2^2$) and 5 were centre points (marked in grey). As observed, the 12 points are divided into 3 blocks, each one consisting of all the combinations (2^2) of 2 of the factors at the high and low levels with the third factor remaining at the central point. The properties characterised for HA reference samples are shown in Table 5.16.

Table 5.15. Box Behnken design for HA reference series

Reference name	Run order	Factor A: PG flow rate (slpm)	Factor B: s.d. (cm)	Factor C: HA feed rate (g/min)
HA1	11	30	3.5	7
HA2	12	42	3.5	7
HA3	14	30	4.5	7
HA4	15	42	4.5	7
HA5	8	30	4	5
HA6	1	42	4	5
HA7	3	30	4	9
HA8	4	42	4	9
HA9	10	36	3.5	5
HA10	16	36	4.5	5
HA11	9	36	3.5	9
HA12	13	36	4.5	9
HA13	2	36	4	7
HA14	7	36	4	7
HA15	5	36	4	7
HA16	17	36	4	7
HA17	6	36	4	7

Table 5.16. Measured properties from the HA reference series

Reference name	Layer Thickness, μm		Roughness, μm		Crystallinity, %		Porosity, %		Vickers Hardness		E, GPa		K_{IC}, MPa·m$^{1/2}$	
	Average	Std. Dev.	Average	Std. Dev.	Average	Std. Dev.	Average	Std. Dev.	Average	Std. Dev.	Average	Std. Dev.	Average	Std. Dev.
HA1	24.3	0.6	6.47	0.21	84.2	3.5	3.8	0.5	334	50	4.6	0.8	0.66	0.10
HA2	13.8	0.5	5.49	0.30	89.1	1.7	2.8	0.4	279	43	3.8	0.5	0.56	0.07
HA3	20.2	0.7	6.30	0.45	84.5	1.4	3.7	0.3	329	47	4.7	1.1	0.66	0.07
HA4	4.8	0.2	6.07	0.47	89.7	1.9	2.5	0.4	244	24	2.9	0.8	0.52	0.04
HA5	15.9	0.9	6.23	0.31	83.9	0.8	3.5	0.7	332	48	4.3	0.6	0.68	0.07
HA6	9.6	0.3	5.50	0.31	89.2	2.3	3.3	0.3	275	47	4.0	1.1	0.64	0.08
HA7	33.0	1.8	6.46	0.60	82.8	0.4	3.9	0.7	351	38	4.5	1.0	0.70	0.06
HA8	17.9	1.1	5.75	0.18	89.1	2.2	2.9	0.4	292	46	3.5	0.8	0.57	0.08
HA9	11.7	0.8	5.84	0.30	86.9	2.3	5.0	0.7	260	42	4.7	0.9	0.53	0.08
HA10	9.9	0.3	5.90	0.41	86.0	1.5	6.0	0.5	271	34	4.3	0.8	0.55	0.05
HA11	24.4	0.8	5.83	0.35	86.6	1.7	4.2	0.6	307	66	4.6	1.1	0.69	0.11
HA12	23.5	0.8	5.82	0.30	86.8	2.2	4.2	0.4	337	41	4.3	1.1	0.71	0.07
HA13	17.4	0.9	6.09	0.56	88.0	1.8	5.0	0.2	332	52	6.4	1.3	0.66	0.09
HA14	19.6	1.0	5.90	0.57	87.5	1.2	4.8	0.4	331	54	4.8	0.8	0.68	0.11
HA15	18.2	1.0	6.06	0.37	87.8	1.3	4.7	0.6	339	49	3.5	0.4	0.68	0.08
HA16	18.5	0.8	5.79	0.53	88.0	0.7	5.7	0.4	278	40	3.1	0.3	0.55	0.09
HA17	19.2	0.8	6.03	0.27	87.1	0.8	4.8	0.8	322	42	4.3	1.1	0.64	0.06

5.3.1. Layer thickness of the HA reference series

The layer thickness was obtained following the procedure detailed in Section 4.6.2. The layer thickness values, which ranged between 4.8-33 μm, are presented graphically in Figure 5.49. Comparing the average values obtained for the five centre points it can be said that the process displayed a reasonable repeatability in terms of layer thickness. The influence of the parameters on the layer thickness was not straightforward, and it is statistically studied later in this section.

Figure 5.49. Layer thickness results for HA reference series

A power transformation ($y'=y^{\lambda}$, λ=1.59) was applied to the response to obtain a better quadratic model fitting. A stepwise automatic reduction algorithm was used to remove insignificant terms (95 % significance). The ANOVA table for layer thickness is given in Table 5.17. A definition of the statistical values which helps to analyse ANOVA results is described in Appendix B.

The model was found to be significant (p <0.0001) and the lack of fit insignificant. The R^2 values were very close to 1, the difference between adjusted and predicted R^2 was smaller than 0.2 and there was an adequate signal to noise ratio (Adeq. Precision>4). In view of this it can be concluded that the model adequately fitted the experimental data obtained.

Table 5.17. ANOVA table for layer thickness (HA reference series)

Source	SS	MS	F-value	Prob>F (p)	Significance
Model	54535.93	9089.32	95.41	< 0.0001	significant
A-PG flow Rate	20792.96	20792.96	218.27	< 0.0001	
B-S.d.	1633.18	1633.18	17.14	0.0020	
C-Feed rate	26843.81	26843.81	281.79	< 0.0001	
AC	3432.30	3432.30	36.03	0.0001	
B^2	1236.78	1236.78	12.98	0.0048	
C^2	694.19	694.19	7.29	0.0223	
Lack of fit	722.80	120.47	2.10	0.2470	not significant
R^2	0.9828		**Pred R^2**		0.9506
Adj R^2	0.9725		**Adeq Precision**		37.268

The layer thickness was found to be affected linearly by the plasma gas flow rate (A) and quadratically by the stand-off distance (B^2) and the HA feed rate (C^2). The interaction between the plasma gas flow rate and the HA feed rate (AC) was found to have an effect on the response too. The equation modelling the layer thickness in terms of the actual factors was:

$$y' = y^{1.59} = -1231.1 + 8.6x_1 + 519.1x_2 + 72x_3 - 2.4x_1x_3$$
$$-68.5x_2^2 + 3.2x_3^2$$

Eq. 5.1

where y is the modelled response (layer thickness, μm), x_1 is the plasma gas flow rate (slpm), x_2 is the s.d. (cm) and x_3 is the HA feed rate (g/min).

Figure 5.50a shows the predicted values plotted against the actual values measured in the experiments. It shows that all the experimental points lie close to the line which represents actual values = predicted values, which means that the layer thickness data is accurately predicted by the model. The perturbation plot, which explains the sensitivity of the layer thickness to the significant factors, is shown in Figure 5.50 b. The greater factor slope indicates the greater sensitivity of the response to this factor; in this case the layer thickness is more sensitive to the amount of HA fed into the system followed by the plasma gas flow rate.

Figure 5.50. Layer thickness model: a) Predicted vs. Actual plot and b) Perturbation plot at central point value for HA reference series

An increase in the thickness was observed when the amount of HA powder fed into the system increased, whatever the plasma gas flow rate. The layer thickness was found to decrease when increasing the plasma gas flow rate, which is consistent with the fact that particles travelling faster (greater plasma gas flow rate) should melt less and are more likely to bounce-off when they hit the coating. The maximum layer increment, which indicates optimal deposition efficiency, was found for a stand-off distance of 3.8 cm, whatever the plasma gas flow rate and the HA feed rate. The effect of the interaction between the plasma gas flow rate and the powder feed rate on the response at a stand-off distance of 3.8 cm is shown in Figure 5.51. A maximum layer thickness occurred at the lowest plasma gas flow rate (30 slpm) and the maximum HA feed rate (9 g/min), and a minimum layer thickness occurred for 42 slpm and 5 g/min respectively.
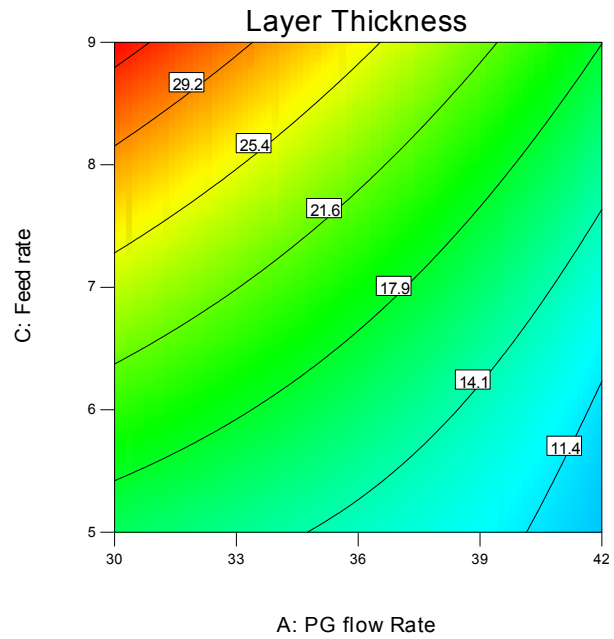
Figure 5.51. Plasma gas flow rate – HA feed rate interaction for layer thickness model (HA reference series)

The model prediction for the interaction AC was proven by examining the cross sections of the coatings sprayed at a stand-off distance of 4 cm (Figure 5.52). The thinner sample HA6 (Figure 5.52a) was sprayed at the predicted worst AC combination (A=42 slpm and C=5 g/min) whereas the thicker sample HA7 (Figure 5.52b) was sprayed at the predicted best AC combination (A=30 slpm and C=9 g/min).
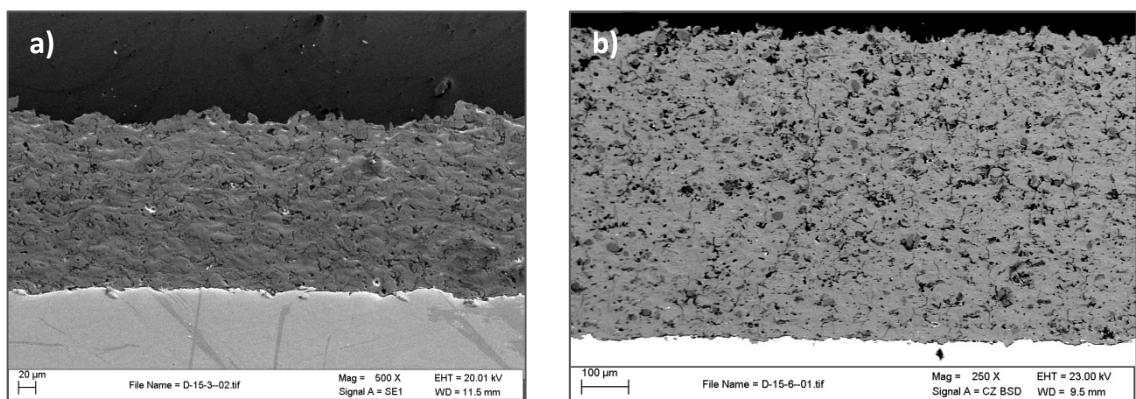
Figure 5.52. Cross sections of samples sprayed at a stand-off distance of 4 cm: a) HA6 (A=42 slpm, C=5 g/min) and b) HA7(A=30 slpm, C=9 g/min)

134

Once the statistical model was established, a statistical optimisation was carried out to determine the combination of factors which led to an optimal layer increment. There were 5 statistical solutions to obtain a maximum thickness of 32.9 µm/layer, which is close to the desired value found in literature (30 µm/layer). All the solution found were for a plasma gas flow rate of 30 slpm and a HA feeding rate of 9 g/min; the stand-off distance ranged between 3.76 and 3.80. The positioning of the stand-off distance has accuracy in the range of millimetres, and therefore the only possible solution in practical terms was 3.8 cm.

5.3.2. Roughness of HA reference series

The roughness was measured following the procedure detailed in Section 4.6.3. The roughness results, which ranged between 5.49-6.47 µm, are shown in Figure 5.53. A statistical model was made to establish the effect of the factors on this response. However, the results of the model have to be interpreted with caution as it can be also seen that the standard deviations of the centre points were nearly as large as the variations produced by different combinations of factors.
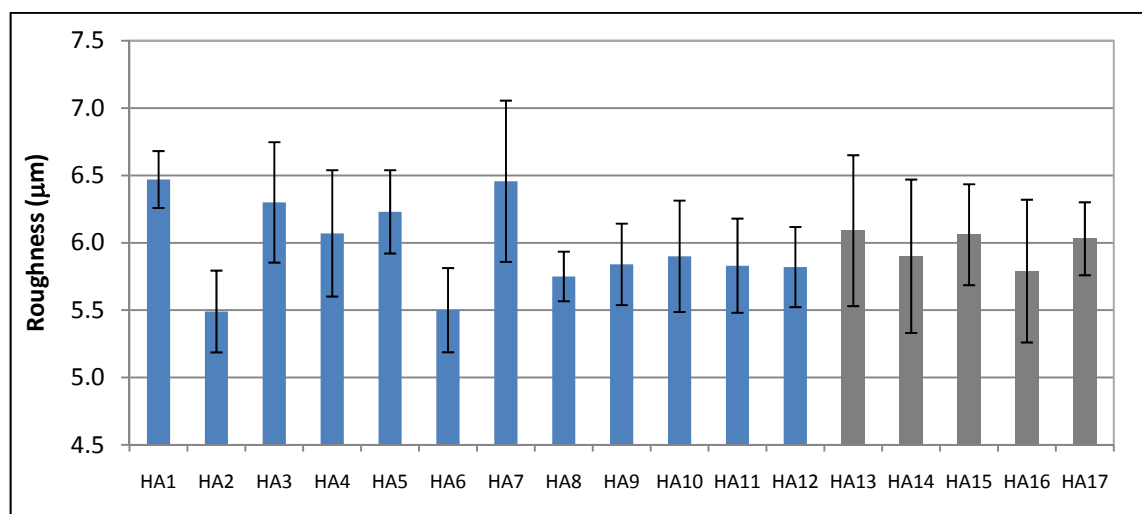
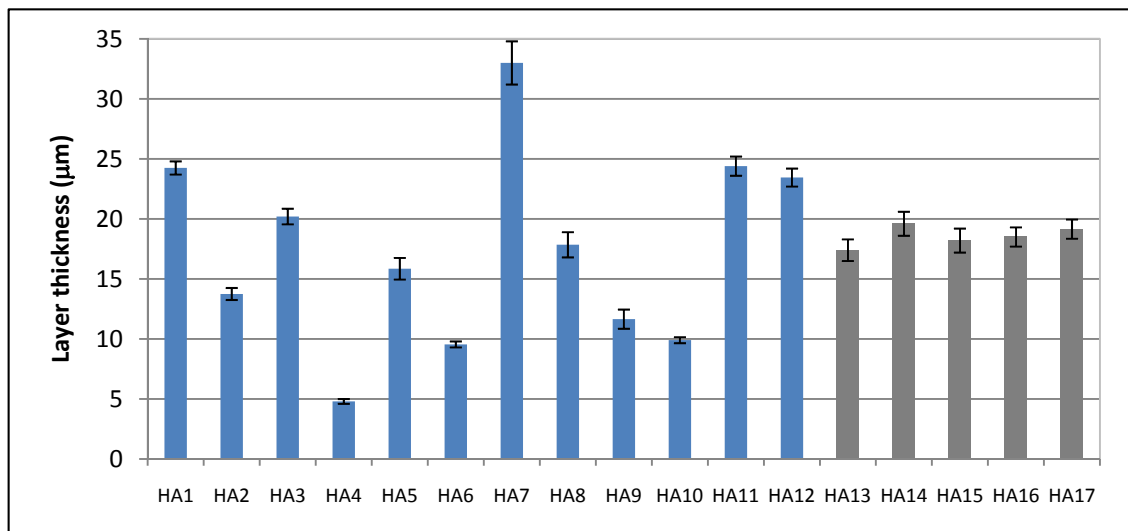**Figure 5.53.** Roughness results for HA reference series

A power transformation (y'=y$^\lambda$, λ=-2.28) was applied to the response to obtain a better 2FI (two factor interaction) model fitting. A stepwise automatic reduction algorithm was used to remove insignificant terms (95 % significance). The ANOVA table for roughness is given in Table 5.18. A definition of the statistical values which helps to analyse ANOVA results is described in Appendix B.

Table 5.18. ANOVA table for roughness (HA reference series)

Source	SS	MS	F-value	Prob>F (p)	Significance
Model	4.542E-5	1.514E-5	18.42	<0.0001	significant
A-PG flow Rate	3.723E-5	3.723E-5	45.30	<0.0001	
B-S.d.	1.684E-6	1.684E-6	2.05	0.1759	
AB	6.506E-6	6.506E-6	7.92	0.0146	
Lack of fit	7.196E-6	8.795E-7	1.27	0.4385	not significant
R^2	0.8096		**Pred R^2**		0.5970
Adj R^2	0.7656		**Adeq Precision**		15.611

The model was found to be significant ($p < 0.0001$) and the lack of fit insignificant. The R^2 value was higher than the recommended value of 0.6 [103], the difference between adjusted and predicted R^2 was smaller than 0.2 and there was an adequate signal to noise ratio (Adeq. Precision>4). The roughness was found to be linearly affected by the plasma gas flow rate (A). The interaction between the PG flow rate and the stand-off distance (AB) was found to have an effect on the response too. The stand-off distance (B) was included to ensure the statistical heredity of the model.

Figure 5.54a shows the predicted values plotted against the actual values measured in the experiments. This plot shows that all the experimental points lie around the line. The perturbation plot (Figure 5.54b) shows that the factor having major influence on the roughness is the plasma gas flow rate (A), which was also found in other research [103]. The effect of factor B is insignificant compared to the large standard deviations in the measurements and, therefore, this effect was not statistically studied.

The roughness was found to decrease when increasing the plasma gas flow rate. This trend was opposite to that reported for conventional plasma spraying systems [103, 225], where a decrease of roughness was found to be caused by a greater melting degree of the particles travelling at lower plasma gas flow rates. On the other hand, the results obtained in this research indicate that the kinetic energy of the impacting particles played a more important role on decreasing the roughness than that of the degree of melting of the particles.
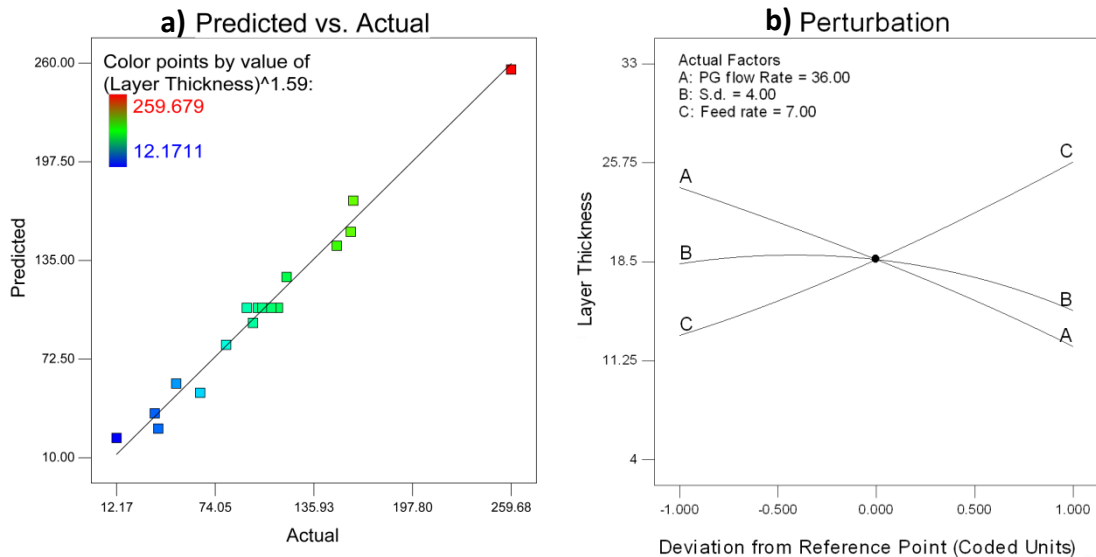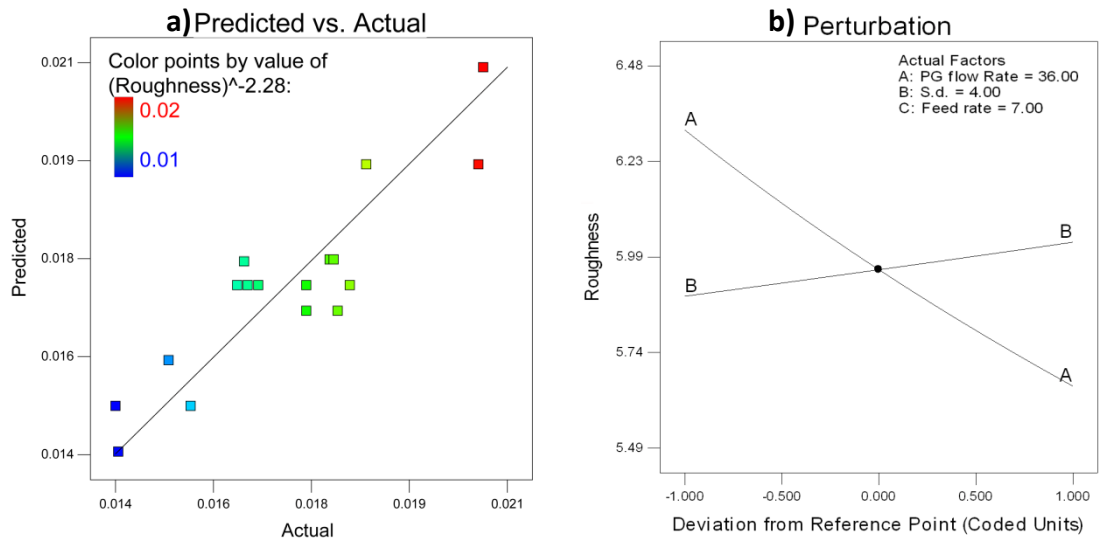
Figure 5.54. Roughness model: a) Predicted vs. Actual plot and b) Perturbation plot at central point value for HA reference series

Figure 5.55 shows the surface of two samples sprayed at different plasma gas flow rates (HA7 @ 30 slpm and HA8 @ 42 slpm), but same stand-off distance (4 cm) and HA feeding rate (9 g/min). It can be noticed that they are not significantly different. In fact, the little range of variation of average roughness observed for this series together with the large standard deviations, justify the selection of the mean of the 17 experiments (6 μm) as a roughness reference value for this series.
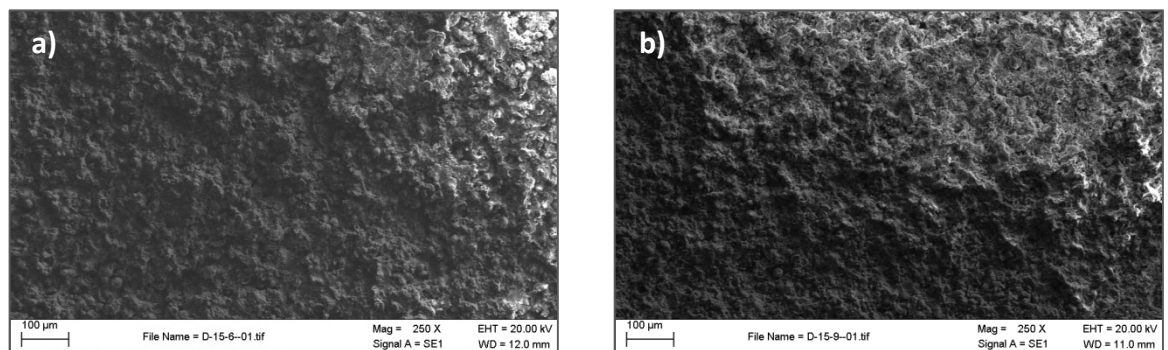
Figure 5.55. Surface images of the samples: a) HA7 (30 slpm) and b) HA8 (42 slpm)

5.3.3. Crystallinity of HA reference series

The crystallinity was measured using the XRD pattern (2θ= 20-60°, 5 sec/step, 0.02 step size) following the procedure detailed in Section 4.6.4. The results, which ranged between 82.8% and 89.7%, are presented graphically in Figure 5.56. By examining this data it is clear that the higher degrees of crystallinity correspond to the samples sprayed at the highest plasma gas flow rates (HA2, HA4, HA6 and HA8). A higher plasma gas flow rate reduces the in-flight time of the powder particles and consequently their melting degree. This indicates that the main source of crystallinity was that of the original powder. Samples sprayed at the lowest flow rate experienced a higher melting degree and presented greater amorphous content due to the rapid cooling on the substrate. It can be stated that the process repeatability in terms of crystallinity was adequate. A more detailed analysis was made in the following during the study of the statistical model for this response.
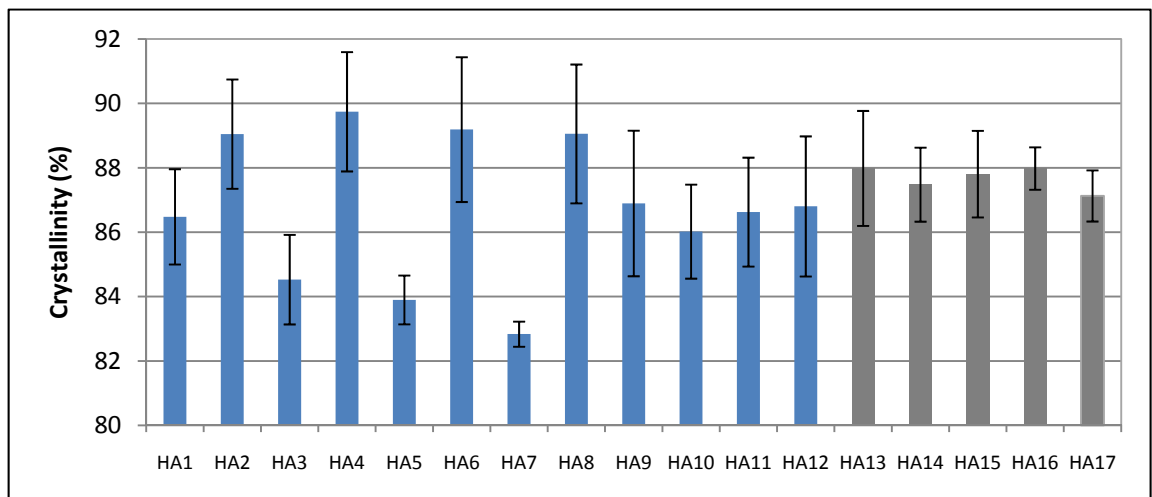
Figure 5.56. Crystallinity results for HA reference series

A power transformation ($y'=y^{\lambda}$, λ=3) was applied to the response to obtain a better quadratic model fitting. A stepwise automatic reduction algorithm was used to remove insignificant terms (95 % significance). The ANOVA table for crystallinity is given in Table 5.19. A definition of the statistical values which helps to analyse ANOVA results is described in Appendix B.

Table 5.19. ANOVA table for crystallinity (HA reference series)

Source	SS	MS	F-value	Prob>F (p)	Significance
Model	2.758E+10	5.516E+10	38.69	<0.0001	significant
A-PG flow Rate	2.365E+10	2.365E+10	165.87	<0.0001	
B-S.d.	2.180E+8	2.180E+8	1.53	0.2420	
C-Feed rate	2.415E+7	2.415E+7	0.17	0.6886	
AB	8.824E+8	8.824E+8	6.19	0.0302	
C^2	2.806E+9	2.806E+9	19.68	0.0010	
Lack of fit	1.282E+9	1.832E+8	2.56	0.1907	not significant
R^2	0.9462		**Pred R^2**		0.8182
Adj R^2	0.9217		**Adeq. Precision**		20.560

The model was found to be significant (p < 0.0001) and the lack of fit insignificant. The R^2 value was close to 1, the difference between adjusted and predicted R^2 was smaller than 0.2 and there was an adequate signal to noise ratio (Adeq. Precision>4). In view of the above, it can be concluded that the model properly fitted the experimental data obtained.

The crystallinity was found to be affected linearly by the plasma gas flow rate (A) and quadratically by the HA feed rate (C^2). The interaction between plasma spray flow rate and s.d. (AB) was found to be significant too. The rest of the parameters (B and C) were included in the model to maintain the heredity. The equation modelling the crystallinity in terms of the actual factors was:

$$y' = y^3 = 7.9 - 10741.5x_1 - 1.9 \cdot 10^5 x_2 + 89218.7x_3 + 4950.9x_1x_2 - 6434.8x_3^2$$

Eq. 5.2

where y is the modelled response (crystallinity, %), x_1 is the plasma gas flow rate (slpm), x_2 is the s.d. (cm) and x_3 is the HA feed rate (g/min).

The Predicted vs Actual plot (Figure 5.57a) shows that the crystallinity data is very well predicted by the model. The perturbation plot (Figure 5.57b) shows that the factor having major influence on the crystallinity is the plasma gas flow rate.
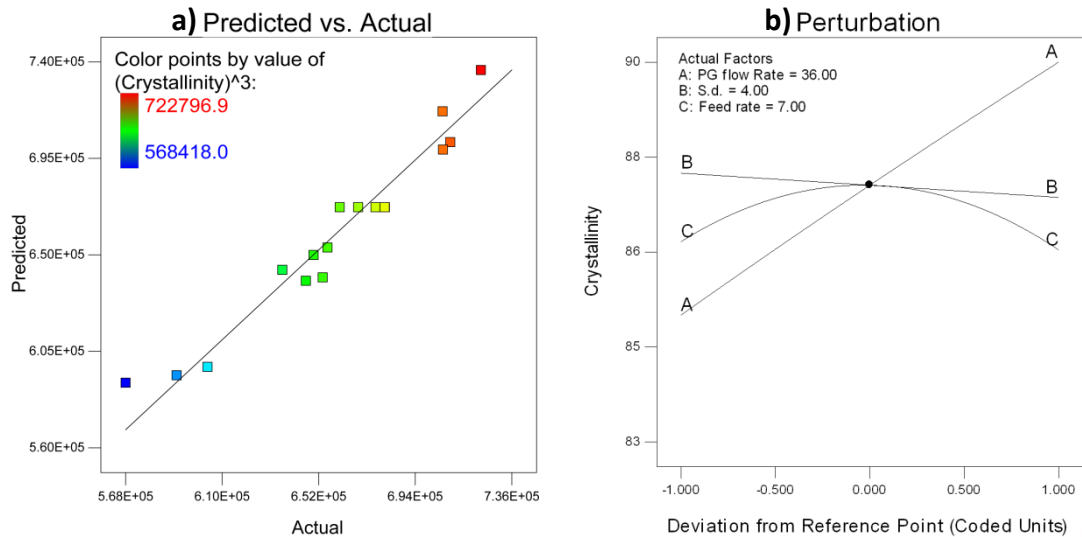
Figure 5.57. Crystallinity model: a) Predicted vs. Actual plot and b) Perturbation plot at central point value for HA reference series

The crystallinity was found to increase when increasing the plasma gas flow rate. This indicates that the main source of crystallinity came from the original powder particles; particles travelling faster through the plume (smallest dwell time) due to greater plasma gas flow rate melt to a lesser degree maintaining higher crystallinity.

Statistically, there was a maximum of crystallinity at the centre point of the feeding rate (7 g/min) whatever the value of the plasma gas flow rate. However, the variation in crystallinity for the different feeding rates is not significant compared to the standard deviations found if the other factors are the same.

The interaction between the plasma gas flow rate and the stand-off distance for a HA feeding rate of 7 g/min can be seen in Figure 5.58. Upon analysis of the contour it can be noted a minimum crystalline content occurring for a plasma gas flow rate of 30 slpm and a stand-off distance of 4.5 cm (sample HA3). The particles travelling slower at this plasma gas flow rate together with the larger stand-off distance increased the particle dwell time and thus the melting degree of the particles resulting in a greater decrease in crystallinity. On the other hand, a maximum crystallinity occurs for a plasma gas flow rate of 42 slpm and a theoretical stand-off distance of 4.5 cm (sample HA4). However, it can be also noticed that the difference in crystallinity along the different stand-off distances at this plasma gas flow rate value was 0.5%, which was

140

considered insignificant. The smaller dwell time of particles at a plasma gas flow rate of 42 slpm prevent them from undergoing a great amorphisation and, therefore, particles maintained a higher crystalline content. In addition, the influence of the stand-off distance in crystallinity at plasma gas flow rates between 36 and 41 slpm seemed to be insignificant as the crystallinity isolines were found to be nearly straight lines.
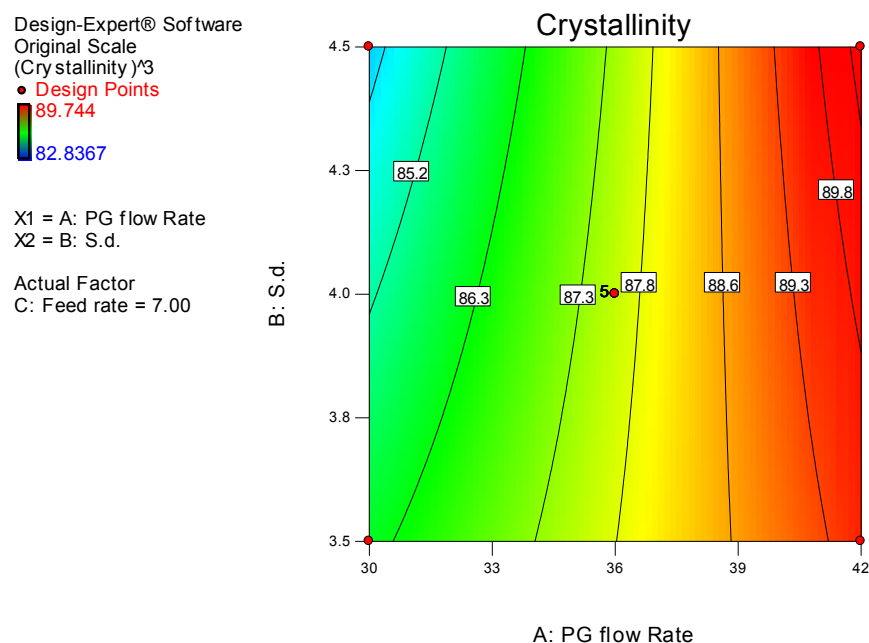
Figure 5.58. Plasma gas flow rate – stand-off distance interaction for crystallinity model (HA reference series)

Figure 5.59 shows the XRD patterns of the samples HA3 and HA4, where a greatest amorphous content of the sample HA3 compared to that of sample HA4 can be noticed. It can also be notice a little texture effect (change in relative intensity between two peaks) on the samples which is more noticeable for sample HA3. This effect indicates that a preferential crystallographic orientation is taking place on the coatings during the processing. The texture effect has also been reported by other authors [233] for low energy plasma systems. Also it has to be highlighted that the texture effect affects the crystallinity measurement as it decreases the intensity of some peaks. Therefore, actual crystallinity values would be always a little higher than the ones reported in this study. As future work texture detailed studies and quantitative analysis of crystallinity using Rietveld methods could be conducted.
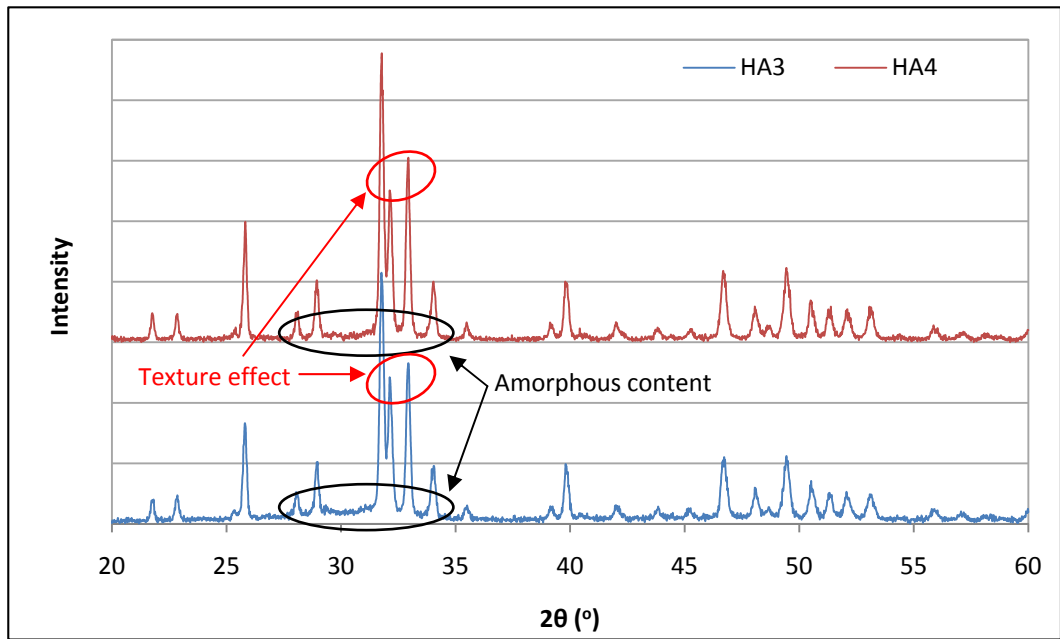
Figure 5.59. XRD patterns of the HA3 and HA4 samples

Once the statistical model was established, a statistical optimisation was carried out to determine the combination of factors which led to a maximum crystallinity. There were 26 statistical solutions to obtain a maximum crystallinity of over 89.7 %. All the solution found were for factor combinations in the following ranges: plasma gas flow rate of 41-42 slpm, stand-off distance of 3.8-4.5 cm and HA feeding rate of 6-8.2 g/min.

5.3.4. Purity of HA reference series

No traces of other calcium phosphates were found studying the XRD patterns of the 17 samples, even though detailed XRD scans were performed around the β-TCP main peak (2θ = 31.78^o) and the OA main peak (2θ = 53.2^o) of the samples sprayed at 30 slpm PG flow rate (greatest amorphous content) and one of the centre point samples (HA14) (Figure 5.60 and Figure 5.61). Therefore, no statistical study was conducted for purity of this series.
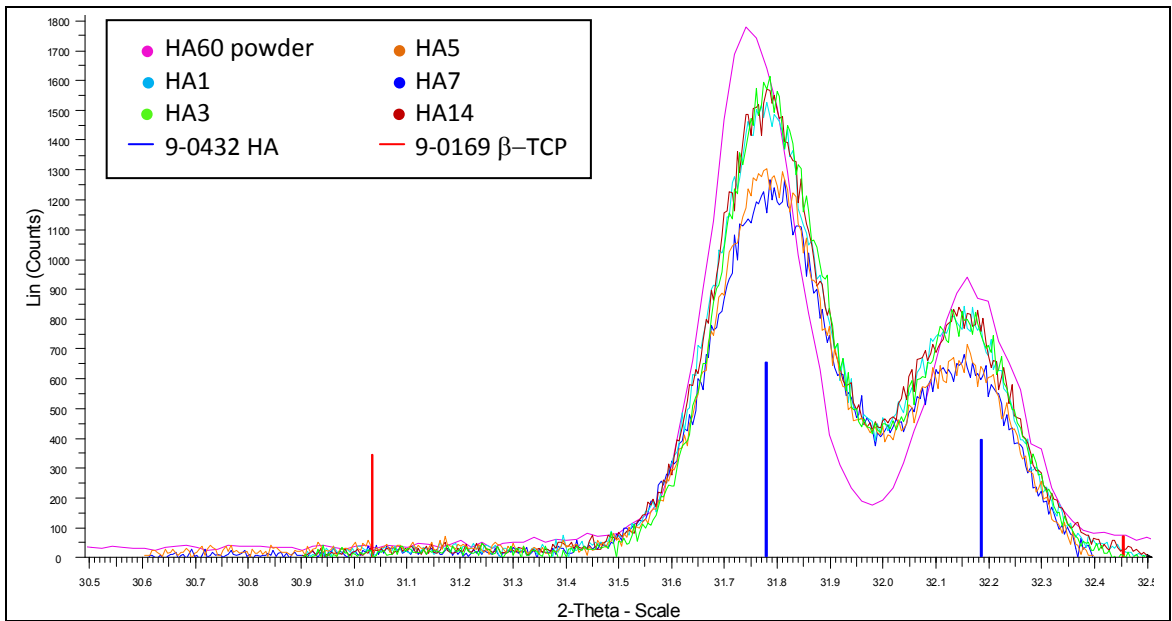
Figure 5.60. Detailed XRD scans around main β-TCP peak for HA reference series
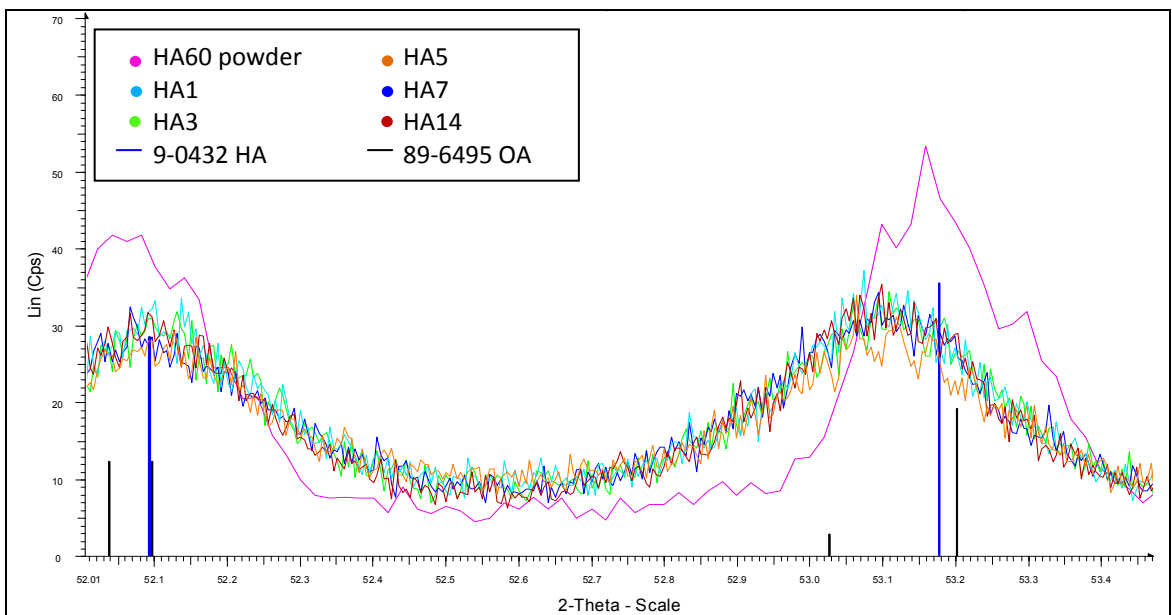
Figure 5.61. Detailed XRD scans around main OA peak for HA reference series

However, it has been reported that X-ray diffraction is not an adequate technique to detect HA dehydroxylation [218]. FTIR studies, following the procedure outlined in Section 4.6.5., were performed on a selected set of samples comprising of samples processed under the hottest and the coldest conditions: the three samples with greater amorphous content (HA7, HA5 and HA3), the two most crystalline samples (HA4 and HA6) and one of the centre points (HA13). The FTIR spectra of these samples,

compared with the HA powder spectra are shown in Figure 5.62. The powder spectrum clearly showed the peaks corresponding to the OH⁻ stretching and flexural vibration modes. On the other hand, the coatings presented different degrees of dehydroxylation showing mainly the peak corresponding to the stretching vibration mode (3571 cm⁻¹).

Samples sprayed at 42 slpm (HA4 and HA6) and the central point sample (HA13) underwent less dehydroxylation. As observed, the stretching mode peak was similar to that of the powder and still included a little peak corresponding to the OH⁻ flexural mode. The most dehydroxylated sample was found to be one of those produced at a plasma gas flow rate of 30 slpm (HA5).
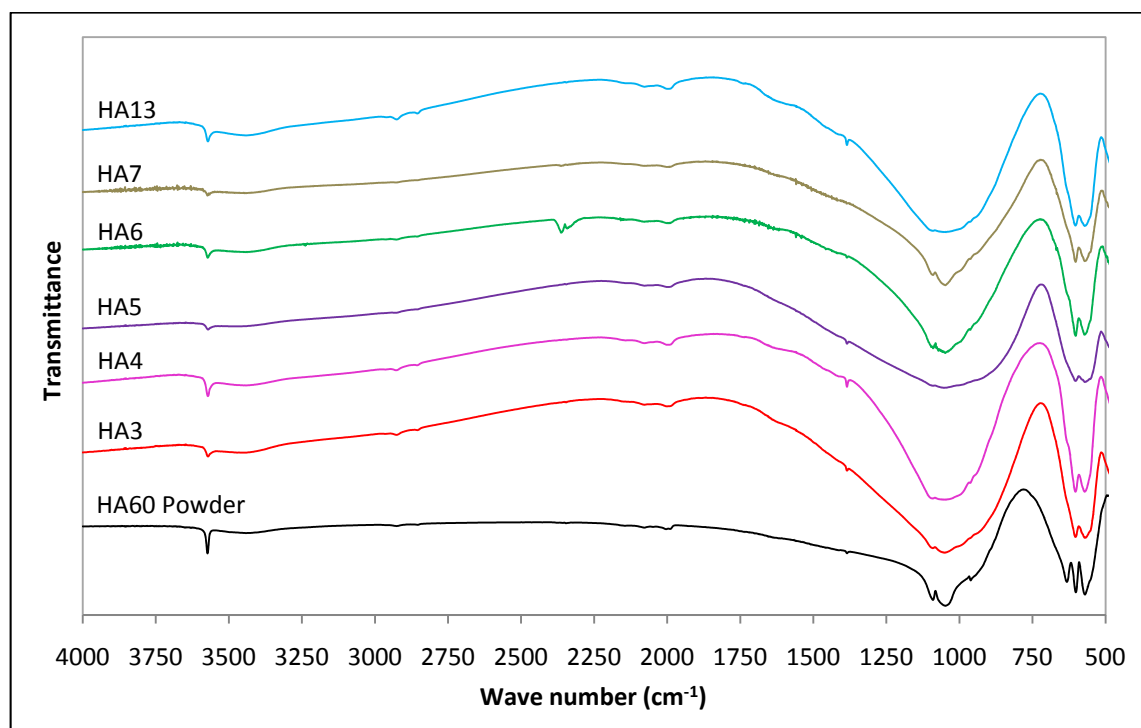
Figure 5.62. FTIR spectra of selected samples (HA reference series)

5.3.5. Porosity on HA reference series

The porosity was measured following the procedure detailed in Section 4.6.6. The results for this response (Figure 5.63) were studied with caution for several reasons:

1. During the metallographic preparation stage some porosity can be hidden or some unmelted particles can be pulled off the coating [234]. This fact makes it difficult to talk about absolute porosity of the coatings, but it is useful in terms of comparison between samples, which have been prepared following the same metallographic procedure. However, samples were prepared in groups of six coatings; hence some differences may arise between the different batches.

2. The quality of the images, their brightness and their contrast can affect the precision of the MATLAB routine to calculate the percentage of porosity.

For all these reasons, this study aimed only to study the approximate range of porosity of this series. The porosity range of variation was found to be 2.5-6% which, in any case, lies far from the required porosity for tissue engineering applications. Therefore, no statistical model was conducted and the reference porosity for this series was taken as the mean of the 17 experiments (4.2%).
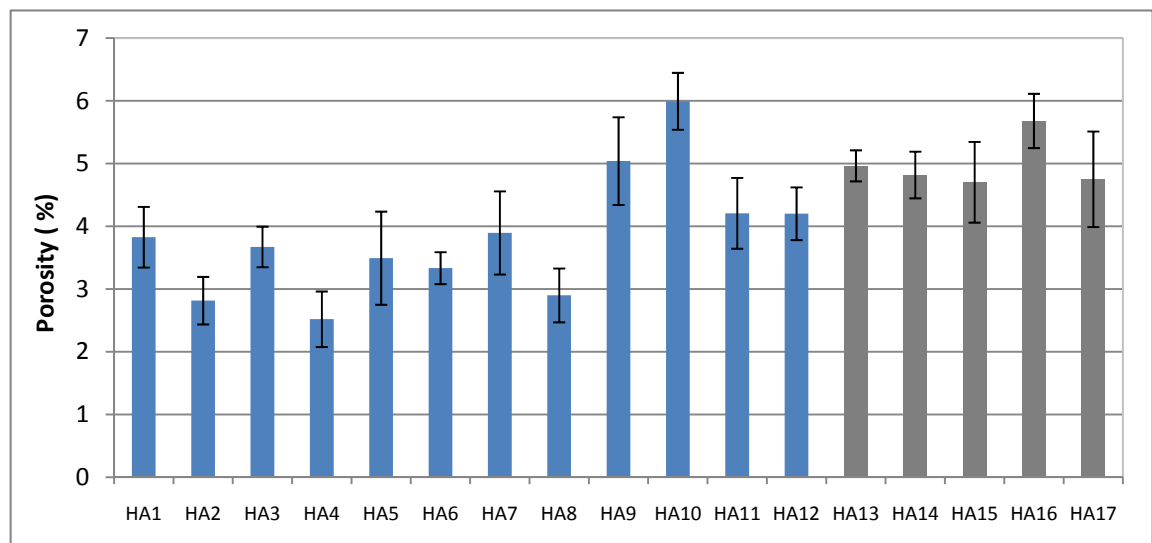
Figure 5.63. Porosity results for HA reference series

Upon analysis of the bar chart it can be seen that the samples sprayed at the highest flow rate have a lower degree of porosity. The opposite has been reported by other authors using conventional plasma spraying [225, 226]. An explanation for this disparity may lie in the difference in energy of both plasma spraying systems. In a conventional system particles are usually melted to a higher degree with their in-flight

properties (temperature and velocity) being significantly affected by the plasma gas flow rate. In general terms, the higher the plasma gas flow rate the faster the particles travel through the plume, resulting in a shorter dwell time and a lower melting degree. This causes less deformation in particles when they strike the substrate, resulting in an increase in porosity. On the contrary, the LEPS system does not have enough energy to fully melt the particles, and thus an increase in kinetic energy may result in both the bouncing-off of unmolten particle cores and a higher density. This explanation is supported by the fact that several unmelted particles can be seen in the cross sections of all the samples produced within this series, and that a decrease in deposition efficiency was observed when increasing the plasma gas flow rate. The SEM images of the cross section of two samples (HA3 and HA10) with different grades of porosity are shown as an example in Figure 5.64.
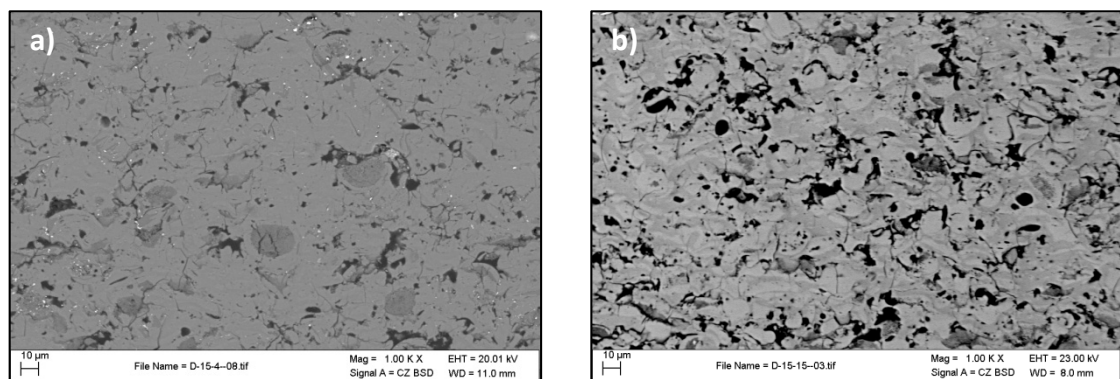
Figure 5.64. Porosity of: a) HA3 and b) HA10 samples

5.3.6. Mechanical properties of HA reference series

Three mechanical properties (micro hardness, elastic modulus and fracture toughness) were obtained using the indentation technique following the procedure indicated in Section 4.6.7. Figure 5.65 shows the Vickers and Knoop indentations made on sample HA12.
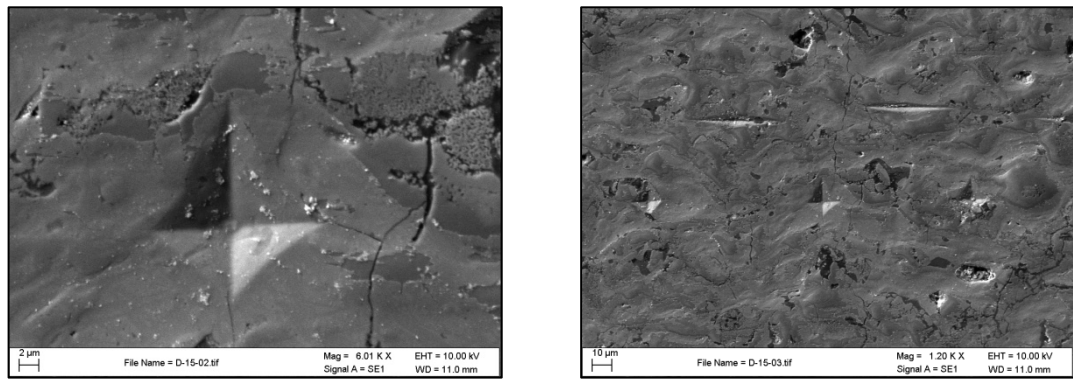
Figure 5.65. Indentations in sample HA12: a) Vickers hardness 50g and b) Knoop hardness

The results for microhardness Vickers at 50 grams load, which ranged from 244 to 351, are shown in Figure 5.66a. The standard deviation for each sample was large; this is quite common in thermally sprayed coatings because of their anisotropic structure and the presence of porosity but may be increased due to lack of cohesion[5] within the coatings. Even though the design was replicated to improve the accuracy of the model, the ANOVA results suggested that the mean value predicts the hardness better than the model. The same applied to the Young's modulus (Figure 5.66b) and fracture toughness (Figure 5.66c), ranging between 2.9-4.8 GPa and 0.52-0.71 MPa·m$^{1/2}$ respectively, which presented even larger standard deviations than hardness. It should be noticed that sample HA13 was withdrawn from the analysis of the Young's Modulus as it is very different from the other centre points and, thus, it is considered an outlier.

Therefore, the reference mechanical properties for subsequent comparison were taken as the means of the series (307 Hv, 4.1 GPa and 0.63 MPa·m$^{1/2}$). However, it can be noticed that as a general trend the coatings which presented the lowest mechanical properties were those sprayed at the greatest plasma gas flow rates. As was observed before, this was also the general trend for porosity. These trends seems to indicate that the density of the layer is greater at higher plasma gas flow rate (lower porosity) but, that the lower melting degree of the particles makes them to stick to each other in lesser degree and, therefore, decrease the cohesion of the layer (lower mechanical properties).

---

[5] Cohesion: Interlamellar bonding
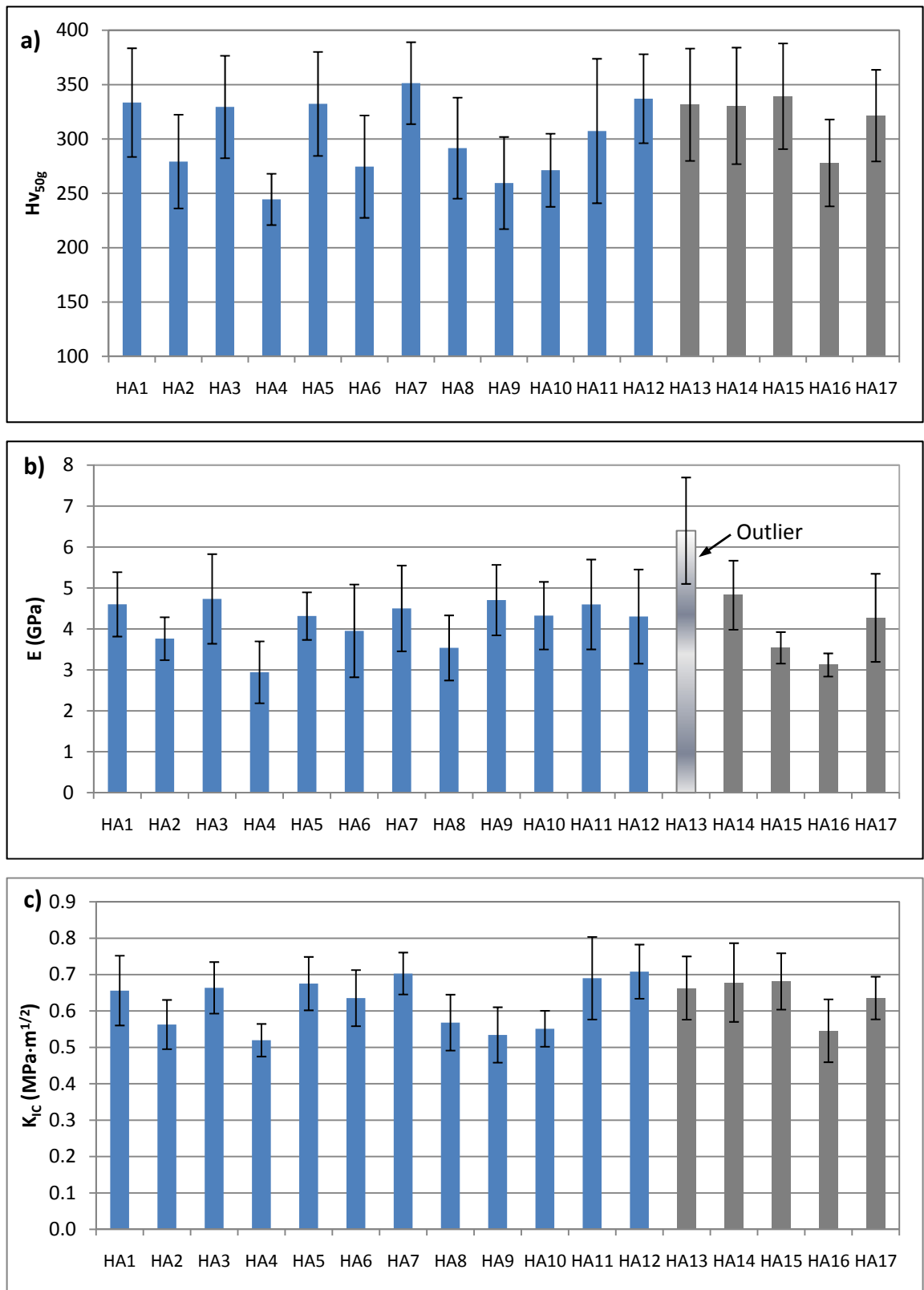
Figure 5.66. Mechanical properties by indentation technique (50 grams): a) Vickers hardness, b) Young's modulus and c) fracture toughness (HA reference series)

5.3.7. Summary of HA reference series

At low plasma gas flow rates the particles travelled slower in the plasma plume, thus the particles melted more and struck the substrate with less kinetic energy. The higher thermal input resulted in increases in both the amorphous content and the extent of dehydroxylation of the HA powders being sprayed, and these changes also occurred in the coatings being deposited. This degree of melting of the particles also increased the HA deposition efficiency as the number of particles bouncing-off the substrate was decreased. Finally, the greater number of melted particles promoted the formation of more cohesive coatings, thus, increasing the hardness of the coating. In addition, the reduced kinetic energy on the impact against the substrate led to rougher surfaces and greater porosity in the deposits. These trends, which apply to the LEPS system, have been reported to be the opposite for conventional plasma spraying systems [103, 225].

As expected, the layer thickness increased when the feeding rate increased. A maximum layer thickness was obtained for a plasma gas flow rate of 30 slpm, a stand-off distance of 3.8 cm and a feeding rate of 9 g/min. Crystallinity has been found to be insensitive to the variation of the stand-off distance when using a plasma gas flow rate in the range 36-41 slpm. For greater plasma gas flow rates, the highest crystallinity was obtained for the upper limit used for s.d. and the opposite was found on the other extreme for the lower plasma gas flow rate. The summary of the properties measured for this series is shown in Table 5.20.

Table 5.20. Range of variation on the properties measured for HA reference series

Response	Measured Range
Layer thickness, μm	4.8 – 33.0
Roughness, μm	5.49 – 6.47
Crystallinity, %	82.8 – 89.7
Porosity, %	2.5 – 6.0
Vickers Hardness, HV	244-351
Young's Modulus, GPa	2.9-4.8
Fracture toughness, MPa$\cdot$m$^{1/2}$	0.52-0.71

In order to produce the composite coating series, the reference parameters had to be set. The selected value for the plasma gas flow rate was the centre point (36 slpm). Lower flow rates have been shown to result in the degradation of HA, and so polymeric second phases would be degraded to a greater extent, perhaps leading to cytotoxic by-products. Greater plasma gas flow rates were found to significantly decrease the deposition efficiency leading to thinner coatings. In addition, coating crystallinity seems to be unaffected by the stand-off distance at a plasma gas flow rate of 36 slpm, which is an advantage if taking into account that the stand-off distance set-up is the most inaccurate of the three factor set-ups. The selected feed rate was 9 g/min because it leads to a maximum layer thickness that is required to fabricate thick coatings and, in a near future, the free-standing components (scaffolds).

Finally, a statistical optimisation was carried out to find the stand-off distance which maximise the responses in the following order of importance: crystallinity (3+), layer thickness (2+) and roughness (1+) for a plasma gas flow rate of 36 slpm and a HA feeding rate of 9 g/min. As observed in Table 5.21, the desirability of the two solution obtained from the optimisation was 0.557. This low value was caused by the opposite trends of crystallinity and layer thickness/roughness with the variation of the plasma gas flow rate. Based on these results and taking into account that the stand-off distance set-up had precision in the order of millimetres, the s.d. solution adopted was 3.8 cm. Therefore, the selected set of parameters to proceed in the manufacturing of the composites series were: A=36 slpm, B=3.8 cm and C=9 g/min.

Table 5.21. Stand-off distance set-up: optimisation goals and solutions

Parameter	Goal (Importance)	Lower Limit	Upper Limit
A: PG flow Rate	is equal to 36	30	42
B: S.d.	is in range 3.5-4.5	3.5	4.5
C: Feed rate	is equal to 9	5	9
Layer Thickness	maximise (2+)	4.8	33
Roughness	maximise (1+)	5.49	6.47
Crystallinity	maximise (3+)	82.8	89.7

Solutions	A	B	C	Layer Thickness	Roughness	Crystallinity	Desirability
1	36	**3.84**	9	26.1	5.93	86.5	0.557
2	36	**3.79**	9	26.1	5.92	86.5	0.557

Table 5.22 shows the responses for the selected three factors, which set the basis of comparison for the composite series presented in the following sections. It is pertinent to note that the reference values for the responses which were statistically studied are those predicted by the respective models, whereas the rest of the reference values are set as the means of the series.

Table 5.22. Responses with the optimum set of parameters (HA reference sample)

Response	Value	Data source
Layer thickness, μm	26.1	Predicted
Roughness, μm	6	Series mean
Crystallinity, %	86.5	Predicted
Porosity, %	4.2	Series mean
Vickers Hardness, HV	307	Series mean
Young's Modulus, GPa	4.1	Series mean
Fracture toughness, MPa·m$^{1/2}$	0.63	Series mean

5.4. HA/PCL composite coatings study

PCL was selected as a second phase to form composite coatings with increased porosity. This polymer was expected to act as a pore former because part of it was due to evaporate during processing and part of it during a post-spray sintering step. It was found during the feasibility tests that severe evaporation occurred during the deposition procedure when the feeding rate of polymer was greater than 0.15 g/min. The coating happened to grow forming columnar structures lacking in stability. A large amount of polymer being evaporated caused the coating to peel off during the deposition process. Therefore, decreasing the polymer feed rate proved to be a solution to improve the stability of the coatings. As the rotation of the feeding plate was already set to its minimum during feasibility tests, a further reduction was achieved by reducing the feeding plate as detailed in Figure 3.3). However, as stated before, the low density of the polymer together with an even smaller feeding rate led to irregular feeding of the polymer in the system. This created inhomogeneity in the coating, which as a result introduced some noise in the statistical models presented at the end of this section.

The LEPS parameters used to produce this series are shown in Table 5.23. They were set based upon the best combination of parameters obtained in the previous section (HA reference series), and also taking into account the observations made during the feasibility tests.

PCL is a very expensive polymer and thus a design with less experimental runs was preferred. A full 2-level factorial design (Table 5.24) was selected, which consisted of 12 experimental runs from which 8 were design points (2^3) and 4 centre points (marked in grey). The design point HP13 (marked in orange) was an extra point, which was not included in the models. For this series the measurements were made at different stages, so blocking was applied to the models in order to minimise the possible effect of environmental working conditions. The properties measured for this series are shown in Table 5.25. It can be noticed that sample HP9 had a very different layer thickness than the other centre points. The reason for this may have been that the polymer partially clogged the injector nozzle during the process, as the layer thickness is close to the HA reference series ones. This sample was the product of an experimental error and was discarded.

Table 5.23. Plasma spray parameters for HA/PCL composite series

Parameter	PCL-LEPS	DOE factor code
Current (Power)	390 A (12 kW)	-
Plasma gas (PG), flow rate	Argon, 36 slpm	-
Carrier gas 1 (CG1), flow rate	Argon, 4.6 slpm	-
Carrier gas 2 (CG2), flow rate	Nitrogen, 10-14 slpm	C
Powder feeding rate 1 – HA60	9 g/min	-
Powder feeding rate 2 – PCL	40-120 mg/min	A
Stand-off distance (s.d.)	3.8 cm	-
Relative gun velocity	20 cm/s	-
Increment y-direction (Δy)	-3 mm	-
Gun configuration[*]	2	-
Injector 1 position	Internal	-
Injector 2 position (d/e/α)	External (<u>17-27mm</u>/13mm/90°)	B
Cooling system	Compressed air @ 6 bar	-

[*] See Appendix A

Table 5.24. Full 2-level factorial design for HA/PCL composite series

Reference name	Run order	Factor A: PCL feed rate (mg/min)	Factor B: Injector distance (mm)[*]	Factor C: CG flow rate (slpm)
HP1	9	40	17	10
HP2	11	120	17	10
HP3	2	40	27	10
HP4	1	120	27	10
HP5	8	40	17	14
HP5	10	120	17	14
HP7	4	40	27	14
HP8	3	120	27	14
HP9	6	80	22	12
HP10	12	80	22	12
HP11	7	80	22	12
HP12	5	80	22	12
HP13	-	650	22	12

[*]The injector distance (d) is measured from the exit of the gun, which was easier from the practical-point of view. The stand-off distance is fixed at 3.8 cm for this series and, therefore it is possible to define the injector distance to the substrate as: d' (mm) = 38 – d.

Table 5.25. Measured properties on HA/PCL reference series

Reference name	Layer Thickness, μm		Roughness, μm		Porosity, %		Vickers Hardness		E, GPa		K_{IC}, MPa·m$^{1/2}$	
	Average	Std. Dev.	Average	Std. Dev.	Average	Std. Dev.	Average	Std. Dev.	Average	Std. Dev.	Average	Std. Dev.
HP1	84.4	1.5	8.28	0.95	4.2	0.6	269	65	3.2	0.7	0.66	0.10
HP2	74.7	1.9	13.51	0.94	4.9	0.9	300	83	3.3	0.4	0.63	0.14
HP3	34.0	0.9	8.23	0.90	7.6	1.4	264	43	2.8	0.5	0.55	0.10
HP4	71.2	3.9	8.28	0.91	5.0	0.6	331	33	3.6	0.6	0.63	0.14
HP5	79.7	1.2	7.76	0.74	5.8	0.7	308	28	2.7	0.4	0.65	0.18
HP5	75.8	2.0	11.89	0.89	5.7	1.0	346	28	3.2	0.3	0.72	0.11
HP7	45.5	0.8	7.93	0.68	5.8	0.5	261	19	2.9	0.6	0.54	0.06
HP8	49.9	3.3	12.20	0.67	7.5	1.4	273	35	2.9	0.3	0.62	0.07
HP9	30.8	2.1	-	-	-	-	-	-	-	-	-	-
HP10	71.2	2.0	9.12	1.08	5.8	0.6	362	34	4.0	0.5	0.78	0.11
HP11	78.6	2.4	9.74	0.85	5.7	0.8	302	65	3.3	0.4	0.59	0.12
HP12	64.2	2.3	9.53	0.96	5.6	0.6	339	58	3.9	0.3	0.62	0.19
HP13	66.5	2.9	35.14	6.14	-	-	-	-	-	-	-	-

5.4.1. Layer thickness of HA/PCL composite series

The layer thickness values obtained following the procedure detailed in Section 4.6.2 are presented graphically in Figure 5.67. The layer thickness of the samples ranged between 34-84.4 µm, which meant an increase in the range of 30-223% with respect to the HA reference layer thickness (26.1 µm). Therefore, it can be stated that the PCL addition significantly increased the coating thickness.

The influence of the parameters on the layer thickness was not straightforward, and it is statistically studied later in this section. However it was noted that 3 out of the 4 samples where the PCL was injected at 27 mm from the gun exit presented the lowest layer thicknesses. As said before sample HP9 was the product of an experimental error and was regarded as an outlier and, therefore, was excluded from the statistical models described in this section.
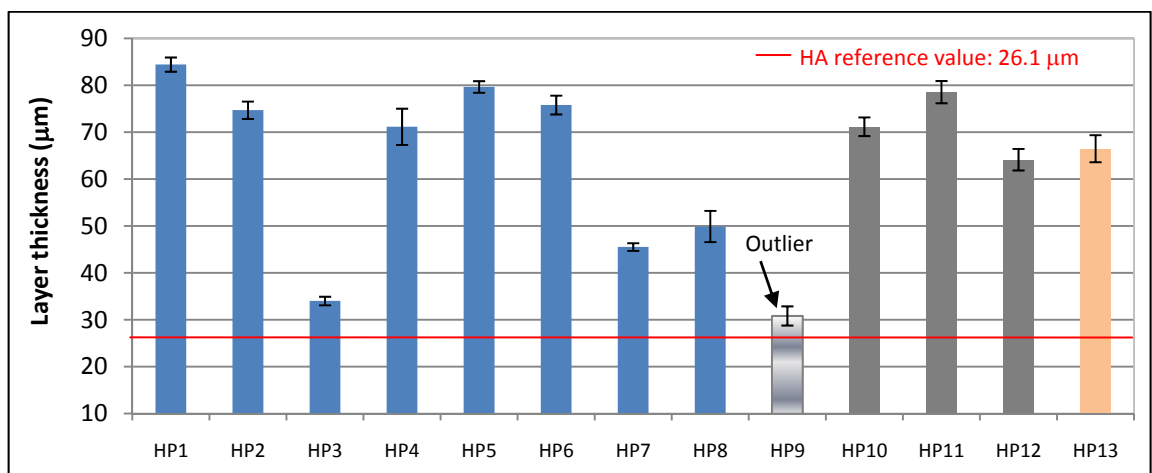
Figure 5.67. Layer thickness results for HA/PCL composite series

A power transformation ($y'=y^{\lambda}$, $\lambda=2.09$) was applied to the response to obtain a better model fitting. A backward automatic reduction algorithm was used to remove insignificant terms (95% significance). The ANOVA table for layer thickness is given in Table 5.26. A definition of the statistical values which helps to analyse ANOVA results are described in Appendix B.

Table 5.26. ANOVA table for layer thickness (HA/PCL series)

Source	SS	MS	F-value	Prob>F (p)	Significance
Model	2.091E+8	6.970E+7	41.56	<0.0001	significant
A-PCL feed rate	3.764E+6	3.764E+6	2.24	0.1462	
B-Injector distance	1.692E+8	1.692E+8	100.81	<0.0001	
AB	3.612E+7	3.612E+7	21.53	<0.0001	
Curvature	6.438E+6	6.438E+6	3.84	0.0609	not significant
Lack of fit	2.861E+7	1.431E+6	0.57	0.8383	not significant
R^2	0.8274		**Pred R^2**		0.7308
Adj R^2	0.8075		**Adeq Precision**		14.418

The model was found to be significant ($p<0.0001$) and the lack of fit not significant. The curvature was not significant, indicating the factor range was adequate. The R^2 value was greater than the recommended value of 0.6 [103], the difference between adjusted and predicted R^2 was smaller than 0.2 and there was an adequate signal-to-noise ratio (Adeq. Precision>4). For these reasons, it can be concluded that the model properly fits the experimental data obtained.

The layer thickness was found to be affected linearly by the injector distance (B) and by the interaction between PCL feed rate and injector position (AB). The factor A was included to maintain the heredity of the model. The equation modelling the layer thickness in terms of the actual factors was:

$$y' = y^{2.09} = 28222.8 - 125x_1 - 1021.8x_2 + 6.1x_1x_2 \qquad \text{Eq. 5.3}$$

where y is the modelled response (layer thickness, μm), x_1 the PCL feed rate (mg/min) and x_2 is the injector distance (mm). It is also possible to obtain the response as a function of the injector distance from the substrate (x_2') by substituting x_2 by (38- x_2') in the formula.

Figure 5.68a shows the predicted values plotted against the actual values measured in the experiments, where all the experimental points lie close to the line, which means

that the layer thickness data was well predicted by the model. Figure 5.68b shows that the PCL injector position has a major effect on the layer thickness.

Figure 5.68. Layer thickness model: a) Predicted vs. Actual plot and b) Perturbation plot at central point value for HA/PCL series

The layer thickness was found to decrease when increasing the injector distance (Figure 5.69) in all cases. However, it can be noticed that the effect of the injector position was greater when the PCL feeding rate was lower (greater slope).
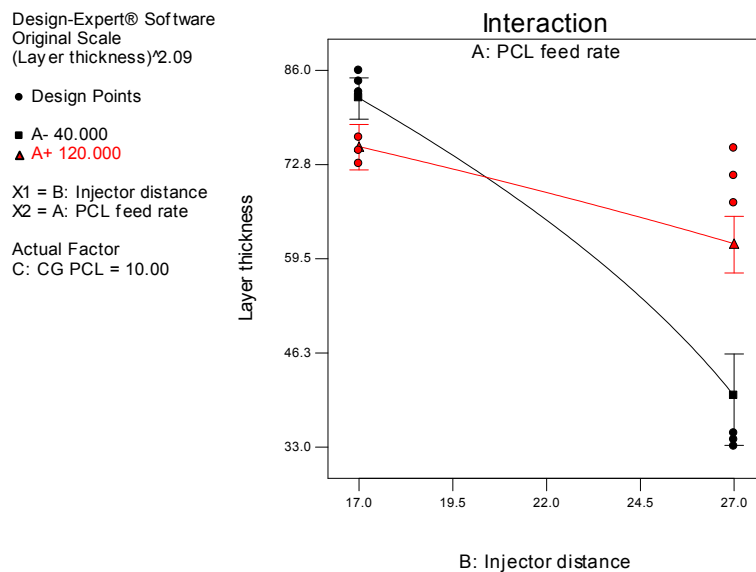
Figure 5.69. Influence of PCL feeding rate-injector distance interaction in layer thickness

The minimum thickness was found to occur for a PCL feeding rate of 40 mg/min when the injector was placed at 27 mm far from the exit of the gun. It seems that the injector was too close to the substrate and the turbulences generated when the plasma gas impinges on the substrate may have prevented the polymer from entering the plume (Figure 5.70). A smaller injector distance (17 mm) allowed most of the polymer to enter the plume, which contributed to the coating build-up increasing the thickness per layer. It has to be highlighted that a maximum layer thickness occurred for a feeding rate of 40 mg/min and not for 120 mg/min. This may have been caused by an inappropriate carrier gas flow rate for the greater feeding rate (120 mg/min) that led to a decrease in deposition efficiency. This fact is proven later during the statistical analysis of roughness.
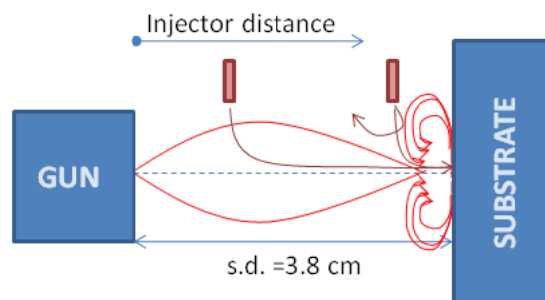
Figure 5.70. Effect of injector distance on PCL trajectories

Figure 5.71 shows the thinnest and thicker coating in the series, which correspond to the samples HP3 and HP1 respectively. It must be highlighted that the only difference between the PSPs used to spray these 2 samples was the injector distance, the remaining parameters being A=40 mg/min and C=10 slpm.
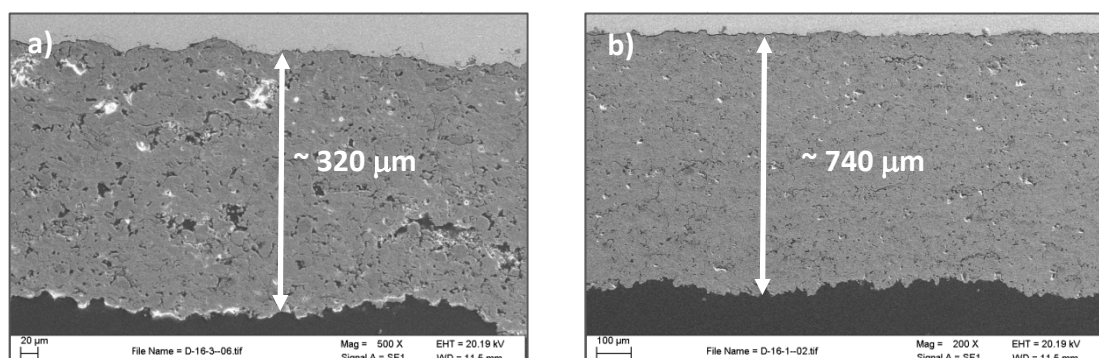
Figure 5.71. Cross sections of: a) the thinnest (HP3) and b) the thickest (HP1) coatings

5.4.2. Roughness of HA/PCL composite series

The roughness results measured following the procedure detailed in Section 4.6.3 are shown in Figure 5.72. The roughness values ranged between 7.76-13.51 μm, which meant an increase in the range of 29-125% with respect to the HA reference roughness (6 μm). As said before sample HP9 was the product of an experimental error and was regarded as an outlier and, therefore, was excluded from the statistical models described in this section. It has to be pointed out that the rougher samples were those with a greater polymer feed rate (120 mg/min) within the design points and the extra point HP13 (650 mg/min). A statistical model was carried out to establish the factors' effect variation on this response in the following.
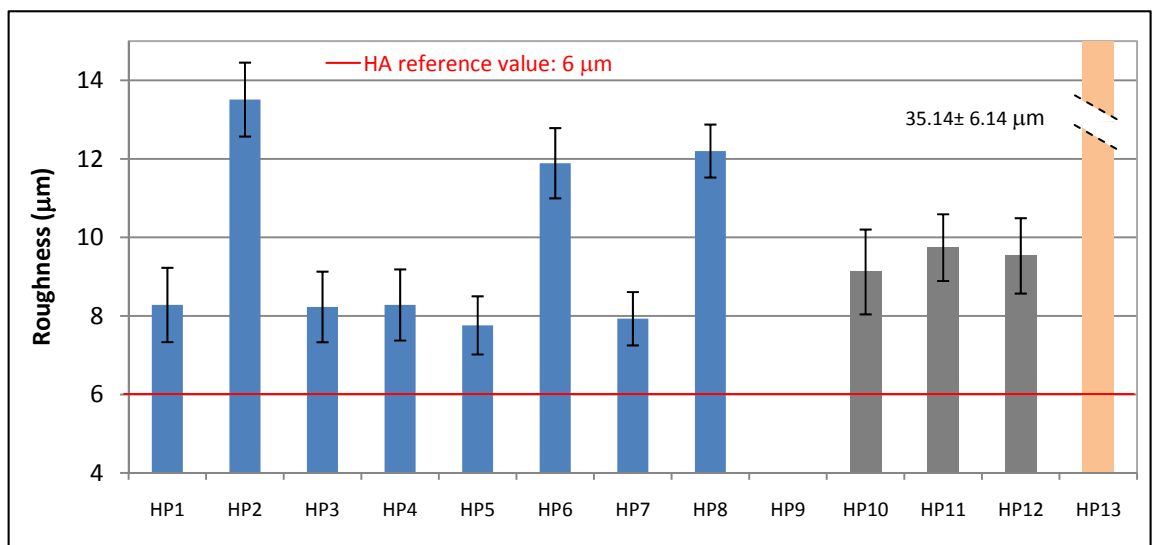
Figure 5.72. Roughness results for HA/PCL composite series

No transformation (y'=y) was applied to this response to obtain a good model fitting. A backward automatic reduction algorithm was used to remove insignificant terms (95% significance). The ANOVA table for roughness is given in Table 5.27. A definition of the statistical values which helps to analyse ANOVA results are described in Appendix B.

The model was found to be significant (p < 0.0001) and the lack of fit not significant. The curvature was not significant, indicating the factor range was adequate. The R^2 value was greater than the recommended value of 0.6, the difference between adjusted and predicted R^2 was smaller than 0.2 and there was an adequate signal-to-

noise ratio (Adeq. Precision>4). For these reasons, it can be concluded that the model properly fits the experimental data obtained.

Table 5.27. ANOVA table for roughness (HA/PCL series)

Source	SS	MS	F-value	Prob>F (p)	Significance
Model	105.9	17.65	23.94	<0.0001	significant
A-PCL Feed Rate	70.41	70.41	95.52	<0.0001	
B-Injector distance	8.55	8.55	11.60	0.0024	
C-CG PCL	0.67	0.67	0.91	0.3505	
AB	10.26	10.26	13.92	0.0011	
AC	4.15	4.15	5.62	0.0265	
BC	11.87	11.87	16.10	0.0005	
Curvature	0.62	0.62	0.84	0.3693	not significant
Lack of fit	14.76	0.87	2.37	0.1460	not significant
R^2	0.8620		**Pred R^2**		0.6895
Adj R^2	0.8260		**Adeq Precision**		12.360

The roughness was found to be affected linearly by the PCL feed rate (A) and the injector distance (B). The two-factor interactions among all three factors were found to affect the response too. The factor C was included to maintain the heredity of the model. The equation modelling the roughness in terms of the actual factors was:

$$y' = y = 25.8 + 0.1x_1 - 0.7x_2 - 1.9x_3 - 3.3 \cdot 10^{-3}x_1x_2$$
$$+5.2 \cdot 10^{-3}x_1x_3 + 0.1x_2x_3 \qquad \text{Eq. 5.4}$$

where y is the modelled response (roughness, µm), x_1 is the PCL feed rate (mg/min), x_2 is the injector distance from the gun exit (mm) and x_3 is the PCL carrier gas flow rate (slpm). It is also possible to obtain the response as a function of the injector distance from the substrate (x_2') by substituting x_2 by (38- x_2') in the formula.

Figure 5.73a shows the predicted values plotted against the actual values measured in the experiments, where all the experimental points lie close to the line, which means that the roughness data was well predicted by the model. Figure 5.73b shows that the

PCL feeding rate has a major effect on the roughness followed by the injector distance and the carrier gas flow rate in this order.

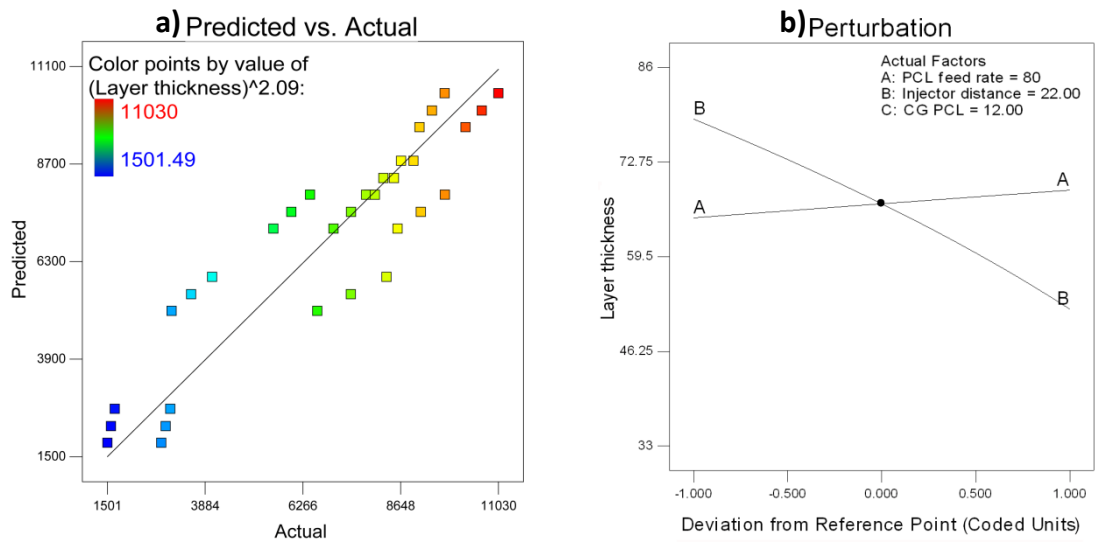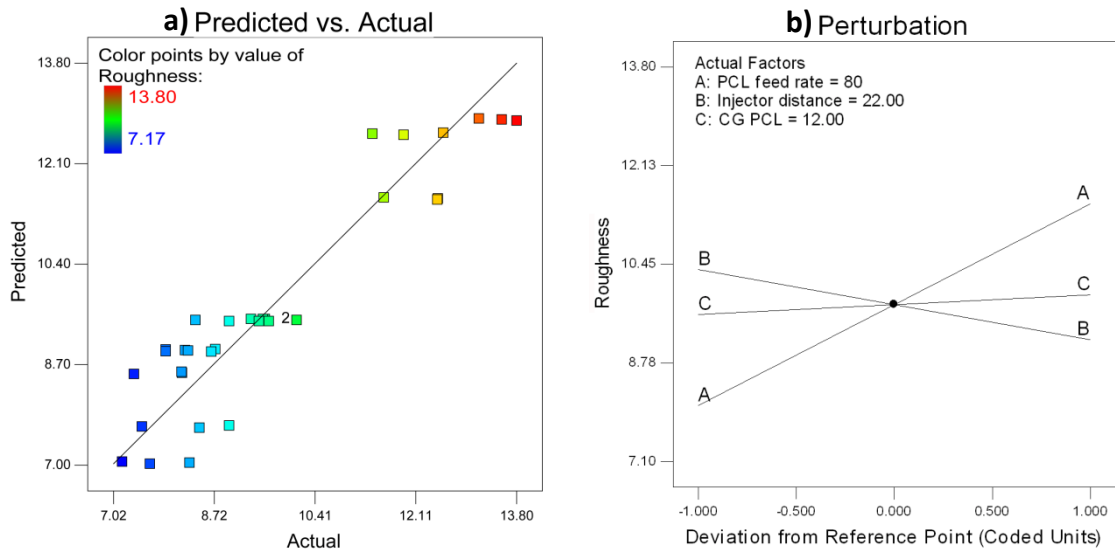**Figure 5.73.** Roughness model: a) Predicted vs. Actual plot and b) Perturbation plot at central point value for HA/PCL series

The roughness was found to increase as the PCL feed rate (A) increased, whatever the value of the other factors. As the amount of polymer increased, the evaporation in the coating became greater and the roughness increased as a result. It was also found that, at a fixed carrier gas flow rate, the greater the PCL feeding rate the greater the influence of the injector distance on the final roughness. In addition, the roughness was found to decrease as the PCL injection got closer to the substrate (Figure 5.74). This trend together with the decrease in thickness with the injector distance shown in Figure 5.69 proved the decrease in deposition efficiency with increasing the injector distance.

The effect of PCL feeding rate on roughness was verified by producing an extra point (HA13) at the centre point parameters but with a feeding rate of 650 mg/min instead of 80 mg/min. The average roughness of the sample HP13 was 35.14 μm. Figure 5.75 illustrates this trend by comparing the surface SEM images of a centre point sample (HP10) and the extra sample (HP13).
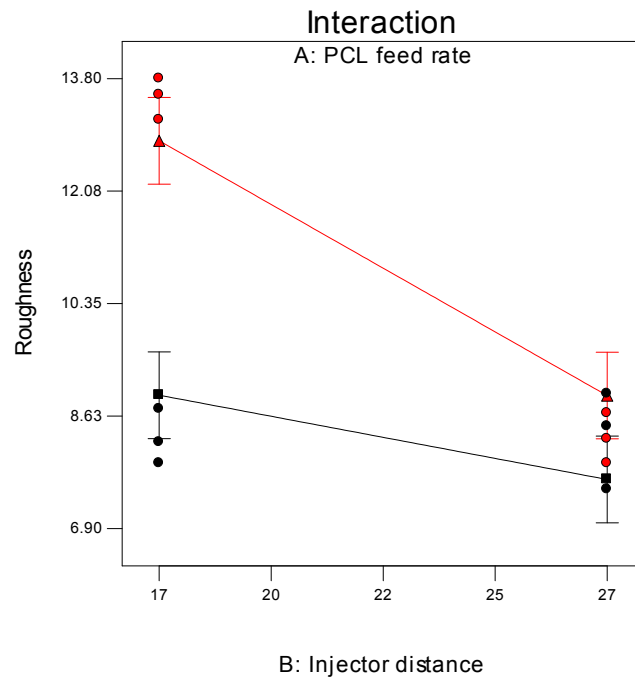
Figure 5.74. PCL feed rate- Injector distance interaction effect on roughness (HA/PCL series)
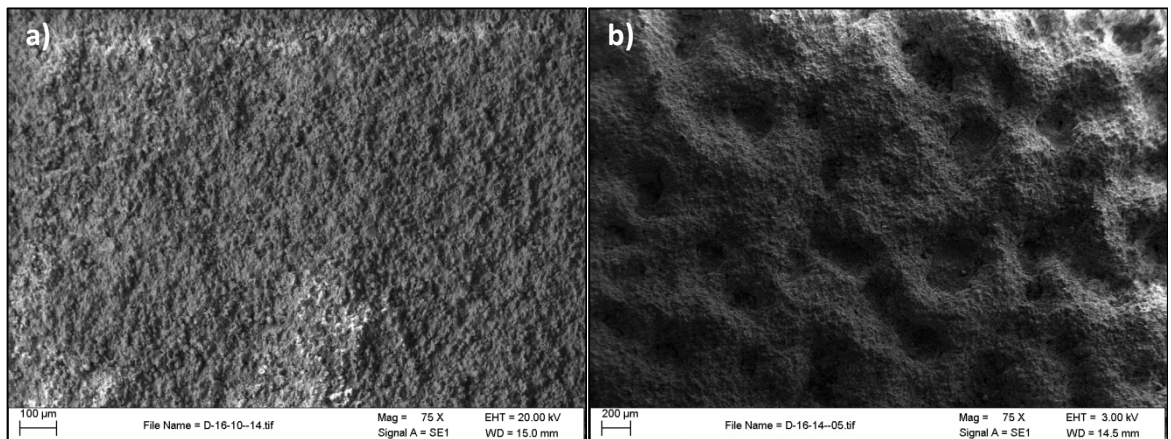
Figure 5.75. SEM images of: a) HP10 and b)HP13 surfaces

From the study of the AC and BC interactions effect on roughness some conclusions can be drawn:

1. For a PCL feeding rate in the range 40-80 mg/min and the PCL injector placed between 17 and 21 mm from the gun exit, a carrier gas of 10 slpm was found to efficiently introduce the polymer into the plume and, therefore, a greater roughness was observed. As the injector distance increased towards 27 mm, it

was necessary to increase the carrier gas flow rate towards 14 slpm in order to counteract the effect of the turbulences close to the substrate and, therefore, introduce the polymer in the plume. The BC interaction effect on roughness for a PCL feeding rate of 80 mg/min is shown as an example in Figure 5.76.

2. For a PCL feeding rate in the range 80-120 mg/min a PCL carrier gas flow rate of 14 slpm was adequate to allow the powder to enter the plasma plume, whatever the injector distance.
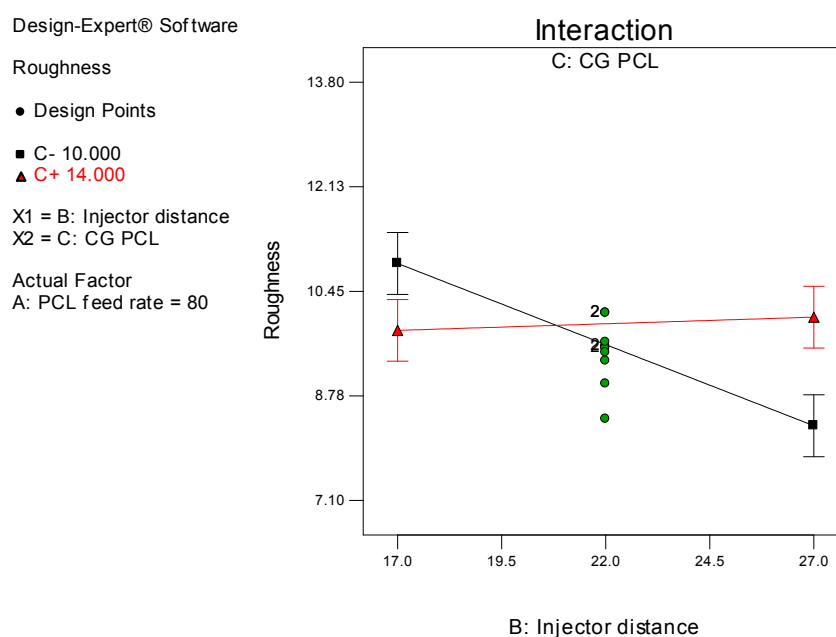
Figure 5.76. Injector distance – PCL carrier gas interaction effect on roughness (HA/PCL series)

5.4.3. Thermal degradation of HA/PCL composite series

FTIR studies were performed on a selected set of samples to check if the PCL had undergone degradation during the spraying process. The FTIR spectra of these samples, compared with the HA and PCL raw powders spectra, are shown in Figure 5.77. It can be noticed that the carbonyl (C=O) stretching band (1730 cm^{-1}) and the CH$_2$ stretching vibration bands (2868 and 2944 cm^{-1}) were present in all samples at different intensities. It can be also noticed that the intensity of these bands are lower for samples HP1, HP7 and HP10. The bands corresponding to the OH$^-$ group at the end of PCL chain and the CO bands were overlapped for the H$_2$O and PO$_4^{-3}$ bands of HA

respectively. No band shifts or new peaks can be observed respect to those present in the original powders. Therefore, from the observation of these spectra it can be stated that PCL did not undergo any significant degradation. In addition, no significant dehydroxylation occurred to the Hydroxyapatite, as the OH$^-$ bands (3571 and 635 cm^{-1}) are present in all spectra.
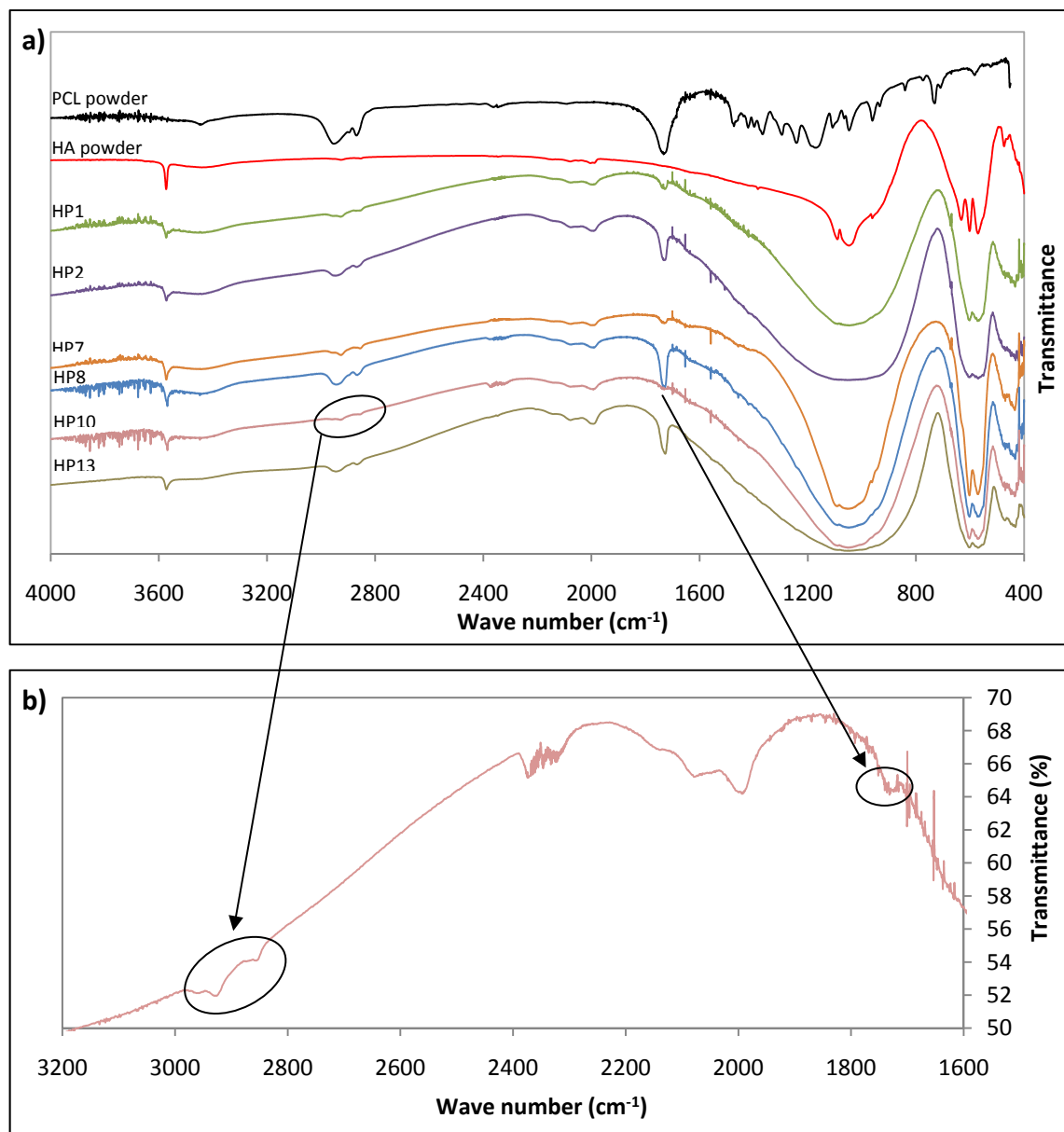
Figure 5.77. a) FTIR spectra of selected samples of HA/PCL composite series and b) detail of the HP10 FTIR spectra

5.4.4. Porosity of HA/PCL composite series

One of the main objectives of this work was to improve the porosity of the HA coatings by adding a pore former polymer (PCL). Part of the PCL was expected to evaporate during the process and part of it during a subsequent sintering step. However, the small amount of polymer fed into the system and the amount of evaporation during the process suggested that no improvement could be achieved by a post-spray sintering step. The measurement of this property was carried out to compare the degree of improvement in the coatings' porosities (due to PCL evaporation) in this series with similar measurements carried out in the HA reference series.

The porosity values measured following the procedure detailed in Section 4.6.6 ranged between 4.2 and 7.6% (Figure 5.78), showing large standard deviations (up to 1.5% for HP3). As said before sample HP9 was the product of an experimental error and was regarded as an outlier and, therefore, was excluded from the statistical models described in this section. The porosity of each sample in this series was found to be equal or higher than that of HA reference value (4.2%). Therefore it can be said that the addition of PCL slightly increased the porosity of the coatings, but this increase was far from the required porosity for tissue engineering applications. In addition, the morphology of the porosity was significantly improved showing interconnectivity as it can be seen in the areas encircled in Figure 5.80. The cross sectional areas of the samples HP1 and HP8, with different levels of porosity, are shown in Figure 5.79 as an example.
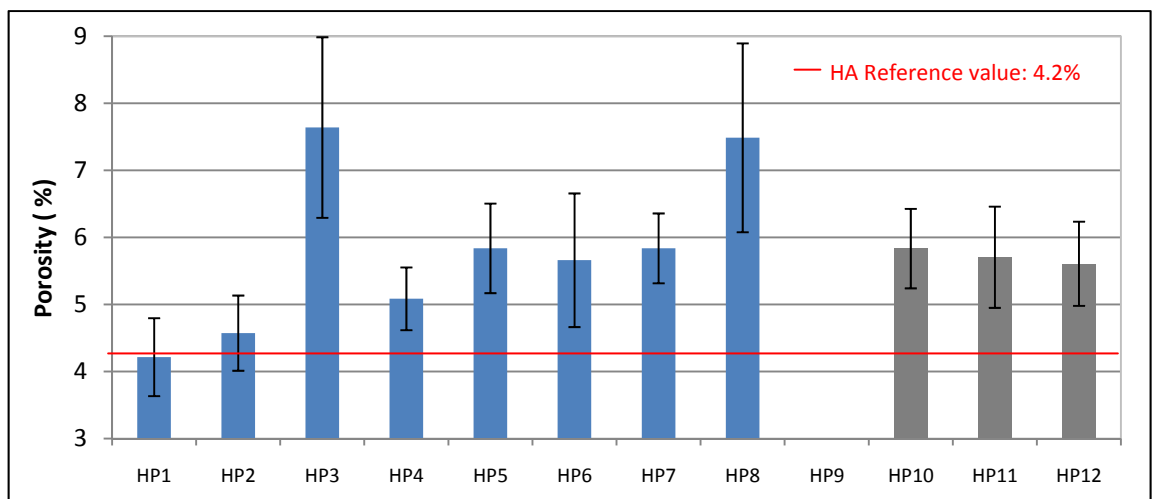
Figure 5.78. Porosity results for HA/PCL composites series
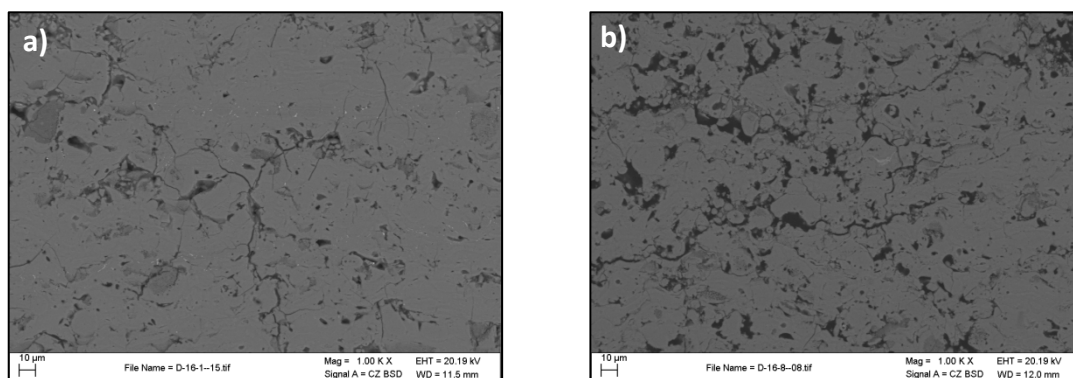
Figure 5.79. Porosity of samples: a) HP1 and b) HP8

The ANOVA table for porosity is given in Table 5.28. Even though a power transformation ($y'=y^{\lambda}$, λ=-0.07) was applied to the response the model did not properly fit the measured data (significant lack of fit, R^2 values lower than the recommended minimum value of 0.6 [103] and difference between adjusted R^2 and predicted R^2 greater than 0.2). A definition of the statistical values which helps to analyse ANOVA results are described in Appendix B. Therefore, this model cannot be used to study the porosity, but it can be stated that the injector distance, the carrier gas flow rate and their interaction have effect in the porosity.

Table 5.28. ANOVA table for porosity (HA/PCL series)

Source	SS	MS	F-value	Prob>F (p)	Significance
Model	2.287E-3	5.718E-4	8.76	0.0001	significant
A-PCL feed rate	3.400E-6	3.400E-6	0.052	0.8213	
B-Injector distance	1.352E-3	1.352E-3	20.72	0.0001	
C-CG PCL	5.657E-4	5.657E-4	8.67	0.0069	
AC	3.658E-4	3.658E-4	5.60	0.0260	
Curvature	1.647E-6	1.647E-6	0.025	0.8751	not significant
Lack of fit	1.590E-3	8.367E-5	11.94	0.0028	significant
R^2	0.5836		**Pred R^2**		0.2268
Adj R^2	0.5170		**Adeq Precision**		8.306

The lack of fit of the model may have been caused by the reasons stated in the previous section (metallographic preparation and image processing) and also by the

effect of irregular feeding of the PCL. This effect can be clearly seen in Figure 5.80. Evaporation occurred in areas where a greater amount of polymer arrived and thus a greater porosity (interconnected) can be seen at these spots (circles in Figure 5.80). On the other hand, the rest of the coating seems to be more compact than those produced in HA reference series. The reason behind this may be that PCL in small amounts acted as cement rather than as a pore former, which would be consistent with the increased thickness found earlier.
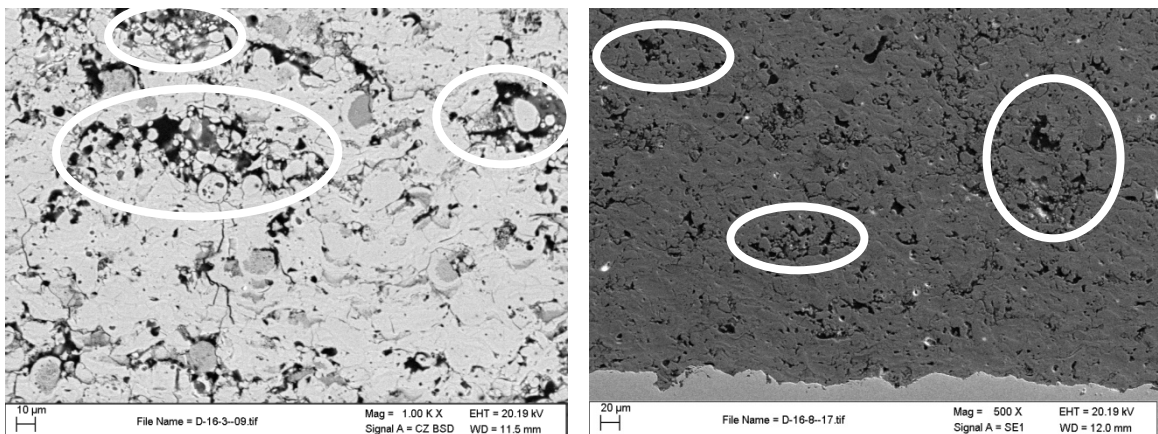
Figure 5.80. Effect of the irregular PCL feed rate in porosity (HA/PCL series)

As a conclusion, it can be said that the amount of PCL deposited determined by the factor combination AC and the injector position B, had a major influence on the coating porosity. It was proven that larger amounts of polymer increased the porosity. It was also noticed that smaller amounts of PCL seemed to increase the cohesion of the coatings acting as cement between HA lamellas. This aspect is studied later in section 5.4.5. In order to control the effect of PCL more accurately, an improved feeding system (i.e. vibration system [128]) would be required in the future to avoid inhomogeneity within the coating.

5.4.5. Mechanical properties of HA/PCL composites series

The polymer was initially expected to improve the porosity only, but it was noticed than under certain conditions PCL addition seemed to improve the cohesion of the coatings. For this reason, the mechanical properties were also studied for this series. Three mechanical properties (micro hardness, elastic modulus and fracture toughness) were measured using the indentation technique, following the procedure indicated in Section 4.6.7. The results for microhardness Vickers at 50 grams load, which ranged

from 261 to 362, are shown in Figure 5.81. The range of variation was found to be similar to the one of HA reference series and the average of the series too (Series HA/PCL: 305, Series HA: 307). The standard deviation for each experiment was large due to the presence of non-homogeneously distributed porosity. It can be seen that the samples with smaller PCL feed rate tended to have a lower hardness than those with greater polymer feed rate (keeping the other PSPs constant). As said before sample HP9 was the product of an experimental error and was excluded from this study.
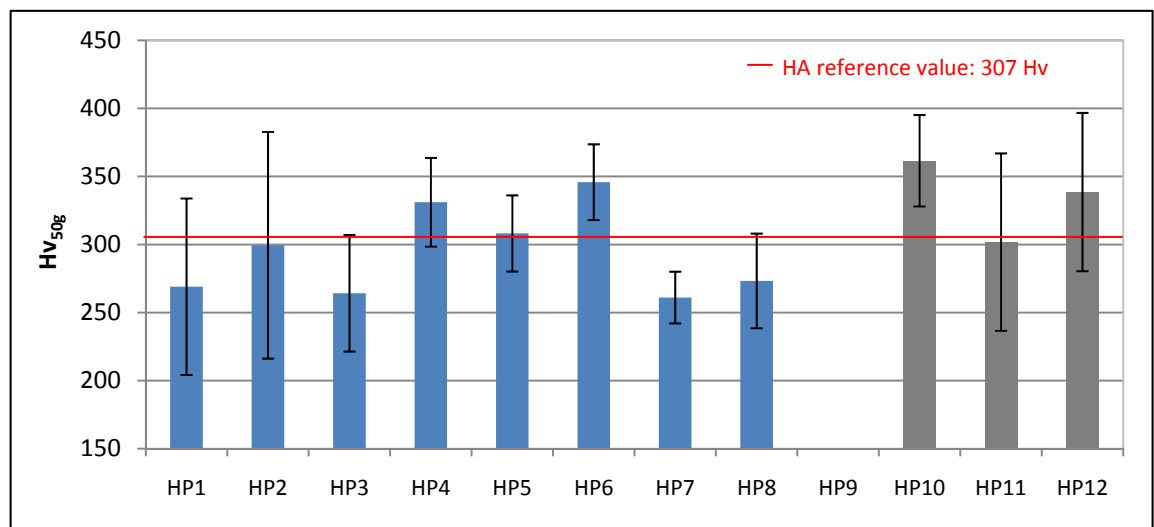
Figure 5.81. Microhardness Vickers results for HA/PCL composite series

The Young's modulus (E) (Figure 5.82) and fracture toughness (K_{IC}) (Figure 5.83) results presented large standard deviations, with values ranging between 2.7-3.9 GPa and 0.54-0.78 MPa·m$^{1/2}$, respectively. The addition of PCL decreased the Young's modulus with respect to that of HA reference series, but did not significantly change the fracture toughness. Therefore, it cannot be said that the coatings became more cohesive with the addition of PCL because this would have resulted in an overall increase in fracture toughness within this series. Instead, it seems that the PCL addition increased the "glueing" between lamellas, acting as a sort of cement.
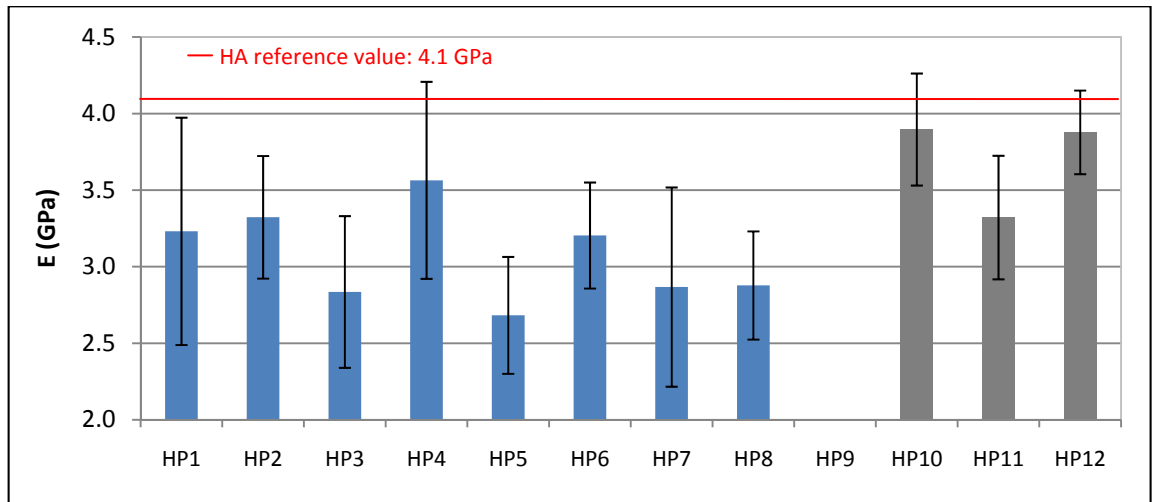
Figure 5.82. Young's modulus results for HA/PCL composite series
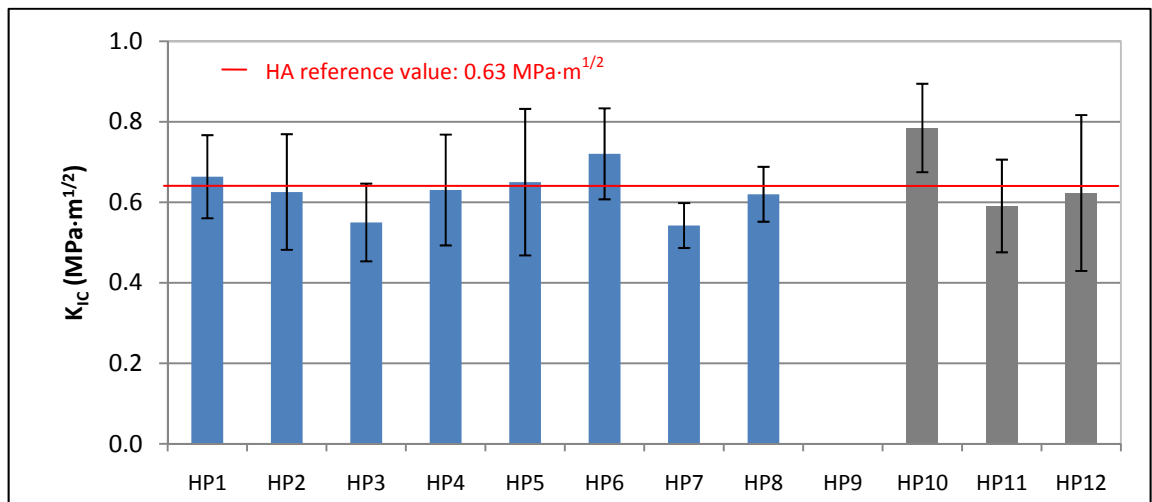
Figure 5.83. Fracture toughness results for HA/PCL composite series

5.4.6. Summary of HA/PCL composite series

The addition of PCL was found to increase porosity, but also to act as a sort of cement between the HA lamellas increasing coating density. The effect of PCL on the coatings depends on its quantity and melting degree, which in turn depend on the three factors A (feeding rate), B (position of the injector) and C (PCL carrier gas flow rate).

The closer the feeding of the polymer was to the substrate the smaller the amount of PCL entering the plasma plume and the lower its deposition efficiency, which led to lower layer thicknesses and roughness. This may be caused by the turbulences

produced by the gas plume impinging on the substrate. Taking into account that the stand-off distance was set to 38 mm during the HA reference series study, the effect of these turbulences can be quite important at an injector distance of 27 mm. These turbulences may also produce agglomerations of polymer which would be deposited as a whole increasing even more the inhomogeneity within the coating when evaporating. In addition, the polymer particles reaching the coating are not totally melted and therefore act as pore formers while evaporating as the coating temperature increases during the process. An additional transient overheating originated by the relative displacement of the plasma plume over the sample would produce an additional evaporation of the polymer. A better control over this phenomenon could be achieved by using liquid CO_2 or liquid nitrogen as cooling system instead of compressed air. Consequently, the PCL injection at 17 mm allows the polymer particles to enter the plume and strike the coating in a completely melted state, acting as cement.

Otherwise, as previously stated the low density of the polymer together with the small feeding rate made the feeding of the polymer unstable. As a result, the porosity measured in the coatings was inconsistent. It seems that PCL is fed in "chunks" rather than constantly due to the accumulation of it within the powder feeding pipes. The effect of this irregular feeding was less noticeable if the injector was placed at 17 mm, as the polymer particles arrive completely melted onto the substrate. On the other hand, when the injector was placed at 27 mm the effect of the irregular feeding became very important. The "chunk" effect may have been increased by the fact that the plasma gas rebounding on the substrate could have overheated the PCL injector and, therefore, partially clogged it increasing the powder agglomeration. In order to accurately assess the influence of the process parameters on the porosity, a most reliable feeding system should be used in future (i.e. vibration system).

A summary of the properties measured for this series is shown in Table 5.29. The addition of PCL turned out to significantly improve the layer thickness (hence deposition efficiency) and the roughness of the coatings. The increasing of layer thickness is desired for free-standing components forming and the improvement of roughness to enhance subsequent cell attachment. The porosity did not significantly

improve and it was unevenly distributed. However, the morphology of the porosity was significantly improved showing local interconnectivity (Figure 5.80). Unfortunately, HA/PCL series porosity still lies far from the requirements for bone scaffolds in tissue engineering applications. Vickers microhardness and fracture toughness were found to be within the same range as HA reference series. As PCL has lower mechanical properties than HA, the fact that the range of variation did not change indicates that the "glueing" of the lamellas compensated for this effect.

Table 5.29. Range of variation on the properties measured for HA/PCL series

Response	HA/PCL series	HA reference values[1]
Layer thickness, μm	34.0-84.5	26.1
Roughness, μm	7.76-13.51	6.00 (5.49-6.47)
Porosity, %	4.2-7.6	4.2 (2.5-6.0)
Crystallinity, %	~	86.5
Vickers Hardness, HV	261-362	307 (244-351)
Young's Modulus, GPa	2.7-3.9	4.1 (2.9-4.8)
Fracture toughness, MPa·m$^{1/2}$	0.54-0.78	0.63 (0.52-0.71)

[1] The non-predicted responses were based on the mean of the series and are followed by the range of variation of the response (Table 5.20 & Table 5.22)

5.5. HA/TiO$_2$ composite coatings study

It was found during the feasibility tests (Section 5.2.3) that the LEPS system lacked the energy to melt Ti particles of 137.4 μm when they were injected through an external injector (gun configuration 2). Titania (TiO$_2$), which has a similar melting temperature than that of Ti, was selected as a second phase to form composite coatings with improved mechanical properties. A Titania powder with an average particle size of 31.3 μm was chosen in order to overcome the difficulties detected during Ti feasibility tests regarding particle size. Although the results were improved with this smaller particle size, the LEPS energy input was still insufficient to adequately melt TiO$_2$ particles with this gun configuration.

During Ti feasibility tests it was also observed that it was not possible to inject the HA and Ti particles separately inside the barrel of the gun (gun configuration 3) without perturbing the plasma plume. Therefore, the solution used to produce the HA/TiO$_2$ composite series was to mechanically mix the two feedstock materials and feed them through the same injector (gun configuration 1). As discussed in Chapter 2, this solution is not totally efficient for the deposition of two powders with different densities, sizes and melting temperatures (Table 5.30). The different particle weight of the 2 powders made it difficult to fix a common carrier gas flow rate, which could efficiently introduce both powders into the plume. In addition, the different melting temperatures had an influence on the melting degree of the particles arriving onto the substrate. All this has a direct influence on the HA and TiO$_2$ deposition efficiencies and as a result in properties such as the layer thickness and roughness.

Table 5.30. Characteristics of HA and TiO$_2$ powders

Powder	HA	TiO$_2$
Average diameter, μm	52.1	31.3
Theoretical Density, g/cm^3	3.16	4.23
Particle weight, μg	0.1755	0.0509
Melting T^e,	1550	1640

The LEPS parameters used to produce this series are shown in Table 5.31. As the powder were mechanically mixed and the matrix material was HA, the parameters were set based on the best parameters obtained for HA reference series (stand-off distance of 3.8 cm and powder feed rate of 9 g/min). The plasma gas flow rate was included again as a factor due to its significant influence on the powder melting and, therefore, on the deposition efficiency.

The study of HA/TiO$_2$ series was carried out using the response surface methodology. The experiments were statistically designed using a 3 factor Box-Behnken design (Table 5.32) consisting of 17 experimental runs from which 12 were design points ($3*2^2$) and 5 were centre points (marked in grey). As it can be seen, the 12 points are divided in 3 blocks; each one consisting of all the combinations (2^2) of 2 of the factors at the high

and low levels with the third factor remaining at the central point. In order to further establish the influence of TiO_2 addition in the mechanical properties of the composite coatings, two extra test points were added with greater TiO_2 content (marked in orange) and the remainder of the parameters at central values. The properties measured for all the samples within this series are shown in Table 5.33.

Table 5.31. Plasma spray parameters for HA/TiO_2 composite series

Parameter	TiO_2-LEPS	DOE factor code
Current (Power)	390 A (12 kW)	-
Plasma gas (PG), flow rate	Argon, 30-42 slpm	A
Carrier gas 1 (CG1), flow rate	Argon, 4.5-5.5 slpm	B
Powder mix TiO_2 content	5-25%wt	C
Powder feeding rate 1 – Mix	9 g/min	-
Stand-off distance (s.d.)	3.8 cm	-
Relative gun velocity	20 cm/s	-
Increment y-direction (Δy)	-3 mm	-
Gun configuration[*]	1	-
Injector 1 position	Internal	-
Cooling system	Compressed air @ 6 bar	-

[*] See Appendix A

Table 5.32. Box-Behnken design for TiO_2 composite series

Reference name	Run order	Factor A: PG flow rate (slpm)	Factor B: CG flow rate (slpm)	Factor C: TiO_2 (%wt)
HT1	3	30	4.5	15
HT2	6	42	4.5	15
HT3	4	30	5.5	15
HT4	5	42	5.5	15
HT5	10	30	5	5
HT6	9	42	5	5
HT7	14	30	5	25
HT8	13	42	5	25
HT9	7	36	4.5	5
HT10	8	36	5.5	5
HT11	12	36	4.5	25
HT12	11	36	5.5	25
HT13	1	36	5	15
HT14	2	36	5	15
HT15	15	36	5	15
HT16	16	36	5	15
HT17	17	36	5	15
HT18	-	36	5	35
HT19	-	36	5	45

Table 5.33. Measured properties on HA/TiO$_2$ reference series

Reference name	Layer Thickness, μm		Roughness, μm		Vickers Hardness		E, GPa		K$_{IC}$, MPa·m$^{1/2}$	
	Average	Std. Dev.	Average	Std. Dev.	Average	Std. Dev.	Average	Std. Dev.	Average	Std. Dev.
HT1	104.0	1.80	6.55	0.42	420	71	4.63	0.80	1.11	0.19
HT2	73.4	2.00	5.85	0.38	284	22	3.01	0.47	0.78	0.10
HT3	97.6	1.60	6.22	0.44	399	58	5.13	0.86	1.02	0.10
HT4	54.8	1.00	5.57	0.17	283	35	3.24	0.49	0.78	0.07
HT5	92.6	1.40	6.16	0.53	348	58	3.98	0.77	0.86	0.14
HT6	73.4	0.80	5.75	0.65	268	20	2.94	0.44	0.75	0.07
HT7	93.6	2.20	6.23	0.51	463	49	5.30	1.11	1.14	0.14
HT8	52.8	1.80	5.72	0.37	271	17	2.67	0.28	0.82	0.06
HT9	93.8	3.20	5.90	0.53	292	32	3.36	0.68	0.85	0.07
HT10	89.8	2.20	5.68	0.37	325	52	3.42	0.48	0.90	0.11
HT11	95.8	1.60	5.88	0.29	331	28	3.32	0.41	0.92	0.09
HT12	68.4	0.80	5.34	0.57	299	30	2.95	0.29	0.87	0.08
HT13	97.0	2.80	5.90	0.44	337	39	3.55	0.47	0.93	0.10
HT14	110.0	3.40	5.91	0.84	332	41	3.40	0.50	0.92	0.09
HT15	94.0	2.00	5.63	0.33	335	40	3.62	0.45	0.95	0.09
HT16	92.6	2.00	6.11	0.66	336	33	3.44	0.29	0.94	0.11
HT17	91.4	2.40	5.77	0.55	341	32	3.62	0.33	0.93	0.09
HT18	63.8	1.40	5.36	0.30	388	57	3.89	0.52	0.98	0.10
HT19	60.7	1.20	5.03	0.54	395	53	4.02	0.89	1.03	0.11

5.5.1. TiO$_2$ deposition efficiency

The layer thickness is directly related to the respective deposition efficiencies of Hydroxyapatite and Titania, which in turn are influenced by the process parameters. Therefore, before studying the layer thickness of this series, a brief study is conducted to find the parameters which most affect TiO$_2$ deposition efficiency.

In Section 5.3 Hydroxyapatite layer increment was found to decrease when increasing the plasma gas flow rate from 30 slpm to 42 slpm during the HA reference series. Titania, with an even higher melting temperature than HA, is expected to follow the same trend. In addition, HA reference series were studied fixing the carrier gas flow rate to 4.6 slpm, and therefore it is not easy to assess which is the effect of carrier gas flow rate variation on HA layer increment. The optimal carrier gas flow rate for this series would also depend on the composition of the initial powder, which is represented by factor C in the statistical models presented in the following.

The TiO$_2$ content in the coatings, which was studied by means of SEM, was found to increase when decreasing the plasma gas flow rate. Figure 5.84 shows an important difference in the amount of TiO$_2$ (white phase) deposited for samples HT1 and HT2. HT1, which was sprayed at a plasma gas flow rate of 30 slpm, presented higher TiO$_2$ deposition than HT2, which was sprayed at a plasma gas flow rate of 42 slpm. The remainder of the parameters was the same for both samples (B=4.5 slpm, C=15 wt% TiO$_2$).
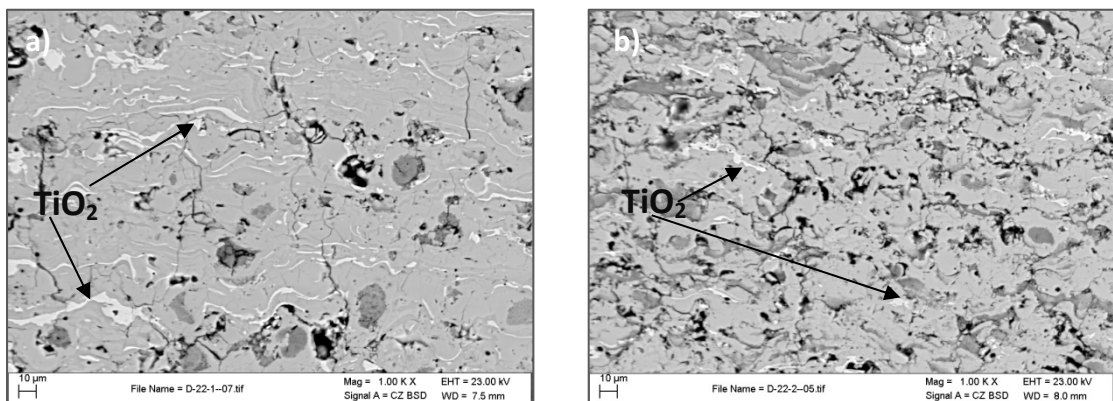
Figure 5.84. TiO$_2$ deposition in coatings sprayed at different plasma gas flow rates: a) HT1 (30 slpm) and b) HT2 (42 slpm) within HA/TiO$_2$ series

It was also found that the deposition efficiency of TiO_2 was greater for the lowest carrier gas flow rate (4.5 slpm), at least when the initial TiO_2 content was greater than 15 wt%. As an example, Figure 5.85 shows the cross section of two samples with different TiO_2 content in the coating: HT11 (A=36 slpm, B=4.5 slpm and C=25 %wt) presented a higher TiO_2 deposition than HT12 (A=36 slpm, B=5.5 slpm and C=25 %wt).
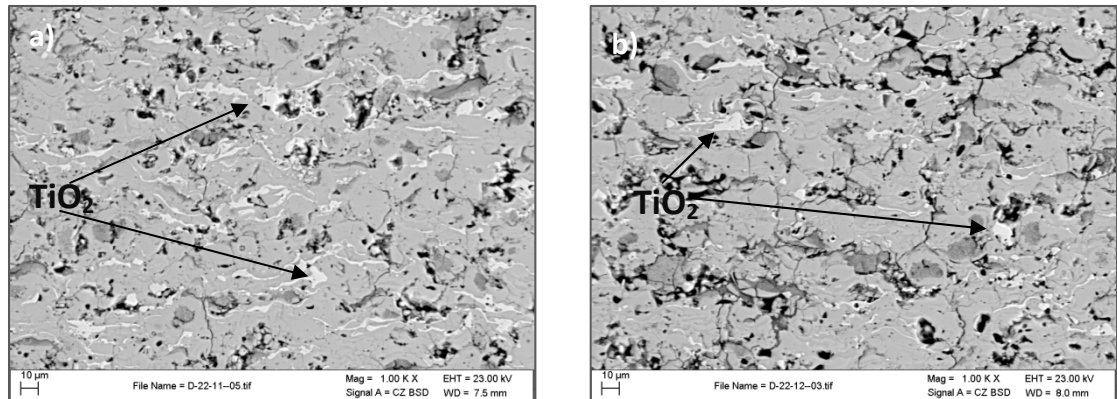
Figure 5.85. TiO_2 deposition in coatings injected using different carrier gas flow rates: a) HT11 (4.5 slpm) and b) HT12 (5.5 slpm) within HA/TiO_2 series

Finally, as expected, an increase of the initial quantity of TiO_2 in the powder resulted in an increase of the amount of TiO_2 retained in the coating when keeping the remainder of the parameters fixed. Figure 5.86 shows the cross sectional areas of samples HT17 (15wt% TiO_2), HT18 (35wt% TiO_2) and HT19 (45wt% TiO_2), all of them sprayed at the same plasma spray parameters (plasma gas flow rate: 36 slpm and carrier gas flow rate: 5 slpm). In addition, it can be noticed that the coating density is greater for the sample produced with less TiO_2 content, HT17. Furthermore, the presence of unmolten particles and defects in coatings HT18 and HT19 indicates that a higher thermal transfer is required when increasing the TiO_2 content to sufficiently melt the Titania particles and, thus, achieve a high coating density; which is in turn associated to a lower plasma gas flow rate or a higher plasma current.

As a summary, it can be stated that the retention of TiO_2 in the coating increased when:

- Decreasing the plasma gas flow rate and keeping the remaining parameters constant.

- Decreasing the carrier gas flow rate and keeping the remaining parameters constant.
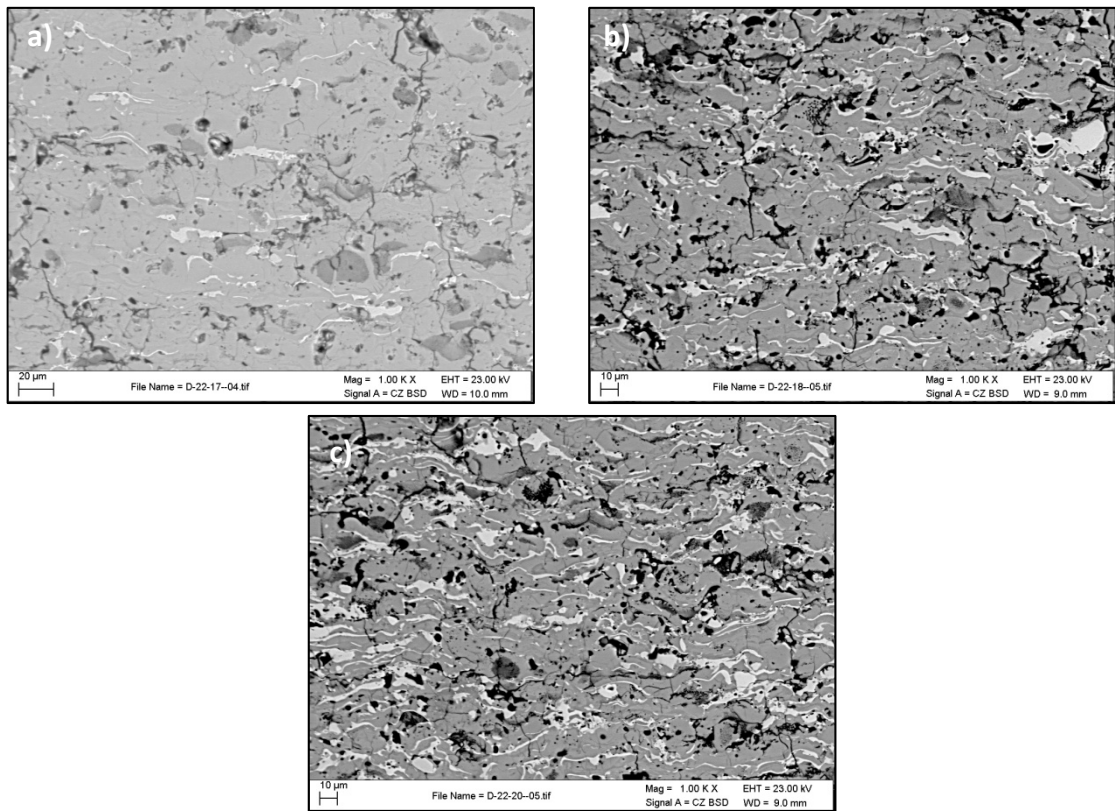
Figure 5.86. TiO$_2$ deposition in coatings for different powder initial compositions: a) HT17 (15wt% TiO$_2$), b) HT18 (35wt% TiO$_2$) and c) HT19 (45wt% TiO$_2$) within HA/TiO$_2$ series

5.5.2. Layer thickness of HA/TiO$_2$ composite series

The layer thickness results obtained following the procedure detailed in Section 4.6.2 are presented graphically in Figure 5.87. It can be seen that one of the centre points was very different from the others. The sample HT14 was found to be an outlier during the modelling and was therefore withdrawn from this study. The layer thickness of the samples ranged between 52.8-104.0 μm, which means an increase in the range of 60-215% with respect to the maximum layer thickness obtained in HA reference series (33 μm). In addition, the highest layer thickness achieved in this series was 23% higher than the highest one obtained for HA/PCL series (84.5 μm). The influence of the parameters on the layer thickness was not straightforward, and it was statistically studied.
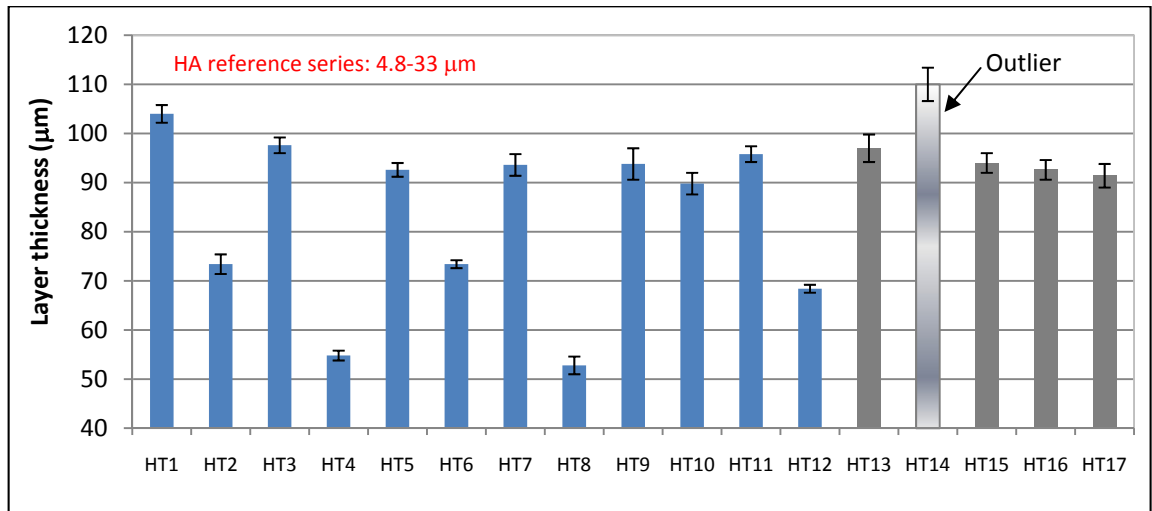
Figure 5.87. Layer thickness results for HA/TiO$_2$ composite series

A power transformation (y'=y$^\lambda$, λ=1.66) was applied to the layer thickness to obtain a better quadratic model fitting. A stepwise automatic reduction algorithm was used to remove insignificant terms (95 % significance). The ANOVA table for layer thickness is given in Table 5.34. A definition of the statistical values which helps to analyse ANOVA results is described in Appendix B.

Table 5.34. ANOVA table for layer thickness (series HA/TiO$_2$)

Source	SS	MS	F-value	Prob>F (p)	Significance
Model	3.083E+6	4.405E+5	45.17	<0.0001	significant
A-PG flow rate	1.954E+6	1.954E+6	200.33	<0.0001	
B-CG flow rate	3.479E+5	3.479E+5	35.68	0.0003	
C	1.410E+5	1.410E+5	14.46	0.0052	
AC	78338.28	78338.28	8.03	0.0220	
BC	1.233E+5	1.233E+5	12.65	0.0074	
A^2	3.171E+5	3.171E+5	32.52	0.0005	
C^2	1.221E+5	1.221E+5	12.52	0.0076	
Lack of fit	58558.05	11711.61	1.81	0.3323	not significant
R^2	0.9753		**Pred R^2**		0.8849
Adj R^2	0.9537		**Adeq Precision**		23.548

The model was found to be significant (p<0.0001) and the lack of fit insignificant. The R^2 value was very close to 1, the difference between adjusted and predicted R^2 was smaller than 0.2 and there was an adequate signal-to-noise ratio (Adeq. precision>4). As a result, it can be concluded that the model properly fits the experimental data obtained.

The layer thickness was found to be linearly affected by B and quadratically affected by the other two factors (A^2 and C^2). The interactions between the TiO_2 content and the other factors (AC and BC) were found to be significant too. The equation modelling the layer thickness in terms of the actual factors is:

$$y' = y^{1.66} = -7311.1 + 515.7x_1 + 109.7x_2 + 298.7x_3 - 2.3x_1x_3 - 35.1x_2x_3 - 7.8x_1^2 - 1.7x_3^2$$

Eq. 5.5

where y is the modelled response (layer thickness, μm), x_1 is the plasma gas flow rate (slpm), x_2 is the carrier gas flow rate (slpm) and x_3 is the TiO_2 content (%wt).

The Predicted vs Actual plot (Figure 5.88a) shows that layer thickness is well predicted by the model. The perturbation plot (Figure 5.88b) indicates that plasma gas flow rate has major effect on this response.
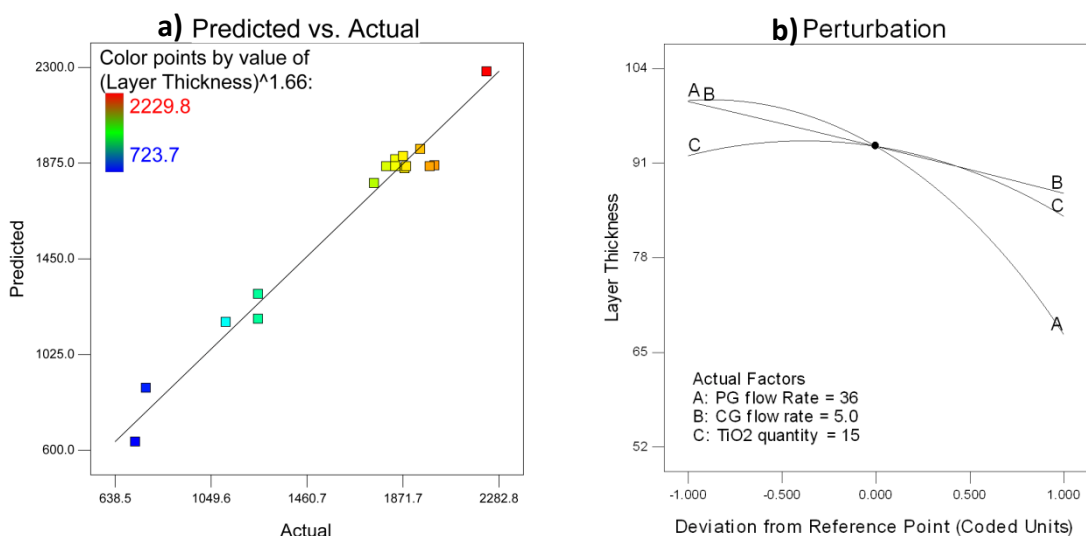
Figure 5.88. Layer thickness model: a) Predicted vs. Actual plot and b) Perturbation plot at central point value (HA/TiO$_2$ series)

Figure 5.89 shows the surface interaction plot between the plasma gas flow rate and the initial TiO_2 content for a carrier gas flow rate of 4.5 slpm. The maximum thickness was predicted to occur for a carrier gas flow rate of 4.5 slpm, a plasma gas flow rate of 30 slpm and an initial Titania content of 20 wt%. It seems that the LEPS system does not have enough energy to melt more than 20 wt% of TiO_2 in the mixture at the lowest plasma gas flow rate studied. As the content of Titania in the initial powder decreased, the highest layer thicknesses were observed for higher plasma gas flow rates, with an optimum in the range of 30-35 slpm for an initial TiO_2 content of 5 wt%. This was expected as result of the higher melting temperature of the Titania. Similar trends were observed for the other carrier gas flow rates.
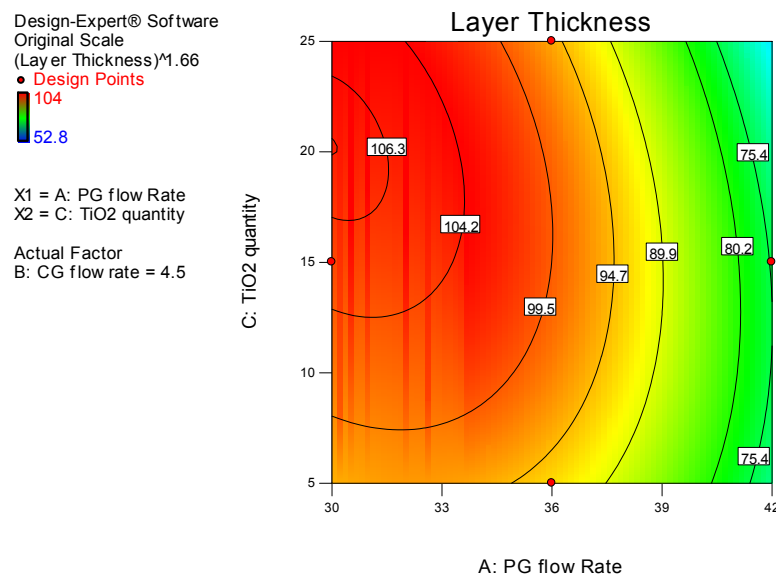
Figure 5.89. Plasma gas flow rate–TiO_2 wt% interaction for layer thickness model (HA/TiO_2 series)

The sensitivity of the layer thickness to the plasma gas flow rate is corroborated by observing the coatings shown in Figure 5.90. An important difference in thickness can be observed for samples HT3 and HT4, which were sprayed at plasma gas flow rates of 30 and 42 slpm respectively, with the remaining parameters kept constant (B=5.5 slpm, C=15 wt% TiO_2).
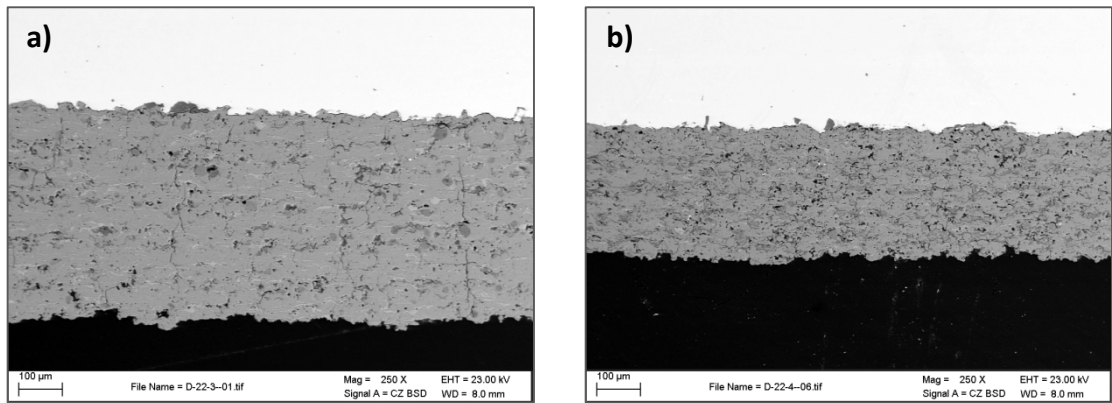
Figure 5.90. SEM images of cross sections of coatings sprayed at different plasma gas flow rates: a) HT3 (30 slpm) and b) HT4 (42 slpm) within HA/TiO$_2$ series

Figure 5.91 shows an example of one of the interaction contours between the carrier gas flow rate and the initial TiO$_2$ content for a plasma gas flow rate of 36 slpm. However, it can be observed that a CG flow rate between 4.5 and 5 slpm produced the greatest layer thicknesses whichever the initial TiO$_2$ content. In addition, the optimum carrier gas flow rate decreased towards 4.5 slpm as the content of Titania approached 20 wt%. Similar trends were observed for the other plasma gas flow rates. The results for a 5 wt% TiO$_2$ provided an estimate of the possible optimum carrier gas to introduce HA in the plume, which seemed to be a little higher than that used during the HA reference series study (~5 slpm).

As said in the introduction of this section, the optimum carrier gas flow rate for a powder depends on the density and size of the particles. A greater carrier gas flow rate is required to introduce lighter particles into the plasma. Theoretically, TiO$_2$ particles are lighter and smaller than HA (Table 5.30). However, the powder production methods may lead to lower densities than the theoretical ones. For instance, agglomerated powders usually are lighter than fused and crushed powders. For this reason and in view of the results obtained HA particles seem to be lighter than TiO$_2$. Therefore, an increase in TiO$_2$ content makes it necessary to inject the powder mixture into the plume using a lower carrier gas flow rate (less kinetic energy). It has to be highlighted that in the internal injection configuration the trajectory of the particles is highly sensitive to the carrier gas flow rate. If a greater or lower carrier gas flow rate is selected, particles tend to strike in the opposite inner wall of the gun or fail to enter the plume, respectively.
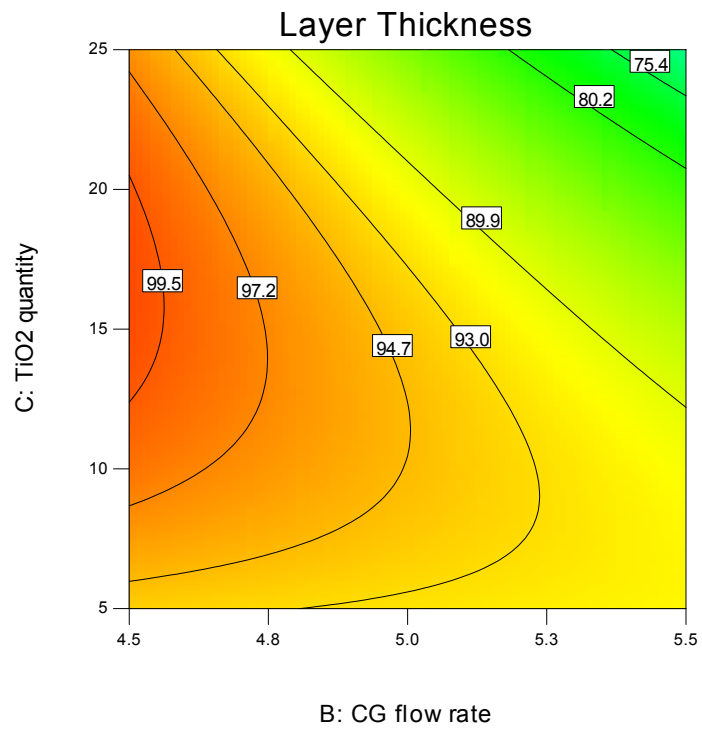
Figure 5.91. Carrier gas flow rate–TiO$_2$ wt% interaction for layer thickness model (HA/TiO$_2$ series)

As a summary, it can be said that layer thicknesses over 100 μm occurred for low plasma gas flow rates (30-35 slpm) and carrier gas flow rates in the range 4.5-4.9 slpm when the amount of Titania was greater than 9 wt%. Within these ranges, as the TiO$_2$ initial content increased a decrease of the carrier gas flow rate was required to introduce the powder mixture into the plume. This gives rise to a higher layer thickness. Above these ranges the deposition efficiencies of both powders decreased and, as a result, the layer thickness too. At lower Titania contents, the maximum thickness occurred for a wider range of carrier gas flow rates (4.5-5.2). These findings indicate that the carrier gas flow rate required for HA was possibly slightly higher than the one used for HA reference series. However, to fully understand the layer thickness evolution a study of the HA reference series including the effect of carrier gas flow rate in the model should be carried out in future.

5.5.3. Roughness of HA/TiO$_2$ composite series

The roughness values measured following the procedure detailed in Section 4.6.3 are shown in Figure 5.92. The roughness values ranged between 5.34-6.55 μm. This small range of variation together with the large standard deviations justified adopting the

182

mean of the series as the series reference roughness (5.78 μm). The roughness values for this series were similar to that of HA reference series and significantly smaller than those of HA/PCL series. It can be observed in the bar chart that the rougher samples were those sprayed at a smaller plasma gas flow rate. As explained before, the LEPS does not provide sufficient energy to fully melt the particles. Consequently, the higher the kinetic energy -due to a greater plasma gas flow rate- the greater the deformation of particles which strike the coating. Figure 5.93 shows the surface of the smoothest (HT12) and the roughest (HT1) samples, and no obvious difference can be observed.
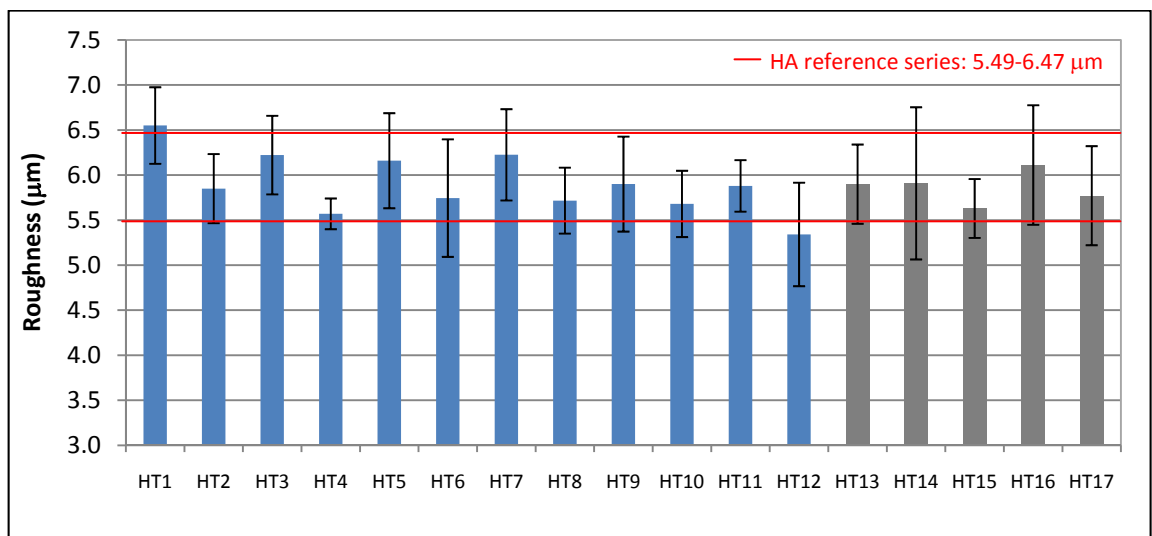
Figure 5.92. Roughness results for HA/TiO$_2$ composite series
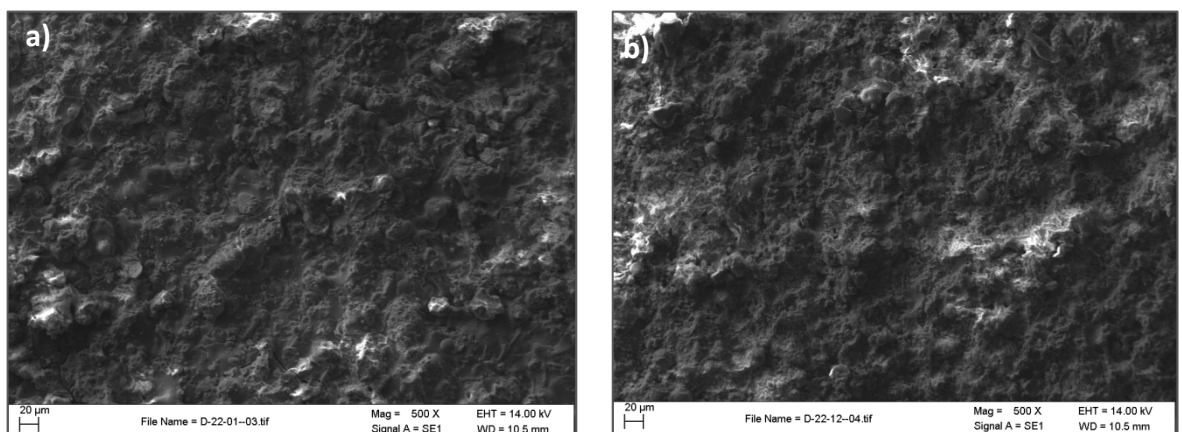
Figure 5.93. SEM image of: a) the smoothest (HT12) and b) the roughest (HT1) surface in HA/TiO$_2$ series

5.5.4. Mechanical properties of HA/ TiO$_2$ composites series

Three mechanical properties (micro hardness, elastic modulus and fracture toughness) were measured using the indentation technique as indicated in Section 4.6.7. It was noticed that for composite deposits, the indentation technique sometimes failed to provide accurate results because in some cases the indentation print did not sit in a representative area of the mixture of materials. As a result, some of the single measurements were closer to those values of HA whereas others were closer to those of TiO$_2$. In order to overcome this limitation the indentation load was set to 100g for this series. By increasing the indentation load, the indented area becomes larger, and therefore, more representative of the actual coating structure. Consequently, the indentation method becomes less sensitive to the composite coatings anisotropy and reflects more accurately the mechanical properties of the samples. Actually, an increase in the mechanical properties was observed when increasing the indentation load from 50 grams to 100 grams.
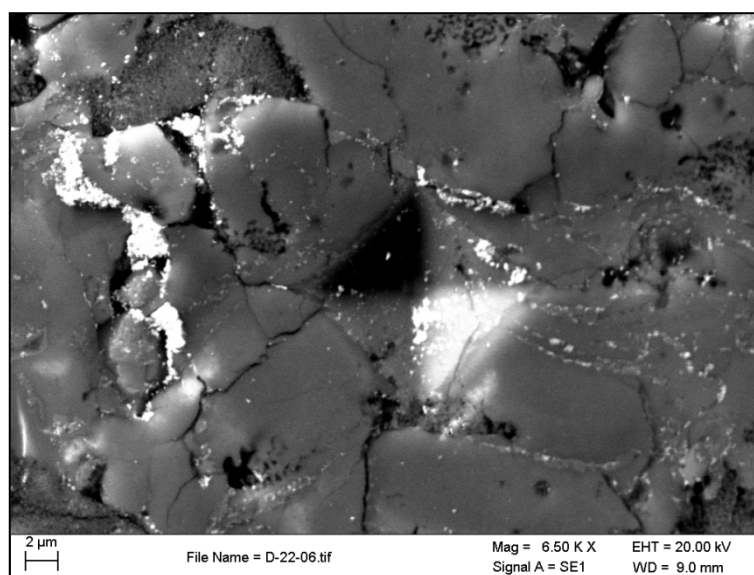
Figure 5.94. Vickers microhardness indentation (100g) on sample HT6

In case of single material coatings such zirconia, it has been reported that the mechanical properties measured by the indentation method do not vary significantly for loads above certain load and if they change, the trend is to slightly decrease as the load increase [215]. It is believed that this load is 50 grams for HA and, therefore, the comparison of the mechanical properties of this series with those of HA reference series is still valid and conservative.

Microhardness

The results for microhardness Vickers at 100 g load, which ranged from 268 to 463 Hv, are shown in Figure 5.95. The range of variation was found to be bigger than the one of HA reference series (244-351 Hv). The hardest sample obtained for HA/TiO$_2$ series (HT7) was nearly 32% harder than the hardest sample produced in the reference series (HA7). The standard deviation for each experiment was large due to the typical anisotropic structure of the thermally sprayed coatings which may be increased due to the presence of a second phase material. It can be seen that the samples sprayed at lower plasma gas flow rate showed greater hardness. A statistical model was carried out to further understand the relationship factors/response.
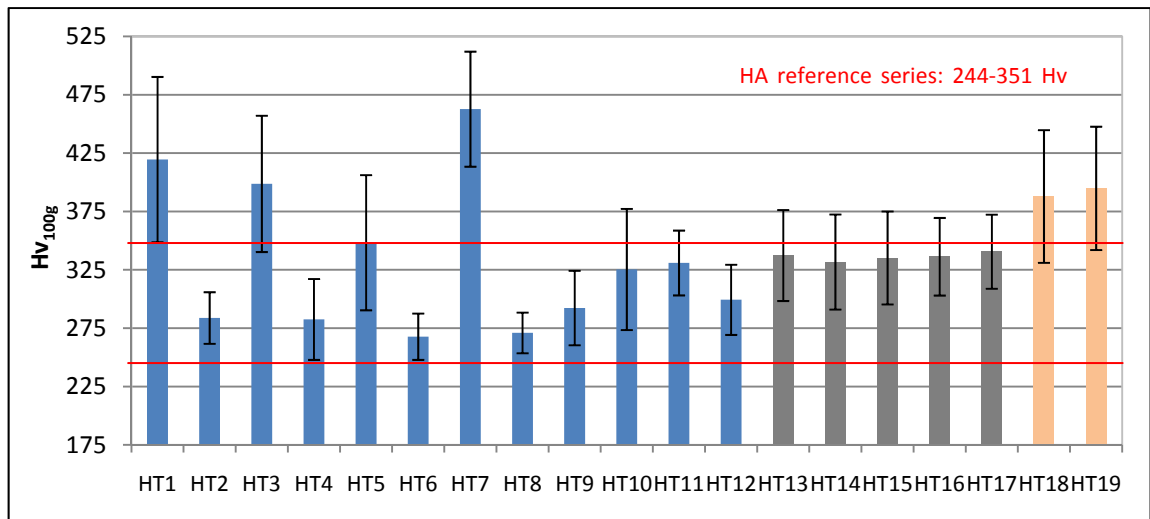
Figure 5.95. Microhardness Vickers results for HA/TiO$_2$ composite series

Observing hardness values of samples HT17, HAT 18 and HT19, it can be noticed that hardness increased as the TiO$_2$ content increased for the remaining parameters kept constant. It also has to be highlighted that the smaller hardness difference between samples HT18 and HT19 can be attributed to the inability of the LEPS system to melt such an amount of TiO$_2$ at the plasma gas flow rate used to spray these samples and the presence of defects in these coatings (Figure 5.86 b/c).

A power transformation (y'=y$^\lambda$, λ=-1.53) was applied to this response. Vickers Hardness was fitted by a quadratic model, for which the design was replicated (3) in order to provide enough data to the DOE software to conduct the lack of fit test. A stepwise

automatic reduction algorithm was used to remove insignificant terms (95 % significance). The ANOVA table for this response is given in Table 5.35. A definition of the statistical values which helps to analyse ANOVA results is described in Appendix B.

The model was found to be significant (p<0.0001) and the lack of fit insignificant. The R^2 value was adequate, the difference between adjusted and predicted R^2 was smaller than 0.2 and there was an adequate signal-to-noise ratio (Adeq. precision>4). As a result, it can be concluded that the model properly fits the experimental data obtained.

Table 5.35. ANOVA table for Vickers hardness (series HA/TiO$_2$)

Source	SS	MS	F-value	Prob>F (p)	Significance
Model	4.521E-8	7.536E-9	62.70	<0.0001	significant
A-PG flow rate	4.836E-8	4.836E-8	319.13	<0.0001	
B-CG flow rate	1.780E-11	1.780E-11	0.15	0.7022	
C- TiO$_2$ quantity	1.241E-9	1.241E-9	10.33	0.0025	
AC	1.338E-9	1.338E-9	11.13	0.0017	
BC	1.871E-9	1.871E-9	15.57	0.0003	
C^2	2.388E-9	2.388E-9	19.87	<0.0001	
Lack of fit	8.555E-10	1.426E-10	1.22	0.3165	not significant
R^2	0.8953		**Pred R^2**		0.8533
Adj R^2	0.8810		**Adeq Precision**		24.885

The hardness was found to be linearly affected by the plasma gas flow rate (A) and quadratically affected by the TiO$_2$ quantity (C^2). The interactions between the TiO$_2$ content and the other factors (AC and BC) were found to be significant too. The equation modelling the hardness in terms of the actual factors is:

$$y' = y^{-1.53} = -2.1 \cdot 10^{-4} + 4 \cdot 10^{-6} x_1 - 3.6 \cdot 10^{-5} x_2 - 2.4 \cdot 10^{-5} x_3 \\ + 1.8 \cdot 10^{-7} x_1 x_3 + 2.5 \cdot 10^{-6} x_2 x_3 + 1.4 \cdot 10^{-7} x_3^2 \qquad \text{Eq. 5.6}$$

where *y* is the modelled response (Vickers hardness, H$_v$), *x$_1$* is the plasma gas flow rate (slpm), *x$_2$* is the carrier gas flow rate (slpm) and *x$_3$* is the TiO$_2$ quantity (%wt).

Figure 5.96a shows the predicted values plotted against the actual values measured in the experiments. It shows that all design points (17) and replicates (34) lie around the line, which proves that the hardness is well predicted by the model. The perturbation plot (Figure 5.96b) indicates that plasma gas flow rate has major effect on this response followed by the initial TiO_2 content. The carrier gas flow rate by itself has minor effect as it is only significant in interaction with the initial TiO_2 content.
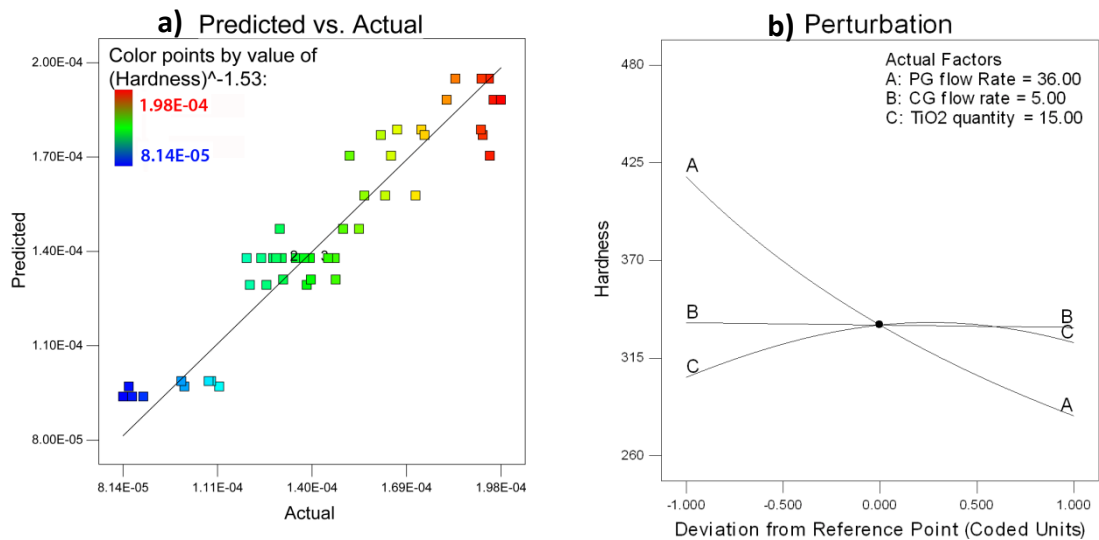
Figure 5.96. Vickers Hardness model: a) Predicted vs. Actual plot and b) Perturbation plot at central point value (HA/TiO_2 series)

The hardness of TiO_2 is higher than that of HA (Table 2.8) so that an increase in deposition efficiency of TiO_2 particles results in an increase in coating hardness. Therefore, the study of the effect of the BC interaction is critical to understand which carrier gas flow rate optimised the injection of the TiO_2. The effect of plasma gas flow rate is also studied for the different TiO_2 contents (AC interaction). A summary of the findings during the study of the BC contours for different plasma gas flow rates is shown in Table 5.36. Several conclusions can be drawn from the study of Table 5.36:

1. Maximum hardness occurs for a plasma gas flow rate of 30 slpm whatever the TiO_2 content. This trend, which matched up with the layer thickness trend, indicated that the maximum deposition efficiency of both materials occurred for a plasma gas flow rate of 30 slpm, as particles melted more.

2. It can be also observed that the minimum hardness for a plasma gas flow rate of 30 slpm is higher than the maximum hardness for a plasma gas flow rate of 36 slpm for each C value. The same was observed between the contours for A=36 slpm and A= 42 slpm.

3. It has to be highlighted that for C=15 wt% the hardness seemed to be the same whatever the carrier gas flow rate. For greater TiO_2 contents the maximum hardness occurred for a carrier gas flow rate of 4.5 slpm, whereas for lower TiO_2 contents it occurred for a carrier gas flow rate of 5.5 slpm. Figure 5.97 shows contour 1 as an example.

Table 5.36. Carrier gas flow rate-TiO_2 content interaction effect on Hardness

Contour	TiO_2 content, wt%	Max. hardness	Min. hardness
Contour 1 **(A = 30 slpm)**	C = 25	470 (B=4.5 slpm)	401 (B=5.5 slpm)
	C = 15	419 (B=4.5 slpm)	416 (B=5.5 slpm)
	C = 5	370 (B=5.5 slpm)	330 (B=4.5 slpm)
Contour 2 **(A = 36 slpm)**	C = 25	344 (B=4.5 slpm)	307 (B=5.5 slpm)
	C = 15	335 (B=4.5 slpm)	332 (B=5.5 slpm)
	C = 5	320 (B=5.5 slpm)	293 (B=4.5 slpm)
Contour 3 **(A = 42 slpm)**	C = 25	279 (B=4.5 slpm)	276 (B=5.5 slpm)
	C = 15	283 (all B)	283 (all B)
	C = 5	264 (B=5.5 slpm)	284 (B=4.5 slpm)
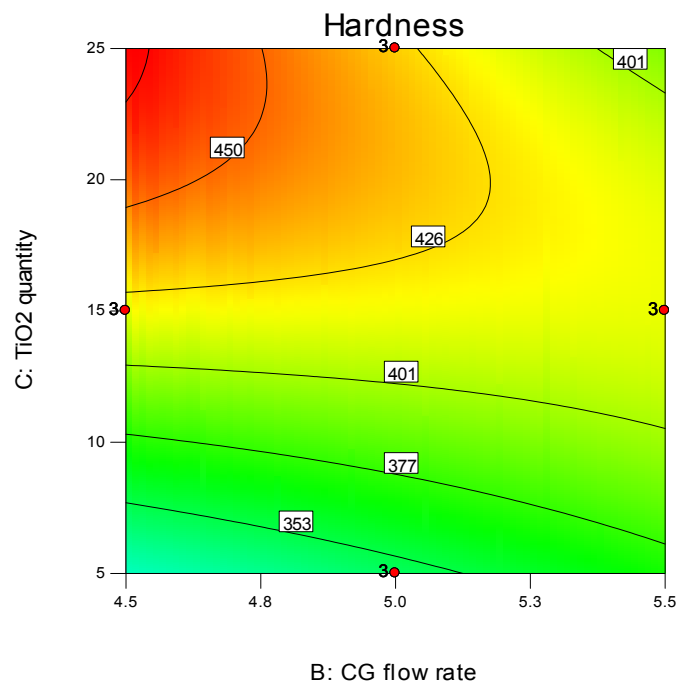
Figure 5.97. Carrier gas flow rate- TiO_2 quantity interaction for hardness model

As observed in Figure 5.98 a maximum hardness occurred for a combination of a 30 slpm plasma gas flow rate and the maximum amount of titanium, 25%wt. As the carrier gas increases the maximum hardness still occurred for a plasma gas flow rate of 30 slpm but for smaller amounts of TiO_2. This indicates that the carrier gas flow rate should be adjusted for each powder composition, to achieve an optimum injection of the mixture.
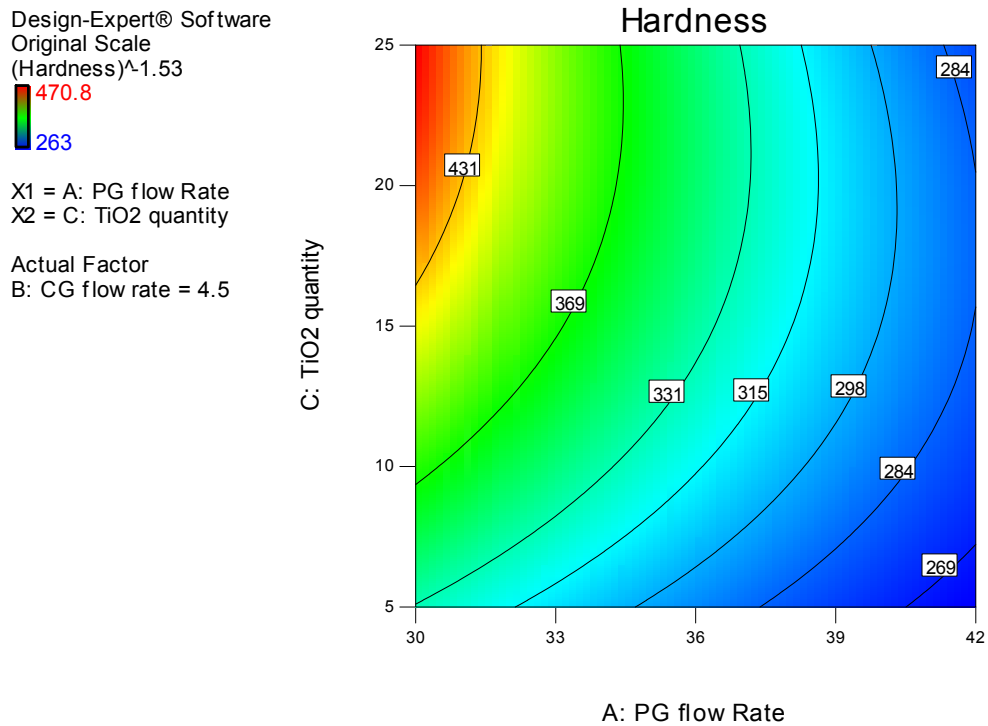
Figure 5.98. Plasma gas flow rate- TiO_2 quantity interaction for hardness model

Young's Modulus

The Young's modulus (E) results (Figure 5.99) presented large standard deviations, with values ranging between 2.67-5.30 GPa. The higher Young's Modulus for this series (HT7) was found to be 10% higher than the maximum value found for HA reference series (HA14). However, in general HA/TiO_2 series presented a similar Young's modulus range compared to the HA reference series. Again it can be noticed that the samples sprayed at lower plasma gas flow rate showed greater Young's Modulus. By observing the values of samples HT17, HAT 18 and HT19, it can be noticed that Young's Modulus increased as the TiO_2 content increased for the remaining parameters kept constant. The effect of the factors on this response was studied using a statistical model.

Figure 5.99. Young's Modulus results for HA/TiO$_2$ composite series

A power transformation (y'=y$^\lambda$, λ=-0.81) was applied to this response. The Young's Modulus was fitted by a quadratic model, for which the design was replicated (3) in order to provide enough data to the DOE software to conduct the lack of fit test. A stepwise automatic reduction algorithm was used to remove insignificant terms (95 % significance). The ANOVA table for this response is given in Table 5.37. A definition of the statistical values which helps to analyse ANOVA results is described in Appendix B.

Table 5.37. ANOVA table for Young's Modulus (HA/TiO$_2$ series)

Source	SS	MS	F-value	Prob>F (p)	Significance
Model	0.12	0.025	42.77	<0.0001	significant
A-PG flow rate	0.10	0.10	177.08	<0.0001	
C- TiO$_2$ quantity	2.223E-4	2.223E-4	0.39	0.5370	
AC	7.325E-3	7.325E-3	12.75	0.0009	
A^2	6.216E-3	6.216E-3	10.82	0.0020	
C^2	8.110E-3	8.110E-3	14.12	0.0005	
Lack of fit	7.188E-3	1.027E-3	2.09	0.0683	not significant
R^2	0.8262		**Pred R^2**		0.7709
Adj R^2	0.8068		**Adeq Precision**		22.293

The model was found to be significant (p <0.0001) and the lack of fit insignificant. The R^2 value was adequate, the difference between adjusted and predicted R^2 was smaller than 0.2 and there was an adequate signal-to-noise ratio (Adeq. precision>4). As a

result, it can be concluded that the model properly fits the experimental data obtained.

The Young's Modulus was found to be quadratically affected by the plasma gas flow rate (A^2) and the TiO$_2$ quantity (C^2). The interaction between the plasma gas flow rate and the TiO$_2$ quantity (AC) was found to affect the response too. The equation modelling the response in terms of the actual factors is:

$$y' = y^{-0.81} = -0.6 + 0.5x_1 - 2 \cdot 10^{-2}x_3 + 4.1 \cdot 10^{-4}x_1x_3 \\ -6.2 \cdot 10^{-4}x_1^2 + 2.5 \cdot 10^{-4}x_3^2$$

Eq. 5.7

where y is the modelled response (Young's Modulus, GPa), x_1 is the plasma gas flow rate (slpm) and x_3 is the TiO$_2$ quantity (wt%).

Figure 5.100a shows the predicted values plotted against the actual values measured in the experiments. It shows that all design points (17) and replicates (34) lie around the line, which proves that the response is well predicted by the model. The perturbation plot (Figure 5.100b) indicates that plasma gas flow rate has major effect on this response.

Figure 5.100. Young's Modulus model: a) Predicted vs. Actual plot and b) Perturbation plot at central point value (HA/TiO$_2$ series)

The elastic modulus of the coating increased as the TiO_2 content increased, which was expected as TiO_2 has higher Young's Modulus than HA. The higher Young's Modulus values occurred for a plasma gas flow rate of 30 slpm (Figure 5.101) whatever the carrier gas flow rate or powder composition. Even if it was not significant for the modelling of this response, the carrier gas flow rate was seen as an important factor to efficiently place the TiO_2 powder into the plume. Therefore, the observations made during the study of hardness also apply for this response.

Figure 5.101. Plasma gas flow rate- TiO_2 quantity interaction for Young's Modulus model

Fracture toughness

The fracture toughness (K_{IC}) results (Figure 5.102) presented large standard deviations, with values ranging between 0.75-1.14 $MPa \cdot m^{1/2}$, which meant an increase in the range of 6-61% respect to the maximum fracture toughness of the HA reference series (sample HA12, 0.71 GPa). This improvement was expected due to the presence of a second phase material, which cause the crack growth to stop. Again it can be noticed that the samples sprayed at lower plasma gas flow rate showed greater fracture toughness. By observing the values of samples HT17, HAT 18 and HT19, it can be noticed that fracture toughness increased as the TiO_2 content increased for the

remaining parameters kept constant. The effect of the factors on this response was studied using a statistical model.
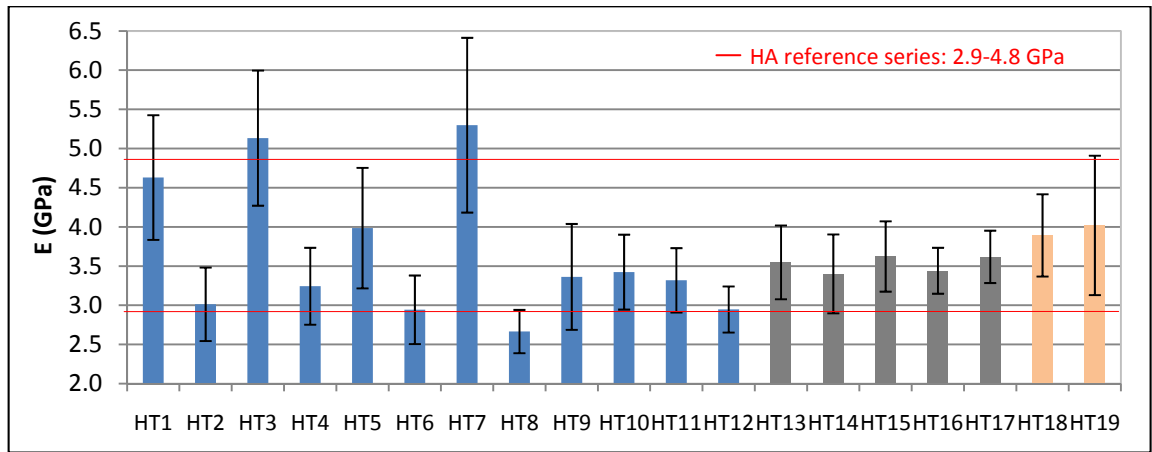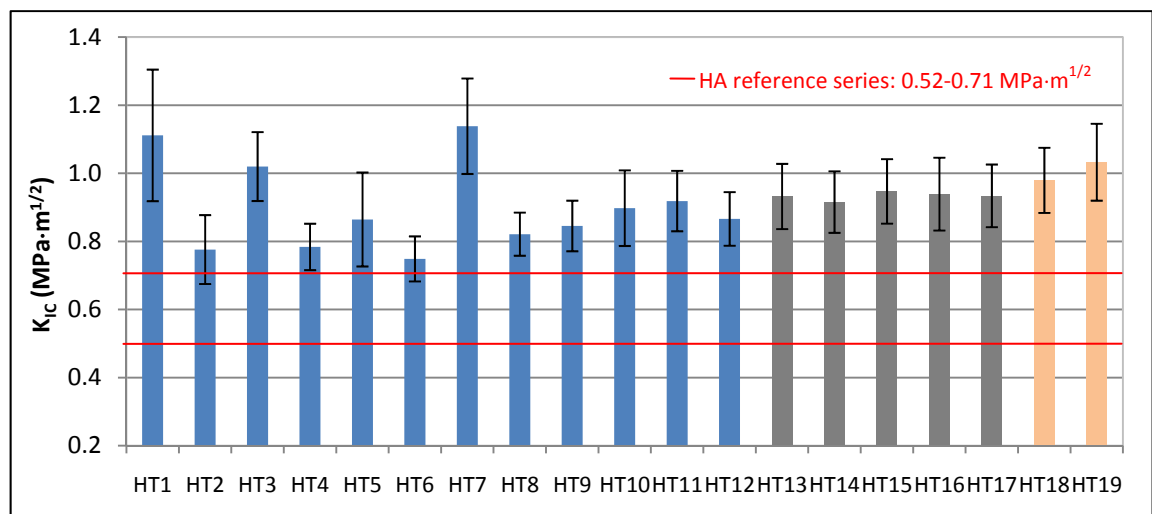

Figure 5.102. Fracture Toughness results for HA/TiO$_2$ composite series

A power transformation (y'=y$^\lambda$, λ=-0.1) was applied to this response. The fracture toughness was fitted by a 2FI (two factors interaction) model, for which the design was replicated (3) in order to provide enough data to the DOE software to conduct the lack of fit test. A stepwise automatic reduction algorithm was used to remove insignificant terms (95 % significance). The ANOVA table for this response is given in Table 5.38. A definition of the statistical values which helps to analyse ANOVA results is described in Appendix B.

Table 5.38. ANOVA table for Fracture toughness (series HA/TiO$_2$)

Source	SS	MS	F-value	Prob>F (p)	Significance
Model	4.129E-3	1.376E-3	27.64	<0.0001	significant
A-PG flow rate	3.339E-3	3.339E-3	67.05	<0.0001	
C- TiO$_2$ quantity	5.732E-4	5.732E-4	11.49	0.0014	
AC	2.183E-3	2.183E-3	4.38	0.0418	
Lack of fit	6.323E-4	7.025E-5	1.57	0.1615	not significant
R^2	0.6432		**Pred R^2**		0.5634
Adj R^2	0.6199		**Adeq Precision**		16.972

The model was found to be significant (p < 0.0001) and the lack of fit insignificant. The R^2 value is adequate ($R^2 > 0.6$), the difference between adjusted and predicted R^2 is smaller than 0.2 and there is an adequate signal-to-noise ratio (Adeq. precision>4). In view of this, it can be concluded that the model properly fits the experimental data obtained.

The fracture toughness was found to be linearly affected by the plasma gas flow rate and the TiO_2 quantity (A, C) and the interaction between them (AC). The equation modelling the response in terms of the actual factors is:

$$y' = y^{-0.1} = +1 + 9.4 \cdot 10^{-4} x_1 - 3 \cdot 10^{-3} x_3 + 7.1 \cdot 10^{-5} x_1 x_3 \qquad \text{Eq. 5.8}$$

where y is the modelled response (fracture toughness, $MPa \cdot m^{1/2}$), x_1 is the plasma gas flow rate (slpm) and x_3 is the TiO_2 quantity (wt%).

Figure 5.103a shows the predicted values plotted against the actual values measured in the experiments. It shows that all design points (17) and replicates (34) lie around the line, which proves that the response is well predicted by the model. The perturbation plot (Figure 5.103b) indicates that plasma gas flow rate has major effect on this response.
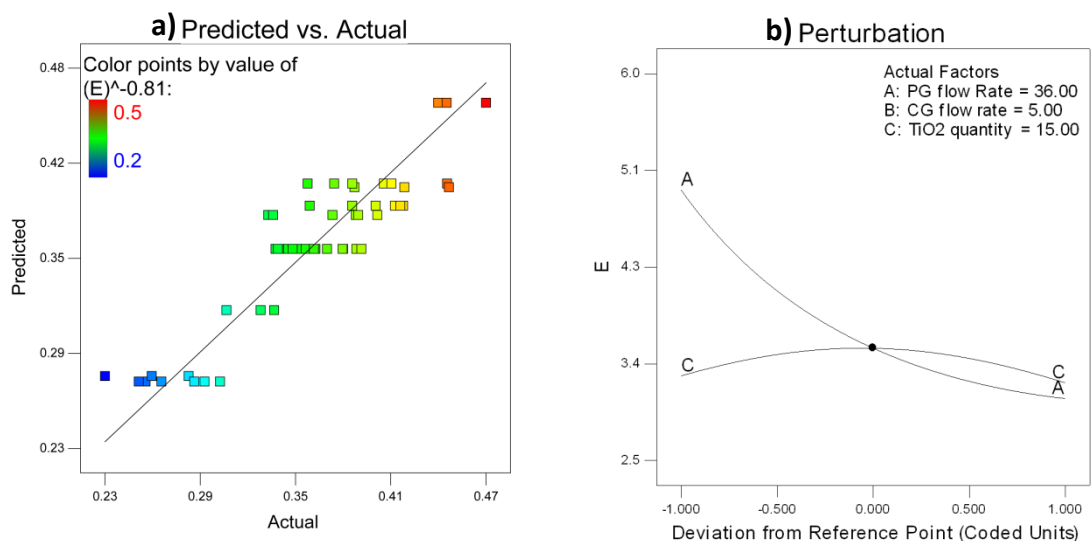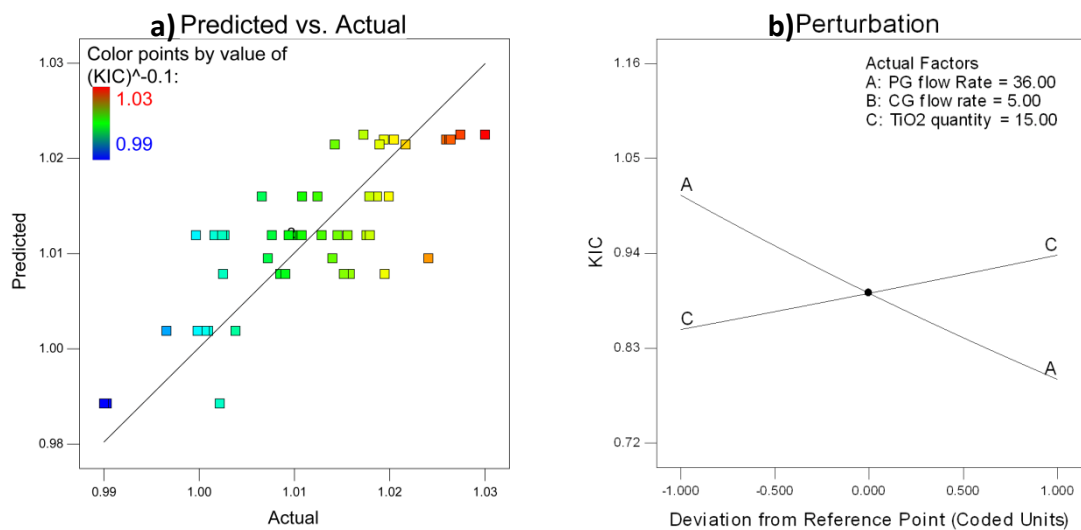

Figure 5.103. Fracture toughness model: a) Predicted vs. Actual plot and b) Perturbation plot at central point value (HA/TiO₂ series)

The fracture toughness of the coating increased as the TiO_2 content increased, which was expected as a greater amount of second phase material introduced more discontinuities within the coatings, which prevented cracks propagation. The higher fracture toughness values occurred for a plasma gas flow rate of 30 slpm (Figure 5.104) for every TiO_2 quantity regardless of the carrier gas flow rate. Even though it was not significant for the modelling of this response, the carrier gas flow rate was seen an important factor to efficiently introduce the TiO_2 powder into the plume. Therefore, the observations made during the study of hardness also apply for this response.
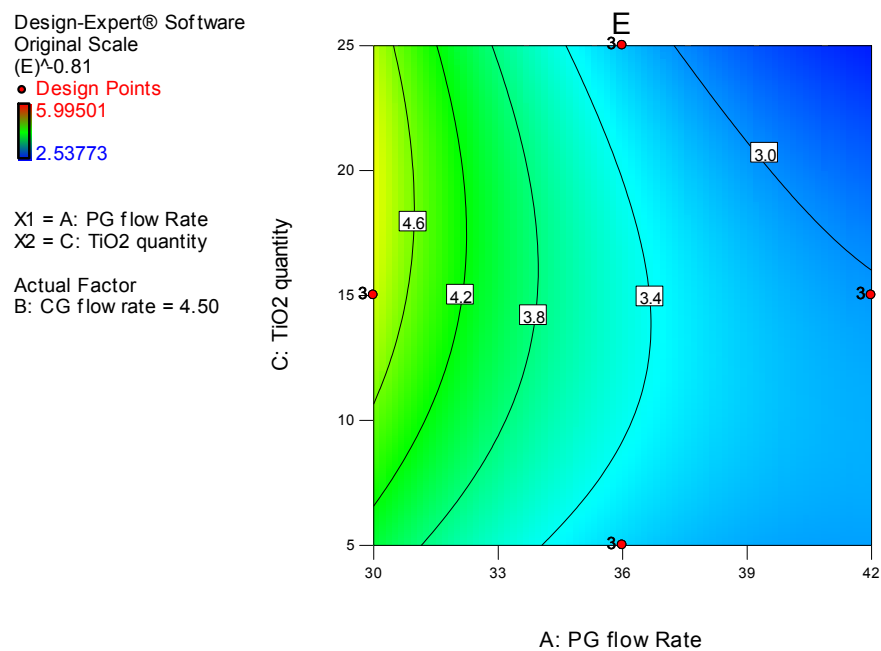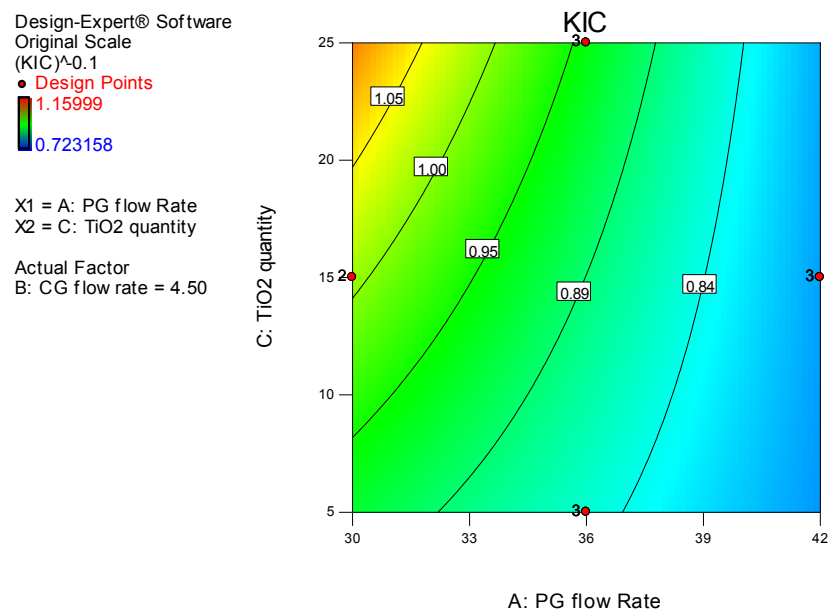

Figure 5.104. Plasma gas flow rate- TiO_2 quantity interaction for fracture toughness

5.5.5. Summary of HA/TiO₂ composite series

The effect of TiO_2 on the coating properties depends on its deposition efficiency and its melting degree, which in turn depend on the three factors studied: A (plasma gas flow rate), B (carrier gas flow rate) and C (initial TiO_2 content in the powder). A summary of the properties measured can be seen in Table 5.39. The addition of TiO_2 to HA significantly increased the layer thickness (60-215%) and the fracture toughness (6-61%) of the coatings. The hardness and Young's modulus presented similar ranges of variation than those found for HA reference series, but there were samples with significantly higher mechanical properties, which were those sprayed at plasma gas flow rates of 30 slpm. The roughness was not affected by the addition of TiO_2.

Table 5.39. Range of variation on the properties measured for HA/TiO$_2$ series

Response	HA/TiO$_2$ series	HA reference series
Layer thickness, μm	52.8-104	4.8-33
Roughness, μm	5.34-6.55	5.49-6.47
Vickers Hardness, HV	268-463	244-351
Young's Modulus, GPa	2.67-5.30	2.9-4.8
Fracture toughness, MPa·m$^{1/2}$	0.75-1.14	0.52-0.71

Firstly, it seems that for all the responses studied, the higher layer thickness and mechanical properties occurred for those samples sprayed at a plasma gas flow rate of 30 slpm. The TiO$_2$ particles have a higher melting temperature than HA particles and therefore the hottest plasma configuration (lower plasma gas flow rate) should be used to increase the deposition efficiency.

Secondly, the amount of TiO$_2$ particles which are efficiently injected into the plume depends on the carrier gas flow rate. The optimal carrier gas to inject TiO$_2$ particles decreased towards 4.5 slpm as the initial TiO$_2$ quantity increased towards 25 wt%, which may be related to the relative number of particles (HA/TiO$_2$) present on the feedstock powder. For instance, it was found that for a 5 wt% of TiO$_2$ a carrier gas close to 5.5 slpm resulted in the higher hardness values. Nevertheless, at such carrier gas flow rates the HA injection was less efficient and therefore the overall layer thickness decreased.

The addition of TiO$_2$ was proposed to enhance the mechanical properties of the coatings, so a statistical optimisation was conducted to find the plasma parameter combination leading to the best mechanical properties. The best solution obtained, which is shown in Table 5.40, had a desirability of 0.902. The optimum set of factors leading to the highest mechanical properties was found to be: plasma gas flow rate of 30 slpm, carrier gas flow rate of 4.5 slpm and initial TiO$_2$ quantity of 25 wt%.

Table 5.40. Predicted optimal set of parameters

Parameter	Goal (Importance)	Lower Limit	Upper Limit
A: PG flow Rate	is in range	30	42
B: CG flow rate	is in range	4.5	5.5
C: TiO_2 quantity	is in range	5	25
Hardness	maximise (3+)	263	470
Young's modulus	maximise (3+)	2.5	5.9
Fracture Toughness	maximise (3+)	0.72	1.15

Solution	A	B	C	Hv_{100g}	E	K_{IC}	Desirability
1	30	4.5	25	474	4.9	1.1	0.902

However, the ultimate goal to be pursued in future would be to produce a composite coating formed by HA/PCL/TiO_2 (Figure 1.1) and the addition of PCL would require fixing the plasma gas flow rate to a higher value (36 slpm), so a statistical optimisation was conducted to find the new plasma parameter combination leading to the best mechanical properties which will be used for comparison. The two solutions obtained, which are shown in Table 5.41, had in this case a desirability of 0.501. As observed, an initial TiO_2 content of 20 wt% would lead to the best set of mechanical properties at a plasma gas flow rate of 36 slpm.

Table 5.41. Predicted optimal set of parameters

Parameter	Goal (Importance)	Lower Limit	Upper Limit
A: PG flow Rate	is equal to 36	30	42
B: CG flow rate	is in range	4.5	5.5
C: TiO_2 quantity	is in range	5	25
Hardness	maximise (3+)	263	470
Young's modulus	maximise (3+)	2.5	5.9
Fracture Toughness	maximise (3+)	0.72	1.15

Solution	A	B	C	Hv_{100g}	E	K_{IC}	Desirability
1	36	4.5	20.10	346	3.4	0.92	0.501
2	36	4.5	19.98	346	3.4	0.92	0.501

6. Conclusions and recommendations for future work

This chapter presents the conclusions of this work, answering the questions which motivated this research. The recommendations for future work are listed in Section 6.1.

Is it feasible to fabricate a HA deposit thick enough to potentially be a scaffold?

Using the LEPS system, Hydroxyapatite free-standing components of thickness close to 3 mm were produced during the selection tests (Section 5.2.1), which is the approximate thickness of cortical bone in female femoral bones [22]. This thickness was produced at a layer increment of 72 μm/layer approximately, with 40 spray layers. The components showed minor cracking which indicated that no major residual stresses built up during the processing. For this reason, it is expected a further increase in thickness could be achieved by increasing the number of spray layers. Complementing this, the addition of a second phase material was found to increase deposition efficiency. A layer increment of 117.3 μm/layer was achieved by adding PEEK to the Hydroxyapatite matrix. The layer increments achieved during the study of composite series HA/PCL (section 5.4) and HA/TiO$_2$ (section 5.5) were found to be significantly higher than those for HA reference series. An increase in layer increment entails a decrease in the processing time for a given thickness, and therefore, has a positive economic impact.

Is it feasible to obtain HA based deposits with the required porosity by adding a polymer?

Hydroxyapatite deposits obtained in Section 5.3 presented closed porosity ranging from 2.5 to 6%. The addition of PCL slightly improved the amount of porosity of the coatings (4.2-7.6%), but significantly improved the morphology of the porosity, which presented local interconnectivity. However, while the percentage of porosity achieved for HA/PCL series lies close to the lower limit of cortical bone range (5-30%) [20, 23], a more evenly distributed porosity through the entire deposit is desired. Furthermore, the pore size was in all cases lower than 20 μm which is proven insufficient to allow cells migration and, therefore, promote tissue growth throughout the deposit [14].

The obtained results could be improved to a certain extent by making several system improvements (vibration feeding system, cooling system, water-cooled injector), but it seen as difficult to fulfil the requirements for bone tissue engineering scaffolds in terms of porosity.

On the other hand, it was found that the addition of PCL significantly improved the roughness of the deposits up to in a 125% respect to that of the HA coatings. This is a positive result, as the roughness plays an important role in cell attachment and differentiation. In the light of this improvement in roughness, it is seen that the addition of PCL could encompass advantages for current plasma sprayed coating applications, such as hip implants.

Is it feasible to produce a HA based deposit with the appropriate mechanical properties to be a scaffold?

Hydroxyapatite is a brittle material with low fracture toughness. The best mechanical properties achieved during the studies of HA and HA/TiO$_2$ series can be seen in Table 6.1, together with the mechanical properties of natural bone [20, 24]. As observed, the addition of Titania improved the hardness by 32%, the young's Modulus by 10% and the fracture toughness by 60%. The improvement of toughness means that deposits produced have similar mechanical properties of those of spongy bone, but they still lie far from those of cortical bone.

Table 6.1. Higher mechanical properties obtained for HA and HA/TiO$_2$ series

Mechanical property	HA series	HA/TiO$_2$	Cortical	Spongy
Hardness, HV	351	463	N/A	N/A-
Young's Modulus, GPa	4.8	5.3	7-30	0.01-3
Fracture toughness, MPa·m$^{1/2}$	0.71	1.14	12	2

Legend: N/A: Not available

As shown in Section 5.5, the effect of Titania on the coatings depends on its quantity and degree of melting, which in turn depend mainly in the plasma gas flow rate used to spray the samples. The lowest plasma gas flow rate gave rise to the greatest TiO$_2$ retention and, as a result, to the better mechanical properties. Therefore, it is seen

that a further reduction of the plasma gas flow rate would lead to improved mechanical properties. However, this reduction would encompass a reduction in crystallinity and maybe in phase purity of the HA, so it should be done with caution.

Otherwise, the use of YSZ was expected to greatly improve the fracture toughness of the composites due to its transformation-toughening mechanism. However, the agglomerated powders produced did not flow in the system. It is seen that an optimisation of the powder production method would improve the powder flowability in the system and, therefore, lead to much better mechanical properties in the composites.

Is Plasma spraying likely to provide a solution to the challenge of manufacturing artificial bone structures?

A high porosity and good mechanical properties, which in general are inversely proportional, are the main requirements for an artificial bone structure.

During the course of this research it was found that it is possible to fabricate composite coatings with porosity close to the lower value of cortical bone but far less than that of spongy bone. On the other hand, it was possible to fabricate composite coatings with mechanical properties adequate for spongy bone substitution, but insufficient for cortical bone substitution.

Once the coatings have good integrity and stability to be handle, the mechanical properties lose importance if the target application is to serve as carrier matrices to growth tissue before implanting. However, this requires greater porosity.

It is assessed that plasma spraying is not an appropriate technique for manufacturing scaffolds. Rapid prototyping techniques are seen as a better option to fabricate such structures with controlled porosity [235]. However, there are important results arising from this work, which may be considered to improve the characteristics and applicability.

- The HA has been proven to undergo minor dehydroxylation by using a low energy plasma spray system. The crystallinity of the HA coatings is high without the need of a post-spray heat treatment.
- It has been shown that the ceramic-ceramic configuration helps to improve the fracture toughness of the deposits produced using the LEPS system.
- It has been proved that polymer can be deposited without major degradation. Particularly, PCL a bioreabsorbable polymer with melting temperature of $60^{o}C$ has been sprayed without degradation.

6.1. Recommendations for future work

- It is seen that the addition of YSZ to the HA can significantly improved the mechanical properties of the composites. Further studies on the agglomeration stage are required to improve the flowability of this agglomerated powder into the system.
- The addition of PCL has been proved to slightly improve the porosity of the deposits. Improvements on the feeding system are required to ensure the constant feeding of this powder. The cladding option, where the HA can protect the core PCL allowing the powders to be fed through the same injector, could also be explored.
- In the future PCL encapsulating thermally stable drugs or bio-molecules can be applied by plasma spray in order to improve the biological response to coated metallic implants.

References

[1] Geesink, R. G., de Groot, K. and Klein, C. P., 'Bonding of bone to apatite-coated implants', J Bone Joint Surg Br, Vol. 70B, no. 1, 1988, pp. 17-22.

[2] Soballe, K., Hansen, E. S., Brockstedt-Rasmussen, H. and Bunger, C., 'Hydroxyapatite coating converts fibrous tissue to bone around loaded implants', J Bone Joint Surg Br, Vol. 75B, no. 2, 1993, pp. 270-278.

[3] Yang, C. Y., Wang, B. C., Chang, E. and Wu, J. D., 'The influences of plasma spraying parameters on the characteristics of hydroxyapatite coatings: a quantitative study', J Mat Sci -Mater M, Vol. 6, no. 5, 1995, pp. 249-257.

[4] Gazdag, A. R., Lane, J. M., Glaser, D. and Forster, R. A., 'Alternatives to autogenous bone graft: efficacy and indications', J Am Acad Orthop Surg, Vol. 3, no. 1, 1995, pp. 1-8.

[5] Nasr, H. F., Aichelmann-Reidy, M. E. and Yukna, R. A., 'Bone and bone substitutes', Periodontology 2000, Vol. 19, 1999, pp. 74-86.

[6] Kokubo, T., Kim, H.-M. and Kawashita, M., 'Novel bioactive materials with different mechanical properties', Biomaterials, Vol. 24, 2003, pp. 2161-2175.

[7] Rodrigues, C. V. M., Serricella, P., Linhares, A. B. R., Guerdes, R. M., Borojevic, R., Rossi, M. A., Duarte, M. E. L. and Farina, M., 'Characterization of a bovine collagen-hydroxyapatite composite scaffold for bone tissue engineering', Biomaterials, Vol. 24, no. 27, 2003, pp. 4987-4997.

[8] Drosse, I., Volkmer, E., Capanna, R., Biase, P. D., Mutschler, W. and Schieker, M., 'Tissue engineering for bone defect healing: An update on a multi-component approach', Injury, Vol. 39, no. 2, 2008, pp. S9-S20.

[9] Roberts, S. J., Howard, D., Buttery, L. D. and Shakesheff, K. M., 'Clinical applications of musculoskeletal tissue engineering', Brit Med Bull, Vol. 86, no. 1, 2008, pp. 7-22.

[10] Reichert, J. C., Saifzadeh, S., Wullschleger, M. E., Epari, D. R., Schütz, M. A., Duda, G. N., Schell, H., van Griensven, M., Redl, H. and Hutmacher, D. W., 'The challenge of establishing preclinical models for segmental bone defect research', Biomaterials, Vol. 30, no. 12, 2009, pp. 2149-2163.

[11] Schieker, M., Seitz, H., Drosse, I., Seitz, S. and Mutschler, W., 'Biomaterials as scaffold for bone tissue engineering', European Journal of Trauma, Vol. 32, no. 2, 2006, pp. 114-124.

[12] Liebschner, M. A. K. and Wettergreen, M. A., 'Optimization of bone scaffold engineering for load bearing applications', In: Topics in Tissue Engineering. N. Ashammakhi and P. Ferretti (eds.) (University of Oulu; 2003).

[13] http://imi.cnrc-nrc.gc.ca/docs/factsheets/scaffold_e.pdf, 'Transient mechanical performance of scaffold', (Research Group in Cartilage/Bone Scaffold Design. Industrial Materials Institute National Research Council Canada; Boucherville, Quebec, Canada, 2003).

[14] Biomaterials, artificial organs and tissue engineering, Hench, L. L. and Jones, J. R. (eds.) (Woodhead Publishing Ltd; Cambridge, UK, 2005).

[15] Mastrogiacomo, M., Muraglia, A., Komlev, V., Peyrin, F., Rustichelli, F., Crovace, A. and Cancedda, R., 'Tissue engineering of bone: search for a better scaffold', Orthod Craniofac Res, Vol. 8, no. 4, 2005, pp. 277-284.

[16] Yan, C., Starly, B., Gomez, C., Fang, Z. and Sun, W., 'On effective properties of heterogeneous bone scaffold', Bioengineering Conference, IEEE (ed.) (IEEE; 2003), pp. 170-171.

[17] Meinel, L., Karageorgiou, V., Fajardo, R., Snyder, B., Shinde-Patil, V., Zichner, L., Kaplan, D., Langer, R. and Vunjak-Novakovic, G., 'Bone tissue engineering using human mesenchymal stem cells: effects of scaffold material and medium flow', Annals of Biomedical Engineering, Vol. 32, no. 1, 2004, pp. 112-122.

[18] The biomedical engineering handbook, Bronzino, J. D. (ed.) (CRC Press; Boca Raton, Florida, USA, 2006).

[19] Karageorgiou, V. and Kaplan, D., 'Porosity of 3D biomaterial scaffolds and osteogenesis', Biomaterials, Vol. 26, no. 27, 2005, pp. 5474-5491.

[20] Standard handbook of biomedical engineering & design, Kutz, M. (ed.) (McGraw-Hill; New York, USA, 2003).

[21] Wang, X. and Ni, Q., 'Determination of cortical bone porosity and pore size distribution using a low field pulsed NMR approach', J Orthopaed Res, Vol. 21, no. 2, 2003, pp. 312-319.

[22] Bousson, V., Meunier, A., Bergot, C., Vicaut, E., Rocha, M. A., Morais, M. H., Laval-Jeantet, A.-M. and Laredo, J.-D., 'Distribution of intracortical porosity in human midfemoral cortex by age and gender', J Bone Miner Res, Vol. 16, no. 7, 2001, pp. 1308-1317.

[23] Wachter, N. J., Krischak, G. D., Mentzel, M., Sarkar, M. R., Ebinger, T., Kinzl, L., Claes, L. and Augat, P., 'Correlation of bone mineral density with strength and microstructural parameters of cortical bone in vitro', Bone, Vol. 31, no. 1, 2002, pp. 90-95.

[24] An introduction to bioceramics, Hench, L. L. and Wilson, J. (eds.) (World Scientific; Singapore, 1993).

[25] Sun, L., Berndt, C. C., Gross, K. A. and Kucuk, A., 'Material fundamentals and clinical performance of plasma-sprayed hydroxyapatite coatings: a review', J Biomed Mater Res-B, Vol. 58, no. 5, 2001, pp. 570-592.

[26] Szucs, T., 'Production of hard tissue scaffolds using three-dimensional printing method', MEng Thesis, (Dublin City University; Dublin, Ireland, 2008).

[27] Eosoly, S., Ryder, G., Tansey, T. and Looney, L., 'Selective laser sintering of bioresorbable microstructures', 8th World biomaterials congress, (Poster presentation; Amsterdam, The Netherlands, 2008).

[28] Levingstone, T., 'Ceramics for medical applications', In: Graduate Level Resources in Materials Engineering. L. Looney (ed.) (Dublin City University; Dublin, 2008).

[29] Kehoe, S., 'Calcium phosphates for medical applications', In: Graduate Level Resources in Materials Engineering. J. Stokes (ed.) (Dublin City University; Dublin, 2008).

[30] Williams, D. F., 'Titanium for medical applications', In: Titanium in medicine. D.M. Brunette (ed.) (Springer; Germany, 2001).

[31] Staiger, M. P., Pietak, A. M., Huadmai, J. and Dias, G., 'Magnesium and its alloys as orthopedic biomaterials: a review', Biomaterials, Vol. 27, no. 9, 2006, pp. 1728-1734.

[32] Mano, J. F., Sousa, R. A., Boesel, L. F., Neves, N. M. and Reis, R. L., 'Bioinert, biodegradable and injectable polymeric matrix composites for hard tissue replacement: state of the art and recent developments', Compos Sci Technol, Vol. 64, no. 6, 2004, pp. 789-817.

[33] Ceramic Matrix Composites, Chawla, K. K. (ed.) (Chapman & Hall; 1993).

[34] Chaikof, E. L., Matthew, H., Kohn, J., Mikos, A. G., Prestwich, G. D. and Yip, C. M., 'Biomaterials and scaffolds in reparative medicine', Annals of the New York Academy of Sciences, Vol. 961, no. Reparative Medicine: Growing tissues and organs, 2002, pp. 96-105.

[35] Wang, M., 'Bioactive Ceramic Matrix Composites', In: Biomaterials and tissue engineering. D. Shi (ed.) (Springer; Germany, 2004).

[36] Evans, S. L. and Gregson, P. J., 'Composite technology in load-bearing orthopaedic implants', Biomaterials, Vol. 19, no. 15, 1998, pp. 1329-1342.

[37] Leng, Y. and Qu, S., 'TEM examination of single crystal hydroxyapatite diffraction', J Mater Sci Lett, Vol. 21, no. 11, 2002, pp. 829-830.

[38] Tanaka, H., Chikazawa, M., Kandori, K. and Ishikawa, T., 'Influence of thermal treatment on the structure of calcium hydroxyapatite', Phys Chem Chem Phys, Vol. 2, 2000, pp. 2647 - 2650.

[39] Yoshida, K., Hashimoto, K., Toda, Y., Udagawa, S. and Kanazawa, T., 'Fabrication of structure-controlled hydroxyapatite/zirconia composite', J Europ Ceram Soc, Vol. 26, no. 4-5, 2006, pp. 515-518.

[40] Silva, V. V., Lameiras, F. S. and Domingues, R. Z., 'Microstructural and mechanical study of zirconia-hydroxyapatite (ZH) composite ceramics for biomedical applications', Compos Sci Technol, Vol. 61, no. 2, 2001, pp. 301-310.

[41] Suchanek, W. and Yoshimura, M., 'Processing and properties of hydroxyapatite-based biomaterials for use as hard tissue replacement implants', J Mater Res, Vol. 13, no. 1, 1998, pp. 94-117.

[42] Chevalier, E., Chulia, D., Pouget, C. and Viana, M., 'Fabrication of porous substrates: A review of processes using pore forming agents in the biomaterial field', J Pharm Sci, Vol. 97, no. 3, 2008, pp. 1135-1154.

[43] Prado da Silva, M. H., Lemos, A. F., Gibson, I. R., Ferreira, J. M. F. and Santos, J. D., 'Porous glass reinforced hydroxyapatite materials produced with different organic additives', J Non-Cryst Solids, Vol. 304, no. 1-3, 2002, pp. 286-292.

[44] Sopyan, I., Mel, M., Ramesh, S. and Khalid, K. A., 'Porous hydroxyapatite for artificial bone applications', Science and Technology of Advanced Materials, Vol. 8, no. 1-2, 2007, pp. 116-123.

[45] Tsui, Y. C., Doyle, C. and Clyne, T. W., 'Plasma sprayed hydroxyapatite coatings on titanium substrates part 1: mechanical properties and residual stress levels', Biomaterials, Vol. 19, no. 22, 1998, pp. 2015-2029.

[46] Rokkum, M., Brandt, M., Bye, K., Hetland, K. R., Waage, S. and Reigstad, A., 'Polyethylene wear, osteolysis and acetabular loosening with an HA-coated hip prosthesis: a folollow-up of 94 consecutive arthroplasties', J Bone Joint Surg Br, Vol. 81B, no. 4, 1999, pp. 582-589.

[47] Khor, K. A., Gua, Y. W., Queka, C. H. and Cheang, P., 'Plasma spraying of functionally graded hydroxyapatitey Ti–6Al–4V coatings', Surf Coat Tech, Vol. 168, 2003, pp. 195-201.

[48] Li, H., Khor, K. A. and Cheang, P., 'Thermal sprayed hydroxyapatite splats: nanostructures, pore formation mechanisms and TEM characterization', Biomaterials, Vol. 25, no. 17, 2004, pp. 3463-3471.

[49] Gibbons, D. E., 'Materials for orthopedic joint prostheses', In: Biocompatibility of orthopedic implants. D. F. Williams (ed.) (CRC Press Boca Raton, Florida, 1982).

[50] Handbook of biomaterial properties, Black, J. and Hastings, G. (eds.) (Chapman & Hall; London, UK, 1998).

[51] Legeros, R. Z., 'Calcium phosphate materials in restorative dentistry: a review', Adv Dent Res, Vol. 2, no. 1, 1988, pp. 164-180.

[52] Yang, Y. C., Chang, E., Hwang, B. H. and Lee, S. Y., 'Biaxial residual stress states of plasma-sprayed hydroxyapatite coatings on titanium alloy substrate', Biomaterials, Vol. 21, no. 13, 2000, pp. 1327-1337.

[53] Manicone, P. F., Rossi, P. and Raffaelli, L., 'An overview of zirconia ceramics: basic properties and clinical applications', J Dent, Vol. 35, no. 11, 2007, pp. 819-826.

[54] Garvie, R. C., Hannink, R. H. and Pascoe, R. T., 'Ceramic steel?' Nature, Vol. 258, no. 5537, 1975, pp. 703-704.

[55] Gremillard, L. and Chevalier, J., 'Durability of zirconia-based ceramics and composites for total hip replacement', Key Eng Mat, Vol. 361-363, 2008, pp. 791-794.

[56] Piconi, C. and Maccauro, G., 'Zirconia as a ceramic biomaterial', Biomaterials, Vol. 20, no. 1, 1999, pp. 1-25.

[57] ASM handbook Vol. 2 -Properties and selection - nonferrous alloys and special-purpose materials, (ASM International; USA, 1992).

[58] Kong, Y.-M., Kim, S., Kim, H.-E. and Lee, I.-S., 'Reinforcement of hydroxyapatite bioceramic by addition of ZrO_2 Coated with Al_2O_3', J Am Ceram Soc, Vol. 82, no. 11, 1999, pp. 2963-2968.

[59] Xie, Y., Liu, X., Ding, C. and Chu, P. K., 'Bioconductivity and mechanical properties of plasma-sprayed dicalcium silicate/zirconia composite coating', Mat Sci Eng C, Vol. 25, no. 4, 2005, pp. 509-515.

[60] Yamashita, D., Kanbara, K., Machigashira, M., Miyamoto, M., Sato, H., Izumi, Y. and Ban, S., 'Proliferation of osteoblast-like cells on zirconia/alumina nanocomposite', Key Eng Mat, Vol. 361-363, 2008, pp. 1099-1102.

[61] Titanium: past, present and future (National Academy Press; Washington D.C., USA, 1983).

[62] Materials handbook, Brady, G. S., Clauser, H. R. and Vaccari, J. A. (eds.) (McGraw-Hill; New York, USA, 2002).

[63] Handbook of chemistry and physics, Lide, D. R. (ed.) (CRC Press; Boca Raton, Florida, USA, 2001).

[64] Steinemann, S. G., 'Titanium - the material of choice?' Periodontology 2000, Vol. 17, no. 1, 1998, pp. 7-21.

[65] Ratner, B. D., 'A Perspective in titanium biocompatibility', In: Titanium in medicine. D.M. Brunette (ed.) (Springer; Germany, 2001), pp. 2-12.

[66] Thomsen, P., Larsson, C., Ericson, L. E., Sennerby, L., Lausmaa, J. and Kasemo, B., 'Structure of the interface between rabbit cortical bone and implants of gold, zirconium and titanium', Journal of Materials Science: Materials in Medicine, Vol. 8, no. 11, 1997, pp. 653-665.

[67] Kokubo, T., Kim, H. M., Kawashita, M. and Nakamura, T., 'Bioactive metals: preparation and properties', J Mat Sci –Mater M, Vol. 15, no. 2, 2004, pp. 99-107.

[68] 'Medical data sheet: Why is titanium the metal of choice for medical applications from head to toe', (International Ti association Colorado, USA, 1999).

[69] Kobayashi, A. and Jiang, W., 'Properties of titania/hydroxyapatite nanostructured coating produced by gas tunnel type plasma spraying', Vacuum, Vol. 83, 2009, pp. 86-91.

[70] Brohede, U., Zhao, S., Lindberg, F., Mihranyan, A., Forsgren, J., Strømme, M. and Engqvist, H., 'A novel graded bioactive high adhesion implant coating', Appl Surf Sci, Vol. 255, no. 17, 2009, pp. 7723-7728.

[71] Forsgren, J., Svahn, F., Jarmar, T. and Engqvist, H., 'Formation and adhesion of biomimetic hydroxyapatite deposited on titanium substrates', Acta Biomaterialia, Vol. 3, no. 6, 2007, pp. 980-984.

[72] Svetina, M., Colombi Ciacchi, L., Sbaizero, O., Meriani, S. and De Vita, A., 'Deposition of calcium ions on rutile (110): a first-principles investigation', Acta Materialia, Vol. 49, no. 12, 2001, pp. 2169-2177.

[73] Vallés, G., González-Melendi, P., González-Carrasco, J. L., Saldaña, L., Sánchez-Sabaté, E., Munuera, L. and Vilaboa, N., 'Differential inflammatory macrophage response to rutile and titanium particles', Biomaterials, Vol. 27, no. 30, 2006, pp. 5199-5211.

[74] Han, Y., Chen, D., Sun, J., Zhang, Y. and Xu, K., 'UV-enhanced bioactivity and cell response of micro-arc oxidized titania coatings', Acta Biomaterialia, Vol. 4, no. 5, 2008, pp. 1518-1529.

[75] Jeffery, B., McDonald, A., Peppler, M. and Lima, R. S., 'Bactericidal effects of HVOF-sprayed nanostructured TiO_2 on pseudomonas aeruginosa', Thermal Spray 2009: Proceedings of the International Thermal Spray Conference, B.R. Marple, M.M. Hyland, Y.-C Lau, C.-J. Li, R.S. Lima and G. Montavon (eds.) (ASM International; Las Vegas, USA, 2009), pp. 376-381.

[76] Maness, P.-C., Smolinski, S., Blake, D. M., Huang, Z., Wolfrum, E. J. and Jacoby, W. A., 'Bactericidal activity of photocatalytic TiO_2 reaction: toward an understanding of its killing mechanism', Appl Environ Microb, Vol. 65, no. 9, 1999, pp. 4094-4098.

[77] Linsebigler, A. L., Lu, G. and Yates, J. T., 'Photocatalysis on TiO_2 surfaces: principles, mechanisms, and selected results', Chem Rev, Vol. 95, no. 3, 1995, pp. 735-758.

[78] Fostad, G., Hafell, B., Førde, A., Dittmann, R., Sabetrasekh, R., Will, J., Ellingsen, J. E., Lyngstadaas, S. P. and Haugen, H. J., 'Loadable TiO_2 scaffolds - a correlation study between processing parameters, micro-CT analysis and mechanical strength', J Eur Ceram Soc, Vol. 29, no. 13, 2009, pp. 2773-2781.

[79] Fried, J. R., 'Poly (ether ether ketone)', In: Polymer data handbook. (Oxford University Press; 1999), pp. 466-470.

[80] Liao, H., Coddet, C. and Simonin, L., 'Mechanical properties of thermal spray PEEK coatings', ITSC 2001: International Thermal Spray Conference, C. C. Berndt, K. A. Khor and E.F Lungscheider (eds.) (ASM International; Singapore, 2001), pp. 315-320.

[81] Kurtz, S. M. and Devine, J. N., 'PEEK biomaterials in trauma, orthopedic, and spinal implants', Biomaterials, Vol. 28, no. 32, 2007, pp. 4845-4869.

[82] Brandt, J., Pfennig, M., Bieroegel, C., Grellmann, W. and Bernstein, A., 'Hydroxyapatite coating improves bone integration and interface strength of polymer implants in bone', Key Eng Mat, Vol. 396-398, 2009, pp. 331-335.

[83] Sagomonyants, K. B., Jarman-Smith, M. L., Devine, J. N., Aronow, M. S. and Gronowicz, G. A., 'The in vitro response of human osteoblasts to polyetheretherketone (PEEK) substrates compared to commercially pure titanium', Biomaterials, Vol. 29, no. 11, 2008, pp. 1563-1572.

[84] Sinha, V. R., Bansal, K., Kaushik, R., Kumria, R. and Trehan, A., 'Poly-ε-caprolactone microspheres and nanospheres: an overview', Int J Pharm, Vol. 278, no. 1, 2004, pp. 1-23.

[85] Polymeric biomaterials, Dumitriu, S. (ed.) (Marcel Dekker; New York, USA, 1994).

[86] Salgado, C. L., Solomao, Z., Silva, P. B., Sanchez, E. and Zavaglia, C., 'Biocompatibility and osteo-differentiation study of poly (ε-Caprolactone) and β-Tricalcium phosphate composite membranes', Key Eng Mat, Vol. 396-398, 2009, pp. 399-402.

[87] Rezwan, K., Chen, Q. Z., Blaker, J. J. and Boccaccini, A. R., 'Biodegradable and bioactive porous polymer/inorganic composite scaffolds for bone tissue engineering', Biomaterials, Vol. 27, no. 18, 2006, pp. 3413-3431.

[88] Ciapetti, G., Ambrosio, L., Savarino, L., Granchi, D., Cenni, E., Baldini, N., Pagani, S., Guizzardi, S., Causa, F. and Giunti, A., 'Osteoblast growth and function in porous poly ε-caprolactone matrices for bone repair: a preliminary study', Biomaterials, Vol. 24, no. 21, 2003, pp. 3815-3824.

[89] Giavaresi, G., Tschon, M., Borsari, V., Daly, J. H., Liggat, J. J., Fini, M., Bonazzi, V., Nicolini, A., Carpi, A., Morra, M., Cassinelli, C. and Giardino, R., 'New polymers for drug delivery systems in orthopaedics: in vivo biocompatibility evaluation', Biomed Pharmacother, Vol. 58, no. 8, 2004, pp. 411-417.

[90] Cheng, L., Guo, S. and Wu, W., 'Characterization and In Vitro Release of Praziquantel from Poly (ε-caprolactone) Implants', Int J Pharm, Vol. 377, no. 1-2, 2009, pp. 112-119.

[91] Rai, B., Teoh, S. H., Hutmacher, D. W., Cao, T. and Ho, K. H., 'Novel PCL-based honeycomb scaffolds as drug delivery systems for rhBMP-2', Biomaterials, Vol. 26, no. 17, 2005, pp. 3739-3748.

[92] Zhang, Y., Zhang, Y., Guo, S. and Huang, W., 'Tyrosine kinase inhibitor loaded PCL microspheres prepared by S/O/W technique using ethanol as pretreatment agent', Int J Pharm, Vol. 369, no. 1-2, 2009, pp. 19-23.

[93] Mayer, G. and Sarikaya, M., 'Rigid biological composite materials: structural examples for biomimetic design', Exp Mech, Vol. 42, no. 4, 2002, pp. 395-403.

[94] Sinha, A., Ingle, A., Munim, K., Vaidya, S., Sharma, B. and Bhisey, A., 'Development of calcium phosphate based bioceramics', B Mater Sci, Vol. 24, no. 6, 2001, pp. 653-657.

[95] Dorozhkin, S., 'Calcium orthophosphate-based biocomposites and hybrid biomaterials', J Mat Sci, Vol. 44, no. 9, 2009, pp. 2343-2387.

[96] Ye, H., Liu, X. and Hong, H., 'Characterization of sintered titanium/hydroxyapatite biocomposite using FTIR spectroscopy', J Mat Sci –Mater M, Vol. 20, no. 4, 2009, pp. 843-850.

[97] Erkmen, Z. E., Genc, Y. and Oktar, F. N., 'Microstructural and mechanical properties of hydroxyapatite-zirconia composites', J Am Ceram Soc, Vol. 90, no. 9, 2007, pp. 2885-2892.

[98] Abu Bakar, M. S., Cheng, M. H. W., Tang, S. M., Yu, S. C., Liao, K., Tan, C. T., Khor, K. A. and Cheang, P., 'Tensile properties, tension-tension fatigue and biological response of polyetheretherketone-hydroxyapatite composites for load-bearing orthopedic implants', Biomaterials, Vol. 24, no. 13, 2003, pp. 2245-2250.

[99] Wong, S.-C., Baji, A. and Gent, A. N., 'Effect of specimen thickness on fracture toughness and adhesive properties of hydroxyapatite-filled polycaprolactone', Compos Part A – Appl S, Vol. 39, no. 4, 2008, pp. 579-587.

[100] Kuo, M. C., Tsai, C. M., Huang, J. C. and Chen, M., 'PEEK composites reinforced by nano-sized SiO_2 and Al_2O_3 particulates', Mater Chem Phys, Vol. 90, no. 1, 2005, pp. 185-195.

[101] Ceramic-matrix composites, Warren, R. (ed.) (Chapman and Hall; 1992).

[102] Iroh, J. O., 'Poly(ε-caprolactone)', In: Polymer data handbook. (Oxford University Press; 1999), pp. 361-362.

[103] Levingstone, T., 'Optimisation of plasma sprayed hydroxyapatite coatings', PhD thesis, (Dublin City University; Dublin, Ireland, 2008).

[104] Ceram-research-Ltd., 'Table 1. Typical physical and mechanical properties of titania.' http://www.azom.com/Details.asp?ArticleID=1179, accessed 19/05/2009, 2002).

[105] Chou, B.-Y. and Chang, E., 'Microstructural characterization of plasma-sprayed hydroxyapatite-10 wt% ZrO_2 composite coating on titanium', Biomaterials, Vol. 20, no. 19, 1999, pp. 1823-1832.

[106] Rapacz-Kmita, A., Slosarczyk, A., Paszkiewicz, Z. and Paluszkiewicz, C., 'Phase stability of hydroxyapatite-zirconia (HAp-ZrO2) composites for bone replacement', J Mol Struct, Vol. 704, no. 1-3, 2004, pp. 333-340.

[107] Heimann, R. and Vu, T., 'Effect of CaO on thermal decomposition during sintering of composite hydroxyapatite-zirconia mixtures for monolithic bioceramic implants', J Mater Sci Lett, Vol. 16, no. 6, 1997, pp. 437-439.

[108] Chiu, C.-Y., Hsu, H.-C. and Tuan, W.-H., 'Effect of zirconia addition on the microstructural evolution of porous hydroxyapatite', Ceram Int, Vol. 33, no. 5, 2007, pp. 715-718.

[109] Chang, E., Chang, W. J., Wang, B. C. and Yang, C. Y., 'Plasma spraying of zirconia-reinforced hydroxyapatite composite coatings on titanium: part I - phase, microstructure and bonding strength', J Mater Sci -Mater M, Vol. 8, no. 4, 1997, pp. 193-200.

[110] Fu, L., Khor, K. A. and Lim, J.-P., 'Effects of yttria-stabilized zirconia on plasma-sprayed hydroxyapatite/yttria-stabilized zirconia composite coatings', J Am Ceram Soc, Vol. 85, no. 4, 2002, pp. 800-806.

[111] Lee, T. M., Yang, C. Y., Chang, E. and Tsai, R. S., 'Comparison of plasma-sprayed hydroxyapatite coatings and zirconia-reinforced hydroxyapatite composite coatings: in vivo study', J Biomed Mater Res-A, Vol. 71A, no. 4, 2004, pp. 652-660.

[112] Lee, T. M., Tsai, R. S., Chang, E., Yang, C. Y. and Yang, M. R., 'Biological responses of neonatal rat calvarial osteoblasts on plasma-sprayed HA/ZrO$_2$ composite coating', J Mater Sci -Mater M, Vol. 13, no. 3, 2002, pp. 281-287.

[113] Evis, Z., Sato, M. and Webster, T. J., 'Increased osteoblast adhesion on nanograined hydroxyapatite and partially stabilized zirconia composites', J Biomed Mater Res A, Vol. 78, 2006, pp. 500–507.

[114] Ning, C. Q. and Zhou, Y., 'On the microstructure of biocomposites sintered from Ti, HA and bioactive glass', Biomaterials, Vol. 25, no. 17, 2004, pp. 3379-3387.

[115] Chu, C., Xue, X., Zhu, J. and Yin, Z., 'Mechanical and biological properties of hydroxyapatite reinforced with 40 vol% titanium particles for use as hard tissue replacement', J Mat Sci –Mater M, Vol. 15, no. 6, 2004, pp. 665-670.

[116] Ning, C. Q., Zhou, Y., Wang, H. L., Jia, D. C. and Lei, T. C., 'Apatite formation on the surface of a Ti/HA composite in a simulated body fluid', J Mater Sci Lett, Vol. 19, no. 14, 2000, pp. 1243-1245.

[117] Li, H., Khor, K. A. and Cheang, P., 'Titanium dioxide reinforced hydroxyapatite coatings deposited by high velocity oxy-fuel (HVOF) spray', Biomaterials, Vol. 23, no. 1, 2002, pp. 85-91.

[118] Vu, T. and Heimann, R., 'Influence of the CaO/TiO$_2$ ratio on thermal stability of hydroxyapatite in the system Ca$_5$(PO$_4$)$_3$OH-CaO-TiO$_2$', J Mater Sci Lett, Vol. 16, no. 20, 1997, pp. 1680-1682.

[119] Lin, C.-M. and Yen, S.-K., 'Characterization and bond strength of electrolytic HA/TiO2 double layers for orthopedic applications', J Mat Sci -Mater M, Vol. 15, no. 11, 2004, pp. 1237-1246.

[120] Kim, H.-W., Kim, H.-E., Salih, V. and Knowles, J. C., 'Hydroxyapatite and titania sol-gel composite coatings on titanium for hard tissue implants; Mechanical and in vitro biological performance', J Biomed Mater Res, Vol. 72B, no. 1, 2005, pp. 1-8.

[121] Ramires, P. A., Romito, A., Cosentino, F. and Milella, E., 'The influence of titania/hydroxyapatite composite coatings on in vitro osteoblasts behaviour', Biomaterials, Vol. 22, no. 12, 2001, pp. 1467-1474.

[122] Yu, S., Hariram, K. P., Kumar, R., Cheang, P. and Khor, K. A., 'In vitro apatite formation and its growth kinetics on hydroxyapatite/polyetheretherketone biocomposites', Biomaterials, Vol. 26, no. 15, 2005, pp. 2343-2352.

[123] Abu Bakar, M. S., Cheang, P. and Khor, K. A., 'Thermal processing of hydroxyapatite reinforced polyetheretherketone composites', J Mater Process Tech, Vol. 89-90, 1999, pp. 462-466.

[124] Quiquerez, M., Peroglio, M., Gremillard, L., Chevalier, J., Chazeau, L., Gauthier, C., Hamaide, T. and Bignon, A., 'Improvement of the mechanical properties of calcium phosphate bone substitutes by polycaprolactone infiltration', Key Eng Mat, Vol. 361-363, 2008, pp. 403-406.

[125] Coombes, A. G. A., Rizzi, S. C., Williamson, M., Barralet, J. E., Downes, S. and Wallace, W. A., 'Precipitation casting of polycaprolactone for applications in tissue engineering and drug delivery', Biomaterials, Vol. 25, no. 2, 2004, pp. 315-325.

[126] Marra, K. G., Szem, J. W., Kumta, P. N., DiMilla, P. A. and Weiss, L. E., 'In vitro analysis of biodegradable polymer blend/hydroxyapatite composites for bone tissue engineering', J Biomed Mat Res-A, Vol. 47, no. 3, 1999, pp. 324-335.

[127] Hermanek, F. J., 'Thermal spraying: what it was and what it has become', Int J Powder Metall, Vol. 38, no. 7, 2002, pp. 35-44.

[128] Handbook of thermal spray technology, Davis, J. R. (ed.) (ASM Thermal Spray Society; Ohio, USA, 2005).

[129] Dorfman, M. R. and Novinski, E., 'Let's talk thermal spray', Products Finishing Magazine, 1993), pp. 41-47.

[130] Herman, H., Sampath, S. and McCune, R., 'Thermal spray: current status and future trends', MRS bulletin, Vol. June, 2000, pp. 17-25.

[131] Berndt, C. C. and Knight, R., 'Thermal spray technology', Course notes in ITSC 2007, Beijing, China (ASM Thermal Spray Society; 2007).

[132] Boulos, M., Fauchais, P. and Heberlein, J., 'Understanding and improving your thermal spray process', Course notes in ITSC 2007, Beijing, China (ASM Thermal Spray Society; 2007).

[133] Fauchais, P., 'Understanding plasma spraying', J Phys D -Appl Phys, Vol. 37, 2004, pp. R86-R108.

[134] Kurzweg, H., Heimann, R. B., Troczynski, T. and Wayman, M. L., 'Development of plasma-sprayed bioceramic coatings with bond coats based on titania and zirconia', Biomaterials, Vol. 19, no. 16, 1998, pp. 1507-1511.

[135] Khor, K. A. and Cheang, P., 'Plasma sprayed hydroxyapatite (HA) coatings produced with flame spheroidised powders', J Mater Process Tech, Vol. 63, no. 1-3, 1997, pp. 271-276.

[136] Kulkarni, A., Vaidya, A., Goland, A., Sampath, S. and Herman, H., 'Processing effects on porosity-property correlations in plasma sprayed yttria-stabilized zirconia coatings', Mat Sci Eng A- Struct, Vol. 359, no. 1-2, 2003, pp. 100-111.

[137] Kweh, S. W. K., Khor, K. A. and Cheang, P., 'Plasma-sprayed hydroxyapatite (HA) coatings with flame-spheroidized feedstock: microstructure and mechanical properties', Biomaterials, Vol. 21, 2000, pp. 1223 - 1234.

[138] Dyshlovenko, S., Pawlowski, L. and Roussel, P., 'Experimental investigation of influence of plasma spraying operational parameters on properties of hydroxyapatite', ITSC 2008 – Thermal spray: Crossing borders, B.P. Marple, M. M. Hyland, Y.-C. Lau, C.-J. Li, R. S. Lima, G. Montavon (eds.), (DVS; Maastricht, 2008).

[139] Tong, W., Chen, J. and Xingdong, Z., 'Amorphization and recrystallization during plasma spraying of hydroxyapatite', Biomaterials, Vol. 16, no. 11, 1995, pp. 829-832.

[140] Sun, L., Berndt, C. C. and Grey, C. P., 'Phase, structural and microstructural investigations of plasma sprayed hydroxyapatite coatings', Mat Sci Eng A -Struct, Vol. 360, no. 1-2, 2003, pp. 70-84.

[141] Lu, Y. P., Li, S. T., Zhu, R. F. and Li, M. S., 'Further studies on the effect of stand-off distance on characteristics of Plasma Sprayed Hydroxyapatite coating', Surf Coat Techn, Vol. 157, 2002, pp. 221-225.

[142] Schadler, L., Laut, K., Smith, R. and Petrovicova, E., 'Microstructure and mechanical properties of thermally sprayed silica/nylon nanocomposites', J Therm Spray Techn, Vol. 6, no. 4, 1997, pp. 475-485.

[143] Niebuhr, D. and Scholl, M., 'Synthesis and performance of plasma-sprayed polymer/steel coating system', J Therm Spray Techn, Vol. 14, no. 4, 2005, pp. 487-494.

[144] Chen, H., Ding, C. and Lee, S., 'Phase composition and microstructure of vacuum plasma sprayed nanostructured zirconia coating', Mat Sci Eng A -Struct, Vol. 361, no. 1-2, 2003, pp. 58-66.

[145] Weng, J., Liu, Q., Wolke, J. G. C., Zhang, X. and de Groot, K., 'Formation and characteristics of the apatite layer on plasma-sprayed hydroxyapatite coatings in simulated body fluid', Biomaterials, Vol. 18, no. 15, 1997, pp. 1027-1035.

[146] Yang, Y.-C. and Chang, E., 'Measurements of residual stresses in plasma-sprayed hydroxyapatite coatings on titanium alloy', Surf Coat Tech, Vol. 190, no. 1, 2005, pp. 122-131.

[147] Kuroda, S. and Clyne, T. W., 'The quenching stress in thermally sprayed coatings', Thin Solids Films, Vol. 200, 1991, pp. 49-66.

[148] Tsui, Y. C. and Clyne, T. W., 'An analytical model for predicting residual stresses in progressively deposited coatings. Part 1- planar geometry', Thin Solid Films, Vol. 306, 1997, pp. 23-33.

[149] Zhang, X. C., Xu, B. S., Wang, H. D. and Wu, Y. X., 'Modelling of the residual stresses in plasma-spraying functionally graded ZrO_2/NiCoCrAlY coatings using finite element method', Mater Design, Vol. 27, 2006, pp. 308-315.

[150] Zhang, X., Gong, J. and Tu, S., 'Effect of spraying condition and material properties on the residual stress in plasma spraying', J Mater Sci Technol, Vol. 20, no. 2, 2004, pp. 149-153.

[151] Jiang, Y., Xu, B.-S. and Wang, H.-D., 'Residual stresses within sprayed coatings', Journal of Central South University of Technology, Vol. 12, no. 2, 2005, pp. 53-58.

[152] Bruno, G., Fanara, C., Guglielmetti, F. and Malard, B., 'Characterization and residual stress analysis of wear resistant Mo thermal spray-coated steel gear wheels', Surf Coat Tech, Vol. 200, no. 14-15, 2006, pp. 4266-4276.

[153] Fang, J. C. and Xu, W. J., 'Plasma spray forming', J Mater Process Tech, Vol. 129, no. 1-3, 2002, pp. 288-293.

[154] Pawloski, L., The science and engineering of thermal spraying coatings (Wiley; New York, 1995).

[155] Clyne, T. and Gill, S., 'Residual stresses in thermal spray coatings and their effect on interfacial adhesion: a review of recent work', J Therm Spray Techn, Vol. 5, no. 4, 1996, pp. 401-418.

[156] Tsui, Y. C., Doyle, C. and Clyne, T. W., 'Plasma sprayed hydroxyapatite coatings on titanium substrates. Part 2: optimisation of coating properties', Biomaterials, Vol. 19, no. 22, 1998, pp. 2031-2043.

[157] Helali, M. M., 'A technique for fabricating complex-shaped thin-walled components in hard materials using a HVOF process', PhD thesis, (Dublin City University; Dublin, Ireland, 1996).

[158] Stokes, J. and Looney, L., 'HVOF system definition to maximise the thickness of formed components', Surf Coat Tech, Vol. 148, no. 1, 2001, pp. 18-24.

[159] Shi, S. and Hwang, J.-Y., 'Plasma spray fabrication of near-net-shape ceramic objects', Journal of Minerals & Materials Characterization & Engineering, Vol. 2, no. 2, 2003, pp. 145-150.

[160] Agarwal, A., McKechnie, T. and Seal, S., 'Net shape nanostructured aluminum oxide structures fabricated by plasma spray forming', J Therm Spray Techn, Vol. 12, no. 3, 2003, pp. 350-359.

[161] Devasenapathi, A., Ng, H. W., Yu, S. C. M. and Indra, A. B., 'Forming near net shape free-standing components by plasma spraying', Mater Lett, Vol. 57, no. 4, 2002, pp. 882-886.

[162] Berndt, C. C., Brogan, J. A., Montavon, G., Claudon, A. and Coddet, C., 'Mechanical properties of metal and ceramic-polymer composites formed via thermal spray consolidation', J Therm Spray Techn, Vol. 7, no. 3, 1998, pp. 337-339.

[163] Khor, K. A., Gu, Y. W., Li, Y., Quek, C. H., Lim, V. J. P. and Cheang, P., 'Novel bioactive composites by thermal spray process', 1[er] ITSC - Thermal spray: surface engineering via applied research, C. C. Berndt (ed.) (ASM International; Montreal, Canada, 2000), pp. 625-633.

[164] Petricova, E., Knight, R. and Schadler, L. S., 'Structure and properties of HVOF sprayed ceramic/polymer nanocomposite coating', 1st UTSC. Thermal spray: a united forum for scientific and technological advances, C. C. Berndt (ed.) (ASM International; Indianapolis, Indiana, USA, 1997), pp. 877-883.

[165] Mateus, C., Costil, S., Bolot, R. and Coddet, C., 'Ceramic/fluoropolymer composite coatings by thermal spraying - a modification of surface properties', Surf Coat Tech, Vol. 191, no. 1, 2005, pp. 108-118.

[166] Brogan, J. A., Gross, K. A., Chen, Z., Berndt, C. C. and Herman, H., 'Investigation of combustion sprayed hydroxyapatite/polymer composite coatings', 7th NTSC - Thermal spray industrial application conference, C. C. Berndt and S. Sampath (eds.) (ASM International; Boston, Massachusetts, USA, 1994), pp. 159-164.

[167] Quek, C. H., Khor, K. A. and Cheang, P., 'Plasma spraying of hydroxyapatite/ Ti-6Al-4V composite coating', 2nd UTSC - Tagunsband Conference Proceedings, E. Lungscheider and P.A. Kammer (eds.) (DVS; Dusseldorf, Germany, 1999), pp. 27-31.

[168] Tufa, K. Y. and Gitzhofer, F., 'DC plasma sprayed polymer composite coatings for abrasion resistant protective surfaces', 15th ITSC -Thermal spray: meeting the challenges of the 21st century, C. Coddet (ed.) (ASM International; Nice, France, 1998), pp. 157-162.

[169] Henne, R. H. and Schitter, C., 'Plasma spraying of high performance thermoplastics', 8th NTSC -Advances in thermal spray science and technology, C. C. Berndt and S. Sampath (eds.) (ASM International; Houston, Texas, USA, 1995), pp. 527-531.

[170] Vardelle, M., Fauchais, P., Vardelle, A., Li, K., Dussoubs, B. and Themelis, N., 'Controlling particle injection in plasma spraying', J Therm Spray Techn, Vol. 10, no. 2, 2001, pp. 267-284.

[171] Lugscheider, E., Loch, M. and Suk, H. G., 'Powder technology-State of the art', 13th ITSC - Thermal spray: international advances in coatings technologies, C. C. Berndt (ed.) (ASM International; Orlando, Florida, USA, 1992).

[172] Costil, S., Mateus, C. and Coddet, C., 'Ceramic/fluoropolymer composite coatings by plasma spraying', Surf Coat Tech, Vol. 201, no. 5, 2006, pp. 2020-2027.

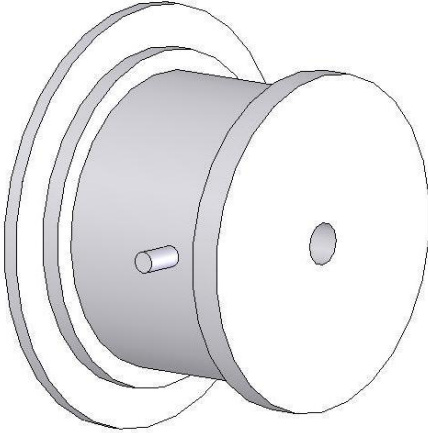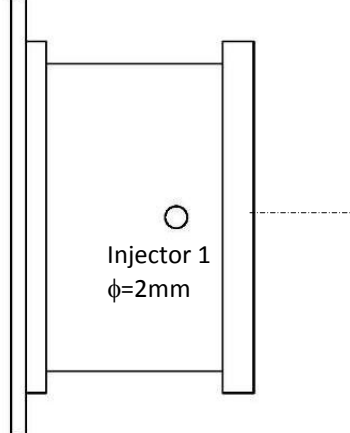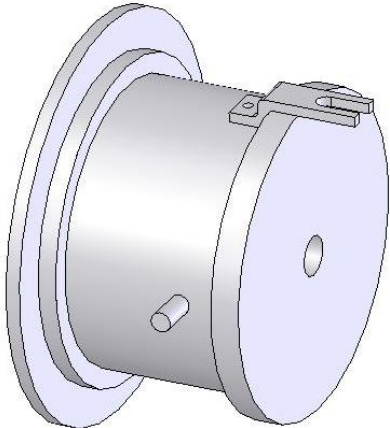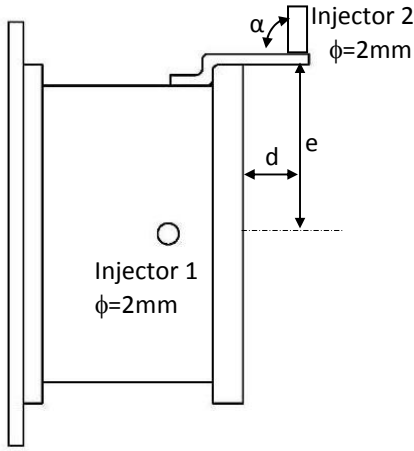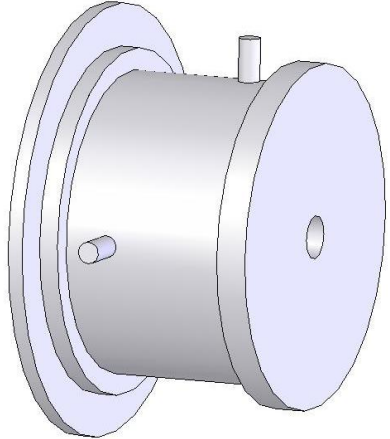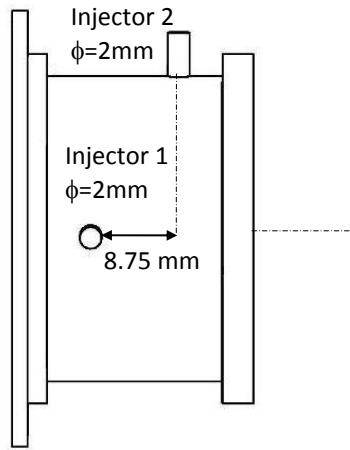[173] Petrovicova, E. and Schadler, L. S., 'Thermal spraying of polymers', Int Mater Rev, Vol. 47, 2002, pp. 169-190.

[174] Bao, Y., Gawne, D. T. and Zhang, T., 'The effect of feedstock particle size on the heat transfer rates and properties of thermally sprayed polymer coatings', Trans Inst Met Finish, Vol. 73, no. 4, 1995, pp. 119-124.

[175] Bao, Y., Gawne, D. T., Vesely, D. and Bevis, M. J., 'Production of polymer matrix composite coatings by thermal spraying', Trans Inst Met Finish, Vol. 72, no. 3, 1994, pp. 110-113.

[176] Liao, H., Beche, E., Berger, F. and Coddet, C., 'On the microstructures of thermally sprayed "PEEK" polymer', 15th ITSC -Thermal Spray: Meeting the challenges of the 21st century, C. Coddet (ed.) (ASM International; Nice, France, 1998), pp. 25-29.

[177] Sweet, G. K., 'Applying thermoplastic/thermoset powder with a modified plasma system', 6th NTSC - Thermal Spray Coatings: Research, Design and Applications, C. C. Berndt and T.F. Bernecki (eds.) (ASM International; Anaheim, California, USA, 1993), pp. 381-384.

[178] Zhang, T., Gawne, D. T. and Bao, Y., 'The effect of deposition parameters on the degradation of plasma sprayed polymer coatings', 9th NTSC - Thermal Spray: practical solutions for engineering problems, C. C. Berndt (ed.) (ASM International; Cincinnati, Ohio, USA, 1996), pp. 231-237.

[179] Chen, J., Tong, W., Cao, Y., Feng, J. and Zhang, X., 'Effect of atmosphere on phase transformation in plasma-sprayed hydroxyapatite coatings during heat treatment', J Biomed Mater Res-A, Vol. 34, no. 1, 1997, pp. 15-20.

[180] Cizek, J., Khor, K. A. and Prochazka, Z., 'Influence of spraying conditions on thermal and velocity properties of plasma sprayed hydroxyapatite', Mater Sci Eng C, Vol. 27, no. 2, 2007, pp. 340-344.

[181] Dyshlovenko, S., Pawlowski, L., Roussel, P., Murano, D. and Le Maguer, A., 'Relationship between plasma spray operational parameters and microstructure of hydroxyapatite coatings and powder particles sprayed into water', Surf Coat Tech, Vol. 200, no. 12-13, 2006, pp. 3845-3855.

[182] Ong, J., Appleford, M., Oh, S., Yang, Y., Chen, W., Bumgardner, J. and Haggard, W., 'The characterization and development of bioactive hydroxyapatite coatings', JOM-J Min Met Mat S, Vol. 58, no. 7, 2006, pp. 67-69.

[183] Kurzweg, H., Heimann, R. B. and Troczynski, T., 'Adhesion of thermally sprayed hydroxyapatite-bond-coat systems measured by a novel peel test', J Mat Sci –Mater M, Vol. 9, no. 1, 1998, pp. 9-16.

[184] Khor, K. A., Gu, Y. W., Pan, D. and Cheang, P., 'Microstructure and mechanical properties of plasma sprayed HA/YSZ/Ti-6Al-4V composite coatings', Biomaterials, Vol. 25, no. 18, 2004, pp. 4009-4017.

[185] Balani, K., Anderson, R., Laha, T., Andara, M., Tercero, J., Crumpler, E. and Agarwal, A., 'Plasma-sprayed carbon nanotube reinforced hydroxyapatite coatings and their interaction with human osteoblasts in vitro', Biomaterials, Vol. 28, no. 4, 2007, pp. 618-624.

[186] Heimann, R. B., 'Thermal spraying of biomaterials', Surf Coat Tech, Vol. 201, no. 5, 2006, pp. 2012-2019.

[187] 'INASMET LEPS data sheet'.

[188] 'Sultzer Metco product catalogue'.

[189] 'NIST/SEMATECH e-Handbook of Statistical Methods' (http://www.itl.nist.gov/div898/handbook/, accessed 05/06/2008).

[190] Pierlot, C., Pawlowski, L., Bigan, M. and Chagnon, P., 'Design of experiments in thermal spraying: a review', Surf Coat Tech, Vol. 202, no. 18, 2008, pp. 4483-4490.

[191] Box, G. E. P. and Behnken, D. W., 'Some new three level designs for the study of quantitative variables', Technometrics, Vol. 2, no. 4, 1960, pp. 455-475.

[192] Allen, T., Particle size measurement (Chapman & Hall; New York, USA, 1981).

[193] Venkataraman, R., Das, G., Singh, S. R., Pathak, L. C., Ghosh, R. N., Venkataraman, B. and Krishnamurthy, R., 'Study on influence of porosity, pore size, spatial and topological distribution of pores on microhardness of as plasma sprayed ceramic coatings', Mat Sci Eng A -Struct, Vol. 445-446, 2007, pp. 269-274.

[194] Benjamin, J. S., 'Dispersion strengthened super alloys by mechanical alloying', Met Trans A - Phys Met Mater Sci, Vol. 1, no. 10, 1970, pp. 2943-2951.

[195] Suryanarayana, C., 'Powder metal technologies and applications', ASM handbook, Vol. 7, 1998.

[196] Kweh, S. W. K., Khor, K. A. and Cheang, P., 'The production and characterization of hydroxyapatite (HA) powders', J Mater Process Tech, Vol. 89-90, 1999, pp. 373-377.

[197] Chou, B.-Y. and Chang, E., 'Plasma-sprayed hydroxyapatite coating on titanium alloy with ZrO2 second phase and ZrO2 intermediate layer', Surf Coat Tech, Vol. 153, no. 1, 2002, pp. 84-92.

[198] Cintas, J., 'Fabricación de aluminio de alta resistencia por mecanosintesis y sinterizacion ', (in Spanish), PhD thesis, (University of Seville; Seville, Spain, 2003).

[199] Cheang, P. and Khor, K. A., 'Addressing processing problems associated with plasma spraying of hydroxyapatite coatings', Biomaterials, Vol. 17, no. 5, 1996, pp. 537-544.

[200] Dowson, G., Powder metallurgy: the process and its products (Springer; New York, USA, 1990).

[201] Hou, H. and Sun, C. C., 'Quantifying effects of particulate properties on powder flow properties using a ring shear tester', J Pharm Sci, Vol. 97, no. 9, 2008, pp. 4030-4039.

[202] Prescott, J. K. and Barnum, B. A., 'On powder flowability', Pharmaceutical Technology, Vol. 24, no. 10, 2000, pp. 60-85.

[203] 'ISO 3252:1999 - Powder metallurgy - Vocabulary', (ISO; 1999).

[204] 'ISO 4490: 2008 - Metallic powders - Determination of flow rate by means of a calibrated funnel (Hall flowmeter)', (ISO; 2008).

[205] 'ISO 3923-1:2008 - Metallic powders - Determination of apparent density - Part 1: Funnel method', (ISO; 2008).

[206] 'ISO 3923-2:1981 - Metallic powders - Determination of apparent density - Part 2: Scott volumeter method', (ISO; 1981).

[207] 'ASTM B527-06 - Standard test method for determination of tap density of metallic powders and compounds ', (ASTM; 2006).

[208] 'ASTM F 2024-00 - Standard Practice for X-ray determination of phase content of plasma-sprayed hydroxyapatite coatings', (ASTM; 2000).

[209] Baji, A., Wong, S.-C., Liu, T., Li, T. and Srivatsan, T. S., 'Morphological and X-ray diffraction studies of crystalline hydroxyapatite-reinforced polycaprolactone', J Biomed Mater Res-B, Vol. 81B, 2007, pp. 343-350.

[210] Hogne, G. W. H., Hemminger, W. F. and Flammersheim, H. J., Differential scanning calorimetry (Springer; Heidelberg, Germany, 2003).

[211] Du, H., Lee, S. and Shin, J., 'Study on porosity of plasma-sprayed coatings by digital image analysis method', J Therm Spray Techn, Vol. 14, no. 4, 2005, pp. 453-461.

[212] Mohammadi, Z., Ziaei-Moayyed, A. A. and Mesgar, A. S.-M., 'Adhesive and cohesive properties by indentation method of plasma-sprayed hydroxyapatite coatings', Appl Surf Sci, Vol. 253, no. 11, 2007, pp. 4960-4965.

[213] Bolelli, G., Lusvarghi, L., Manfredini, T. and Mantini, F. P., 'Comparison between plasma- and HVOF-sprayed ceramic coatings. Part I: microstructure and mechanical properties', Int J Surf Sci Eng, Vol. 1, no. 1, 2007, pp. 38-61.

[214] Riester, L., Bell, T. J. and Fischer-Cripps, A. C., 'Analysis of depth-sensing indentation tests with a knoop indentor', J Mater Res, Vol. 16, no. 6, 2001, pp. 1660-1667.

[215] Singh, J. P., Sutaria, M. and Ferber, M., 'Use of indentation technique to measure elastic modulus of plasma-sprayed zirconia thermal barrier coating', 21st annual conference on composites, advanced ceramics, materials, and structures, (Ceramic engineering and science proceedings; Cocoa Beach, Florida, USA, 1997), pp. 191-200.

[216] Rabilloud, G., High-performance polymers: conductive adhesives (TECHNIP; Paris, France, 1997).

[217] Stanford, M. K., Dellacorte, C. and Eylon, D., 'Particle morphology effects on flow characteristics of ps304 plasma spray coating feedstock powder blend', (NASA; USA, 2002).

[218] Rapacz-Kmita, A., Paluszkiewicz, C., Slósarczyk, A. and Paszkiewicz, Z., 'FTIR and XRD investigations on the thermal stability of hydroxyapatite during hot pressing and pressureless sintering processes', J Mol Struct, Vol. 744-747, 2005, pp. 653-656.

[219] Fougnies, C., Damman, P., Dosiere, M. and Koch, M. H. J., 'Time-resolved SAXS, WAXS, and DSC Study of melting of poly(aryl ether ether ketone) (PEEK) annealed from the amorphous state', Macromolecules, Vol. 30, no. 5, 1997, pp. 1392-1399.

[220] Wang, Y., Qin, Y., Li, G., Cui, Z. and Zhang, Z., 'One-step synthesis and optical properties of blue titanium suboxide nanoparticles', J Cryst Growth, Vol. 282, no. 3-4, 2005, pp. 402-406.

[221] Le Page, Y. and Strobel, P., 'Structural chemistry of Magnéli phases Ti_nO_{2n-1} ($4 \leq n \leq 9$). I. Cell and structure comparisons', J Solid State Chem, Vol. 43, 1982, pp. 314-319.

[222] Heimann, R., 'Design of novel plasma sprayed hydroxyapatite-bond coat bioceramic systems', J Therm Spray Techn, Vol. 8, no. 4, 1999, pp. 597-603.

[223] Fazan, F. and Marquis, P. M., 'Dissolution behavior of plasma-sprayed hydroxyapatite coatings', J Mater Sci -Mater M, Vol. 11, no. 12, 2000, pp. 787-792.

[224] Dyshlovenko, S., Pateyron, B., Pawlowski, L. and Murano, D., 'Numerical simulation of hydroxyapatite powder behaviour in plasma jet', Surf Coat Tech, Vol. 179, no. 1, 2004, pp. 110-117.

[225] Berndt, C. C. and Gross, K. A., 'Characteristics of hydroxylapatite biocoatings', 13th ITSC - Thermal spray: international advances in coatings technology, C.C. Berndt (ed.) (ASM International; Orlando, Florida, USA, 1992), pp. 465-470.

[226] Khor, K. A. and Cheang, P., 'Characterization of plasma sprayed hydroxyapatite powders and coatings', 6th NTSC - Thermal Spray Coatings: Research, Design and Applications, C. C. Berndt and T.F. Bernecki (eds.) (ASM International; Anaheim, California, USA, 1993), pp. 347-352.

[227] 'BS ISO 13779-2:2000 - Implants for surgery- hydroxyapatite. Part 2: coatings of hydroxyapatite', ISO (ed.) 2000).

[228] Gross, K. A., Berndt, C. C. and Herman, H., 'Amorphous phase formation in plasma-sprayed hydroxyapatite coatings', J Biomed Mater Res, Vol. 39, no. 3, 1998, pp. 407-414.

[229] Weng, J., Liu, X.-G., Li, X.-D. and Zhang, X.-D., 'Intrinsic factors of apatite influencing its amorphization during plasma-spray coating', Biomaterials, Vol. 16, no. 1, 1995, pp. 39-44.

[230] Wolke, J. G. C., Klein, C. P. A. T. and de Groot, V., 'Plasma-sprayed hydroxylapatite coatings for biomedical applications', 3rd NTSC - Thermal spray research and applications, T.F. Bernecki (ed.) (ASM International; Long Beach, California, USA, 1990), pp. 413-417.

[231] Di Vona, M. L., Marani, D., D'Epifanio, A., Traversa, E., Trombetta, M. and Licoccia, S., 'A covalent organic/inorganic hybrid proton exchange polymeric membrane: synthesis and characterization', Polymer, Vol. 46, no. 6, 2005, pp. 1754-1758.

[232] Simonin, L. and Liao, H., 'Characterization of flame-sprayed PEEK coatings by FTIR-ATR, DSC and acoustic microscopy', Macromol Mater Eng, Vol. 283, no. 1, 2000, pp. 153-162.

[233] Zhao, L., Bobzin, K., Ernst, F., Zwick, J. and Lugscheider, E., 'Study on the influence of plasma spray processes and spray parameters on the structure and crystallinity of hydroxylapatite coatings', Materialwissenschaft und Werkstofftechnik, Vol. 37, no. 6, 2006, pp. 516-520.

[234] Puerta, D., Anderson, F. and Geary, M., 'The metallographic characterization of thermal spray coatings microstructures', ITSC 2008 - Thermal spray: crossing boarders, L. Lugscheider (ed.) (ASM International; Maastricht, The Netherlands, 2008).

[235] Eosoly, S., 'Selective Laser Sintering polycaprolactone composite scaffolds', PhD thesis, (Dublin City University; Dublin, Ireland, 2009).

Appendix A - LEPS gun configurations

CONFIGURATON 1

CONFIGURATON 2

CONFIGURATON 3

Appendix B - Analysis of Variance (ANOVA) statistical output

Prior to understanding the ANOVA output some statistical terminology and definitions should be listed:

1. Terminology:

   - Term: Each of the listed factors or factor interactions (A, B, AB, AB^2, etc.) having an effect on the model.

   - Residual: Terms not included in the model which are used to estimate experimental error.

   - Model: Terms estimating factor effects.

   - Pure error: Amount of variation in the response in replicated design points.

   - Lack of fit (LOF): Variation of the data around the fitted model. LOF is significant if the model does not fit the data properly.

   - Curvature: Variable which compares the average of the actual centre points to the estimated value of the centre point calculated as an average from all factorial points. A strong curvature is undesirable as it can mask the effect of the factors. If curvature is found to be significant it indicates the requirement for reduction of the factor ranges.

2. Definitions:

   - Term sum of squares (SS): The number of factorial experiments divided by 4 times the squared factor effect.

   - Term degrees of freedom (DF): It is the number of levels for a factor minus 1.

   - Term mean square (MS): Estimate term variance, which is calculated as term SS/DF.

   - Term F value: It is calculated as term mean square divided by the residual mean square. The term is less likely to have an effect on the response if the term variance is close to the residual variance (ratio ≈ 1).

- Term Prob>F: Probability of observing the calculated F value if there is no factor effect. This probability corresponds to the area under the F-distribution beyond the calculated F value. If (Prob>F)<0.05 the individual term on the model has significant effect on the response.

- Model SS: Total of the sum of squares for the terms in the model.

- Model DF: It is the number of model terms (p) minus 1.

- Model MS: Estimate model variance, which is calculated as $MS_{model}=SS/DF=SS/p-1$.

- Model F value and Prob>F: The same as for terms but with the model variables.

- Residual SS: Sum of squares of all the terms not included in the model

- Residual DF: Corrected total DF (number of experimental runs (n) minus 1) minus model DF. Therefore, (n-1)-(p-1) = n-p.

- Residual mean square (MSE): The estimate of process variance, which is $MS_{residual}=SS/DF=SS/n-p$.

- Pure error SS: Pure error sum of squares from replicate points.

- LOF SS: Residual SS - pure error SS.

- LOF Prob>F: In this case a small value of this variable means that the LOF is significant. Therefore, a LOF (Prob>F)>0.1 is preferable.

3. <u>ANOVA output:</u>

- Standard deviation (Std Dev) associated to the experiment: $\sqrt{MSE}$

- Mean: Average of all the response data.

- Coefficient of variance (C.V.): (Std Dev / Mean)*100.

- Predicted Residual Error Sum of Squares (PRESS): It is an indicator of the accuracy of the model to predict each design point. It is calculated predicting where each point would be in a model which contains all the other points. Then the squared residuals (difference between actual and predicted values) are summed up.

- R-squared (R^2): This value indicates the variability of the data around the mean described by the model and it provides a measure of the model accuracy to predict future points. R^2 value can vary from 0 to 1 and the closer it is to 1 the better the model is.

$$R^2 = 1 - \frac{SS_{residual}}{SS_{model} + SS_{residual}} = 1 - \frac{SS_{residual}}{SS_{total}}$$

- Adjusted R-squared (R^2_{adj}): This value adjusts R^2 for the number of terms in the model. It decreases if increasing the number of non-significant terms in the model.

$$R^2_{adj} = \frac{\frac{SS_{residual}}{DF_{residual}}}{\frac{SS_{model}}{DF_{model}} + \frac{SS_{residual}}{DF_{residual}}} = \frac{n-1}{n-p}(1 - R^2)$$

- Predicted R-squared (R^2_{pred}): This value indicates the variability in new data described by the model. This value and the previous one should be within 0.2 of each other.

$$R^2_{pred} = 1 - \frac{PRESS}{SS_{total} - SS_{block}}$$

- Adequate precision: This value reflects the signal to noise ratio and, therefore, the ratio of the predicted response to its associate error. A value greater than 4 is required to obtain adequate model discrimination.

Appendix C - Health and safety in plasma spaying

The plasma spraying technique is a safe process whilst the equipment should be treated with caution. The user must follow correct spraying practices and should take specific precautions against a number of hazards to avoid any accident or health problems in future. Preferably, the equipment should be automated and enclosed in a cabinet or a booth especially designed to extract fumes, reduce noise levels and prevent direct viewing of the plasma plume. If the equipment does not meet these safety requirements, the following hazards should be taken into account:

1. <u>Gases, fumes and dust particles</u>:

Proper extraction facilities are needed to ensure personal safety, but also to improve the quality of sprayed coatings. The use of breathing masks, fitted with suitable filters is strongly recommended where the equipment cannot be isolated.

The thermal spray booth design guidelines [1] prepared by the ASM-TSS Safety Committee establish that the typical air flow velocities in a booth should be in the range of 23-61 m/min (spray boxes will allow capture greater velocities because of the smaller sizes). The total air flow for large booths (plasma lab at DCU) should provide between 1.5 – 5 air changes per minute of the entire space volume per minute.

- *Gases*: Gas issued from the atmosphere dissociation and recombination from Plasma Spaying (NO_x, O_3) including the asphyxiating gases existing from the plasma torch (Ar, H_2, He and N_2). The NO_x together with the moisture present in lungs produce nitric acid [2].
- *Vapors and dust particles*: The atomisation of molten materials produces dust and fumes. When spraying certain materials specific hazards should be taken into account:
    - o Fine metal particles are potentially pyrophoric and none should be allowed to accumulate.

- Certain materials such as aluminum, zinc and other base metals may react with water to evolve hydrogen, which is potentially explosive. Special precautions are necessary.
- Some fumes, like those of zinc and copper alloys are unpleasant to smell, and may cause a fever-type reaction.
- Vapors resulting from particle vaporisation during the residence time in the plasma plume. This phenomenon is emphasised particularly when feedstock materials exhibit high vapor pressure [3].

2. Noise:

Plasma spraying equipment uses compressed gases which produce noise. Sound levels vary with the type of spraying equipment, the material being sprayed and the operating parameters. Levels as high as 125 dB(A) have been noted in APS processes [1, 4].

The Occupational Safety and Health Administration (OSHA) in United States require hearing protection at any exposure over 85 dB(A). Therefore, spray booths should be noise isolated. If this is not the case, the user should wear ear plugs and ear muffs to reduce the noise level. The ear plugs are designed for a reduction of 15-30 dB(A) of the total noise and the ear muffs for 17-28 dB(A). Using both pieces of safety equipment the noise level would be reduced to 67-93 dB (A), so the maximum exposure per day would be limited to 3 hours in the worst case [2].

3. Non-ionising radiation (Infrared and Ultraviolet radiation):

High temperature jets generate radiation in a broad range of wavelengths from Ultraviolet (UV) to visible and Infrared (IR) [3]. IR and UV light may damage delicate body tissues such as eyes and skin. Spray enclosures should be fitted with ultra-violet absorbent dark glass. Where this is not possible operators and others in the vicinity should wear protective goggles or welding masks containing a comfort shade number of 14 (Arc current: 400-800 A), being the minimum safe shade 10 [2]. Opaque screens should be placed around spraying areas. The nozzle of the gun should never be viewed directly unless the equipment is switched off.

4. <u>Thermal risks:</u>

The thermal effect of the plasma plume can be detected as far as 1m away from the plasma gun. The heat transfer to the surrounding area can cause severe burns by contact if the required precautions are not taken.

5. <u>Shock hazards:</u>

Plasma guns operate at low voltages, but at relatively high currents. Proper insulation of the gun and electric devices is absolutely necessary.

References

[1] Gifford, D., Pollard, L., Wuest, G. and Fletcher, R. C., 'Designation SG003-03: Thermal Spray Booth Design Guidelines', (ASM-TSS, 2003)

[2] Berndt, C. C. and Knight, R., 'Thermal Spray Technology', In: Course notes in ITSC 2007, Beijing, China (ASM Thermal Spray Society; 2007).

[3] Hériaud-Kraemer, H., Montavon, G., Coddet, C., Hertert, S. and Robin, H., 'Harmful risks for workers in thermal spraying: A review completed by a survey in a French company', J Therm Spray Techn, Vol. 12, no. 4, 2003, pp. 542-554.

[4] Gross, K. A., 'Noise emissions in thermal spray operations', J Therm Spray Techn, Vol. 11, no. 3, 2002, pp. 350-358.

Appendix D - J.C.P.D.S. powder diffraction files

Elements	Symbol	Formulae	Peak 2θ (^{o})	J.C.P.D.S.
Calcium Phosphates				
• Hydroxyapatite	HA	$Ca_{10}(PO_4)_6(OH)$	31.8	9-432
• α-Tricalcium Phosphate	α-TCP	α-$Ca_3(PO_4)_2$	30.8	9-348
• β-Tricalcium Phosphate	β-TCP	β-$Ca_3(PO_4)_2$	31.1	9-169
• Tetracalcium Phosphate	TTCP	$Ca_4(PO_4)_2O$	29.8	25-1137
• Calcium oxide	CaO	CaO	37.3	37-1497
• Oxyapatite	-	$Ca_{10}(PO_4)_6O$	31.7	89-6495
Titanium Oxides				
• Rutile	Rutile	TiO_2		21-1276
• Titanium oxide	-	Ti_9O_{17}		50-0791
• Titanium oxide	-	Ti_8O_{15}		50-0790
• Titanium oxide	-	Ti_7O_{13}		50-0789
• Titanium oxide	-	Ti_5O_9		51-0641
Yttria-stabilised Zirconia				
• Yttrium Zirconium Oxide	-	$Zr_{0.92}Y_{0.8}O_{1.96}$		48-0224
• Zirconium Oxide	Baddeleyite	ZrO_2		37-1484
Titanium				
• Titanium	-	Ti		44-1294

Appendix E - Porosity measurements

The MATLAB routine used to measure the porosity is shown in Table E.1. Basically, the image is read from the file and it is converted from 'rgb' (colour) to gray scale, and later to a binary image (black: porosity; white: material) using a threshold. The threshold was adjusted for the different images, depending on the brightness and contrast levels. Once the image has been threshold, the black pixels under 0.5 are removed as they are considered noise. Finally, the black and white pixels are quantified and the percentage of porosity is calculated. An SEM cross section and its threshold image can be seen as an example in Figure E.1.

Table E.1. MATLAB routine to measure porosity

```
❖  X=imread('c:/image.tif');
❖  X=rgb2gray(X);
❖  Threshold= 0.36
❖  bw = im2bw(X, Threshold); figure, imshow(bw)
❖  se = strel('disk',2);
❖  bw2=imclose(bw,se);
❖  figure, imshow(bw2)
❖  figure, imshow(X)
❖  A=size(find(bw2<0.5));
❖  IM=size(X);
❖  IMT=IM(1)*IM(2)
❖  porosity=(A(1)/IMT)*100
```
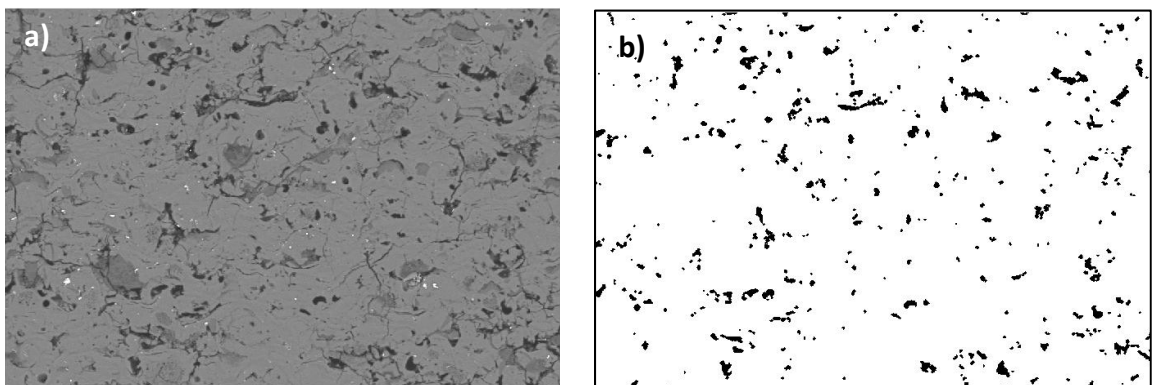

Figure E.1. Image processed by MATLAB: a) original image and b) threshold image